Electrical, Mechanical & Morphological Characterisation of Nanosheet Networks

Cian Gabbett

a thesis submitted for the degree of
Doctor of Philosophy

Under the supervision of
Professor Jonathan N. Coleman

school of physics
Trinity College Dublin

2021

Declaration

I declare that this thesis has not been submitted as an exercise for a degree at this or any other university and it is entirely my own work.

I agree to deposit this thesis in the University's open access institutional repository or allow the library to do so on my behalf, subject to Irish Copyright Legislation and Trinity College Library conditions of use and acknowledgement.

Elements of this work that have been carried out jointly with others or by collaborators have been duly acknowledged in the text wherever included.

Cian Gabbett

Electrical, Mechanical & Morphological Characterisation of Nanosheet Networks

Abstract

Networks of two-dimensional nanosheets have demonstrated significant promise across a host of applications that span the breadth of materials science. While this has driven research into nanosheet-based devices at a remarkable pace, a prevailing observation has been that the superlative physical properties of nanosheets do not naturally translate to their networks. To begin to address this dichotomy and realise their full potential, the electrical, mechanical and morphological properties of nanosheet networks are investigated in this work.

Composites of 2D nanosheets mixed with 1D single-walled carbon nanotubes (SWNTs) represent an exciting class of materials for electrochemical applications. Active material is supplied by the nanosheets while SWNTs provide mechanical reinforcement and enhanced electrical conductivity. Although charge transport in these systems has been studied, their mechanical properties have not yet been quantitatively examined. Here, both the mechanical and morphological character of SWNT / MoS_2 1D:2D nanocomposites are investigated as a function of SWNT volume fraction, φ. Microscopic analysis reveals the reinforcing SWNT network to evolve from a loosely connected structure for $\varphi < 1$ vol % to an entangled and continuous architecture for $\varphi > 1$ vol %. This transition has a considerable effect on the composite mechanical properties. Below 1 vol %, the composite modulus and failure-strain exhibit short-fibre composite behaviour. However, above 1 vol % both increase with φ in a manner consistent with fibrous networks. The composite tensile strength similarly evolves from a regime limited by the matrix-fibre interface at low-φ, to one limited by the strength of the nanotube ropes for $\varphi > 1$ vol %. Crucially, while the composite tensile toughness is constant at low-φ, it increases rapidly for $\varphi > 1$ vol % consistent with percolation theory. Quantitative models are presented to describe this mechanical evolution, which renders the composites robust at additive levels as low as ~ 5 vol % SWNTs.

Owing to the diverse electronic properties of their constituent nanosheets, 2D networks are well-placed to feature prominently in the growing field of printed electronics. While it is known that electrical performance in printed 2D networks is impeded by inter-nanosheet junctions, work to characterise this effect has been limited. To address this, the electrical conductivity of printed nanosheet networks is investigated as a function of constituent nanosheet length, l_{NS}. A family of size-selected WSe_2, graphene and silver 2D inks, each

spanning an order of magnitude in l_{NS}, are synthesised and printed. The in-plane conductivity of spray-coated WSe_2 networks is observed to decrease by an order of magnitude as l_{NS} is reduced from 462 nm to 62 nm. Significantly, the conductivity in both graphene and silver nanoplatelet networks exhibits the opposite response, scaling with ${l_{NS}}^{-1}$. A model to describe this length-dependent conductivity scaling in networks of solution-processed nanosheets is developed. This allows inter-nanosheet resistances of ~ 9 Ω, 31 kΩ and 120 MΩ to be approximated for silver, graphene and WSe_2, respectively.

To conclude, focused ion beam and scanning electron microscope nanotomography (FIB-SEM NT) is presented as a novel technique to assess the morphology of nanostructured systems. This is demonstrated through a length-dependent investigation of printed graphene networks for $l_{NS} = 947$, 630 and 215 nm. The network porosity is observed to steadily decrease from ~ 49 % to ~ 40 % as the constituent nanosheet length is reduced from 947 nm to 215 nm. Interestingly, the pore volume in each network is found to be highly contiguous with > 99 % of the total pore volume contained in a single open pore. A reduction in nanosheet size is seen to increase the specific surface area of the printed networks from ~ 14 $m^2 g^{-1}$ to ~ 23 $m^2 g^{-1}$ as l_{NS} is decreased from 947 to 215 nm. Notably, both pore size and shape are found to be a function of nanosheet length. Finally, the alignment of each printed network is evaluated using Fourier transforms, where networks comprising larger nanosheets demonstrate enhanced alignment.

Publications

1. Gabbett, C., Boland, C.S., Harvey, A., Vega-Mayoral, V., Young, R.J. and Coleman, J.N. (2018). The effect of network formation on the mechanical properties of 1D:2D nano:nano composites. *Chemistry of Materials*, 30(15), pp.5245-5255.

2. Abdul-Jabbar, N.M., Poerschke, D.L., Gabbett, C. and Levi, C.G. (2018). Phase equilibria in the zirconia–yttria/gadolinia–silica systems. *Journal of the European Ceramic Society*, 38(9), pp.3286-3296.

3. Harvey, A., Backes, C., Boland, J.B., He, X., Griffin, A., Szydlowska, B., Gabbett, C., Donegan, J.F. and Coleman, J.N. (2018). Non-resonant light scattering in dispersions of 2D nanosheets. *Nature Communications*, 9(1), pp.1-11.

4. Biccai, S., Boland, C.S., O'Driscoll, D.P., Harvey, A., Gabbett, C., O'Suilleabhain, D.R., Griffin, A.J., Li, Z., Young, R.J. and Coleman, J.N. (2019). Negative gauge factor piezoresistive composites based on polymers filled with MoS_2 nanosheets. *ACS Nano*, 13(6), pp.6845-6855.

5. Boland, J.B., Tian, R., Harvey, A., Vega-Mayoral, V., Griffin, A., Horvath, D.V., Gabbett, C., Breshears, M., Pepper, J., Li, Y. and Coleman, J.N. (2020). Liquid phase exfoliation of GeS nanosheets in ambient conditions for lithium ion battery applications. *2D Materials*, 7(3), p.035015.

6. O'Suilleabhain, D., Kelly, A.G., Tian, R., Gabbett, C., Horvath, D. and Coleman, J.N. (2020). Effect of the Gate Volume on the Performance of Printed Nanosheet Network-Based Transistors. *ACS Applied Electronic Materials*, 2(7), pp.2164-2170.

7. Tian, R., Griffin, A., McCrystall, M., Breshears, M., Harvey, A., Gabbett, C., Horvath, D.V., Backes, C., Jing, Y., Heine, T., Park, S.H., Coelho, J., Nicolosi, V., Nentwig, M., Benndorf, C., Oeckler, O. and Coleman, J.N. (2021). Liquid Exfoliated SnP_3 Nanosheets for Very High Areal Capacity Lithium-Ion Batteries. *Advanced Energy Materials*, 11(4), 2002364.

Acknowledgements

I would like to begin by thanking Johnny for giving me the incredible opportunity to be a part of his group. When this PhD started and I was told that the fun was only beginning, I had my doubts. However, four Pavinars and innumerable "firings" later, it seems he was a man of his word. I would especially like to thank him for the encouragement and guidance that he has patiently provided me with throughout the PhD - his optimism in the face of appalling results was always a source of solace.

I am immensely grateful to the Coleman group for the support and friendship that they have given me over the last four years. I want to thank Andrew for mentoring me and consistently sharing his encyclopedic knowledge of all things nano. Our victory in the 2016 exfoliation-off still dwarfs all scientific achievements that followed. While I owe a significant debt to Adam for his countless pep talks and scientific guidance, I am most thankful to him for being the focal point of degeneracy and taking the heat off of me. To Dan and Aideen, I have been remarkably fortunate to share the last four years with both of you, we changed the glühwein game. To Sonia, JB, Domhnall, Yash and Mark in Westland Row; I've heard that "real" offices don't have holes in their microwaves or a constant stream of projectiles, so thank you for keeping me on my toes and for making work seem like it wasn't. To the rest of the group past and present; Conor, Dave, Victor, Beata, James, Shixin, Dominik, Ruiyuan, Harneet, Seb and Tingting, thank you for putting up with me for a wonderful four years.

I would also like to thank the staff in the School of Physics and CRANN for their help along the way.

To my friends who were wise enough to get real jobs, thank you for the good times and great company over the last few years - and for nodding along as we both pretended to know what I was talking about.

I am immensely thankful to my Mam and Dad for the support, belief and encouragement that they have always selflessly given me. I'd like to thank Ellen for always keeping me going and for the weekly updates on Bob and Doug. To my Nana and Grandad, the weekly fry was an island of respite away from research that I am hugely grateful for, while I owe Maeve a debt for looking out for me in the big city and ensuring that I never fully sobered up.

Finally, I'd like to express my gratitude to Siobhán, without whom this would not have been possible. Thank you for putting up with me for 11 years of adventures - and for your patience, kindness and boundless positivity along the way. Someday when I grow up and leave college, I'll make it up to you.

I *will* get this research group to Tipperary.

Contents

List of Figures

To mam and dad.

“ Scientific progress goes “boink”? ”

Hobbes

In the beginning the Universe was created. This has made a lot of people very angry and been widely regarded as a bad move.

Douglas Adams

1

Introduction & Outline

Many of humanity's greatest advances have been predicated on the discovery and manipulation of novel materials. While this has facilitated our remarkable progression from flint tools to the brink of nuclear fusion, the pace of advancement only continues to accelerate. As digital technologies become increasingly integrated into the fabric of society, be it through smart toasters or satellite constellations, this will need to be matched by improvements in both material performance and sustainability. It is fortunate then, that this latest technological upheaval has coincided with the emergence of low-dimensional nanomaterials.

Nanoscience represents an interdisciplinary effort on the grandest scale, to study the properties of materials at the smallest. Nanomaterials are classified using their dimensionality, where at least one of their spatial dimensions are limited to be < 100 nm in size.[1] At this length scale the fundamental properties of materials can be investigated and manipulated. Indeed, while the field of nanoscience is only in its infancy, it has already revealed a cornucopia of new physics and extended the frontier of possible material properties. The characteristics of the low-dimensional nanomaterials used in this work will be discussed in Chapter 2.

While the term "nanoscience" may induce images of science-fiction, nanomaterials are historically pervasive.[2] Hair dyes comprised of galena nanocrystals have been traced as far back as Greco-Roman times,[3] while metallic nanoparticles have been utilised to colour glasses since the Bronze age.[4] Mayan artists even inadvertently exploited nanomaterials to synthesise blue pigments, which have stood the test of time for over 18 centuries.[5] The first true "nanoscientist" may have been Michael Faraday, who synthesised a colloidal solution of gold nanoparticles in 1857.[6] However, it would take another 100 years of scientific advancements and the advent of electron microscopy for the world of nanomaterials to come into sharp focus.

While the low-dimensional family was initially limited to nanoparticles, these were soon joined by fullerenes and carbon nanotubes towards the end of the 20th century.[7,8] However, it was the 2004 isolation of monolayer graphene that demonstrated both the existence and incredible properties of two-dimensional (2D) materials.[9] The intervening 16 years have seen remarkable leaps made, and now an entire library of 2D materials have been identified and synthesised.[10] While the seminal work was performed using scotch tape, a collection of diverse strategies now exist to produce 2D materials.[11] These will be discussed in Chapter 3, with an emphasis on exfoliation, stabilisation and size-selection in the solution phase.

Although the 2D "Gold-rush" arose from the properties of individual nanosheets,[12] it is their nanostructured networks that form the central motif of this thesis. Networks of nanosheets have already demonstrated significant promise across myriad applications from thin-film electronics to energy storage. This has catalysed considerable research into the deposition and characterisation of solution-phase nanosheets and their networks. A discussion of this forms the basis of Chapter 4, while a brief summary of the current limitations of 2D networks and their nanostructured composites is provided in Chapter 5.

As global energy demands continue to grow and diversify from electric cars to wearable electronics, the need for improved batteries and supercapacitors is quickly becoming apparent. Networks of 2D materials are well-placed to play a central role here due to the immense specific surface area and pore volume they present. However, such 2D networks are mechanically weak, which limits their device performance. A means to address this is presented in Chapter 6, where 1D carbon nanotubes are used to reinforce a 2D nanosheet matrix, forming a 1D:2D nano:nano composite. An initial study on the mechanical performance and morphological evolution in these composites is performed as a function of nanotube additive level.

Improvements in the solution-phase production of 2D materials have coincided favourably with developments in the field of printed electronics. As the 2D family comprises conductors, insulators and semiconductors, an array of all-printed nanosheet devices have been demonstrated. However, a consistent observation has been that the exceptional properties of nanosheets do not naturally confer to their networks. Indeed, research into printed 2D networks remains in its nascent phase and both the transport and morphological properties of these systems are not fully understood at present. Work to address this forms the basis of Chapters 7 & 8.

The dichotomy in electrical performance between nanosheets and their networks is often attributed to the presence of interfacial junctions. While these interfaces are known to stifle the progression of charge carriers through the network, few quantitative studies have been performed. Before printed 2D networks can compete with printed organics or silicon technologies a means to optimise these systems must be developed. To address this, the conductivity of printed WSe_2, graphene and silver nanosheet networks is investigated as a function of nanosheet size in Chapter 7. By considering semiconducting, semi-metallic and metallic 2D materials, this work aims to inform on the transport mechanisms in these disordered networks.

Though the morphology of a nanosheet network is known to play a dominant role in determining its resultant properties, methods to quantitatively assess this remain limited. Network properties such as porosity, specific surface area and nanosheet alignment heavily influence the physical and chemical attributes of 2D networks. Thus, a means to characterise and tailor these properties would open a rich parameter space for optimisation. By using focused ion beam and electron microscopy in tandem, a novel technique to assess each of these characteristics is presented in Chapter 8. This is performed using printed networks of size-selected graphene nanosheets. Here, the morphological properties of these architectures are again characterised as a function of constituent nanosheet length.

This work will then conclude by evaluating the central findings and propose avenues to expand upon the results presented. It is hoped that this thesis will make a contribution to the growing body of knowledge on nanosheet networks and facilitate further progress in this emerging field.

Plainly there is no way back. Like it or not, we are stuck with science. We had better make the best of it. When we finally come to terms with it and fully recognise its beauty and its power, we will find in spiritual as well as practical matters, that we have made a bargain strongly in our favour.

Carl Sagan

2

Low-Dimensional Nanomaterials

Low-dimensional nanomaterials represent a paradigm shift in materials science. By constraining a bulk material to its zero, one or two-dimensional form, its material properties can be significantly altered. Indeed, aside from revealing an array of fundamental physical processes, low-dimensional nanomaterials have exhibited some of the most remarkable physical attributes ever observed.[13] The nascent roots of modern nanoscience can be traced back to late 20th century, when carbon nanotubes supplanted fullerenes as the preeminent topic in materials science.[14,15] However, it was the 2004 experimental isolation of monolayer graphene that demonstrated both the possibility of purely two-dimensional materials and their superlative properties.[9] The subsequent scramble to

characterise these remarkable attributes was soon extended to other layered crystals, catalysing the rapid progression of nanoscience into the scientific behemoth it is today.

Two-dimensional (2D) materials arise from an anisotropy in the bonding of their parent crystal. In layered materials, such as graphite, the constituent carbon atoms in each plane are covalently bonded while individual layers are weakly bound by van der Waals (vdW) forces. This discrepancy in bond strength allows for pristine layers to be delaminated, or exfoliated, from the parent crystal to produce 2D nanosheets. Within such nanosheets, electron wavefunctions experience quantum confinement and electron motion is restricted to a 2D plane. This has significant implications for the optical and electrical properties of the material, while the absence of interlayer attractions has a considerable influence on the electronic band structure. Owing to their covalently-bonded and planar geometry, 2D materials similarly demonstrate remarkable chemical and mechanical properties. Spurred on by this, a comprehensive toolkit for the synthesis and manipulation of nanosheets was soon developed. 2D materials could now be isolated as individual monolayers, or *en masse* in the solution phase, for an array of applications that rapidly spanned the breadth of materials science. This has seen a library of over 150 materials beyond graphene exfoliated and their constituent nanosheets characterised.[16] This chapter serves as a brief introduction to the primary nanomaterials studied in this work, with an emphasis on their electrical, mechanical and chemical properties.

2.1 Graphene

Though the seminal work on graphene was published in 2004,[9] the concept of a graphitic monolayer has been a source of scientific interest for over 100 years. In 1859, Benjamin Brodie remarked on the lamellar structure of chemically reduced graphite, noting its composition of "minute flat plates".[17] At the turn of the 20th century the structure of graphite was examined using x-ray diffraction by Debye,[18]

Hull,[19] and Bernal independently. Bernal even described how the "atoms of carbon lie in planes in which they form nets of hexagons".[20] We now know these nets to be graphene sheets; atomically-flat monolayers of sp^2 hybridised carbon atoms that are tightly packed into a 2D honeycomb lattice, as shown in Fig. 2.1A. The concept of graphene was first explored by PR Wallace in 1947, where he used graphitic monolayers to model the tight-binding band structure of graphite.[21] Here, both the linear dispersion relation of graphene and its semi-metallicity were first predicted.

In the following decades, the graphitic monolayer was primarily used as an academic material to model the properties of other graphitic allotropes.[22] Both theoretical predictions and experimental observations suggested that purely 2D materials were thermodynamically unstable and could not exist unsupported.[23,24] Thus, graphene remained a conceptual crutch until its unlikely experimental demonstration by Geim and Novoselov in 2004.[9] Prompted by the remarkable electronic properties reported in this seminal work, it was soon found that graphene is not perfectly flat, but exhibits $\sim$ nanometre-scale wrinkling off axis.[25] This gentle crumpling serves to suppress the thermal vibrations that would otherwise destroy the 2D lattice.[26] With this existential crisis averted, the superlative properties of graphene were soon characterised, precipitating the 2D materials "Gold Rush".[27]

The remarkable physical properties of graphene stem from both its two dimensional nature and sp^2 hybridised honeycomb structure. This is shown schematically and from scanning probe microscopy in Fig. 2.1A-B. Each sp^2 hybridised carbon atom forms three σ-bonds of length 1.42 Å in the plane of the lattice.[20] These σ-bonds are responsible for the remarkable mechanical properties of the 2D lattice and preserve the basal plane against crystallographic defects and dislocations.[30] The solitary p_z-orbital, orthogonal to the honeycomb lattice, covalently binds with neighbouring atoms to form the half-filled π-band of delocalised electrons. This is responsible for the exceptional basal plane transport properties of graphene.[21]

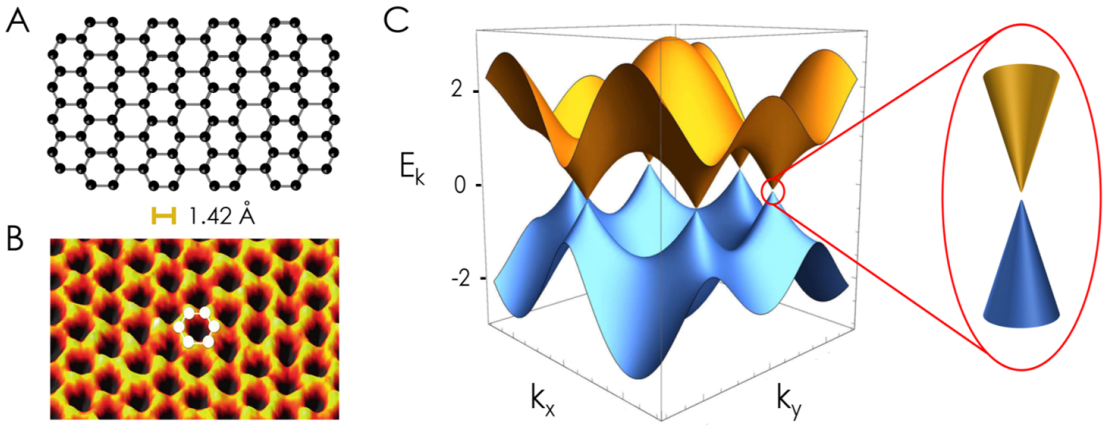

Figure 2.1: Graphene: A) Schematic and **B)** High-resolution scanning probe microscope image showing the hexagonal honeycomb lattice of graphene. [Adapted from Ref. [28]] **C)** Tight-binding band structure of graphene π-bands, considering only nearest-neighbor hopping. E_k is energy, and k_x and k_y are the *x*- and *y*-components of the wave vector. [Adapted from Ref. [29]]

Both graphene and its bilayer are semi-metallic as a result of their band structure at the vertices of the honeycomb lattice, shown in Fig. 2.1C. Electrons interacting with the periodic potential of the hexagonal lattice experience a linear dispersion relation at these points, known as Dirac points, shown expanded in Fig. 2.1C. This results in a zero effective electron mass at low excitations, whereby the electrons behave as relativistic quasiparticles known as Dirac fermions.[31] In the vicinity of the Dirac points, these massless fermions are now described by the $(2+1)$-dimensional Dirac equation, in place of the Schrödinger equation.[32] This leads to the demonstration of quantum electrodynamics (QED) phenomena in graphene, but with a Fermi velocity of $v_F = 1 \times 10^6\ \mathrm{m\,s^{-1}}$ or $\sim 0.03\ c$ for charge carriers.[33] The suppression of charge carrier back-scattering for Dirac fermions, coupled with high-quality crystallinity along the basal plane, results in ballistic transport over micron distances and exceptional carrier mobilities.[34] Indeed, charge carrier mobility in graphene is only weakly dependent on temperature, meaning μ is primarily limited by impurity scattering and substrate interactions.[33]

By mounting graphene on hexagonal boron nitride (h-BN), deleterious electronic interactions with the substrate can be screened. This has led to the demonstration of μ-values of 125,000 $cm^2\,V^{-1}\,s^{-1}$ at room temperature, and 270,000 $cm^2\,V^{-1}\,s^{-1}$ at 4.2 K where extrinsic scattering is eliminated.[35]

Complementary to its remarkable electronic properties, graphene is among the strongest materials ever tested. Owing to its sp^2 hybridised σ-bonds, the tensile strength and elastic modulus of graphene have been reported to be $\sim$ 130 GPa and $\sim$ 1 TPa respectively.[36] For comparison, the tensile strength and elastic modulus of carbon fibres are $\sim$ 3 GPa and $\sim$ 300 GPa.[37,38] Coupled with an exceptional specific surface area of $\sim$ 2600 $m^2\,g^{-1}$,[39] this has seen graphene extensively used to mechanically reinforce composite materials due to superior stress-transfer.[40] Despite its tensile strength, graphene is also remarkably supple and forms ripples when compressed.[41] This is the foundation of strain-based graphene electronics, where geometrically induced carrier scattering alters its transport properties.[42] However, the mechanical prowess of graphene is likely best demonstrated by its peerless specific strength. When announcing the 2010 Nobel prize it was remarked that a 1 m^2 graphene hammock could comfortably support a 4 kg cat, despite being only a single atom thick and weighing less than one of its whiskers.[43]

In the 16 years since its experimental demonstration, graphene has matured from "an unwelcome newcomer" to precipitate the entire field of 2D nanomaterials.[27] While graphene has many other superlatives to its name,[44] its electrical and mechanical properties are of primary interest in this work. Notably, graphene-based inks have demonstrated promise as a printable conductor for thin-film electronics. However, a common observation is that the remarkable properties of the monolayer do not naturally translate to their networks and strategies to address this are an active area of research.

2.2 Transition Metal Dichalcogenides (TMDs)

Though currently undergoing an academic resurgence, the transition metal dichalcogenide (TMD) family has captured the interest of materials scientists for the best part of a century. The structure of the archetypal TMD, MoS_2, was determined to consist of "hexagonal crystals with a very complete basal cleavage" by Dickinson and Pauling in 1923.[45] In the ensuing 40 years around 60 TMD compounds were described, with at least 40 of them having a layered vdW crystal structure.[46] Indeed, few-layer MoS_2 nanosheets were first delaminated from a parent crystal using adhesive tape as far back as 1963 by Frindt *et al.*[47] Within a year, the same group had isolated bilayer MoS_2 and even characterised the exitonic response as a function of layer number.[48] Though a monolayer suspension of MoS_2 nanosheets was produced through lithium ion intercalation in 1986,[49] it was the unveiling of graphene in 2004 that catalysed a level of research into 2D TMDs commensurate to their superlative electronic,[50] optical,[51] thermal,[52] mechanical,[53] and tribological properties.[54]

Group *IV-VII* TMDs crystallise as vdW-stacked crystals with a MX_2 stoichiometry, where M is a transition metal and X is a chalcogen (S, Se or Te). The multiple possible M-X configurations for the layered TMDs are shown in Fig. 2.2A, which give rise to a host of diverse of physical properties. Most notably, the TMD family encompasses the entire electronic spectrum, from true and semi-metals like VSe_2 and TeS_2, to semiconducting MoS_2 and insulating HfS_2. The structure of a layered TMD is shown in Fig. 2.2B, where a monolayer is comprised of a hexagonal plane of transition metal atoms sandwiched between two displaced hexagonal layers of chalcogen atoms. Due to this stacked X-M-X configuration, TMD monolayers demonstrate thicknesses of 6 - 7 Å.[56] As with graphene, the metal-chalcogen bonds in the plane of the TMD monolayer are primarily covalent and stabilised against thermal fluctuations by a corrugation of their structure.[57,58] However, individual layers are weakly

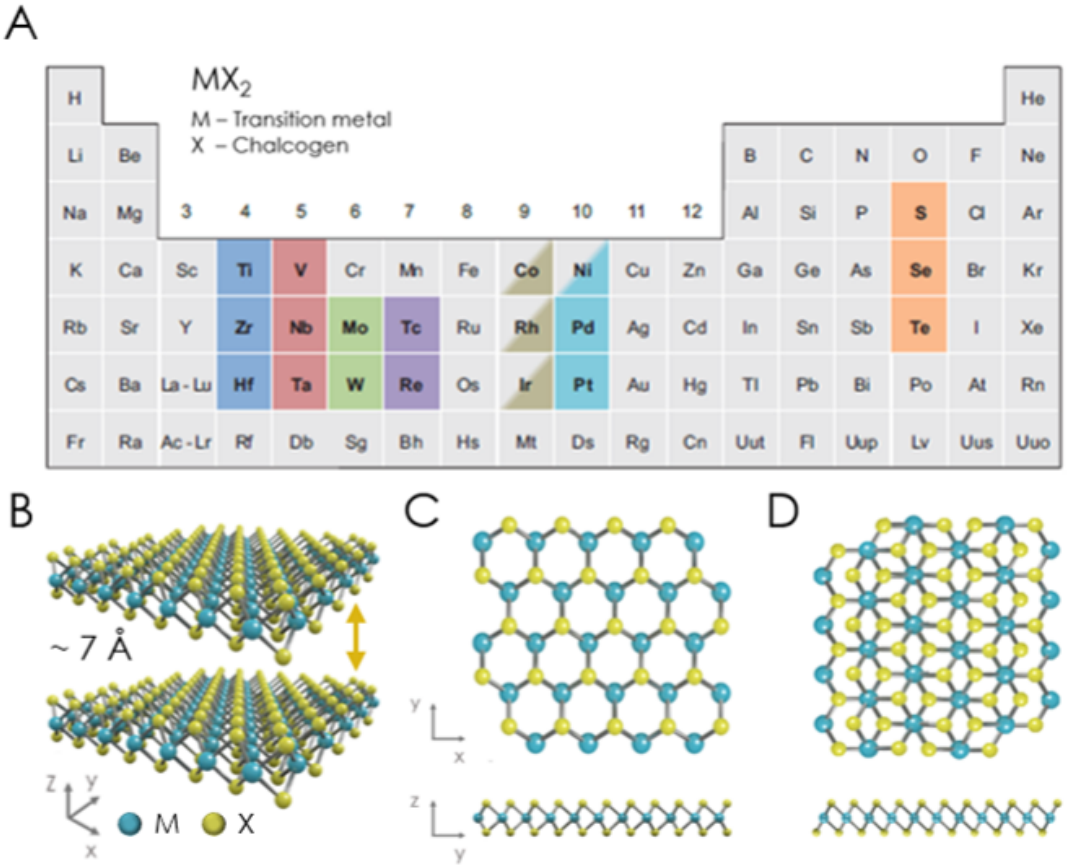

Figure 2.2: Transition Metal Dichalcogenides: A) Periodic table showing the possible combinations of group IV-X transition metals with chalcogens. [Adapted from Ref. [55]] **B)** Typical structure of a TMD monolayer. Possible monolayer configurations showing the **C)** Triagonal prismatic and **D)** Octahedral coordination geometries.

coupled through vdW bonds, leading to an anisotropy in the material properties and facilitating delamination of the bulk crystal. [59]

Owing to their more complex crystal structure, layered TMDs occur as different *polymorphs* (metal coordination geometry) and *polytypes* (monolayer stacking). [60] Each transition metal atom in a TMD monolayer is six-fold coordinated with chalcogen atoms to give either a triagonal prismatic (1H) or octahedral (1T) geometry. Here, one phase is thermodynamically preferred depending on both the *d*-electron count of the transition metal and the relative size of the M-X atoms. The triagonal prismatic

geometry exhibits AbA stacking in the monolayer, while in the octahedral arrangement the chalcogen atom positions are staggered to give AbC stacking. The capital and lower case letters denote chalcogen (S, Se and Te) and metal (W and Mo) atoms respectively. Both polymorphs are shown in Fig. 2.2C-D. As monolayer TMDs exhibit two possible *polymorphs*, this facilitates a variety of available stacking *polytypes* for bulk TMDs. The most commonly encountered polymorphs are 1T (triagonal), 2H (hexagonal) and 3R (rhombohedral), where the numbers denote the number of monolayers in the stacking sequence. Polymorphism or metal coordination can have a significant influence on the electronic properties of TMDs. As an example, MoS_2 is commonly found in the semiconducting 2H phase, where the stacking sequence is AbA BaB. However, its octahedrally coordinated polymorph, 1T-MoS_2, is semi-metallic and demonstrates conductivities $\sim 10^7$ greater than its 2H phase.[61]

The electronic band structure of TMD materials is a function of both the coordination environment and *d*-electron count of its transition metal atoms. The orbital filling of the non-bonding *d*-bands for a group VI TMD is shown in Fig. 2.3A. Here, the *d*-orbitals are split into three groups as a result of their triagonal prismatic symmetry, showing a gap on the order of ~ 1 eV between the first two groups of orbitals.[55] Octahedrally coordinated transition metal centres form degenerate orbitals that can accommodate up to 6 *d*-electrons. Thus, as the non-binding *d*-bands are progressively filled moving from group IV to group X, the TMD family exhibits a plethora of diverse electronic properties. When the highest orbitals are partially filled the TMD exhibits metallic conductivity (1T-ReS_2), however, if the bands are fully occupied the TMD behaves as a semiconductor (2H-MoS_2). Moreover, the transition metal *d*-electron count determines the preferred phase adopted by a TMD. Group IV TMDs display d^0 transition metal centres and are all octahedrally coordinated, while group VI TMDs exhibit d^2 transition metal centres and are primarily found in triagonal prismatic geometry. Indeed, manipulation of the *d*-electron count through alkali metal intercalation has been shown to

induce phase changes in some TMDs, most notably in MoS_2.[62] Here, the transfer of a valence electron from the alkali metal to the MoS_2 *d*-band induces a destabilization of the original semiconducting 2H phase and transformation to the semi-metallic 1T-MoS_2 polymorph.[63] Interestingly, experiments have shown that this is not a simple binary process, and that intermediate polymorphic 2H-1T phases can be formed to create metal-semiconductor hybrid structures.[64] Though the transition metal plays the dominant role in determining the electronic band structure, the chalcogen atoms also contribute. This manifests as a broadening of the *d*-bands and concomitant narrowing of the bandgap as the chalcogen atomic number is increased.[65] Thus, moving from bulk 2H-MoS_2 to 2H-$MoTe_2$ the bandgap is seen to decrease from 1.3 to 1.0 eV.[46]

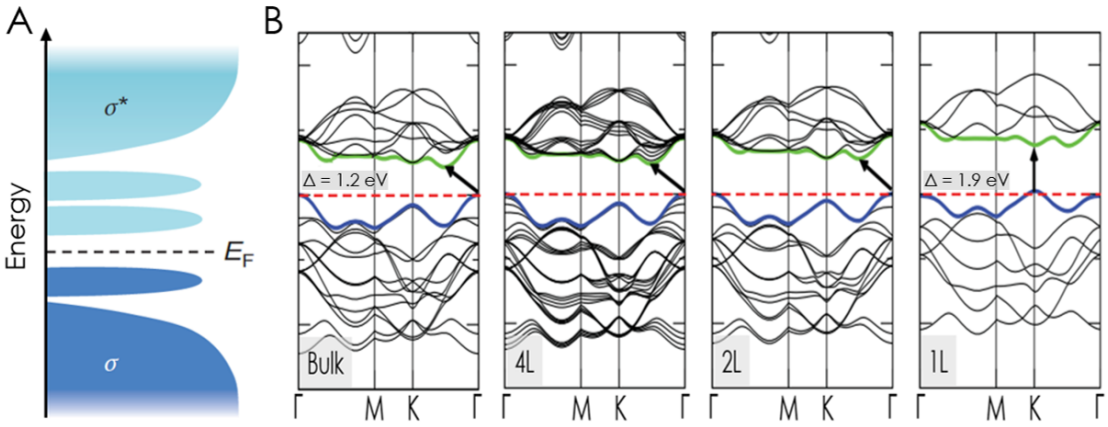

Figure 2.3: MoS_2 Band Structure: A) Typical band structure and filling of the non-bonding *d*-orbitals for a 2H phase TMD. [Adapted from Ref.[60]] **B)** DFT calculated band structure of Bulk, 4 layer, bilayer and monolayer MoS_2. The horizontal dashed lines indicate the Fermi level. The arrows indicate the fundamental bandgap (indirect and direct). The top of the valence band and bottom of conduction band are coloured blue and green respectively. [Adapted from Ref.[66]]

Changes in the crystal symmetry, interlayer coupling and degree of quantum confinement as layered TMDs are thinned towards their 2D limit have led to the demonstration of some remarkable properties.[67] The evolution of the band structure of MoS_2, as it progresses from bulk to monolayer, is shown in Fig. 2.3B. Bulk MoS_2 is an indirect-gap semiconductor with a bandgap of $\sim$ 1 eV. Its

valence band maximum (VBM) is located at the Γ-point and its conduction band minimum (CBM) is situated at midpoint of the Γ-K symmetry lines. However, monolayer MoS_2 is a direct-gap semiconductor with both the VBM and CBM coincident at the K-point. This arises from a shift in the hybridization of the sulfur p_z-orbitals and molybdenum d-orbitals, driven by quantum confinement and layer coupling effects about the Γ-point.[68] In the group VI TMDs this transition has considerable effects for the optical and electronic properties. Most notably, the monolayer exhibits a 10^4 increase in the photoluminescence (PL) intensity and $\sim$ 50 % increase in bandgap when compared with its parent crystal, as shown in Fig. 2.3B.[69] Crucially, this confers a tunable bandgap of 1 - 2 eV to the group VI TMDs as the crystal is thinned, which is compatible with modern silicon technologies.

As with graphene, the layered TMD family exhibits a breadth of remarkable properties beyond the scope of a single thesis. Among these, the energy storage and electrical transport properties of the group VI TMDs are of central interest in this work. Owing to their high theoretical capacity, cycling ability and specific surface area, networks of TMD nanosheets have been intensely investigated as electrode materials for lithium ion batteries.[70] However, the limiting factor in many cases is that disordered nanosheet networks demonstrate poor cycling stability and conductivity.[71] Methods to address this are an area of active investigation, with the addition of graphene or carbon nanotube additives demonstrating promising electrical and mechanical enhancement.[72] Alternatively, owing to the ease of exfoliation and diversity of electronic properties across the TMD family, inks comprised of TMD nanosheets are uniquely poised to play a central role in the field of printed electronics. In particular, the semiconducting group VI TMDs have demonstrated reasonable performance in printed thin-film transistors and photodetectors.[73,74]

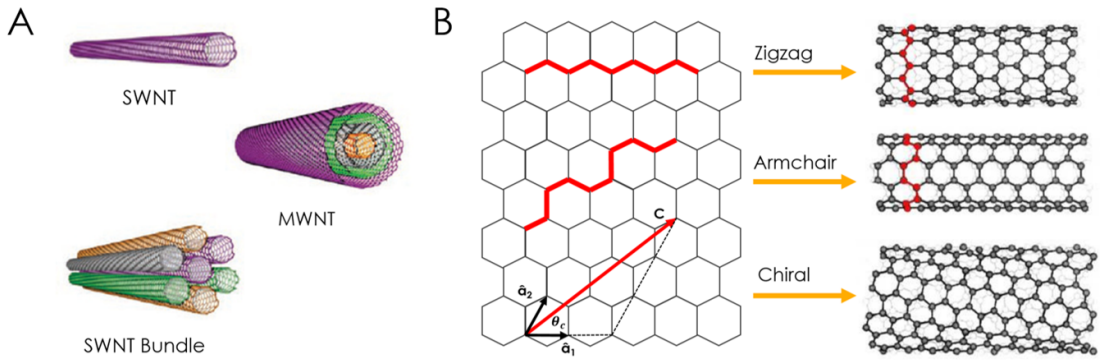

Figure 2.4: Carbon Nanotubes: A) Schematic representations of single- and multi-walled nanotubes, as well as a single-walled nanotube fibre. [Adapted from Ref. [75]] **B)** Rolling of a graphene sheet to form zigzag, armchair and chiral SWNTs. [Adapted from Ref. [76]]

Carbon nanotubes are the archetypal one dimensional nanomaterial and can be considered as a seamless cylinder of rolled up graphene.[77] Though first experimentally observed in 1991 by Iijima *et al.*,[14] carbon nanotubes were unwittingly used by Syrian blacksmiths to produce enhanced blade-steel over 400 years ago .[78] Depending on the number of concentric cylinders of rolled graphene, carbon nanotubes can exist in single-walled (SWNT) or multi-walled (MWNT) configurations, as shown in Fig. 2.4A. SWNTs exhibit walls a single carbon atom thick, with diameters on the order of a nanometre and lengths ranging from tens of nanometres to $\sim$ 55 cm long.[79] MWNTs are comprised of an array of such cylinders formed concentrically and spaced by 0.35 nm, similar to the basal plane separation in graphite.[80] Carbon nanotubes are commonly synthesised using arc discharge,[81] laser ablation,[82] chemical vapour deposition,[83] and high-pressure carbon monoxide disproportionation (HiPCO).[84] Owing to their one dimensional nature and sp^2 hybridised bonds, carbon nanotubes demonstrate superlative physical properties and remain among the most-researched low dimensional nanomaterials.

A graphene sheet may be rolled up infinitely many ways to form a carbon nanotube, as shown in Fig. 2.4B. However, each configuration can be uniquely identified by its chiral vector, $\mathbf{c} = n\hat{\mathbf{a}}_1 + m\hat{\mathbf{a}}_2$, where $\hat{\mathbf{a}}_1$ and $\hat{\mathbf{a}}_2$ represent the graphene lattice vectors and (n, m) are integers. The properties of a given carbon nanotube can vary dramatically with $\mathbf{c}$, such as its spatial symmetry group or band structure. Depending on the (n, m) indices, a given nanotube can be either metallic or semiconducting: where $(n-m)/3$ is an integer the nanotube is metallic, otherwise it is semiconducting.[85] As shown in Fig. 2.4B, carbon nanotubes can be broadly classified into 3 spatial symmetry groups depending on their (n, m) indices. Armchair nanotubes have indices such that $n = m$ and are always metallic. Zigzag nanotubes are given by $(n, 0)$ and are semiconducting, unless the index n is an integer multiple of 3. All other combinations of indices are classified as chiral nanotubes and are semiconducting.[86]

This electronic behaviour arises from "cutting" 1D slices from the 2D band structure of graphene. By confining electron wavefunctions to one dimension, the allowed electronic states now constitute a line of points or "band".[87] Here, one of the electron wave vectors remains quasi-continuous while the two wave vectors perpendicular to the nanotube axis become strongly quantised. This confinement and quantisation has a dramatic effect on the electronic properties of nanotubes. Electron states in a SWNT can only scatter into a very limited number of empty electronic states and such events require a large momentum transfer.[88] This facilitates ballistic transport, whereby the inelastic electron mean free path can be on the order of tens of microns in metallic nanotubes.[89] In this limit, delocalised π electrons are coherent along the entire length of a SWNT and electron-phonon scattering is essentially absent. As a result of this, the electrical conductivity of individual carbon nanotubes can reach values of 10^6 - 10^7 $\mathrm{S\,m^{-1}}$ (*cf.* silver $\sim 6 \times 10^7$ $\mathrm{S\,m^{-1}}$).[90,91] Furthermore, metallic SWNTs can sustain current densities of $\sim 4 \times 10^9$ $\mathrm{A\,cm^{-2}}$ and are insusceptible to electromigration due to the stability and

excellent thermal conductivity of the covalently bonded carbon lattice.[87,92] Semiconducting SWNTS (s-SWNTs) exhibit similarly exotic electronic properties, such as theoretical mobilities of $\sim$ 120000 $cm^2\,V^{-1}\,s^{-1}$[93] and diameter-dependent bandgaps.[94] As most synthesis strategies produce nanotubes of varying diameter and chirality, this can result in an inhomogeneity in their electronic and optical properties.[95] However, a means to sort nanotubes by their diameter and chirality is provided through density gradient ultracentrifugation, which allows homogeneous fractions to be isolated.[96]

Much like their 2D analogue, carbon nanotubes demonstrate exceptional mechanical properties as a result of their sp^2 hybridised σ-bonds.[97] In the absence of sufficient quantities for mechanical measurements, Overney *et al.* simulated the rigidity of a short SWNT to be 1.5 TPa in 1993.[98] The first experimental measurements on MWNTs followed four years later and determined their elastic modulus to be $\sim$ 1 TPa.[99] However, what truly distinguishes carbon nanotubes is their tensile strength. Theoretical calculations predict that defect-free SWNTs may exhibit tensile strengths of $\sim$ 100 GPa. Indeed, the largest experimentally demonstrated tensile strength of $\sim$ 63 GPa exceeds its macroscopic analogue, the carbon fibre, by over an order of magnitude.[80] More recently, individual shells in MWNTs have displayed strengths on the order of 100 GPa.[100] When combined with reported densities of 1300 – 1400 kgm^{-3},[101] this means that the specific strength of SWNTs surpass values for ultra-strong steels by two orders of magnitude.[102]

Carbon nanotubes have demonstrated promise across a diverse range of applications including transparent conductors,[103] sensors,[104] and as filler materials in composites.[105] Of particular interest is the aggregation of individual SWNTs to form nanotube bundles, as shown in Fig. 2.4A. These bundles are comprised of vdW-bonded SWNTs in a close-packed array and their utility in nanocomposite reinforcement will be discussed in Chapter 5. Metallic SWNTs are used in this work to provide both mechanical reinforcement and conductive pathways in novel nanocomposite materials.

That's the whole problem with science. You've got a bunch of empiricists trying to describe things of unimaginable wonder.

Bill Watterson

3

Nanomaterials Synthesis

The experimental demonstration of graphene and its superlative properties marked the arrival of two dimensional nanomaterials on the global stage.[9] However, a key obstacle stifling the establishment of the 2D hegemony is the controlled synthesis of defect-free nanosheets on an industrial scale. To realise the potential of 2D nanomaterials and mount a challenge against mature technologies, the economical production of pristine nanosheets with tightly-controlled dimensions is prerequisite. Synthesis methods can be broadly classed into two groups depending on how the monolayer is isolated. Bottom-up methods such as chemical vapour deposition[106] (CVD) and atomic layer deposition[107] (ALD) involve synthesising atomically-thin films using elemental precursors. Top-down methods, generally referred

to as exfoliation, involve delaminating layers from the bulk parent crystal and include mechanical, [108] chemical, [109] and liquid phase exfoliation. [110] To this point, no one technique has presented itself as a *panacea* for the mentioned requirements, meaning the above techniques are interchanged depending on the application. For proof-of-concept measurements on the intrinsic properties of monolayers, micromechanical cleavage remains the preferred choice. However, for nanoscale electronics, CVD is often chosen due to precise growth it affords. Though bottom-up methods produce pristine monolayers, they are limited by their scalability and yield.

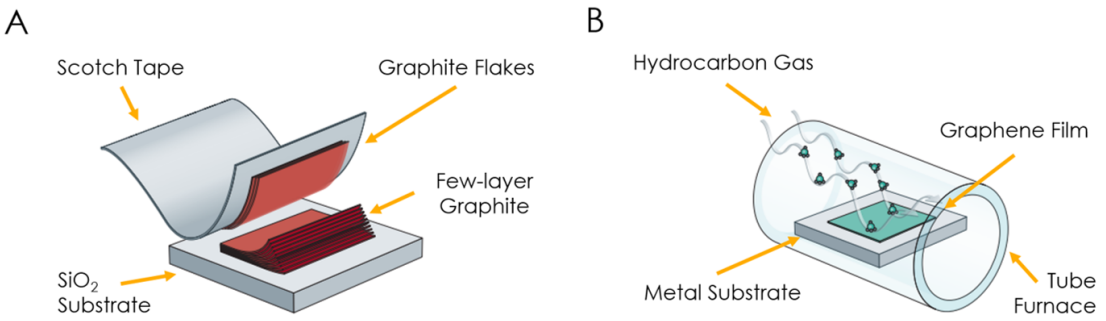

Figure 3.1: Top-Down & Bottom-Up Synthesis of Graphene: Schematics of both the **A)** Micromechanical cleavage and **B)** Chemical vapour deposition techniques for graphene synthesis. [Adapted from Ref. [111]]

Micromechanical Exfoliation

Though famously first used to demonstrate a graphene monolayer in 2004, [9] micromechanical cleavage has been used for decades by crystallographers. [112] Frindt *et al.* demonstrated peeling of $\sim$ 100 Å thick layers from a MoS_2 crystal as far back as 1962, [113] while Lu *et al.* postulated that "extensive rubbing of the graphite surface against other flat surfaces" could result in few or single layer graphite in 1999. [114] The experimental process is shown schematically in Fig. 3.1A. Adhesive tape is placed onto and then peeled from the surface of a graphite crystal. The graphite flakes are preferentially cleaved along the basal plane due to the weaker van der Waals bonding present here. By repeated peeling

steps it is possible to isolate few and single-layer graphene sheets that are only limited in dimension by the lateral size of the parent single crystal. These flakes, reaching millimetres in length,[27] can then be transferred to a desired substrate for characterisation. This method has since been extended to hexagonal boron nitride,[115] TMDs,[59] and even layered superconductors.[116] Micromechanical cleavage arguably remains the best method to obtain high-quality and few-layer 2D materials for academic purposes. However, its low throughput and yield does not lend it to scalable industrial applications.

Chemical Vapour Deposition (*CVD*)

Chemical vapour deposition is a bottom-up process that has been used to deposit thin films in the semiconductor industry for several decades.[117] This process has since been refined in order to grow wafer-scale films of layered materials such as graphene,[118] MoS_2,[119] WS_2 and WSe_2[120] by changing the growth conditions and precursors. Indeed, the first CVD synthesis of graphene may have been inadvertently performed by Kholin *et al.*[121] in 1984, while investigating the catalytic properties of indium. A process for CVD growth of graphene is shown in Fig. 3.1B. At temperatures of $\sim$ 1000 °C inside a furnace, the precursor hydrocarbon gas decomposes and carbon atoms nucleate on the metal foil, ultimately forming large single-crystal or polycrystalline domains. These films can then be transferred to a desired substrate, though often with the introduction of defects.[122] By virtue of its compatibility with the technologies used in semiconductor manufacturing, monolayer CVD growth is predominantly geared towards high-end electronic and optical applications.[123] Here, the degree of control over crystal dimension and quality is unhindered by the need for equipment overhaul and its associated costs. However, as with other bottom-up growth methods such as ALD, the scalability of CVD is its Achilles' heel. Intrinsically limited by substrate material and dimension, as well as furnace size,[124] the low yields afforded by CVD render it unsuitable for most high-mass applications.

3.1 Solution-Phase Production

The demonstration of monolayer materials through CVD or micromechanical exfoliation served to catalyse research into more scalable methods of 2D materials synthesis. This led to the development of a suite of techniques to produce nanomaterials in the solution phase, which confers numerous advantages. Firstly, solution-phase production is broadly scalable, resulting in drastically improved yields when compared to bottom-up techniques or micromechanical cleavage.[110] Further, dispersions of nanosheets can be rapidly characterised using spectroscopic techniques, with numerous metrics to assess the dispersed nanosheet lengths and thicknesses in the literature.[125] Finally, liquids are the optimum medium for further processing whereby the suspended nanosheets can be readily sorted and selected for desired applications. These advantages lend solution-processed nanomaterials to myriad different applications including printed electronics, composites, energy storage and catalysis.

Intercalative Exfoliation

Chemical exfoliation is likely the most seasoned of the liquid phase exfoliation strategies. In 1859 Benjamin Brodie oxidised graphite by exposing it to a mixture of nitric acid and potassium chlorate to form "graphic acid" - or graphite oxide - noting its composition of "minute flat plates".[17] This method was refined in the early 20th century by Hummers and Offerman, employing a considerably less lethal cocktail of oxidisers. This eponymous method remains the preferred approach to synthesise graphite oxide.[126] The oxidation of graphite results in basal plane functionalisation with hydroxyl, epoxide and carboxyl groups. The resulting hydrophillicity promotes water intercalation and swelling of the parent crystal. Upon agitation, by means of ultrasonication or thermal shock, the bulk crystal is delaminated into graphene oxide (GO) nanosheets, with the dispersed flakes stabilised against aggregation by their

induced negative surface charge.[127] The produced GO nanosheets are primarily monolayers with dimensions on the order of ~ 1 μm.[128] By subsequent reduction of the GO nanosheets in dispersion, the oxides can be removed to produce reduced graphene oxide (rGO). Hans Boehm may have been the first to isolate and image few and single-layer rGO in a TEM in 1961.[129] It was the same author who formally defined a single graphitic layer as *graphene* in 1994.[130] Oxidation of graphite is currently the most cost-effective manner to exfoliate bulk graphite to few and single-layer species, with its one-pot oxidation and reduction of particular appeal to industry. However, structural defects and vacancies arising from the oxidation are inimical to the crystal electronic mobility. This renders rGO unsuitable for applications where the superlative transport properties of graphene are required.[110] However, rGO remains highly promising for applications where its mechanical strength and thermal properties can offset its mobility shortcomings, such as in filters for water purification or nanocomposites.[131,132]

The manipulation of a parent crystal through the formation of inclusion complexes, known as ion intercalation, has also been employed to exfoliate numerous layered materials.[133] The process is shown schematically in Fig. 3.2A. Adsorption of guest molecules, generally ionic or covalent species, serves to dilate the interlayer spacing as a function of the intercalant size. This distension weakens the interlayer adhesion and lowers the barrier for subsequent exfoliation, generally via thermal shock[134] or ultrasonication.[135] Additionally, intercalants such as iodine monobromide (IBr) or *n*-butyllithium can facilitate charge transfer to the layers, further reducing the interlayer adhesion.[134] Ion intercalation has been demonstrated to well-exfoliate bulk crystals of TMDs,[136] TMOs,[137] clays,[138] and as far back as 1841, graphite.[139] The resulting nanosheets, often negatively charged, are stabilised against aggregation by the electrostatic surface charges[140] or surfactants.[141]

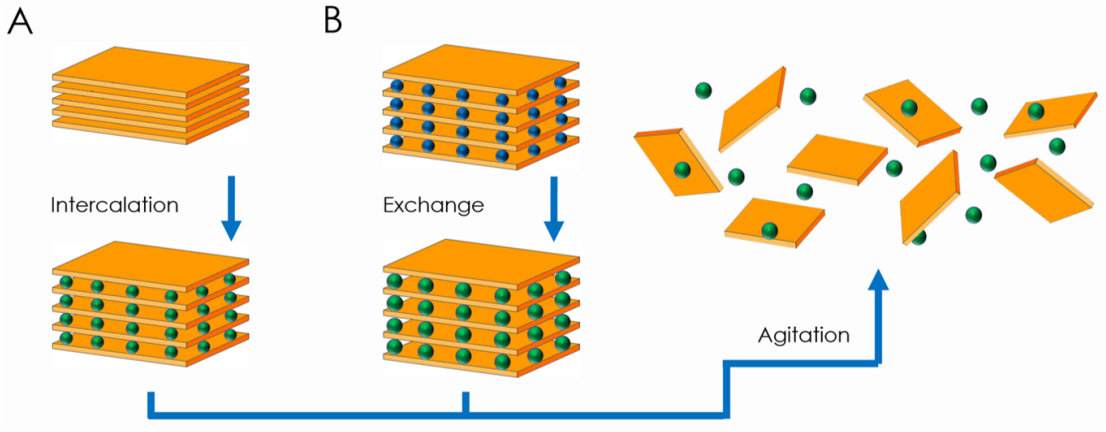

Figure 3.2: Intercalative Exfoliation: Illustration of the **A)** Ion intercalation and **B)** Ion exchange exfoliation techniques.

A similar concept is employed in the ion exchange technique, shown in Fig. 3.2B. Here, layered materials such as layered double hydroxides,[142] clays,[143] and metal oxides[144] already contain an exchangeable interlayer of cationic counterions to balance the layer charges. By supplanting these ions with more bulky equivalents, the parent crystal is again dilated and primed for subsequent exfoliation. TiO_2 nanosheets, tens of microns in lateral dimension, have been experimentally demonstrated in this manner by replacing the Cs^+ counterions with more substantial tetrabutylammonium cations.[145]

While intercalation methods have been widely used to exfoliate myriad layered crystals, some issues remain. This technique is quite sensitive to ambient conditions,[146] and material specific, with ionic intercalants applied to a given material on an *ad hoc* basis. The procedural complexity is increased by the need to remove the ionic species post-exfoliation.[147] Finally, as with chemical exfoliation, the produced nanosheets can be quite distinct from their pristine counterparts. Ion intercalation in MoS_2 has been observed to induce defects in the form of sulfur vacancies,[148] while charge imbalances from lithium intercalation can precipitate a rearrangement of the atomic structure and induce a transition from the semiconducting 2H to metallic 1T phase.[135]

Liquid Phase Exfoliation

The liquid phase exfoliation (LPE) technique arose from the need for a more simple and versatile means to isolate two dimensional nanomaterials. First demonstrated by Coleman *et al.* in 2008,[110] the LPE method is used to mechanically delaminate the parent vdW crystal in the presence of a stabilising fluid. By overcoming the vdW interlayer attractions using shear or ultrasonic energy, LPE offers a universally applicable and low-cost means for the scalable production of nanosheets that are defect-free and unfunctionalised.[149] Indeed, the versatility of the technique was recently demonstrated by Harvey *et al.* where 2D nanosheets were successfully produced from cat litter and sand.[150] The LPE process is generally considered as having three steps; exfoliation of the parent crystal, stabilisation of the nanosheets in solution, and size-selection of the dispersed nanosheets. Each of these steps will be addressed in the coming sections.

Ultrasonication

Initially developed as a means to detect submarines during the first world war,[151] the field of ultrasonics has since be adapted for applications including medicine, communications and sonochemistry. In ultrasonic exfoliation, a transducer is used to convert high-frequency mechanical oscillations into ultrasonic waves in solution. These waves promote exfoliation of layered crystals through two main energetic inputs; vibrations and cavitations.[152] The mechanism of probe-driven ultrasonic exfoliation is depicted in Fig. 3.3A. A transducer drives the probe to vibrate at frequencies of $\sim$ 20 kHz with an amplitude of $\sim$ 100 µm. This generates high intensity ultrasonic waves at the probe tip that propagate through the liquid.[153] This transmission of ultrasonic energy causes molecules in the liquid to oscillate about their mean position. With sufficient negative pressure the intermolecular distance exceeds

the limit required to hold the liquid intact and voids or cavitations are formed. These bubbles then undergo expansion across a few acoustic cycles, before collapsing into high-energy jets. [154] This generates a highly energetic local environment that exerts tensile and shear stresses on the bulk crystal, leading to exfoliation and fragmentation. [155–157] A similar but lower-energy process is utilised in bath sonication, where ultrasonic waves propagate through the tank establishing standing waves. These waves can induce vibrational modes within the parent crystal with enough energy to delaminate nanosheets. [152]

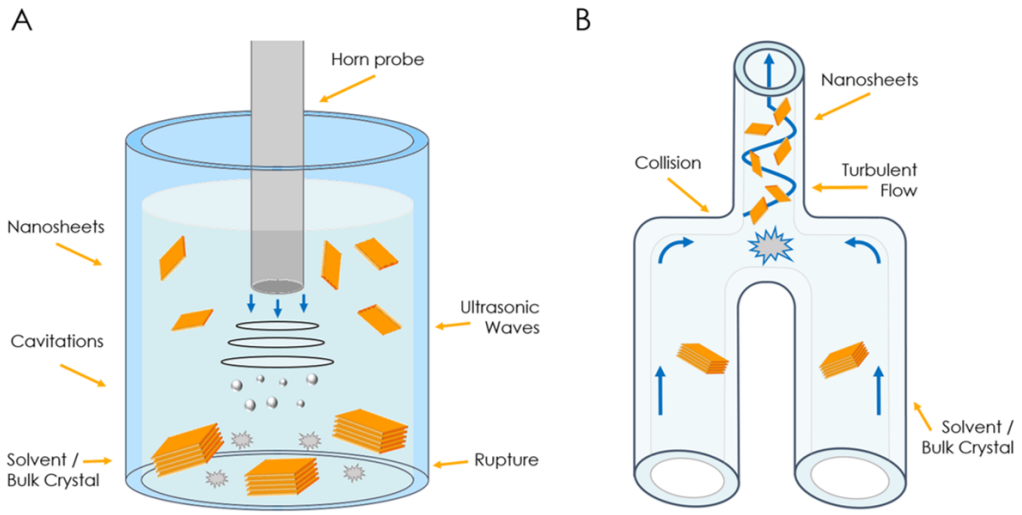

Figure 3.3: Liquid Phase Exfoliation: Schematics depicting the exfoliation mechanism for both the **A)** Tip ultrasonication and **B)** Wet jet milling techniques.

Ultrasonication is the ubiquitous technique for lab-scale LPE as it is both accessible and has been shown to reliably produce mono- and few-layer nanosheets from a host of layered crystals. [158,159] Tip sonication results in nominally high concentrations, however, as the intensity under the probe decays rapidly in both the axial and radial directions it has limited scaling potential. [160] An inhomogeneous intensity field throughout the sample volume is an affliction shared by bath sonication. Here, the presence of constructive and destructive interference regions in the tank are detrimental to the technique reproducibility. [161] It is worth noting that this can be largely mitigated by the ensemble characterisa-

tion afforded by spectroscopic techniques and subsequent size-selection to isolate desired fractions. Though the highly-energetic tip sonication process has been observed to inducing basal plane scission in some nanosheets,[161] it has widely been determined that the produced nanosheets are pristine.[155] Interestingly, it has been suggested that basal plane defects are primarily a function of the quality of the parent crystal.[162] From an applications standpoint, ultrasonic exfoliation offers a means to produce unfunctionalised and defect-free nanosheets at a reasonable throughput. Though the technique is the most prominent of the solution-processing methods for 2D materials, there is still a rich parameter space for optimisation. For example, Turner *et al.* have recently demonstrated *in situ* control over the produced graphene flake size by controlled sonication, achieving $\sim$ 20 % yields of few-layer graphene after 3 h sonication time.[154] Probe sonication is used throughout this work to produce 2D dispersions.

Shear-based Exfoliation

In order to address the scalability shortcomings of ultrasonication, alternative methods to delaminate layered crystals in solution have been explored. This culminated in the exfoliation of graphite by high-shear laminar flow using a rotor-stator shear mixer in 2014.[163] Interestingly, it was demonstrated that the sole requirement to exfoliate a parent crystal is a minimum shear rate of $\sim 10^4$ s^{-1}, which was soon followed by the unlikely trinity of a kitchen blender, household detergent and graphitic monolayers.[164] Crucially, both of these methods are highly scalable, with some of the highest production rates in the literature achieved using high-shear mixing.[165]

More recently, techniques such as wet jet milling (WJM) have emerged as promising candidates for the defect-free exfoliation of layered materials on an industrial scale.[166] The procedure, adopted from its conventional usage in pharmaceutical[167] and ceramic processing,[168] is shown in Fig. 3.2B.

The solvent and bulk crystal are pressurised and driven to the processor by a hydraulic mechanism and piston. Here, the initial stream is divided into two highly pressurised jets, which are then collided and forced through a smaller aperture generating turbulent flow.[169] A similar action is utilised in microfluidisation, where turbulent flow occurs as a result of the suspension being forced through the microchannel.[170] The agitated flow results in a high velocity gradient orthogonal to the flow direction. This generates shear stresses on the layered crystal and precipitates sliding of the layers along the basal plane, leading to exfoliation. The most salient difference between WJM and microfluidisers versus other LPE techniques is the sample process time. Here, the exfoliation takes place at the nozzle over a fraction of a second, instead of hours in ultrasonication or shear mixing.[171] What follows are nanosheet production rates as large as 24 $g\,h^{-1}$, among the highest in the literature.[172] While the procedural complexity is increased by the need for sequential piston passes to improve the degree of exfoliation, this technique is in its nascent phase and holds much promise.

3.2 Stabilisation

Successful exfoliation of a layered crystal is contingent not just on the disruption of the interlayer adhesion, but also the stabilisation of the subsequent dispersion. An appropriate stabiliser will perform this role, while simultaneously reducing the energetic cost of exfoliation through stabiliser-nanosheet binding.[162] The preeminent strategies employed are solvent[173] and surfactant[174] stabilisation, though steric repulsion using polymers has also been demonstrated.[175] These methods work through independent mechanisms to prevent reaggregation and enhance the dispersion stability.

Solvent Stabilisation

Solution thermodynamics predicts that efficient stabilisation will occur when the net energetic cost of mixing a solvent and solute is minimised.[176] This is achieved when the solvent and solute solubility parameters are matched. Initial work on solvent-stabilised carbon nanotubes demonstrated that stable dispersions could be achieved by matching the solvent and nanomaterial surface energies.[177] Within a year, this was extended to 2D nanosheets stabilised in N-methyl-2-pyrrolidone (NMP) by Hernandez *et al.*[110] Subsequent solvent studies demonstrated that the concentration of dispersed graphene could be tuned over an order of magnitude by appropriate surface energy matching - unfortunately with a correlation between solvent performance and toxicity.[178] NMP and dimethylformamide (DMF) are the prototypical LPE solvents due to their matching of surface tension and solubility parameters with dispersed nanomaterials.[179] However, while observed to broadly apply, Hernandez *et al.* proposed that a more comprehensive model considering multiple intermolecular interactions was needed to fully describe the stabilisation process.[178] This is most simply elucidated through consideration of the Gibbs free energy of the system, ΔG_{mix}, which determines whether the spontaneous mixing of nanosheets and solvent is favourable through

$$\Delta G_{mix} = \Delta H_{mix} - T\Delta S_{mix} \tag{3.1}$$

where T is the absolute temperature and ΔH_{mix}, ΔS_{mix} are the enthalpy and entropy of mixing respectively. To advocate mixing, ΔG_{mix} must be minimised.[180] Due to their dimensions and rigid shape, the entropy component is restricted to be small for nanomaterials.[181] This means that ΔH_{mix} must be minimised. This is primarily achieved through manipulation of the Flory-Huggins interaction parameter, χ, on which ΔH_{mix} depends.[182] For $\chi < 0$, solvent-solute interactions dominate, resulting

in a stable dispersion. However, solute-solute interactions reign for $\chi > 0$, which induces aggregation. A form of this parameter relevant to the colloidal dispersions encountered in LPE is given by Eqn. 3.2

$$\chi = \frac{\nu_0}{kT}(\delta_A - \delta_B)^2 \tag{3.2}$$

The interaction is described through the molecular volume, ν_0, the absolute temperature, T, and the Hildebrand solubility parameters of both components of the system, δ_i. The solubility parameter, δ, was developed by Joel Hildebrand in 1936 and provides a numerical value indicating solvency behavior.[183] This is given by the square root of the cohesive energy density, $E_{C,T}/V$. Here, $E_{C,T}$ is the total molar cohesive energy and V is the molar volume of the solvent. Matching of the δ components in a system has been shown to be largely effective for non-polar solutes,[184] though it appeared additional criteria had to be met for polar solutes. This was addressed by Charles Hansen in 1967 by breaking the solvent-solute interaction, expressed in terms of cohesive energy density, into its dispersive, D, polar, P, and hydrogen bonding, H, components[185]

$$\frac{E_{C,T}}{V} = \frac{E_{C,D}}{V} + \frac{E_{C,P}}{V} + \frac{E_{C,H}}{V} \quad \rightleftharpoons \quad \delta^2 = \delta_D^2 + \delta_P^2 + \delta_H^2 \tag{3.3}$$

where the square root of each of these components δ_D, δ_P and δ_H is a Hansen solubility parameter describing the dispersive, polar and hydrogen bonding interactions respectively. For polar solutes, it is necessary to match each of the Hansen solubility parameters for a stable dispersion.[185] Replacing the Hildebrand parameters in Eqn. 3.2 with their Hansen Solubility components in Eqn 3.3, we arrive at

the general expression for χ in Eqn. 3.4 [186]

$$\chi = \frac{v_0}{kT}\left[(\delta_{D,A} - \delta_{D,B})^2 + \frac{(\delta_{P,A} - \delta_{P,B})^2}{4} + \frac{(\delta_{H,A} - \delta_{H,B})^2}{4}\right] \tag{3.4}$$

By reducing χ through Hansen parameter matching, the enthalpy and free-energy of the system can be minimised to result in a solvent-stabilised dispersion. [187] It is worth remarking that dynamic processes during exfoliation also play a role in the solvent stabilisation mechanism. The archetypal solvents, NMP and DMF, are known to be susceptible to sonochemical polymerisation and degradation during exfoliation. [188,189] These polymeric by-products have been observed to further stabilise the exfoliated nanosheets through solvation and steric repulsion. [190] This has led to increased yields for LPE MoS_2 [189] and enhanced resistance to degradation for environmentally sensitive materials like black phosphorous. [173] Importantly, these effects are not transient in nature. TMD nanosheets that were exfoliated in NMP, but transferred to isopropanol (IPA), exhibit enhanced stability at elevated concentrations when compared to IPA exclusive processes. [191] However, despite the proliferation of NMP as a solvent, it is not a *panacea* – least of all in the corporeal sense due to its teratogenic and toxic effects. [192,193] With this in mind, efforts to develop more environmentally and personally benign solvents are being made. This work includes using aqueous solvents at elevated temperatures, [194] or co-solvent blends to tune the rheological properties and surface energy. [195]

Surfactant Stabilisation

As an alternative to high-boiling point and potentially toxic solvents, [196] exfoliated nanosheets can also be stabilised by non-covalent adsorption of surfactant molecules in water. [174] As is the case with many aspects of 2D materials research, this is built on the knowledge gained from preceding work

on solution-processed carbon nanotubes.[197] Surfactants are amphiphilic organic compounds. The hydrophobic tail group interacts with the nanosheet basal plane by London interactions, while a hydrophilic head group interacts with the polar aqueous environment to drive the dispersion stability.[198] Re-aggregation of the stabilised nanosheets is prevented by electrostatic and / or steric repulsion, depending on whether the surfactant is anionic, cationic, zwitterionic or non-ionic.[199] Prevalent surfactants include sodium dodecylbenzenesulfonate (SDBS)[200] and sodium cholate (SC),[201] which have been used to exfoliate myriad layered crystals including graphene,[125] TMDs,[202] and h-BN.[203]

Surfactant stabilisation works through the formation of an electrical double layer (EDL) that envelops the exfoliated nanosheets and electrostatically inhibits re-aggregation.[198] At room temperature, polar head groups migrate away from the tail groups by Brownian motion, remaining electrostatically bound in the vicinity as a diffuse cloud of charge. This disassociation leads to an effective negative charge on the nanomaterial from the bound tail groups, meaning surfactant-coated nanomaterials will electrostatically repel each other. The conditions where this repulsion exceeds the attractive vdW interactions were investigated by Derjaguin and Landau,[204] and independently by Verwey and Overbeek,[205] to give the eponymous DVLO theory of stabilisation.[206] By considering the attractive and repulsive potential energies of model spherical particles of radius, r, and separation, D, an expression for the potential energy of the system, V, can be derived[207]

$$V = \frac{\varepsilon_0 \varepsilon_r r^2 \zeta^2}{D} e^{-\kappa D} - \frac{A r}{12 D} \tag{3.5}$$

where ζ is the zeta potential of the colloidal dispersion,[208] A is the Hamaker constant,[209] and ε_0 and ε_r are the vacuum and liquid permittivity respectively. A measure of the effective thickness of the EDL is given by the Debye screening length, κ^{-1}.[210] As surfactant coated nanomaterials approach, the total

potential energy of the system rises to form a potential barrier, as shown in Eqn. 3.5. However, if this is overcome, there is a deep potential well at closer separations that quickly causes re-aggregation. Crucially, the magnitude of this barrier, and thus the dispersion stability, can be tuned using both κ^{-1} and ζ. Increasing ζ has been demonstrated to increase the barrier magnitude, with values of $\pm$ 30 mV (depending on whether surfactant is anionic or cationic) identified as the minimum potential required for long term stability.[211] The stabilising barrier can also be augmented by increasing κ^{-1}. This is achieved by increasing the surfactant concentration to its critical micele concentration (CMC).[207]

From an industrial, economical and safety perspective, exfoliation of nanomaterials in water would appear to grant the keys to the kingdom. Furthermore, surfactant assisted delamination of the parent crystal has been shown to produce smaller and more thin nanosheets when compared to solvent-based LPE.[212] However, the benefits in stability are heavily countered by limitations for further processing. In applications where pristine nanosheets are required, such as in printed electronics, a nanosheet-surfactant-nanosheet interface is detrimental to the transport properties. Furthermore, the viscosity of aqueous solutions is prohibitive for certain printing strategies, such as inkjet printing, while more volatile solvents are preferred for the aerosol jet printing process. Potential strategies to mitigate this include surfactant-assisted exfoliation followed by a solvent transfer, or by using liquid surfactants such as Triton-x. This allows the surfactant to be removed from a deposited network by annealing at temperatures above 270°C or via mechanical calendering.[213]

3.3 Size-Selection

Dispersions of solution-processed nanosheets are inherently polydisperse in both length and thickness. This can arise from the intrinsic properties of the parent crystal or exfoliation-driven mechanisms. It is known that sonication does not always yield complete delamination of the parent crystal, leading

to broad distributions in the exfoliated nanosheet thicknesses. The energetic environment can also induce scission along the basal plane of exfoliated nanosheets, further compounding the polydispersity.[214] Finally, in ultrasonic processing the energetic distribution is not homogeneous throughout the sample volume. This polydispersity must be addressed as many applications require particular nanosheet sizes: larger nanosheets offer enhanced mechanical reinforcement in nanocomposites,[215] while smaller nanosheets are ideal for catalysis.[216] This is further elucidated in the case of printed electronics, where the material bandgap scales with the number of monolayers.

The two preeminent methods for size-selection of solution-processed nanosheets are density gradient ultracentrifugation (DGU) and liquid cascade centrifugation (LCC). Adapted from its origins in pharmaceutical research, DGU works by exploiting subtle differences in buoyant density. The nanomaterials are loaded into a density graded medium (DGM) and will sediment towards their isopycnic point under the action of a centrifuge. This technique was initially applied by Hersam *et al.* to separate SWNTs by diameter,[217] but has subsequently been applied to separate exfoliated nanosheets by thickness.[218] However, the applicability of the DGU technique is constrained by its low yields, involved procedure and the potential for residual DGM on the size-selected fractions.

Liquid cascade centrifugation works through the principle of sedimentation-based separation. By applying a centrifugal force it is possible to isolate different nanosheet fractions as a function of their mass, shape and size. The rate at which a nanosheet fraction sediments is described by the Svedberg equation,[219] and is given by its sedimentation coefficient, s. This represents the velocity of the particle per unit gravitational acceleration and is described through Eqn. 3.6

$$s = \frac{m\,(1 - \nu\rho)}{f} \tag{3.6}$$

where m is the particle mass, v is the volume of one gram of the material in solution, ρ is the density of the solvent and f is the frictional coefficient. Under the action of a centrifugal force, large and thick nanosheets will sediment fastest, leaving small and thin nanosheets suspended in the dispersion. Taking inspiration from the iterative nature of gas-separation centrifugation cascades, this technique was augmented to size-select multiple nanosheet fractions from a stock dispersion by Backes *et al.* in 2016.[220] The LCC process is shown through an illustrative cascade in Fig. 3.4.

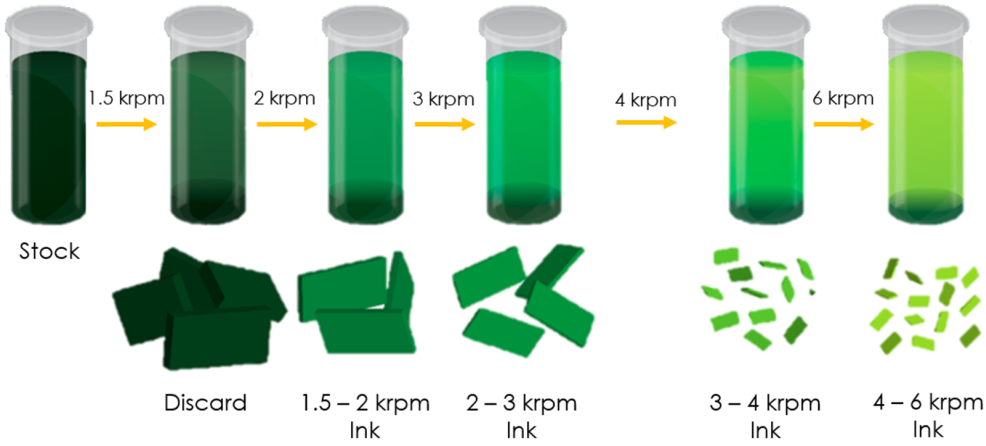

Figure 3.4: Liquid Cascade Centrifugation: Size-selection of nanosheets by sequential centrifugation runs. [Adapted from Ref.[220]]

Starting with a dispersion of nanosheets, an initial centrifugation step is performed at 1.5 krpm in order to confine any unexfoliated crystallites to the sediment. This sediment is then discarded, or can be subjected to a second exfoliation to produce more nanosheets. The supernatant now comprises a stock dispersion of well-exfoliated nanosheets having a broad distribution of sizes and thicknesses. This is then subjected to a further centrifugation step at a higher speed, 2 krpm in this case, and the sediment collected. This sediment is labelled as 1.5 - 2 krpm in Fig. 3.4, as it was trapped between these centrifugation speeds and contains the larger sized nanosheets from the distribution. The super-

natant, now containing all but the largest nanosheets, can then be iterated though sequential cascades, collecting the sediment at each step as shown in Fig. 3.4. As the trapping speeds of the LCC bands increase, the length and thickness of the nanosheets in each fraction decrease. Crucially, the trapped sediment at each point can be easily redispersed in solution with only mild sonication being needed.[221]

The intrinsic benefits of the LCC technique are its versatility, accessibility and efficiency. As material is collected after each cascade, it is a very low-wastage process while simultaneously achieving increased mass yields when compared to DGU.[222] Furthermore, with each subsequent cascade the monolayer content in the supernatant increases, reaching ~ 75 % in the inaugural work.[220] Finally, if nanosheets of a specific size distribution are required, LCC can be combined with published spectroscopic metrics to isolate desired fractions through appropriate selection of the upper and lower rpm. A crucial disadvantage of the LCC technique, and LPE in general, is that monolayer enriched fractions contain very small nanosheets ~ 50 nm in length. Indeed, as LCC essentially separates nanosheet fractions by their mass, and the thickness and length of LPE nanosheets are intrinsically coupled through energetic constraints, this appears to be a fundamental problem.[223] A further complication is that folded or crumpled nanosheets will sediment more quickly than their pristine counterparts due to changes in the sedimentation coefficient. This can cause smaller folded sheets to be trapped with comparatively larger nanosheets and broaden the distribution of lengths in a given size-selected fraction. Considerable work is being undertaken to improve both the degree of selectivity LCC offers and to increase the lateral dimension of LPE produced monolayers. Liquid cascade centrifugation is used extensively in this work to produce size-selected 2D dispersions for composite formation and printing.

* A note on nomenclature: As discussed in this chapter, LPE produced nanosheets are polydisperse in both length and thickness. To improve readability, the term "graphene" is used to refer to both mono- and few-layer nanosheets in this thesis.

Your assumptions are your windows on the world. Scrub them off every once in a while, or the light won't come in.

Isaac Asimov

4

Deposition & Characterisation

The ability to produce 2D materials in the solution-phase has catalysed their rapid proliferation across modern materials research. Networks of nanosheets can now be deposited using a suite of diverse strategies, with each technique influencing the resultant properties. Crucially, these advancements have coincided with the development of comprehensive characterisation methods, which has enabled optimisation of both the precursor dispersions and fabricated networks. The primary deposition and characterisation techniques used in this work are outlined in this chapter.

4.1 Printed Nanomaterials

4.1.1 Spray Coating

First conceived in 1876 as a means to retouch photographs, the airbrush took its recognisable form in 1883.[224] An inherently simple and scalable method, spray coating found use in the domains of art, cosmetics and manufacturing throughout its first century of operation. It was during investigations into alternatives to the ubiquitous transparent conductor, ITO, that carbon nanotubes were first spray coated in 2004.[225] Stemming from its diverse applicability, the spray coating technique soon became a workhorse for the large-area deposition of carbon nanotube, metallic nanowire, quantum dot and 2D nanosheet inks, where precise patterning is not necessary.[226–229]

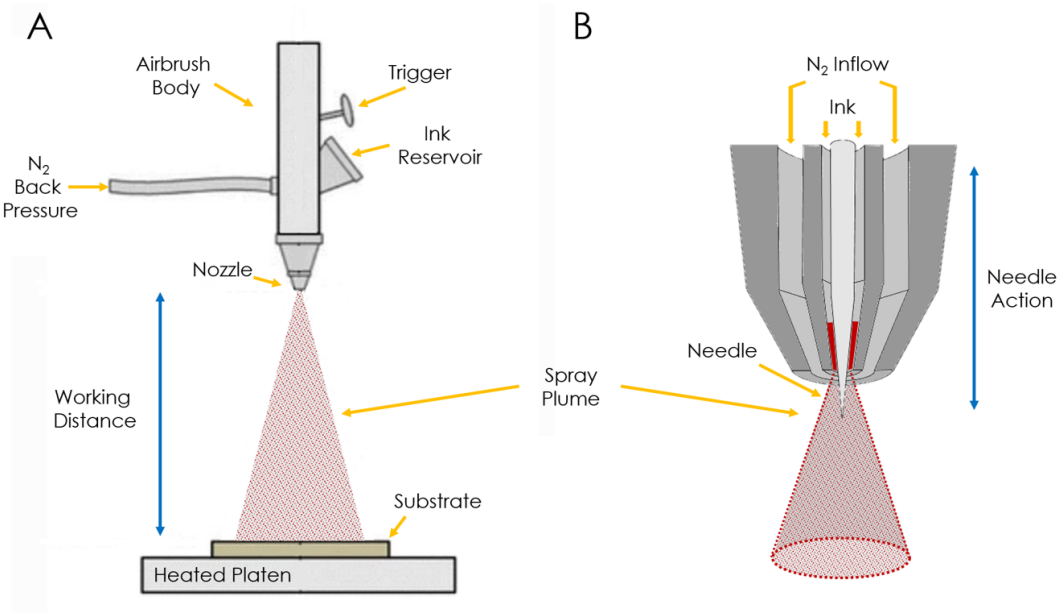

Figure 4.1: Spray Coating: A) Schematic of the spray coating process for a functional 2D ink. **B)** Cross-section of the sprayer nozzle showing the needle action and aerosol formation. [Adapted from Ref.[230]]

The spray coating process is shown schematically in Fig. 4.1A. A functional ink is gravity-fed from

its reservoir into the spraying nozzle, shown expanded in Fig. 4.1B. Engaging the airbrush trigger has a two-fold effect – it simultaneously retracts the needle and activates the N_2 back pressure, causing liquid ink in the nozzle to be released. Ligaments and droplets tens of microns in size are then sheared from the bulk fluid by the velocity gradient in the nozzle to generate an aerosol. This is then guided to the heated substrate by the flow of N_2 gas where the dispersing solvent is evaporated, leaving a uniform colloidal deposit. For large area deposits the airbrush is rastered in the xy-plane with repeating passes until a desired film thickness is achieved. The compatibility of this method across many different solvents[231] and substrates[232] arises from the aerosol generation. This relaxes the need for ink additives and allows for the decoupling of various constraints imposed by other common deposition techniques, such as inkjet printing.[233]

Though there is a procedural simplicity to the mechanism, the spray coating technique offers considerable scope for optimisation. Tunable parameters include the airbrush stand-off distance and raster speed, the N_2 flow rate and back pressure, the substrate temperature and nozzle diameter. The stand-off distance determines the area of impact of the spray plume and the deposited mass per unit area, while the flow rate and nozzle diameter determine the droplet density. Through multivariate analysis on sprayed silver nanowire (AgNW) networks it was found that the parameter with most influence on the uniformity of the resultant network is the N_2 backpressure.[227] An enhanced N_2 backpressure serves to increase the fluid velocity through the nozzle, precipitating the formation of smaller droplets. Further work determined that increased backpressures serve to tighten and skew the overall droplet size distribution to smaller values.[234] The combined result is a more homogeneous distribution of smaller droplets when compared to lower backpressures. Smaller droplets result in expedited solvent evaporation, which leads to reduced droplet coalescence and "coffee ring" staining to give increased network uniformity.[235] Indeed, by increasing the backpressure from 15 to 30 psi a significant

reduction in the average droplet size was observed by Scardaci *et al.*, with a corresponding reduction in deposit aggregation and improved AgNW film uniformity.[227] Complementary to this, both substrate temperature and solvent volatility considerably effect the drying and droplet coalescence rates. Elevated substrate temperatures ($\sim$ 70 °C for IPA) are employed to expedite solvent evaporation and increase uniformity.[236]

While the simplicity and high-throughput of the spray coating technique is useful for the indiscriminate deposition of thin films over large areas, it is not a direct-write process. Thus, fine-feature traces can only be spray coated with the help of masks or stencils. This is largely acceptable for applications where scalability is paramount such as displays, solar cells and electrochromic devices.[237] However, as demands for increased functionality and component density intensify, the need for higher resolution, direct-write and digitally-driven printing methods has become apparent.

4.1.2 Aerosol Jet Printing

Aerosol jet printing (AJP) is an emerging technique for the selective and non-contact deposition of functional inks onto an array of non-planar and conformal substrates.[238] The AJP process is shown schematically in Fig. 4.2. A nanomaterial ink is first atomized to form an aerosol mist comprised of micron-scale liquid droplets entrained in an inert carrier gas. This mist is then transported to the deposition head where it is focused and manipulated into a highly-collimated jet for deposition onto a substrate. AJP offers drastically improved versatility and resolution when compared with other more mature printing strategies, including the ubiquitous inkjet printing (IJP) method. By aerosolising the ink, the viscosity component can be decoupled and many of the rheological constraints of other printing techniques can be avoided. While IJP is generally limited to ink viscosities in the 8 - 20 cP range, the AJP technique can pattern inks having viscosities ranging from 1 - 1000 cP.[239] Coupled with this

enhanced material compatibility, the use of a collimated aerosol jet confers increased printing resolution at enhanced stand-off distances. This enables consistent patterning over non-planar samples and existing structures at substrate-nozzle distances in the 1 - 5 mm range.

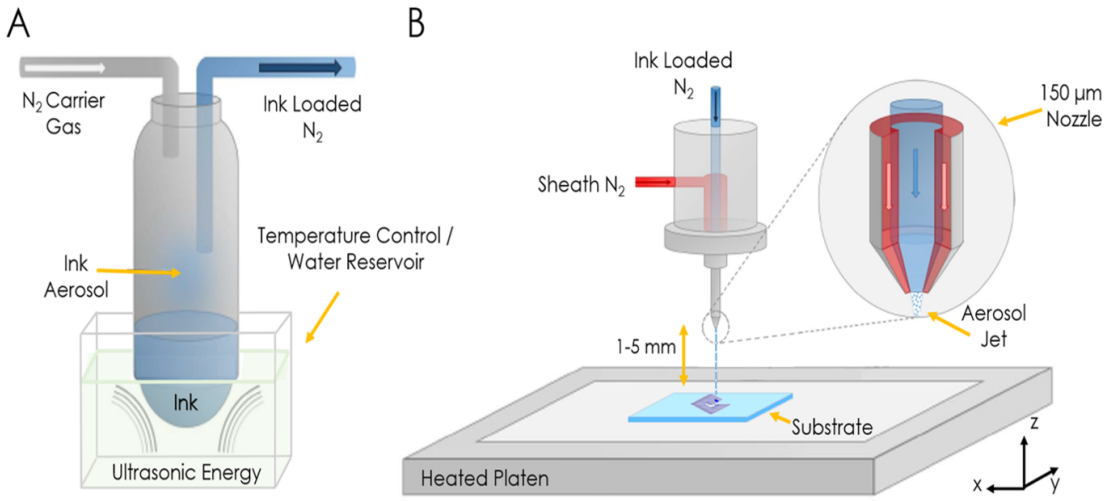

Figure 4.2: Aerosol Jet Printing: Schematics illustrating the key physical processes in aerosol jet printing. **A)** Ultrasonic atomization of the 2D ink to form an aerosol mist. **B)** Aerosol jet focusing, collimation and deposition. [Adapted from Ref.[240]]

The generation of an ideal aerosol for jetting is contingent on both the atomization process and the rheological properties of the ink. The interplay between the physical process and the ink viscosity, surface tension and volatility must be carefully tailored to produce a high-density and monodisperse aerosol. The ultrasonic atomization process, shown schematically in Fig. 4.2A, is used to produce aerosols from small volumes (1 - 2 ml) of low viscosity inks (1 - 20 cP). An ultrasonic transducer submerged in a reservoir of coupling fluid, typically distilled water, oscillates in the $\sim$ MHz frequency range to generate pressure waves. These waves are coupled to the ink vial through the distilled water, where they generate capillary waves at the ink surface by constructive superposition. Ink droplets with diameters on the order of 2 – 5 µm are then detached from the bulk fluid through local shear at the peaks of these waves to form a dense aerosol mist.[241]

Both the size and quantity of the atomized ink droplets are a function of process and rheological parameters. The size distribution of generated droplets is dependent on the capillary wavelength, which itself is determined by both the ink surface energy and density, as well as the transducer output.[242] Furthermore, the power required to atomize an ink, dictating the droplet generation rate, is restricted by viscous damping of the pressure waves.[243] This is a multifaceted process, but it can be optimised by tailoring the rheological properties of the inks both before atomization and *in situ*. With respect to the latter, temperature control of the water reservoir not only ensures a consistent process environment for atomization, but also allows for modulation of the ink viscosity for more favourable atomization.

Once a suitable aerosol has been produced, it is acted upon by an inert N_2 carrier gas, which drives the aerosol towards the deposition head through a PTFE mist tube. The droplet size is largely stabilised in transit to the deposition head as the dry carrier gas quickly becomes saturated with solvent vapour. This stability can be further ensured through the use of low-volatility cosolvent blends,[244] or by pre-saturating the N_2 carrier gas with solvent vapour using a bubbler. However, even accounting for drying effects the aerosol composition can drift in the few seconds it takes to reach the print head. The primary culprit is transport losses, which through gravitational settling and diffusion serve to remove the largest and smallest droplets from the aerosol respectively.[245] Aside from altering the aerosol composition, condensation of these droplets in the mist line can lead to the deposition of macroscale liquid droplets - much to the detriment of the sample and the operators emotional well-being.

Upon its arrival to the deposition head, the aerosol mist is acted upon by an annular N_2 sheath gas and focused using both a virtual and physical nozzle, as shown in Fig. 4.2B. The high-velocity sheath gas accelerates, collimates and aerodynamically focuses the aerosol jet, while preventing accumulation of material on the walls of the deposition nozzle.[246] This sheath-driven collimation is characteristic of the AJP process, enabling consistent deposition onto complex substrate topographies at stand-off

distances in the 1 - 5 mm range. Furthermore, the sheath flow forms a virtual nozzle within the physical deposition nozzle, with an aperture size dependent on the gas flow rate. Coupled with the jet collimation, this allows the AJP process to pattern traces with lateral dimensions $\sim 1/10$ the size of the physical nozzle aperture, on the order of 10 μm (*cf.* IJP resolution > 20 μm).[247]

There are myriad factors that can determine the final AJP deposition profile. However, the ratio of the sheath and carrier gas flow rates, known as the focusing ratio, has been proposed to be particularly important. Taken in isolation, the carrier gas flow rate determines the amount of material reaching the deposition head, while the sheath flow rate influences the impinging velocity and deposited linewidth. However, these two flows dynamically interact within the deposition head and so must be considered in tandem, with a focusing ratio of ~ 2 reported as the sweet spot.[248] A common artefact of AJP is overspray around the central deposit via small satellite droplets. Here, solvent evaporation drives a reduction in the suspended droplet size until they do not have enough inertia to impinge the substrate along the focusing axis. As discussed, low volatility cosolvents have proven useful to alleviate this effect and preserve the aerosol composition.

A final factor to discuss is the substrate-aerosol interaction. The resultant film morphology is heavily dependent on the wetting of the substrate and matching of aerosol-substrate surface energies. A wet film is expected to flow, fill voids, and reduce porosity, while the deposition of dry particles is associated with more aggregated and granular structures.[245] However, surface energy mismatches or excessive wetness in the deposited aerosol can lead to surplus solvent on the substrate, resulting in macroscopic droplets, flow and increased line spreading.[249] Once again, this can be managed through the use of high / low volatility cosolvent blends, or through pre-treatment and heating of the substrate.

Though the AJP technique holds significant promise for the rapid and precise patterning of 2D inks, this work is only in its nascent phase. With a paralysing choice of process parameters to vary, the

AJP process remains heavily guided by user intuition. However, work is underway to develop quantitative models and establish operating windows analogous to the Z-number framework employed in inkjet printing.[250] In the interim, the AJP technique has been used to pattern devices from silver, ceramic, polymer, carbon nanotube and 2D inks.[251–255] Conductive silver nanoparticle electrodes and 2D nanosheet traces were patterned using an Optomec Aerosol Jet Printer (AJP300) in this work.

4.2 Characterisation

4.2.1 Spectroscopic Characterisation

UV-Vis Spectroscopy

Ultraviolet-visible spectroscopy is among the most prevalent characterisation techniques for solution-processed nanomaterials. A simple, non-destructive and analytical technique, UV-Vis measurements provide information on the electronic structure of the dispersed material.[256] In recent years the utility of this method has been expanded to provide *in-situ* information on the concentration, length and thickness of dispersed nanosheets through the development of spectroscopic metrics.[203] Here, the information garnered from an extinction spectrum is extracted from the ensemble of billions of nanosheets. This contrasts with the statistical subsets of a few hundred measurements used in the more expensive and time-consuming TEM and AFM techniques.[212]

The experimental setup of a dual beam UV-Vis spectrometer is shown in Fig. 4.3. The dispersion is first diluted to a suitable optical density and added to a matched quartz cuvette of known path length (4 mm). A companion cuvette containing only solvent is used to provide a baseline reference, which is subtracted from the sample spectrum. This separates the material and solvent contributions, while also accounting for intensity losses due to reflections and scattering from the cuvette. The visible-

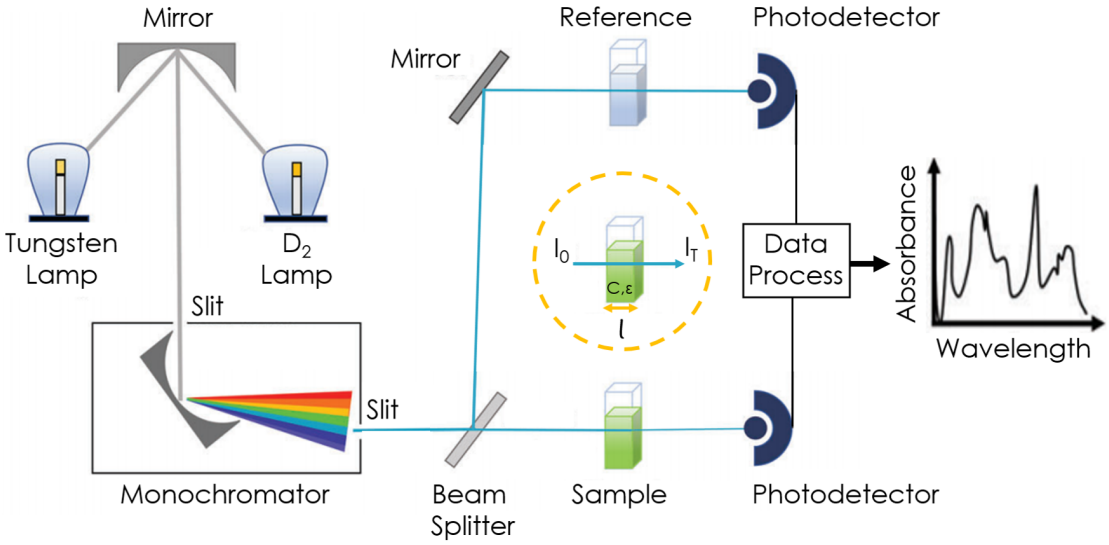

Figure 4.3: UV-Vis Spectrometer: Schematic of a dual-beam UV-Vis spectrometer. [Adapted from Ref.[257]]

infrared and ultraviolet light are generated from tungsten halogen and deuterium arc lamps respectively.[258] This is then selectively filtered into discreet wavelengths by a monochromator comprising slits, mirrors and a diffraction grating. Depending on the system, the finely tuned beam is either passed through both the sample and reference simultaneously using a beam splitter, as shown in Fig. 4.3, or alternates between both using a chopper. In both cases, the transmitted beams are incident on InGaAs photodiodes, where the difference between the transmitted reference (I_o) and sample intensities (I_T) are recorded as a function of wavelength to generate an extinction spectrum.[258]

The reduction in beam intensity post-specimen arises due to absorption and scattering mechanisms within the sample. In molecular solutions it is often sufficient to consider only absorption, however, dispersions of nanosheets are known to induce considerable scattering as a function of their lateral size.[259] Thus, spectra of nanosheet dispersions are often discussed in terms of extinction, $\varepsilon(\lambda)$, which

is the sum of absorption, $\alpha(\lambda)$, and scattering, $\sigma(\lambda)$, contributions

$$\varepsilon(\lambda) = \alpha(\lambda) + \sigma(\lambda) \tag{4.1}$$

The sample absorption and extinction can be decoupled by inserting an integrating sphere into the spectrometer. The sphere has a rough, white, and reflective internal coating that diffuses light, causing the intensity level inside to reach a steady state. By collecting both the transmitted and scattered light in this manner, the absorption component, $\alpha(\lambda)$, can be determined. Through characterising both $\varepsilon(\lambda)$ and $\alpha(\lambda)$, the scattering contribution can then be readily extracted through Eqn. 4.1.

Absorption occurs in a sample when the incident photon energies are sufficient to excite electronic transitions in the material. The corresponding decrease in irradiance is measured as an increase in the absorbance by the spectrometer. Semiconducting 2D materials, such as MoS_2, display rich absorption spectra once the incident photon energies exceed the bandgap. Absorption peaks, representing the relative strength of a transition, offer insight into the joint density of states through Fermi's golden rule.[260] However, it is important to note that other effects play a role in the spectrum. As mentioned, suspended nanosheets reduce the transmitted beam intensity through inelastic and elastic scattering mechanisms, broadening the absorption peaks. Further spectral broadening occurs when suspended nanosheets / molecules are densely packed, influencing each others energy levels.[256] Finally, vibrational and rotational states may be superimposed onto the electronic states, which further contributes to the peak broadening.[256]

Beam attenuation in the sample is described through the Beer-Lambert Law (though the initial observation was made on a glass of red wine by Pierre Bouguer some 30 years earlier).[261–263] As shown in Fig. 4.3, if the beam intensity through the sample is I_T and the intensity through the reference is I_o,

the beam has been attenuated by the sample with the extinction given by Eqn. 4.2

$$Ext = -\log(T) = -\log\left(\frac{I_T}{I_0}\right) = \varepsilon Cl \tag{4.2}$$

where T is the transmittance. Beer and Lambert stated that extinction will scale proportionally with both the path length of the sample, l, and the amount of attenuating material - given by the dispersion concentration, C. Furthermore, each material will have a different wavelength dependent extinction coefficient, ε. These are combined to give the recognisable form of the Beer-Lambert law in Eqn. 4.2. Recent work by Harvey *et al.* has shown that the scattering coefficient, $\sigma(\lambda)$, for 2D dispersions in the non-resonant regime exhibits a power law dependence on nanosheet size.[264] Here, it was found that nanosheets larger in lateral dimension will scatter more light at longer wavelengths than their smaller counterparts. This has been exploited to develop further spectroscopic metrics, which can be used to infer the nanosheet dimensions in a dispersion from its scattering spectrum. UV-Vis extinction spectra are used throughout this work to characterise the size-selected nanosheet fractions and measure their concentration. These spectra were recorded using Varian Cary 6000i (175 - 1800 nm) and 50 (190 - 1100 nm) UV-Vis-NIR spectrometers.

Raman Spectroscopy

Named in honour of Sir. Venkata C. Raman, the eponymous Raman effect was discovered in 1927 and has since developed into one of the most important techniques for nanomaterial characterisation.[265] Based on the inelastic scattering of light by matter, Raman spectroscopy is used to probe sample lattice vibrations in the form of optical phonons. These displaced atoms can be modelled as harmonic oscillators where the quantized vibrations are a function of the bond strength, and thus

a signature of the material. By studying energy shifts in the inelastically scattered photons, Raman spectroscopy offers an accessible and non-invasive means to characterise the physical and chemical properties of materials, as well as environmental stimuli that may alter them. [266]

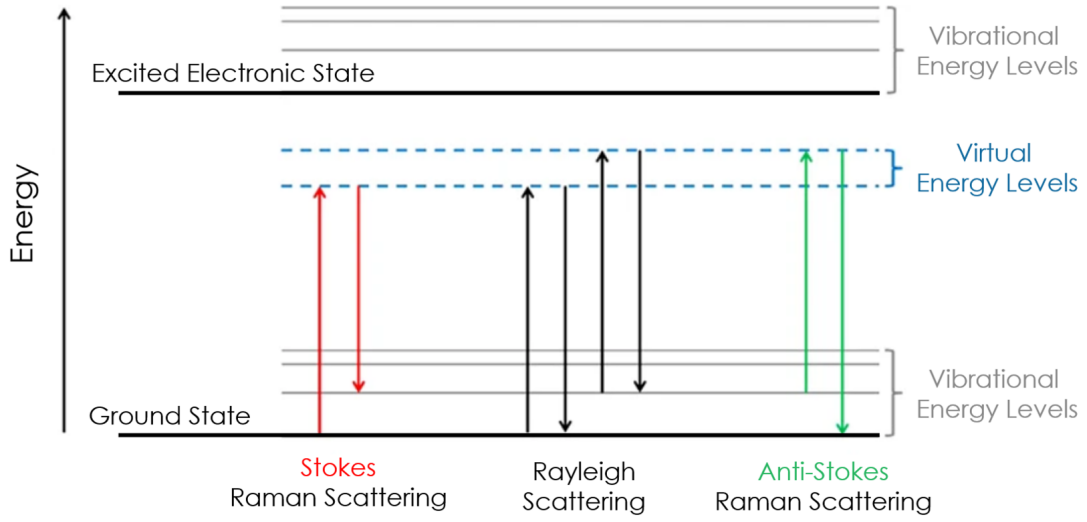

Figure 4.4: Raman Scattering: Diagram of the energetic transitions involved in Raman scattering. [Adapted from Ref. [267]]

When a monochromatic beam is scattered by a sample, the energy exchange between the radiation field and sample is considered as two single-photon transitions. Initially, the oscillating electric field of an incident photon may interact with the sample's electron cloud, inducing a dipole moment. The strength of this interaction is determined by polarizability of the sample material. [266] Through this perturbation of the electron cloud the photon is said to be absorbed to a *virtual* transition state, shown in Fig. 4.4. This constitutes a brief distortion in the electronic distribution, as opposed to a stationary state. [268] Upon relaxation, the electron cloud then scatters energy into a second photon, which is emitted as a scattered photon. In the perfectly elastic case, the scattered and incident photons have equivalent energies and the process is known as Rayleigh scattering. [269] Most incident photons are Rayleigh scattered, as the wavelength of photons is much larger than atoms or molecules.

However, for one in every ten million photons the induced dipole moment also drives vibrations of the atomic lattice. Such photons are said to be Raman scattered as they will have lost / gained energy by creating / absorbing an optical phonon. In the case of the former, the photon creates a phonon in the material leaving the sample atom in an excited vibrational state. The resultant scattered photons will be red-shifted by the process, known as Stokes scattering. If the sample atom is already in an excited vibrational state, the scattered photon may absorb a phonon, returning the atom to its ground state. These scattered photons are blue-shifted by a process known as anti-Stokes scattering. Both mechanisms are shown schematically in Fig. 4.4. The frequency shift of the scattered light, ν, is indicative of the energy gained or lost by the material in the interaction [268]

$$\nu = \frac{1}{\lambda_i} - \frac{1}{\lambda_s} \tag{4.3}$$

where λ_i and λ_s are the wavelengths of incident and scattered light. The intensity distribution of ν forms the basis of the Raman spectrum. The peak positions and their relative intensities are used to identify specific bond vibrations, which when combined across the spectrum establish a chemical fingerprint for a material. For 2D materials, Raman shifts also provide information on doping, defects, stress and the degree of interlayer coupling in nanosheets. [270] This is complimented by compositional information on nanostructured composites. [271] The Raman spectroscopy in this work was performed by Dr. Victor Vega using a Horiba LabRam HR800 spectrometer.

4.2.2 Electron Microscopy

Developed to overcome the resolution limits of optical microscopy ($\sim$ 200 nm), electron microscopy is a ubiquitous technique for the characterisation of both isolated nanomaterials and their networks.

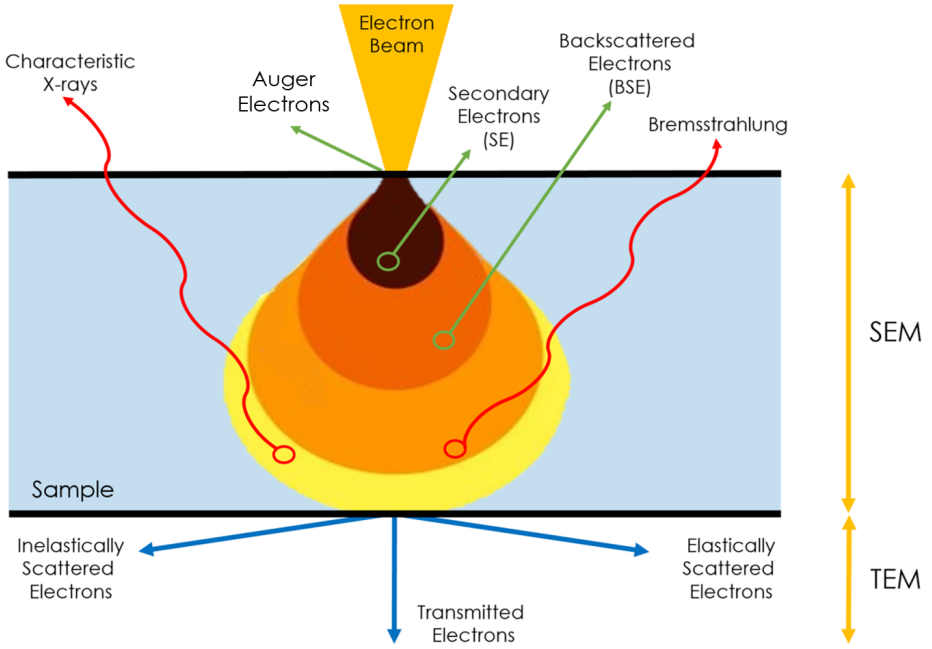

Figure 4.5: Beam-Sample Interactions: Schematic depicting the potential beam-sample interactions in both a scanning (SEM) and transmission (TEM) electron microscope. [Adapted from Ref.[272]]

By modulating the electron velocity in an applied electric field its de Broglie wavelength, λ, can be reduced to values in the picometre range. This occurs via $\lambda = h/m\,v$,[273] where h is Planck's constant and m, v are the electron mass and velocity respectively. Modern instruments can produce electron wavelengths in the 1- 40 pm range, facilitating analysis of the position and chemistry of individual atoms.[274] Furthermore, the reduced wavelength and charged nature of electrons vastly increases the number of beam specimen interactions and information carrying signals.[275] The origin of these signals within the interaction volume are shown schematically in Fig. 4.5 and will be discussed in the coming sections.

Scanning Electron Microscopy (SEM)

Due to its comparatively lower resolution, the demonstration of the scanning electron microscope in 1942 was met with a degree of indifference by the already established TEM community.[276] Fortunately, its potential for surface characterisation of bulk samples was recognised and in the ensuing 80 years the technique has matured to become "the monkey wrench on the garage wall" of sample characterisation.[277] A modern SEM facilitates morphological and compositional characterisation of bulk powders, nanostructured networks and their composites across many length scales.

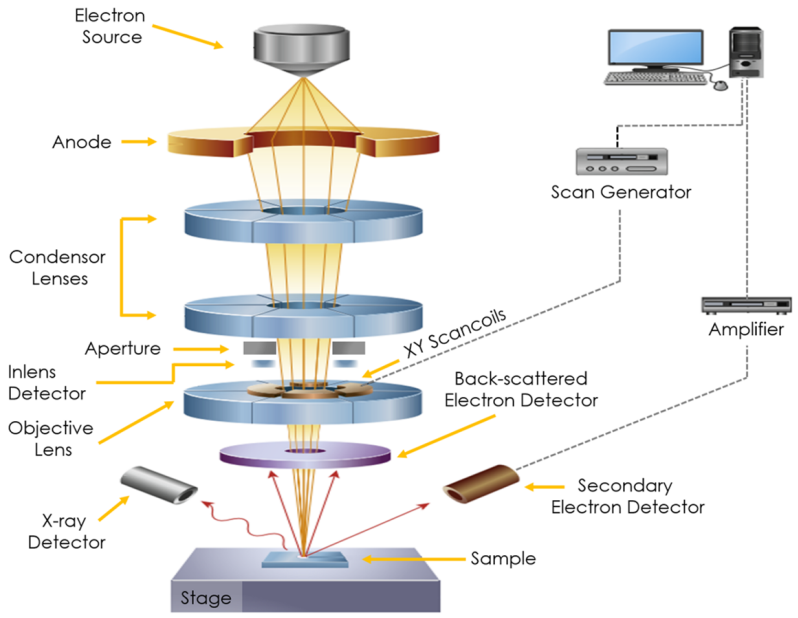

Figure 4.6: SEM: Schematic of a SEM Column. [Adapted from Ref.[272]]

A representative schematic of the Carl Zeiss Ultra Plus SEM used in this work is shown in Fig. 4.6. The probe electrons are generated by field emission from a negatively biased single-crystal tungsten tip. The emitted electrons, having energies in the range of 0.1 – 30 keV, are then accelerated down the column where the beam profile and intensity are modulated by the electromagnetic condenser lenses

and aperture. An optimised electron probe then passes through the electromagnetic objective lens where it is focused into a spot a few nanometres in diameter on the sample surface. This beam is then rastered across the sample using the *xy*-scan coils, where the probe-sample interaction at each point is recorded and mapped into a surface image.

The primary signals generated when an electron beam interacts with a sample are shown in Fig. 4.5, and include secondary electrons (SE), backscattered primary electrons (BSE) and x-rays.[278] BSE are probe electrons that undergo Rutherford scattering with atomic nuclei in the sample and are scattered through 90 - 180°.[272] These are useful for phase identification in composite and bulk samples as the repulsive power of the nucleus, and so the intensity of BSE, is a function of atomic number. Thus, elements in a sample having different atomic numbers can be distinguished by their relative brightness in BSE imaging mode. Further compositional analysis is achievable through energy dispersive x-ray spectroscopy (EDS). Materials generate both *Bremsstrahlung* and characteristic x-rays when bombarded with electrons of sufficient energy. Characteristic x-rays are generated when primary electrons displace an electron from an atomic shell in the sample. The subsequent transition of an electron from a higher energy state to fill the vacancy causes emission of an x-ray with an energy characteristic of the transition. As characteristic x-ray energies can be directly attributed to the specific elements in the sample that generated them, EDS can be used to identify the elemental composition of a sample (to within a few *wt* %) in a non-destructive manner.

Secondary electrons are of the most relevance to the imaging performed in this work. SEs are generated via inelastic scattering mechanisms with atoms in the sample, whereby a primary probe electron ionizes electrons in the specimen.[272] These low energy electrons (< 50 eV) are then emitted from the sample as secondary electrons. Depending on where in the interaction volume the SEs emerge, they are collected by a different detector. Secondary electrons that leave the specimen at the probe-sample

incidence point are known as SE1 electrons. These are collected by the in-lens detector located inside the pole piece.[279] Secondary electrons that undergo multiple scattering events before emerging away from the point of incidence are known as SE2 electrons. These are collected by an Everharte-Thornley detector to the side of the chamber.[280] As SE1 electrons are generated by direct interaction with the probe, they carry the most spatial resolution and surface information. Due to their low kinetic energies, only SEs generated within $\sim$ 20 nm of the sample surface have enough energy to overcome inelastic collisions and the specimen work function to escape. Thus, SE imaging is remarkably sensitive to the local sample topography, with slopes, ridges and edges exhibiting enhanced SE emission. For high resolution images that give 3D information on the topography of a nanostructured network, the imaging mode of choice is secondary electron mode.

Transmission Electron Microscopy (TEM)

The elder sibling of the SEM, the transmission electron microscope was first demonstrated in 1931 by Knoll and Ruska.[281] The TEM utilises significantly higher electron energies (80 – 300 keV) to pass them through electron transparent samples $<$ 100 nm thick. The transmitted electrons are then collected by a detector to create a 2D projection of the 3D sample, with resolutions in modern aberration-corrected systems approaching 1 Å.[282]

As in the SEM, an electron probe is first generated by the illumination system. The source used is dependent on the desired resolution; thermionic emission from a LaB_6 or tungsten filament source is used for routine TEM, while Schottky or cold field emission guns are used for high resolution imaging. The electrons in the probe, having energies of 80 – 300 keV (*cf.* SEM 1 – 30 keV), are then focused into a beam of controlled diameter and convergence on the sample by the condenser system of electromagnetic lenses and apertures. Here, the TEM produces many of the same interactions as with the

SEM. However, electrons can also be transmitted through the sample, either directly or through elastic and inelastic scattering mechanisms. These interactions are summarised in Fig. 4.5. The transmitted electrons then pass through the imaging system, which determines the magnification and spatial resolution of the image. An initial image and diffraction pattern are formed by the post-specimen objective lens, which is then magnified onto the detection system, generally a cooled CCD.[283]

Through the use of post-specimen apertures, a TEM can operate in many different imaging modes including bright-field, dark-field and diffraction.[280] All TEM imaging in this work was performed in the bright-field mode, where an image is formed exclusively from unscattered electrons. Scattered electrons that have been transmitted are filtered out using an objective aperture in the back focal plane of the objective lens. In a bright-field image, areas of the specimen which are scattering will transmit fewer electrons meaning regions of increased thickness, mass, atomic number and grain boundaries will appear with darker contrast.[280] The TEM measurements in this work were performed by Dr's Andrew Harvey and JB Boland using a JEOL 2100 TEM system at a 200 kV accelerating voltage.

4.2.3 Focused Ion Beam Microscopy (FIB)

Initially developed in the 1970s,[284] the focused ion beam (FIB) microscope is broadly similar to the SEM, only with a beam of accelerated ions taking the place of electrons in the probe. This confers additional micromachining functionalities to the tool for sample milling, lamella preparation, material deposition and microstructural analysis.[285] Modern FIB systems are generally operated in a dual beam FIB-SEM configuration, as shown in Fig. 4.7A. Here, the sample is manipulated using the ion beam while its interaction with the sample is imaged *in situ* by the SEM.

In the majority of modern FIB systems probe ions are generated using a gallium-based liquid metal ion source (LMIS). The LMIS is comprised of a gallium reservoir attached to a tungsten needle of

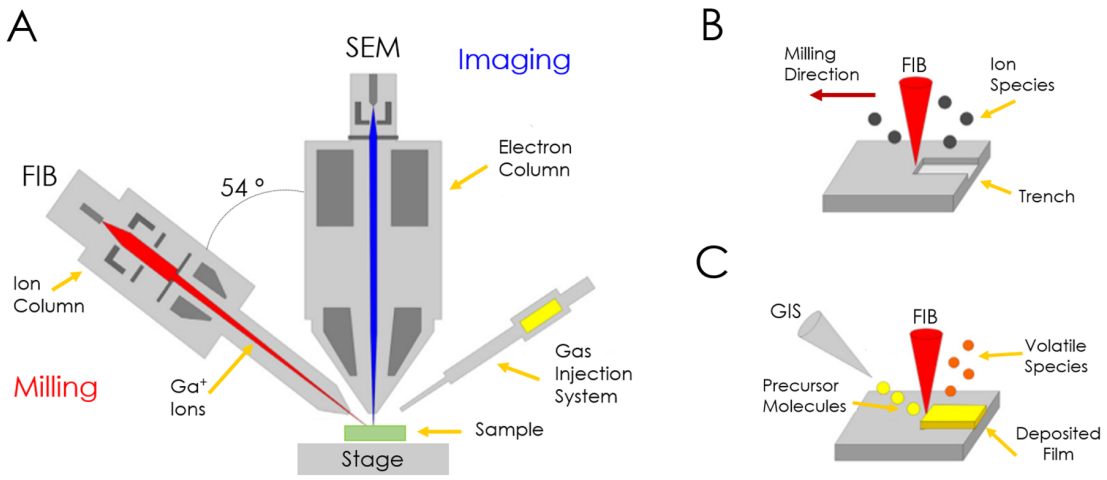

Figure 4.7: The FIB-SEM Microscope: A) Cross-sectional schematic of a FIB-SEM showing the FIB, SEM and GIS geometry for sample milling, imaging and deposition respectively. **B)** Ion-beam milling of the sample showing removed material and scattered ion species. **C)** Ion beam assisted deposition of a molecular film from molecules released from the gas-injection needle. [Adapted from Ref.[286]]

radius 2 - 5 μm. During operation, the gallium is heated, flows, and wets the tungsten needle. An extractor just below the tip is held at a negative potential of ∼ 6 keV, which generates a large electric field at the tip and ionizes the gallium. The balance between electrostatic forces and surface tension draws the liquid gallium into a fine tip of radius ∼ 5 nm, named a Taylor-Gilbert cone.[287] Ga^+ ions are then emitted from the apex of this cone by field evaporation and accelerated down the column by applied voltages of 5 - 50 kV.[288]

In order to define, focus and raster the ion probe, the beam is acted upon by a series of apertures, electrostatic lenses and deflection plates. In practical terms, the most relevant component is the beam limiting aperture. By changing the aperture size, the beam current can be adjusted from a few pA to tens of nA, determining the image quality or sample milling / deposition rate.[289] Reduced beam currents are used for increased imaging and milling resolution, while larger apertures promote enhanced milling rates. As in the SEM column, the ion beam is initially defined and focused onto the sample using condenser and objective lenses, where it is then scanned over the surface using deflection plates.

However, as the focusing strength of electromagnetic lenses used in a SEM are proportional to the charge per unit mass of the particle, they are unsuitable for considerably more massive ions. Thus, the focusing and steering of probe ions in the FIB column is performed using electrostatic components, which depend only on the ion's charge. To prevent unwanted sample milling, a high-speed beam blanker, such as a Faraday cup, is used to deflect the beam from the sample. The imaging / milling resolution of modern FIB microscopes, such as the Zeiss Auriga used in this work, is primarily limited by beam-sample interactions to $\sim$ 10 nm.[290]

A FIB can also be used to deposit metallic or dielectric materials via ion beam induced deposition (IBID). For the metallic depositions in this work, a gas injection system (GIS) is used to introduce precursor organometallic molecules to the sample surface where they are adsorbed. In the presence of an ion beam, these molecules can be disassociated such that the volatile organic components are sputtered from the sample, leaving a non-volatile metallic deposit on the sample surface. This process is shown in Fig. 4.7C. Conductive deposits are essential for high-quality sample milling, especially in the case of disordered nanosheet networks. A homogeneous deposit over the region of interest serves to smooth the sample surface, which prevents the formation of milling artefacts such as curtaining.[289] Furthermore, the deposited film acts as a sacrificial layer that protects the sample from destructive milling by the beam. A similar process utilises the electron beam in place of the ion beam and is often performed before the IBID process as it is comparatively more gentle. This allows an initial protective deposit to be formed before the ion beam is used, reducing the chances of sample damage.

Ion-solid interactions are what underpin the imaging and milling functionalities of the FIB microscope. Ions incident on a sample lose their kinetic energy through a variety of elastic and inelastic interactions with the sample atoms. Through inelastic interactions, known as electric energy loss, the ion loses energy to the sample electrons. This causes ionization and emission of both electrons and

electromagnetic radiation from the sample in the form of secondary electrons, x-rays, phonons and cathodoluminescence.[291] However, it is the elastic interactions, known as nuclear energy loss, that are most relevant to sample milling. Here, energy is transferred as translational energy to sample atoms, leading to their displacement and potential sputtering from the sample surface. According to the collision cascade model, if the energy transferred to a target atom exceeds a critical value known as the displacement energy ($\sim$ 20 eV), the atom is knocked from its original site leaving a vacancy.[292] This primary recoil atom may have sufficient energy to displace further atoms, generating a volume where considerable numbers of atoms have excess kinetic energy. If these collisions occur near the sample surface, these atoms may be emitted from the solid, leading to sputtering. Though the majority of nuclear energy loses manifest as atomic vibrations and sample heating, a single incident 30 keV Ga^+ ion can sputter between 1 - 20 atoms.[293] This is the basis of FIB milling, shown in Fig. 4.7B. Sample sputtering is a highly complex process that depends not only on the beam parameters, such as current and accelerating voltage, but also on the sample type, orientation, incidence angle and redeposition of sputtered material. A recent development in the characterisation of nanostructured samples is the sequential milling and imaging of sample cross-sections to extract three dimensional information on the sample morphology and composition. This is known as FIB-SEM tomography and its application to printed nanosheet networks will form the basis of Chapter 8.

To achieve great things, two things are needed; a plan, and not quite enough time.

Leonard Bernstein

5

Solution-Processed Nanosheet Networks & Their Applications

Networks of solution-processed nanosheets and their composites are undeniably attractive building blocks for a variety of electronic, optical, thermal and mechanical applications.[294–296] This stems from their superlative physical properties, as addressed in Chapter 1. However, as myriad examples in the literature will demonstrate, the remarkable properties of the constituent nanosheets do not naturally translate to their networks. This arises from the fact that the electrical transport and mechanical stability of such networks is now limited by the presence of vdW interfacial junctions between the nanosheets.[297] This is not a fatal indictment, as even in these wholly unoptimised systems nanosheet

networks demonstrate comparable transport properties to amorphous silicon, organics and nanotube networks in large-area applications.[298] Further, though nanosheet networks display vastly inferior mechanical properties to their constituent nanosheets,[299] carefully designed nanocomposites are now suitably robust such that their excellent storage and catalytic properties can be capitalised upon. This coming section aims to briefly discuss charge transport in solution-processed 2D networks, followed by an introduction to nano:nano composites and their potential for electrocatalytic applications.

5.1 Electrical Transport in Nanosheet Networks

The explosion of interest in flexible and wearable consumer electronics has provoked a commensurate level of research into solution-processed thin-film electronics. The unsuitability of silicon due to restrictive substrate sizes, high costs and prohibitively large processing temperatures has necessitated the emergence of high-throughput solution-processed films. Networks of organics are at a relatively mature stage and present the current benchmarks in many applications.[300] However, their sensitivity to environmental conditions means they are predisposed to rapid performance degradation in an ambient setting.[301] This has precipitated significant interest into large area thin-films comprised of inorganic nanomaterials, owing to their stability, versatility and device performance.

Solution-processed networks of 2D nanosheets offer a variety of advantages over networks of zero- (0D) or one-dimensional (1D) nanostructures, as shown in Fig. 5.1. Electrical transport in thin films constructed from 0D nanomaterials, such as quantum dots, is limited by grain boundary densities on the order of 10^5 μm^{-2}. Such interfaces are associated with chemical disorder that arises from a termination of the bulk lattice, surface species and misalignment between randomly oriented crystals.[298] These disordered interfaces are detrimental to charge transport, forming trapping sites and transport barriers,[302] as shown in Fig. 5.1A.

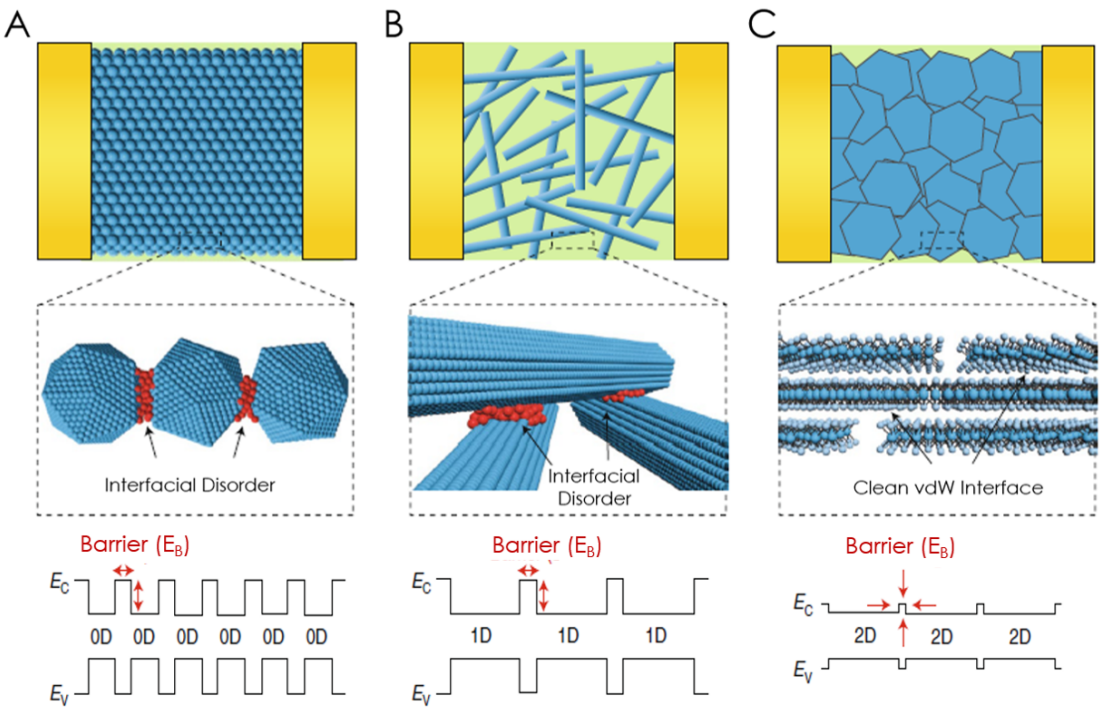

Figure 5.1: Low Dimensional Thin Films: Schematic illustration of thin films based on **A)** zero-dimensional (0D), **B)** one-dimensional (1D) and **C)** two-dimensional (2D) nanostructures. The band diagrams reflect both the frequency and amplitude of energetic barriers to charge transport in each system. [Adapted from Ref.[298]]

Films comprised of 1D metallic nanowires have been widely researched due to their potential as flexible transparent conductors,[303] while networks of semiconducting SWNTS have demonstrated promising performance in biologically friendly integrated circuits.[304] However, 1D films are often limited by relatively incomplete surface coverage, shown schematically in Fig. 5.1B.[305] Networks of 2D nanosheets can potentially address the shortcomings of their 0D and 1D counterparts and thus represent the ideal geometry for solution-processed electronics.[305] As shown in Fig. 5.1C, 2D nanosheets can be uniformly tiled upon each other solely through vdW forces with atomically-clean interfaces. Here, the vdW forces that attract adjacent crystals effectively squeeze out trapped contaminants,[306,307] which in the optimised limit can mimic the natural interfaces of the parent crystal.[308] This network

geometry is driven by the large aspect ratio of 2D nanosheets and serves to increase the surface coverage and reduce the grain boundary density, while facilitating improved charge transport through large-area conformal contacts.

5.1.1 Network Mobility and Interfacial Junctions

Despite their inherent advantages over other low dimensional nanostructures, a persistent observation has been the dichotomy between the transport properties of 2D nanosheets and their networks. A clear demonstration of this was performed by comparing the carrier mobility of printed networks with the mobility of their constituent nanosheets by Kelly *et al.* in 2017.[191] The network mobility was found to trail the nanosheet mobility by a factor of $10^2 - 10^3$ for printed networks of MoS_2, WS_2, WSe_2 and $MoSe_2$, with the disparity increasing as the mobility of the constituent nanosheets increased. More generally, while TMD and graphene nanosheets demonstrate mobilities on the order of 10 - 200 $cm^2(Vs)^{-1}$ and 10,000 $cm^2(Vs)^{-1}$ respectively,[9,309] their corresponding networks exhibit mobilities in the 0.01 – 10 $cm^2(Vs)^{-1}$ range for TMDs and $\sim$ 100 $cm^2(Vs)^{-1}$ for graphene.[310,311] As this discrepancy exists across a variety of preparation and deposition methods, solvents and nanosheet types, it is suggestive of an underlying global mechanism.

Charge transport in solution-processed nanosheet networks is limited by interfacial junctions between adjacent nanosheets. These junctions represent areas where nanosheets are in close contact, with charge transport across the vdW gap occurring via quantum tunnelling or hopping mechanisms at low temperatures, and thermal activation above $\sim$ 100 K.[312] The deleterious impact of interfacial junctions on the network mobility can be crudely demonstrated through Matthiessens' rule by considering the network mobility as a combination of both the intra- and inter-nanosheet mobilities[313]

$$\frac{1}{\mu_{Network}} \approx \frac{1}{\mu_{Nanosheet}} + \frac{1}{\mu_{Junction}} \tag{5.1}$$

It is clear from Eqn. 5.1 that a reduced mobility at these junctions has the potential to dominate the carrier mobility of the overall network. This is of particular relevance to solution-processed networks where the 2D inks are often polydisperse in nature.[314] The resultant networks are often reasonably well-aligned in the plane of the film, but contain significant porosity and limited basal plane overlap as a result of the inhomogeneous packing.[315] This leads to a broad distribution of junction types and the formation of many point like contacts between nanosheets. In this scenario, the limited nanosheet overlap is expected to increase the junction resistance and reduce the network mobility.

The role of junctions in the electrical transport of nanosheet networks was recently demonstrated for networks of MoS_2 nanosheets. Published conductivity values for both printed and filtered MoS_2 primarily lie in the 10^{-5} - 10^{-6} S m^{-1} region.[316] However, Lin *et al.* have recently reported a spin-coated network of highly-aligned MoS_2 nanosheets with a conductivity of 0.1 S m^{-1}.[308] Cross-sectional SEM images of the networks revealed tiled nanosheets with basal plane contacts that were nearly indistinguishable from the natural vdW interfaces. This would be expected to drastically reduce the junction resistance, leading to the exceptional conductivity mentioned above, as well as a network mobility of 10 cm^2(Vs)$^{-1}$ - approaching that of the nanosheets themselves.[308] A similar improvement in electrical transport has been demonstrated in spray coated graphene networks through mechanical compression of the network by calendering.[213] Compression of the deposited networks by a factor of $\sim$ 2 served to reduce the porosity, while increasing the alignment and basal plane overlap of the nanosheets. The corresponding decrease in junction resistance (among other surfactant effects) produced a six-fold increase in the network conductivity. Though it is clear that junction effects are a fundamental issue

limiting electrical transport in 2D networks, they are currently not fully understood. However, we can look to more mature low-dimensional systems for strategies to mitigate their adverse effect on charge transport in nanosheet networks.

Semiconducting-SWNT and Colloidal Nanocrystal Networks

Owing to their potential for low-cost macroelectronics, the selective isolation and deposition of semiconducting single walled nanotubes (s-SWNTS) has been an area of intense research for some years.[317] As such systems are broadly analogous to nanosheet networks, some parallels can be drawn to inform the 2D case. Electrical transport in s-SWNT networks is well-reported to be limited by inter-nanotube junctions, where the transport bottleneck arises from the hopping of charges from one nanotube to another. This results in s-SWNT networks exhibiting junction resistances that are orders of magnitude greater than the resistances of the nanotubes themselves, with charge transport in such systems often modelled as a random resistor network of inter-nanotube junctions.[318,319] What follows is a length-dependent mobility scaling in s-SWNT networks,[320] and thermally activated behaviour that is associated with inter-nanotube hopping.[321] Notably, the junction resistance, and correspondingly the overall network mobility, is found to be a function of both the junction morphology and the intrinsic nanotube properties. As with nanosheet networks, junction morphology and overlap area are key parameters, with larger area junctions associated with reduced junction resistances and increased inter-nanotube mobilities.[322] Additionally, the network carrier mobility in mixed SWNT networks has been shown to depend on the nanotube density of states (DOS). This manifests as inter-nanotube junction resistances that vary with nanotube type, from 250 kΩ for metallic-metallic junctions to 500 kΩ for junctions between semiconducting nanotubes.[323] It follows from this that the carrier mobility in a s-SWNT network will scale with the carrier density, as recently shown by Schießl *et al.*[318] This is

in agreement with reported nanosheet network data, whereby semiconducting networks with carrier densities $< 10^{22}$ m^{-3} display inferior mobilities to metallic / semi-metallic networks, which generally exhibit carrier densities $\gg 10^{23}$ m^{-3}.[191,324]

As with nanotube and nanosheet networks, the carrier mobility in colloidal nanocrystal networks is often limited by inter-crystal hopping.[325] However, through the promotion of inter-crystal coupling by atomic necking, essentially increasing the inter-nanocrystal contact area, the network mobility is found to increase asymptotically towards that of the individual nanocrystals.[326] This result, coupled with the 2D analogue of large-area tiled MoS_2 junctions mentioned above, offers compelling evidence as to the importance of junction morphology in these disordered systems. However, as with networks of s-SWNTs, it has been shown that junction effects alone are not sufficient to fully describe charge transport in these systems. The intrinsic nanocrystal properties must also be accounted for. To probe this, charge transport in colloidal nanocrystal systems has been widely investigated as a function of temperature, generally reporting the network conductivity to display Arrhenius-like scaling with temperature, T, such that[327]

$$\sigma_{Net} = \sigma_0 \, exp\left(-\frac{E_A}{k_B T}\right) \tag{5.2}$$

where σ_{Net} and σ_0 are the network conductivity and a constant pre-exponential factor respectively. E_A is the activation energy for the disordered network and can be considered as the energy required to thermally excite charge carriers to participate in transport. Recent work on sprayed networks of silicon nanocrystals by Aigner *et al.* is of particular relevance here.[328] Through temperature-dependent field effect transistor (FET) measurements, both the network carrier density and mobility were found to display Arrhenius-like behaviour, each with its own activation energy. Thus, the total activation energy of the network, E_A, can be decomposed into carrier density and carrier mobility components

as

$$E_A = E_{A,n} + E_{A,\mu} \tag{5.3}$$

where $E_{A,n}$ is related to the thermal excitation of carriers from the Fermi level. The $E_{A,\mu}$ term is proposed to describe thermally-activated charge transfer across energy barriers at the nanocrystal interfaces.[328] An interesting observation is that the charge carrier activation energy, $E_{A,n}$, is found to be similar for each of the sprayed silicon networks, even under different testing conditions. Furthermore, the network carrier density is found to be reasonably similar to the nanocrystal carrier density in most networks, but reduced by some scaling factor to account for porosity and percolation pathways.[328] In contrast, the mobility activation energy, $E_{A,\mu}$, was found to depend on the specific film and the experimental conditions. What follows is that, in the simplest case, the network properties that are material specific are described by the carrier density, while the extrinsic junction related properties are contained within the mobility. Thus, to rapidly improve the electrical performance of nanosheet networks, especially TMD networks who share Arrhenius conductivity scaling with temperature,[73] the tailoring of their network properties such as alignment, porosity and junction overlap will be key.

5.1.2 Routes to Optimisation

Fortunately, solution-processed nanosheet networks offer a rich parameter space for optimisation. Though charge transport through the network can be improved by tuning both the nanosheet and network properties, it appears that alleviating the network-imposed transport bottlenecks offers the most reward at this point. Numerous strategies are currently being investigated to this end, with some promising results. As mentioned, post-deposition treatments such as mechanical compression have demonstrated considerable improvements in the network mobility by increasing the nanosheet

alignment and basal plane overlap.[213] However, though such strategies are compatible with roll-to-roll processing, it is unclear if the method is applicable to printed devices and vertical heterostacks. Thermally-driven phase inversion is another post-treatment that has demonstrated potential to tailor the microstructure of printed graphene films, whereby the network conductivity can be tuned over an order of magnitude.[329] Direct efforts to engineer improved inter-nanosheet contacts are also being vigorously explored. Solution-phase decoration of TMD nanosheets with gold nanoparticles holds potential to improve network mobilities, as the nanoparticles preferentially bind at nanosheet edges and basal plane defect sites.[330] A similar molecular approach involves healing sulfur vacancies along both the nanosheet basal plane and edge sites using thiol molecules.[152]

One crucial parameter that has received only limited attention is the effect of nanosheet dimension on the electrical and morphological properties of the resultant network.[331] This is especially critical for printed films, where in the absence of monodisperse inks there will be inhomogeneous packing and porosity present in the printed traces. Such data could inform on how to deposit well-aligned and pinhole-free films, with the potential to tune the film morphology as a function of nanosheet size. Further, changing the constituent nanosheet size will affect both the quantity and nature of the junctions in the network. For liquid phase exfoliated 2D inks, which are easily prepared and readily size-selected, this offers a simple means to tune the network properties over an order of magnitude of nanosheet lateral dimensions. More generally, due to the importance of network morphology and the plethora of parameters that are known to contribute including; deposition method,[251] ink formulation,[236] processing and post-processing conditions,[332] it is essential that a means to quantitatively characterise these 2D architectures is developed.

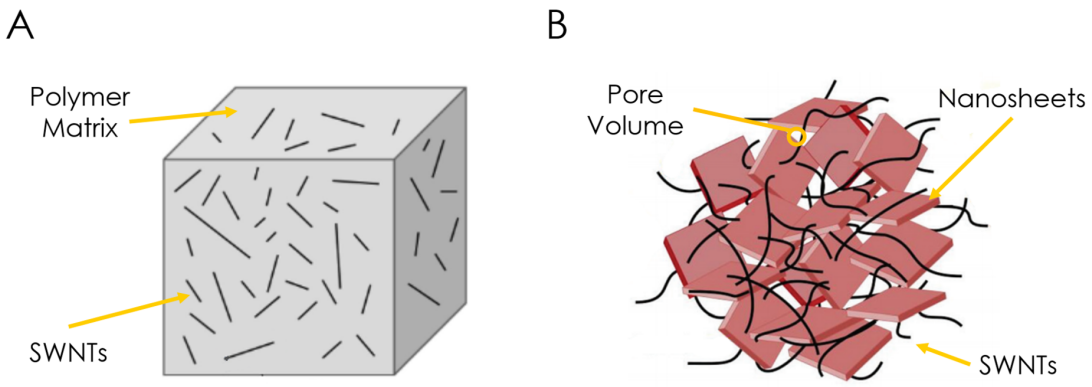

Figure 5.2: Nanocomposites: Representative schematics of a **A)** Traditional polymer-matrix nanocomposite reinforced with SWNTs and **B)** 1D:2D SWNT-Nanosheet nano:nano composite, showing the discontinuous and porous nature. [Adapted from Ref. [333]]

Though nanocomposites have been intensively studied for decades, their nascent roots can be traced back to the Lycurgus cup in the fourth century AD.[334] Comprised of a matrix phase combined with a nanoscale filler, nanocomposites have infiltrated most facets of modern materials research. By incorporating trace amounts of nanostructured additives, the physical properties of a host matrix can be tailored for a desired application. Among the most well-studied nanoscale filler materials are graphene nanosheets[335] and carbon nanotubes,[336] which have been used to significantly improve the electrical, mechanical, and thermal properties of the original matrices.[337–339] The traditional nanocomposite family includes an array of different matrix materials including polymer, ceramic and metal-matrix composites.[340] A property common to each of these systems is that the additives are embedded in a continuous-phase matrix, as shown in Fig. 5.2A. This paradigm has recently been disrupted by the emergence of a new class of composite, known as the nano:nano composite.

5.2.1 1D:2D Nano:nano Composites

Nano:nano composites are mixtures of two different nanomaterials, such as carbon nanotubes and nanosheets, and they present fundamentally different properties to their traditional nanocomposite counterparts. A model 1D:2D nano:nano composite comprised of SWNTs and nanosheets is shown in Fig. 5.2B. As both constituents are nanostructured and neither are continuous, the definition of matrix and filler is no longer determined by structural conditions. Thus, these composites are remarkably porous, which lends them to electrochemical applications where electrolyte can be introduced into the considerable pore volume.[341] Indeed, in recent years a menagerie of different nano:nano composite subclasses have been reported including 0D:1D,[342] 0D:2D,[343] 1D:2D,[344] 2D:2D[345] and even 0D:1D:2D systems,[346] primarily for use in applications such as battery or supercapacitor electrodes[347,348] or electrocatalytic systems.[349]

Solution-processed nanosheets represent an ideal candidate for such applications due to the ease of processing and high material throughput. Owing to their remarkable lithium storage potential, 2D materials are primed to play a role as next-generation anode materials in lithium ion batteries, with SnP_3 nanosheets demonstrating theoretical capacities of 1670 mAh g^{-1} (*c.f* graphite 372 mAh g^{-1}).[350] The porosity that these networks exhibit is advantageous for applications where increased accessible surface area is needed for electrolyte insertion or catalysis. However, battery performance in these networks is often electrically limited by their constituent nanosheets[351] and mechanically limited by their weak vdW bonds.[352] Taking MoS_2 networks as a model system, one of the most common approaches has been the addition of conductive graphene nanosheets to form 2D:2D composites. Such systems have demonstrated improved battery performance by augmenting the network conductivity while preserving the high lithium storage capacity of MoS_2.[353]

However, it has been proposed that the introduction of metallic SWNTs to form a 1D:2D nanocomposite will offer significant advantages. It is thought that SWNTs will form conductive pathways at much lower additive levels than nanosheets, owing to their 1D geometry and flexibility. Furthermore, by entangling in three dimensions and preventing atomically-clean nanosheet tiling, 1D fillers will increase the network porosity when compared to their 2D:2D counterparts. By increasing the network conductivity, the limitations on charge transfer between lithium storage sites and the external circuit are relaxed and markedly improved battery performance is observed.[105] Thus, the dominant role played by filler nanomaterials to this point has been to facilitate charge distribution by augmenting the matrix conductivity. However, it is becoming apparent that mechanical reinforcement of the network is equally as important.[347]

Mechanical Reinforcement of Nano:nano Composites

The need for mechanical reinforcement in nano:nano composites is best demonstrated in the case of electrode materials. An upper limit is imposed on the thickness of solution-processed particulate electrodes by a phenomenon known as the critical crack thickness (CCT).[354] When a thin film of wet colloidal particles is dried on a rigid substrate, evaporation of the solvent concentrates the particles into a close-packed array. Further evaporation causes liquid menisci along the top layer of the network to exert compressive capillary forces on the network. As the film is adhered to the substrate, it resists deformation in the transverse direction, leading to transverse tensile stresses. In the case of the rigid nanoparticles in these networks, the film eventually cracks in order to relieve these stresses.[355] The mechanical instabilities above this well-defined thickness are clearly an issue to be addressed for battery and catalytic electrodes, as the thicker the particulate film, the more storage / active sites that are accessible.[356] Similarly, nano-particulate electrode films suffer from mechanical degradation caused by

repeated cycling. This manifests as electrode fragmentation in battery and supercapacitor electrodes due to repeated charge / discharge cycles, while gas evolution in catalytic electrodes displays similar mechanical degradation.[357] Traditionally the deterioration of these films has been addressed using polymer binders.[358] However, it has recently been shown that drastically improved mechanical performance can be achieved at significantly lower additive levels by employing nano:nano composites with mechanically robust fillers, such as carbon nanotubes.[359]

5.2.2 Nanotube Networks

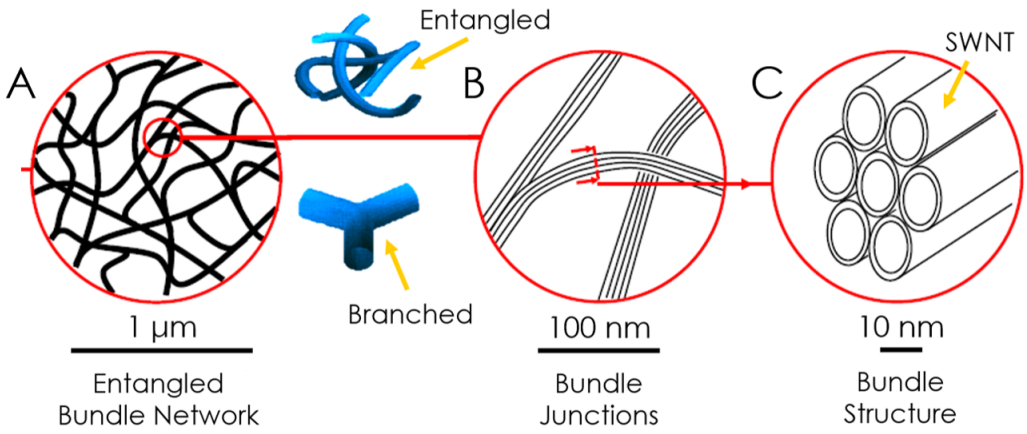

Figure 5.3: Nanotube Networks: Hierarchical microstructure of the reinforcing nanotube network showing the nature of the network, the constituent bundles, and their junctions at different length scales. [Adapted from Ref.[360]]

Though improved mechanical performance has been demonstrated through the use of robust 1D fillers such as SWNTs, the underlying mechanisms are not fully understood. However, some parallels can be drawn between the reinforcing mechanism in 1D:2D composites and nanotube-only networks to gain some insight. A network of carbon nanotubes, often referred to as a "buckypaper" in homage to Richard Buckminster Fuller,[361] comprises a network of entangled, branched and randomly aligned nanotube ropes, as shown in Fig. 5.3A. Both the composition and assembly of the network are known

to influence the resultant properties.[362] As individual SWNTS are very difficult to isolate, a typical buckypaper is made up of entangled bundles of SWNTs, as shown in Fig. 5.3C.

These bundles comprise close-packed SWNTs bound together by vdW forces. Through a similar mechanism these bundles can then combine to form entangled nanotube ropes many orders of magnitude longer than the constituent nanotubes, as shown in Fig. 5.3A-B.[363] Owing to the superlative mechanical properties of their SWNT building blocks, these ropes and their entangled networks boast remarkable mechanical properties, provided the network is dense enough.[364] This is the key for mechanical reinforcement of 1D:2D nanocomposites. It is known that electrical conductivity in such systems follows percolation theory, whereby a crucial volume fraction of nanotube additives must be present before a complete current carrying path spans the sample.[340] It is thus plausible that at some increased nanotube additive level a mechanically robust nanotube network will span the composite and dominate its mechanical response. Thus, insight into the evolution of the composite mechanical properties as a function of nanotube additive level will be pivotal to their development as genuine contenders for energy storage and catalytic applications. Work to address this forms the basis of the coming chapter.

Of course it's exhausting, having to reason all the time in a universe which wasn't meant to be reasonable.

Kurt Vonnegut

6

The Mechanical & Morphological Properties of 1D:2D Nano:nano Composites

The concept of employing high aspect ratio additives as a reinforcing component can be traced as far back as 4000 BC.[365] Though some 6000 years have passed and the place of mud and straw has been taken by low-dimensional nanostructures, this strategy remains valid today. Mixtures of 1D carbon nanotubes and 2D nanosheets, known as 1D:2D nano:nano composites, represent an exciting class of materials for electrochemical applications.[270] Comprised solely of nanotube fillers in a nanosheet matrix, 1D:2D composites constitute a paradigm shift from traditional nanocomposite materials as they contain significant pore volume. As described in Section 5.2.1, the nanosheets provide active material

for energy storage or catalysis, while carbon nanotubes provide conductive pathways and mechanical reinforcement. Though the electrical attributes of such composites have been studied,[341] the crucial role their mechanical properties play has only recently become apparent.[347] Here, the addition of 1D fillers was found to drive improved cycling stability in nanosheet-based battery, supercapacitor and catalytic electrodes.[366] However, only a limited number of papers have reported performing mechanical measurements on 1D:2D nano:nano composites,[294,345] while none have engaged in mechanistic analysis. This chapter aims to address this gap by performing detailed mechanical measurements and analysis on a model 1D:2D nano:nano composite comprising carbon nanotubes in a matrix of MoS_2 nanosheets. MoS_2 was chosen as the matrix material due to its significant potential for electrochemical applications,[367] while single-walled carbon nanotubes (SWNTs) were selected due to their superlative physical properties.[368] Crucially, it was also envisioned that nanotube entanglement would lead to the formation of fibrous networks and substantial mechanical reinforcement within the composite.[369]

6.1 Materials & Methods

The bulk powders used in this work were commercially sourced. MoS_2 powder was purchased from Sigma Aldrich (<2 μm, 98%) and P3-SWNTs (1 – 3 atomic % carboxylic acid groups) were acquired from Carbon Solutions Inc. HPLC N-Methyl-2-pyrrolidinone (NMP) and dimethylformamide (DMF) were purchased from Sigma Aldrich. Polyester track-etched membranes (PETE, pore size 0.1 μm, 47 mm diameter) and Whatman Anodisc alumina membranes (pore size 0.02 μm, 47 mm diameter) were purchased from Sterlitech and GE Healthcare respectively.

Nanomaterial dispersions were prepared using liquid phase exfoliation, as outlined in Section 3.1. MoS_2 bulk powder was dispersed in 80 ml of NMP at a concentration of 100 $g.l^{-1}$. This initial dispersion was then tip sonicated for 1 h using a Sonics Vibra-cell VCX-750 ultrasonic processor at 60

% amplitude. The process temperature was maintained at 7 °C using a chiller and the tip action was pulsed at a 6 - 2 on / off ratio to prevent solvent evaporation and overheating of the horn probe. The resultant dispersion was then centrifuged for 1 h at 4900 rpm and decanted. This step serves to remove any potential contaminants from the starting powder.[221] The retained sediment was redispersed in 80 ml of fresh NMP and sonicated for 8 h at 60 % amplitude, with a 4 - 4 tip pulsing action. The produced dispersion was then centrifuged for 1 h at 1000 rpm to remove unexfoliated material, which could be subjected to further exfoliation steps to produce additional material. The supernatant was centrifuged for a further 2 h at 4900 rpm to trap all but the smallest nanosheets in the sediment. The NMP supernatant was then decanted and the MoS_2 sediment in each vial was redispersed in 10 ml of DMF using an ultrasonic bath (Thermo Fisher Scientific, FB11201, 37 kHz). The concentration of the MoS_2 dispersion was found by filtration onto an alumina membrane and weighing.

P3-SWNT powder was dispersed in DMF at a concentration of 1 $g.l^{-1}$ using tip sonication. A 20 ml dispersion was sonicated for 2 h using a tapered-probe sonic tip at 25 % amplitude and pulsed at a 6 - 2 on / off ratio. As both the MoS_2 nanosheets and P3-SWNTs were dispersed in the same solvent, composite dispersions of any desired SWNT:nanosheet ratio could be formed by mixing predetermined amounts of each dispersion. In this manner, a series of SWNT:MoS_2 composite dispersions were formed with SWNT content ranging from 0 - 6 wt %. Each composite dispersion was vacuum filtered onto a PETE membrane and dried overnight at room temperature. Free-standing SWNT:MoS_2 composite films were then peeled off and cut into strips 2.5 mm wide. Film thicknesses in the range of 20 - 50 μm were measured using a digital micrometer with a torque-limiting ratchet stop.

High-resolution images of the prepared films were obtained using a Zeiss Ultra Plus SEM (2 - 3 kV accelerating voltage, 30 μm aperture). The mean MoS_2 nanosheet length was found using bright field TEM as described in Section 4.2.2 using a JEOL 2100 TEM operated at 200 kV. Statistical analysis of

the TEM-measured flake dimensions was performed by measuring the longest axis of each nanosheet and assigning it as its length. Raman spectroscopy was performed on the composite films using a Horiba LabRAM spectrometer with a 632.8 nm wavelength under ambient conditions (0.2 mW, 1.5 μm spot size). A 600 grooves per mm grating was using to achieve a spectral resolution of $\sim 1.2\ cm^{-1}$. Mechanical measurements were performed using a Zwick-Roell tensile tester (Xforce P, 100 N load cell) at a strain rate of $0.5\ mm.min^{-1}$ and 5 mm gauge length. Four-terminal electrical measurements were performed by patterning equally spaced electrodes onto composite strips using conductive silver paint. The I-V curve for each sample was then measured using a Keithley 2400 source meter. Each electrical and mechanical data point is the average of 4 measurements.

6.2 Composite Characterisation

An initial survey was performed to characterise both the SWNTs and MoS_2 nanosheets used in this work. A representative TEM image of the MoS_2 nanosheets is shown in Fig. 6.1A, demonstrating the nanosheets be well-exfoliated two-dimensional objects. The measured mean lateral dimension of the exfoliated nanosheets was found to be 340 nm using statistical TEM, with the distribution of measured lengths given in the inset of Fig. 6.1A. Following exfoliation, the nanosheets were transferred to dimethylformamide (DMF) to facilitate the blending of composite dispersions and further solution processing. SEM analysis of vacuum filtered MoS_2 networks revealed disordered arrays of nanosheets that are partially aligned in the plane of the film, as shown in Fig. 6.1B-C. Consistent with previous reports, these networks appear to contain significant porosity. [162]

A vacuum filtered network of the commercially sourced P3-SWNTs is shown in Fig. 6.1D. Such networks are often referred to as "buckypapers" and the heavily entangled and bifurcated character shown here is well-reported. [370] This image is emblematic of the type of reinforcing network pro-

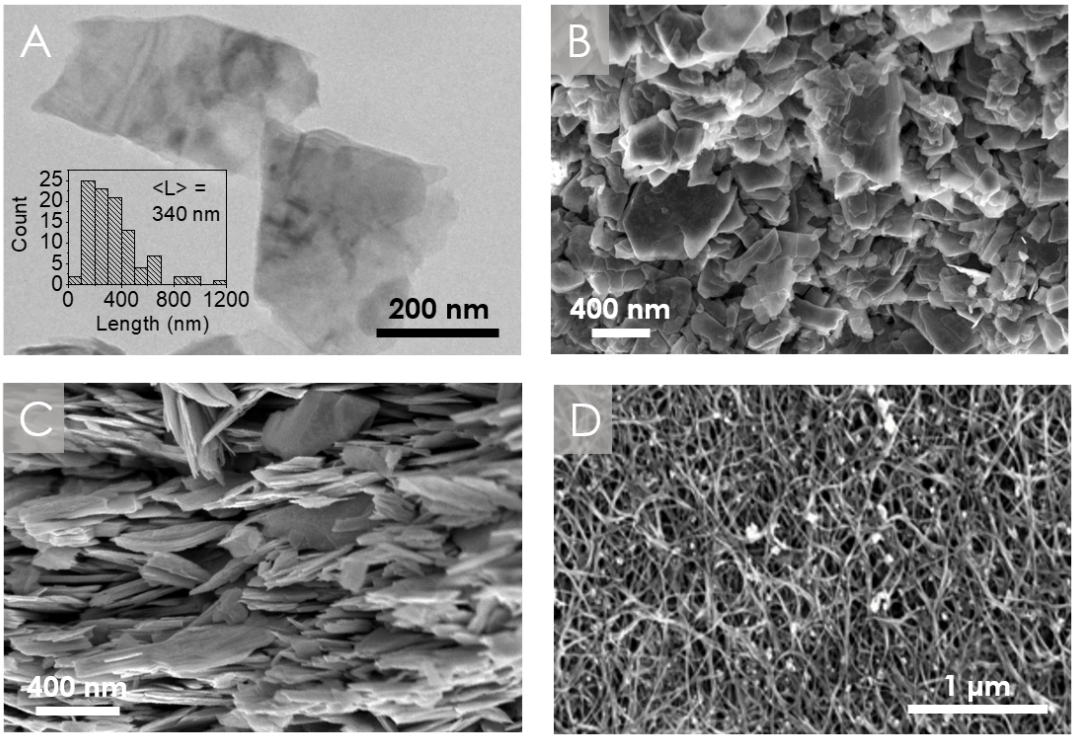

Figure 6.1: Materials Characterisation: A) Representative TEM image of liquid phase exfoliated MoS_2 nanosheets. Inset: Lateral size distribution. **B-C)** Planar and cross-sectional SEM images of vacuum filtered MoS_2 nanosheet networks. **D)** SEM image of a vacuum filtered network of SWNTs.

posed to form in 1D:2D nano:nano composites at large SWNT additive levels, only with larger pores wherein the MoS_2 nanosheets will reside. Dispersions of nanosheets and nanotubes, both suspended in DMF, were mixed to give composite dispersions for a range of nanotube mass fractions, M_f, from 0 to 6 wt %. The composite mass fraction is given by Eqn. 6.1

$$M_f = \frac{M_{NT}}{M_{NT} + M_{NS}} \tag{6.1}$$

where M_{NT} and M_{NS} are the mass contributions of the nanotubes and nanosheets respectively. These composite dispersions were then vacuum filtered to create free-standing films of thickness 20 - 50 µm,

as shown in Fig. 6.2A. Each film was then cut into strips 2.5 mm wide for electromechanical characterisation, as shown for both a SWNT:MoS_2 composite and SWNT buckypaper in Fig. 6.2B. Raman spectroscopic analysis on a 6 wt % SWNT:MoS_2 composite, shown in Fig. 6.2C, demonstrates the expected modes associated with both MoS_2 and SWNTs. Furthermore, the composite uniformity and composition can be quantitatively assessed by comparing the relative intensities of the characteristic SWNT and MoS_2 Raman peaks across each sample. Assuming that the Raman signal intensity, or peak height, for a sample mode is proportional to the mass of that sample under the beam, the ratio of MoS_2 and SWNT intensity peaks can be related to the SWNT mass fraction through Eqn. 6.2

$$\frac{I_{MoS_2}}{I_{SWNT}} \propto \frac{1}{M_f} - 1 \tag{6.2}$$

where I_{MoS_2} and I_{SWNT} are the peak heights for a given mode of MoS_2 and SWNTs in the composite sample.[371] For uniformly mixed SWNT:MoS_2 composites it is expected that the peak intensity ratio will scale linearly with $(M_f^{-1} - 1)$.[371] This relationship can be seen to hold in Fig. 6.2D, where the ratio of the MoS_2 (A_{1g}) and SWNT (2D) peak intensities scale linearly with $(M_f^{-1} - 1)$ using values from 20 randomly selected regions across each sample. This demonstrates that the produced composites were well-mixed with tightly-defined additive loading levels.

The 1D:2D composites in this work differ from more commonly studied systems as they contain significant porosity. For this reason, the filler volume fraction, φ, is a more meaningful parameter for analysis. The most simple definition for the SWNT volume fraction is $\varphi = V_{NT}/V_{Film}$, where V_{NT} and V_{Film} are the total nanotube and film volumes respectively. As the film volume has contributions from nanosheets, nanotubes and pores, we can define the film volume as $V_{Film} = V_{NS} + V_{NT} + V_P$. Here, V_{NS} and V_P denote the total nanosheet and pore volumes. Within this definition the matrix

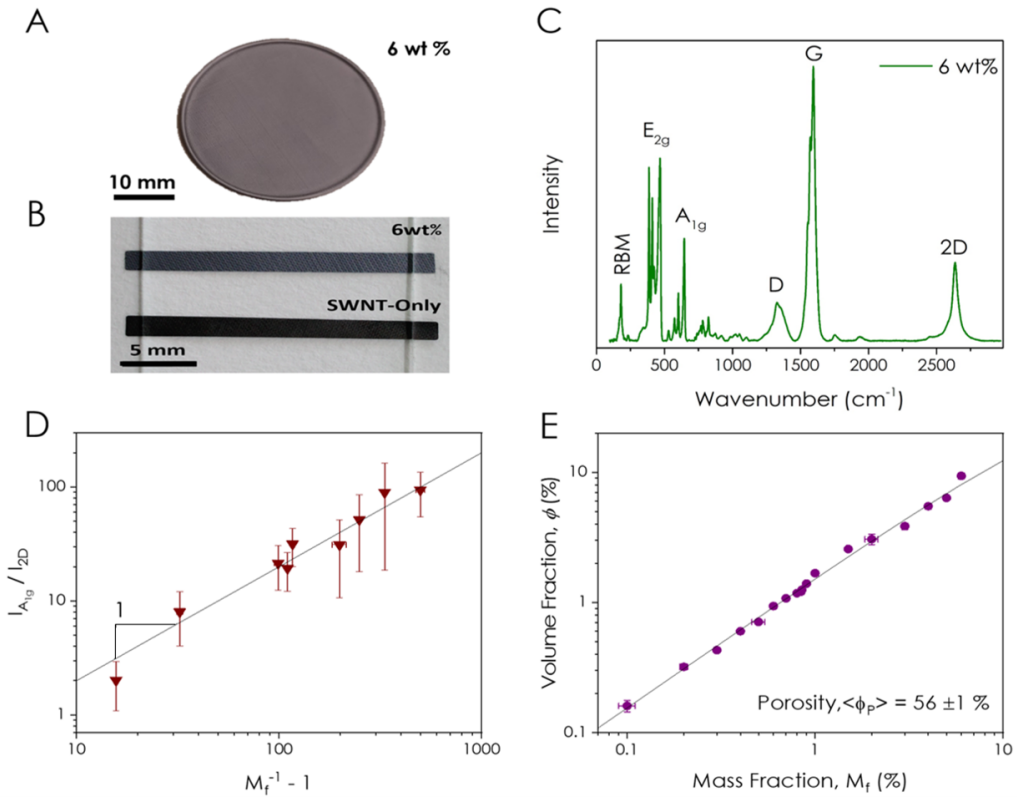

Figure 6.2: MoS_2:SWNT Composite Characterisation: Photographs of a **A)** Vacuum filtered SWNT:MoS_2 composite film (6 wt %, 20 µm thick) as well as **B)** SWNT:MoS_2 and SWNT-only strips used for measurements. **C)** Raman spectrum of a 6 wt % composite showing modes associated with both MoS_2 (E_{2g} and A_{1g}) and SWNTs (RBM, D, G and 2D). An excitation wavelength of 632.8 nm and spot size of 1.5 µm were used. **D)** Intensity ratio of A_{1g} and 2D modes showing linearity when plotted versus $(M_f^{-1} - 1)$. **E)** SWNT volume fraction plotted versus SWNT mass fraction. The line is a fit to Eqn. 6.4, which yields a mean film porosity of 56 $\pm$ 1 %.

consists of nanosheets and pores. Under these conditions the SWNT volume fraction can be related to the mass fraction through Eqn. 6.3, where ρ_{NT} and ρ_{Film} are the nanotube and film densities

$$\varphi = \frac{V_{NT}}{V_{Film}} = \frac{M_{NT}}{M_{Film}} \frac{\rho_{Film}}{\rho_{NT}} = M_f \frac{\rho_{Film}}{\rho_{NT}} \tag{6.3}$$

By measuring the density of all composite films, a mean value of 2080 $\pm$ 30 kg m^{-3} was found. When combined with the known value of $\rho_{NT} = 1400\,\mathrm{kg\,m^{-3}}$, the SWNT volume fraction can be calculated for each sample, which is plotted against the mass fraction in Fig. 6.2E. By consideration

of the constituent masses and volumes, as well as the film porosity, $\varphi_P = V_P/V_{Film}$, a relationship between φ and M_f in terms of experimentally measurable quantities and φ_P can be determined. This is derived in Appendix A.1 and given by Eqn. 6.4

$$\varphi = \frac{(1-\varphi_P)}{1+\left(\left(M_f^{-1}-1\right)\left(\frac{\rho_{NT}}{\rho_{NS}}\right)\right)} \tag{6.4}$$

By taking $\rho_{NS} = 5060\,\mathrm{kg\,m^{-3}}$,[372] and fitting Eqn. 6.4 to the data in Fig. 6.2E a mean film porosity of $\varphi_P = 56 \pm 1\,\%$ is found. This value is similar to those found for both solution-processed nanosheet-only[191] and nanotube-only[373] networks. Crucially, the porous nature of these composites primes them for electrochemical applications, where electrolyte can be introduced into the pore volume.

6.3 Electrical Characterisation

To fully exploit the exceptional charge storage capacity of nanosheet networks for energy storage applications, it is essential that conductive pathways for charge transport are present. To quantify this for 1D:2D nano:nano composites, the electrical conductivity of the composite films was measured as a function of SWNT loading. The effect of nanotube additive level, given in terms of its volume fraction, φ, is immediately apparent in Fig. 6.3A. An increase from $\sim 10^{-5}\,\mathrm{S\,m^{-1}}$ for the MoS_2-only network to $\sim 8000\,\mathrm{S\,m^{-1}}$ for the $\varphi = 9.4$ vol % sample is shown.

The dramatic scaling in conductivity with φ shown in Fig. 6.3A is usually described using percolation theory. This is a mathematical framework where the network conductivity increases only above the percolation threshold, $\varphi_{c,e}$. This corresponds to the critical volume fraction where the first complete nanotube path spanning the sample appears. Below $\varphi_{c,e}$ there are not enough nanotubes to form a continuous pathway through the composite and the MoS_2 conductivity will dominate. How-

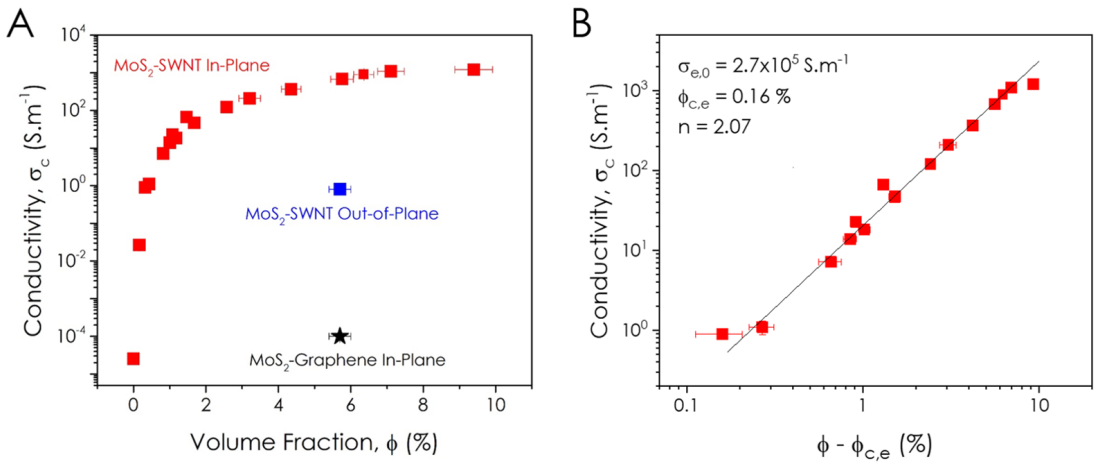

Figure 6.3: Composite Electrical Conductivity: A) MoS_2:SWNT and MoS_2:graphene composite conductivity as a function of additive volume fraction, φ. **B)** Percolation plot of the in-plane MoS_2:SWNT electrical data with a fit to Eqn. 6.5.

ever, above this critical threshold a contiguous nanotube network spans the sample and the composite conductivity, σ, will scale with nanotube volume fraction, φ, as

$$\sigma = \sigma_{e,0}(\varphi - \varphi_{c,e})^n \tag{6.5}$$

where $\sigma_{e,0}$ is related to the conductivity of a nanotube-only network and n is the electrical percolation exponent. As shown in Fig. 6.3B, this equation fits the data well. The value for the conductivity of an MoS_2-only network is in agreement with previous studies, as is the fitted value of $\sigma_{e,0} \sim 10^5$ S m^{-1} for a SWNT network.[371] The value of $\varphi_{c,e}$ = 0.16 % for the percolation threshold is consistent with theory, which predicts $\varphi_{c,e}$ to be approximately given by the ratio of mean nanotube length to diameter.[374] Such a low value for $\varphi_{c,e}$ also suggests that very little active material needs to be sacrificed to form a conductive pathway spanning the composite. Notably, the percolation exponent, n = 2.07 $\pm$ 0.01, is remarkably close to its universal value of 2.0.[375] In composites with a continuous phase matrix, such as a polymer, this exponent is often $\gg$ 2.[374] This deviation is attributed to a broad range

of junction resistances arising from the presence of polymer chains in the vicinity of the nanotube-nanotube junctions.[376,377] Here, the discontinuous nature of the MoS_2 nanosheet matrix facilitates intimate contact of nanotubes at junction sites. This narrows the distribution of junction resistances and the percolation exponent tends towards 2.0.

To investigate the alignment and orientation of the SWNT network within the composite, the out-of-plane conductivity of a $\varphi \gg \varphi_{c,e}$ composite was measured. As shown in Fig. 6.3A, the out-of-plane conductivity of the 5.8 vol % SWNT:MoS_2 composite was found to be $\sim 1\,S\,m^{-1}$. This is over three orders of magnitude less than its corresponding in-plane conductivity, showing these composites to be highly anisotropic with the nanotubes predominantly aligned in the plane of the nanosheets. In addition, the in-plane conductivity of a 5 wt % graphene:MoS_2 composite was measured to be $\sim 10^{-4}\,S\,m^{-1}$. As shown in Fig. 6.3A, graphene additives provide drastically inferior improvements in conductivity at comparable loading levels to nanotubes. This is consistent with graphene-filled 2D:2D composites exhibiting increased percolation thresholds, on the order of 20 wt %,[371] when compared with nanotube-filled 1D:2D composites. By offering enhanced composite conductivities at greatly reduced additive levels, this primes 1D:2D nano:nano composites for use in applications such as catalysis and energy storage.

6.4 Network Formation and Composite Morphology

Due to the importance of mechanical robustness from an applications standpoint, the unexplored mechanical properties of 1D:2D nano:nano composites pose a significant gap in the literature. The MoS_2-only film was found to be so delicate that it was not possible to extract reliable mechanical data from it. In fact, it was non-trivial to produce free-standing films of appreciable thickness without the film fracturing upon drying, as shown in Fig. 6.4A.

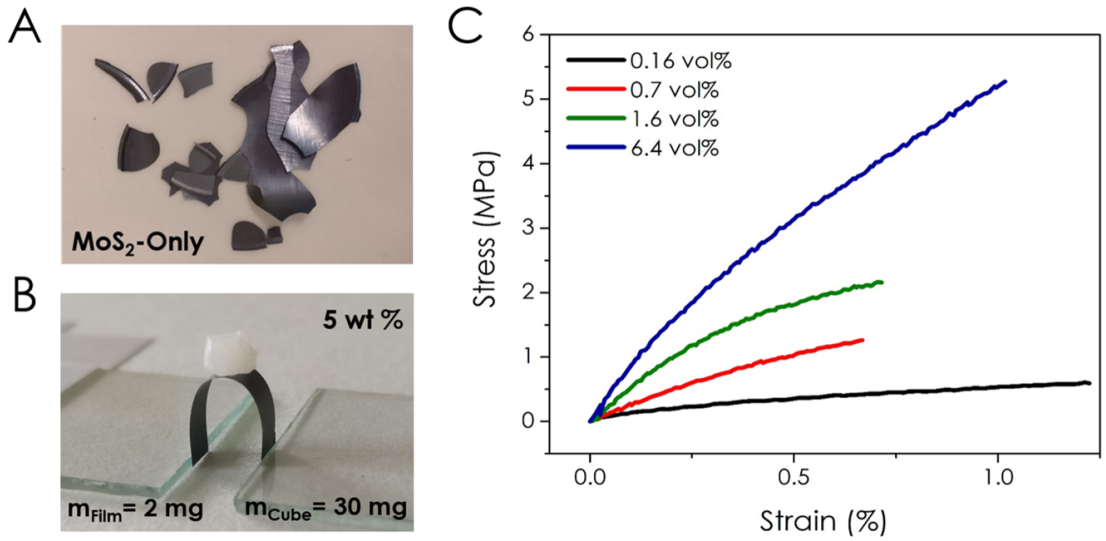

Figure 6.4: Mechanical Reinforcement with φ: Photographs of a **A)** MoS_2-only film and **B)** 5 wt % SWNT:MoS_2 composite. **C)** Representative stress-strain curves for a subset of 1D:2D nano:nano composites at four different SWNT loading levels.

However, upon addition of just 5 wt % (6.3 vol %) SWNTs, the composite became mechanically robust to the point that it could be handled and bear a load. This is shown in Fig. 6.4B, where the film is shown supporting a 30 mg polyurethane cube. Such a transformation would suggest that the SWNT additives are augmenting the composite mechanical properties. To address this, tensile tests were performed on a number of composite strips for each volume fraction. A subset of representative stress-strain curves for four different composite volume fractions are shown in Fig. 6.4B. The composite stress-strain curves are slightly sublinear, displaying a clear increase in stress at all strains as the nanotube content was increased. By analysing the measured stress-strain curves it is possible to extract the composite elastic modulus, E_c, tensile strength, σ_c, breaking strain, ε_c and tensile toughness, T_c, for each composite volume fraction, φ. This data will be discussed in detail in Section 6.5.

To investigate the mechanism driving this change in the mechanical properties with φ, extensive SEM characterisation was performed on composite planar surfaces (i.e. top and bottom surfaces of

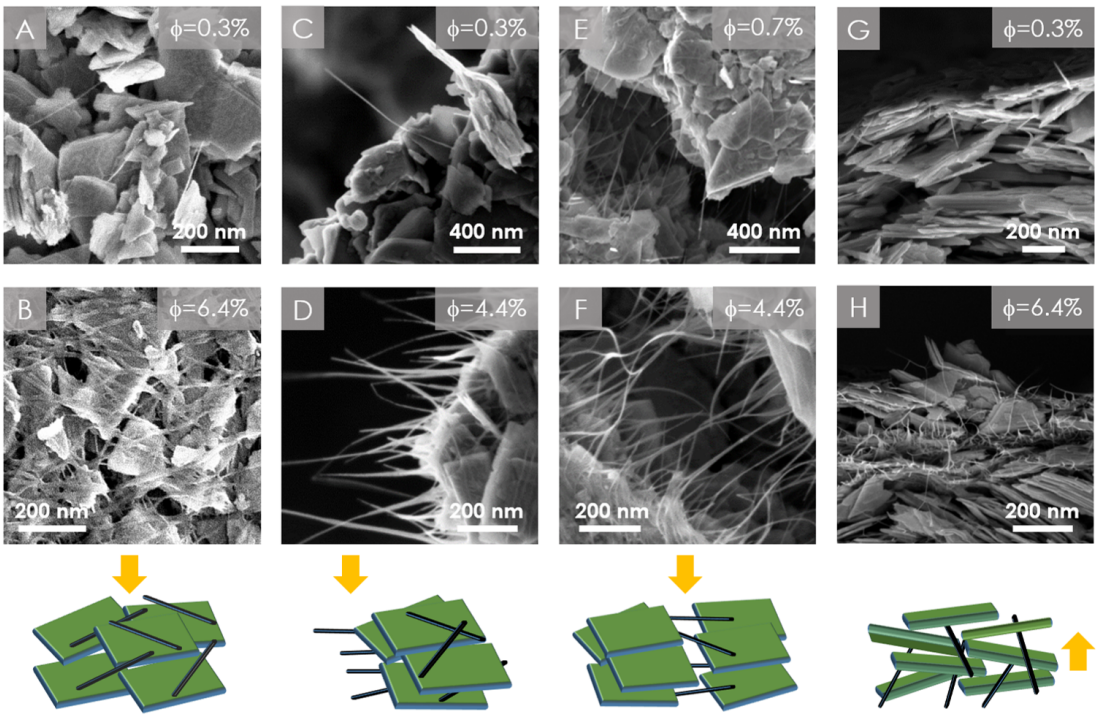

Figure 6.5: Nano:nano Composite Evolution with φ: SEM images of different composite regions at low (top row) and high (bottom row) SWNT loading levels. A schematic depicting the region of the composite film being imaged is shown below each pair of images and marked with an arrow. **A-B)** Composite planar (i.e. top and bottom) surfaces. **C-D)** Fracture surfaces, taken perpendicular to the direction of applied stress to highlight the thickening and bundling of nanotube fibres. **E-F)** Surface cracks in the composite films bridged by nanotubes. **G-H)** Cross-sectional images of fracture surfaces to reveal the internal network morphology.

the films) and fracture surfaces for a range of loading levels. Representative images comparing low-φ (Fig. 6.5 A,C,E,G) and high-φ (Fig. 6.5 B, D, F, H) composites are shown in Fig. 6.5. These images are arranged into those collected from planar surfaces (A-B), fracture surfaces (C-D), surface cracks (E-F) and cross-sections (G-H). A representative schematic is shown below each set of images, with an arrow highlighting the region being imaged. In all cases these images follow a similar narrative.

At the lowest loading levels (Fig. 6.5 A,C,E,G), the images exhibit relatively small numbers of isolated 1D objects. Individual nanotubes are rarely found in liquid exfoliated samples without elaborate centrifugation cascades so these objects likely represent individual bundles of nanotubes.[378] However,

for the higher loading level samples (Fig. 6.5 B, D, F, H), all bundles now appear to exist within a dense network that spans the sample. This high-φ network appears to be comprised of more thick one-dimensional ropes than those observed for $\varphi < 1$ vol %. While it is impossible to determine the true length of such one-dimensional objects directly from SEM images, it would also appear that the bundles in the $\varphi > 1$ vol % composites are significantly longer than their low-φ counterparts.

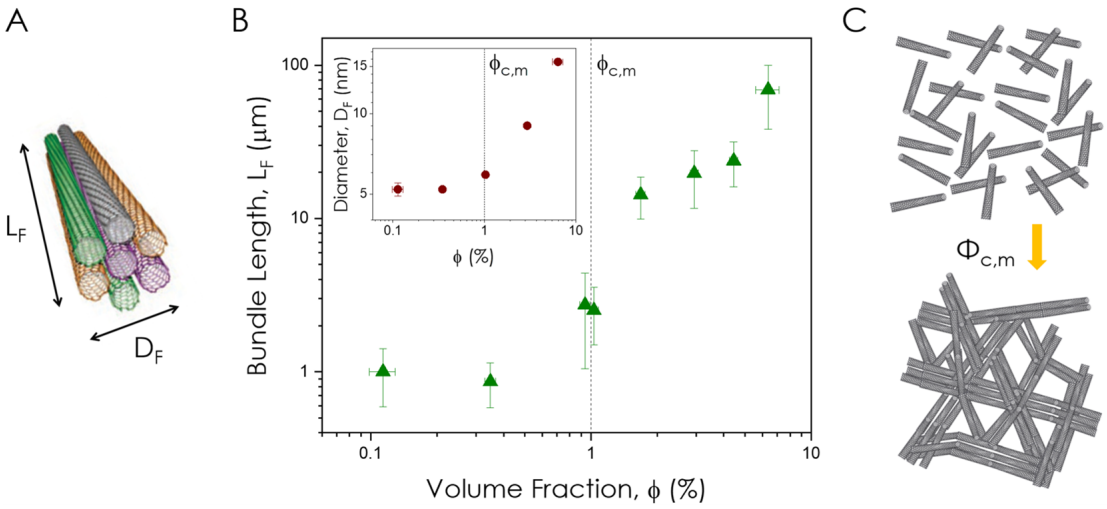

Figure 6.6: Nanotube Network Evolution: A) Schematic of a nanotube bundle showing both its length, L_F, and diameter, D_F. **B)** Mean nanotube bundle length as a function of volume fraction, φ. Inset: Bundle diameter as a function of φ. The mechanical percolation threshold, $\varphi_{c,m}$, is denoted by the dashed line. **C)** Schematic of the proposed nanotube network morphology above and below $\varphi_{c,m}$.

To quantify this transition from isolated individual bundles to a collective network of entangled fibres, it was necessary to measure how the dimensions of the imaged 1D fibres scaled with φ. A SWNT fibre and its relevant dimensions are shown schematically in Fig. 6.6A. The mean fibre diameter, D_F, was directly measured from SEM images for a number of φ-values above and below $\varphi = 1$ vol %. This is plotted as a function of φ in the inset of Fig. 6.6B and is initially seen to be invariant with φ, displaying a value of $D_F \sim 5$ nm. However, a smooth increase in the bundle diameter with φ is observed above 1 vol %, with D_F reaching 15 nm in the 6.4 vol % composite. This implies that aggregation of individual

nanotube bundles into thicker fibres becomes important above 1 vol % SWNTs. Direct measurements of the fibre lengths were non-trivial as very few fibres were found with both ends visible in a given SEM image. However, it is possible to indirectly measure the length of the 1D fibres by noting that the number of fibre ends per unit area on the composite surface, (N_{ends}/A), can be given by

$$\frac{N_{ends}}{A} = 2\left(\frac{N_F}{A}\right)$$

where (N_F/A) is the areal density of fibres. Moreover, we can express the total fibre length per unit area, $(L_{F,T}/A)$, in terms of this areal density of fibres as

$$\frac{L_{F,T}}{A} = L_F\left(\frac{N_F}{A}\right)$$

where L_F is the mean length of the one dimensional fibres in the image. By combining the above definitions we arrive at Eqn. 6.6

$$L_F = 2\left(\frac{L_{F,T}}{A}\right)\left(\frac{N_{ends}}{A}\right)^{-1} \tag{6.6}$$

Crucially, this expresses the mean fibre length, L_F, in terms of readily measurable quantities. This process is described in detail in Appendix A.2. The evolution of L_F with increasing nanotube volume fraction, φ, is shown in Fig. 6.6B. At low values of φ, the mean fibre length is seen to be $\sim$ 1 μm. This value is typical of small bundles of nanotubes and matches the manufacturer-quoted bundle length. Interestingly, for $\varphi > 1$ vol % the mean fibre length increases sharply with φ, reaching values on the order of $\sim$ 70 μm for nanotube loadings of 6.4 vol %. This dramatic increase in L_F, coupled with the comparatively modest increase in D_F, has implications for the fibre aspect ratio, (L_F/D_F). Indeed,

this parameter is seen to increase from $\sim$ 200 for composites where $\varphi < 1$ vol %, to $\sim$ 4700 for the $\varphi = 6.4$ vol % sample.

Such an evolution of the reinforcing fibre network would be expected have a considerable effect on the mechanical properties of the composites. Based on the qualitative SEM evidence and measured increase in the fibre length with φ, the following narrative is proposed. At nanotube volume fractions below the electrical percolation threshold, $\varphi_{c,e} = 0.16$ vol %, the nanotube bundles are either isolated or exist in small network fragments. In line with percolation theory, it is only when the nanotube volume fraction reaches $\varphi_{c,e}$ that a connected, current-carrying nanotube network first spans the sample. However, though conducting nanotube networks exist just above $\varphi_{c,e}$, they are not thought to be mechanically robust as the average number of inter-bundle junctions is too low. While a minimum of two connections per bundle are required to transfer charge, it has been proposed that a minimum of 4 junctions per bundle are necessary for mechanical stability of the network as a whole.[379] Thus, there are a range of volume fractions just above $\varphi_{c,e}$ where the nanotube network is effectively embedded in the nanosheet matrix. Here, the nascent SWNT network would rely on the nanosheet matrix for stability, behaving analogously to polymer- or ceramic-matrix composites.

The nature of the nanosheet matrix in 1D:2D nanocomposites is expected to play a novel part here. Its ability to constrain reorganization of the nanotube additives during film formation is limited by its mechanically weak and discontinuous character. Thus, when compared to composites having a continuous matrix phase, new behaviours are expected to emerge as the nanotube volume fraction is increased in these systems. It is proposed that a critical value of φ exists where the nanotube network transforms from a poorly connected and sparse state, to a heavily interconnected, entangled and mechanically robust framework. This critical volume fraction is denoted as the mechanical percolation threshold, $\varphi_{c,m}$, and the transition can be seen at $\varphi = 1$ vol % in the fibre length and diameter data Fig.

6.6B. This complete network will consist of extremely long fibres comprised of entwined bundles. A schematic depicting the nature of the network above and below $\varphi_{c,m}$ is shown in Fig. 6.6C.

It is proposed that for $\varphi > \varphi_{c,m}$, the mechanical properties of the system are dominated by the nanotube network, with minimal contribution from the nanosheet matrix. The reinforcing networks would resemble a nanotube buckypaper, only with larger inter-nanotube pores wherein the nanosheets and pore volume reside. The data shown in Fig. 6.6B implies that this transition occurs at $\sim$ 1 vol %, which will be seen to correlate with the mechanical data in the coming section. Interestingly, the electrical conductivity data in Fig. 6.3 is completely unperturbed by this morphological transition at $\varphi_{c,m}$. This suggests that, although the transition from sparsely connected bundles to an entangled network has significant mechanical implications, the current-carrying capability of the network is unaffected.

It is difficult to directly characterise this morphological transition using SEM, as the network structure is obscured by the presence of MoS_2 nanosheets (95 - 99.5 wt %). However, the morphological evolution of dip-coated nanotube networks has been reported by *Song et al.*[380] Here, a flexible polyethylene terephthalate (PET) substrate was repeatedly dipped into a SWNT dispersion and the evolution of the deposited SWNT network was observed as a function of the number of dips. After 100 dips, the nanotube networks are sparse and comprised of axially-crossed bundles whose individual character is clearly visible. However, after 400 dips the network morphology has dramatically changed. A continuous and entwined network of thick ropes where individual bundles and their ends are no longer visible now exists. These ropes display crossing, threading and Y-shaped bifurcations that act like inter-rope junctions, but would be expected to be more robust. It is proposed that a similar evolution in the SWNT network occurs in 1D:2D nano:nano composites as a function of φ.

6.5 Mechanical Measurements and Models

Tensile stress-strain curves were measured for each 1D:2D nano:nano composite sample. From these curves the composite elastic modulus, strength, stress-at-break and tensile toughness can be determined as a function of SWNT volume fraction, φ. While each of these properties will be discussed, a central theme across the mechanical data is the presence of φ-dependent discontinuities. These will be shown to coincide remarkably well with the SWNT network evolution about $\varphi = 1$ vol % observed in Section 6.4. With this transition from weak and sparse to robust and entangled networks in mind, simple, yet quantitative, models can be developed to describe the mechanical properties of 1D:2D nano:nano composites.

6.5.1 Young's Modulus, E_c

The composite elastic modulus, E_c, is plotted as a function of φ in Fig. 6.7. This parameter is given by the ratio of the tensile stress to tensile strain in the elastic (or linear) region of its stress-strain curve. A near-linear increase in the composite modulus can be seen up to $\varphi \sim 1$ vol %, while the reduction in E_c at $\varphi \sim 1$ vol % is indicative of a change in the aggregation state of the filler.[381] As φ is increased, the modulus then trends upwards to reach a value of ~ 1 GPa for the highest volume fraction composite at 9.4 vol %. Interestingly, the elastic modulus data exhibits a well-defined discontinuity in the region of $\varphi_{c,m}$. This suggests that the mechanisms responsible for E_c follow different regimes above and below this critical nanotube volume fraction.

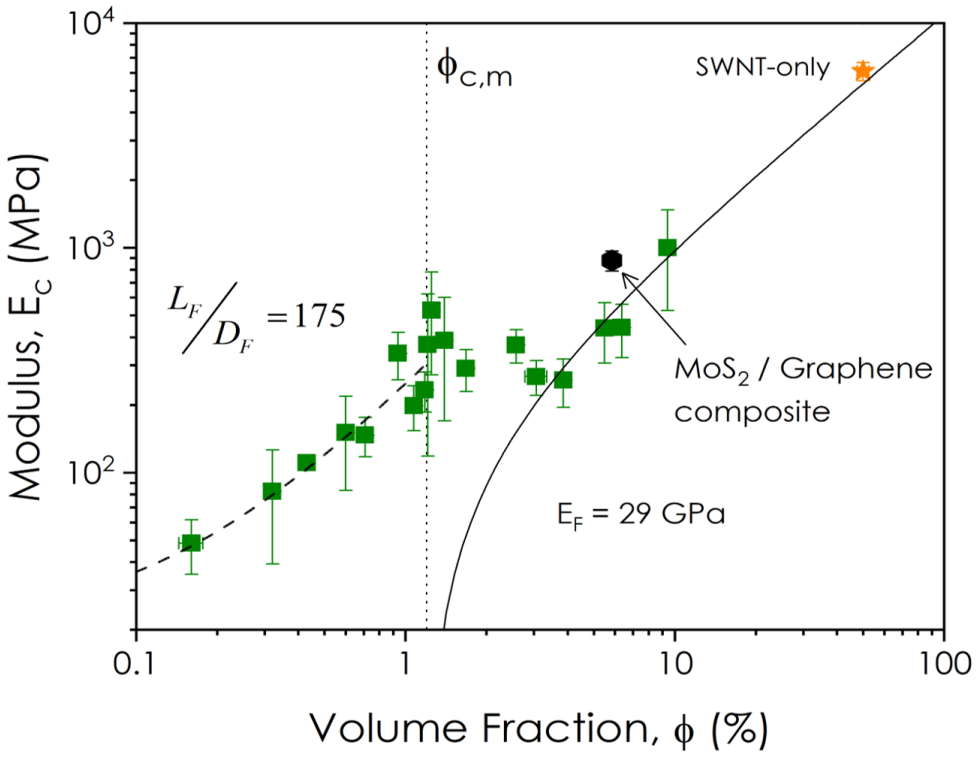

Figure 6.7: Composite Elastic Modulus: Plot of the 1D:2D nano:nano composite elastic modulus as a function of φ. The black octagon represents a graphene:MoS_2 composite, while a SWNT buckypaper is denoted by an orange star. The dashed black line is a fit of Eqn. 6.9 to the modulus data for $\varphi < \varphi_{c,m}$, which yields a mean nanotube bundle aspect ratio of 175 $\pm$ 30. The solid black line is a fit of Eqn. 6.10 to the modulus data above $\varphi_{c,m}$ and provides a value of $E_F = 29 \pm 4$ GPa for the nanotube fibre modulus.

Low-φ Elastic Modulus: $\varphi < \varphi_{c,m}$

At low SWNT loading, the composite can considered as a sparse network of either isolated or weakly-connected nanotube bundles suspended in a MoS_2 nanosheet matrix. Assuming that some stress can be transferred at the nanosheet-nanotube interface, the modulus of such a composite can be modelled using a version of the rule of mixtures adapted to incorporate shear-lag theory, as given by Eqn. 6.7 [340]

$$E_c = \eta_0 \eta_L E_F \varphi + E_M (1 - \varphi) \tag{6.7}$$

where η_0 is the filler efficiency factor, η_L is the filler length efficiency factor, E_F is the filler modulus and E_M is the matrix modulus. The filler orientation factor describes the orientation and alignment of the reinforcing fibres throughout the composite.[382] The filler efficiency factor is described by Eqn. 6.8 and accounts for the finite length of the reinforcing fibres and the efficiency of stress transfer from the matrix to the fibres[340]

$$\eta_L = 1 - \frac{tanh\left(nL_F/D_F\right)}{nL_F/D_F} \qquad where: \qquad n = \left[\frac{2E_M}{E_F\left(1+\nu_M\right)ln\left(1/\varphi\right)}\right]^{1/2} \tag{6.8}$$

where n is a dimensionless constant that is related to the stress distribution along the fibre and ν_M is the Poisson ratio of the matrix. By assuming that the modulus of the nanotube fibres far exceed that of the MoS_2 nanosheet matrix, such that $E_F >> E_M$, the hyperbolic tangent in Eqn. 6.8 can be Taylor expanded.[383] Through this expansion and substitution of the expressions in Eqn. 6.8 back into Eqn. 6.7, an expression for the Young's modulus of a fibre-reinforced 1D:2D composite in the low-φ regime can be derived

$$E_c = E_M\left(1 - \varphi + \frac{2L_F^2}{3D_F^2}\frac{\eta_0}{\left(1+\nu_M\right)}\frac{\varphi}{ln\left(1/\varphi\right)}\right) \tag{6.9}$$

Eqn. 6.9 is expected to apply to composites with low modulus matrixes, as is the case for 1D:2D nano:nano composites. It is noteworthy that the composite modulus, E_c, is independent of the fibre modulus, E_F, in this regime. This is in agreement with models developed by Young *et al.* to describe the reinforcement of polymeric matrixes with stiff graphene nanoplatelets,[383] as well as the Guth-Gold relationship that is often used to model the effect of stiff fillers on the modulus of elastomers.[384,385] This can be seen to fit the data well in Fig. 6.7 for $\varphi < 1$ vol %. Taking $\nu_M = 0.5$ and $\eta_0 = 3/8$ (appropriate when the fillers are aligned in-plane),[386] the fit to the data yields a bundle aspect ratio of

$L_F/D_F = 175 \pm 30$. This value is in strong agreement with both the SEM-measured values in Fig. 6.6A, and the average bundle aspect ratio given by the manufacturer of ~ 200. Furthermore, this fit gives a matrix modulus of 16 ± 2 MPa, which is reasonably in line with a previously reported value of 26 ± 7 MPa for the stiffness of a MoS_2 nanosheet network.[347]

High-φ Elastic Modulus: $\varphi > \varphi_{c,m}$

For composites in the $\varphi > 1$ vol % regime, the reinforcing nanotubes are expected to have formed an entangled network. Analogous to a scaffold, this network is envisioned to bear load independent of the nanosheet matrix. Clearly, the model developed for the low-φ modulus regime is not appropriate to such a system. However, the original version of shear-lag theory was designed to describe similar networks.[387] Paper is the archetypal example of a bonded-fibre network and has been extensively modelled in the literature using shear-lag theory.[388] Furthermore, the stiffness of entangled polymer networks is known to scale with network density, analogous to increasing φ in these composites.[389,390] Provided that a fibre network is adequately dense, its elastic modulus can be modeled by Eqn. 6.10. This model is fully developed in Appendix A.3.

$$E_c = \eta_0 E_F \left(\varphi - \varphi_{c,m}\right) \tag{6.10}$$

where $\varphi_{c,m}$ is the mechanical percolation threshold. This model is fitted to the modulus data for $\varphi > 2$ vol % in Fig. 6.7. By taking $\varphi_{c,m} = 1.2$ vol % and $\eta_0 = 3/8$, the modulus of the reinforcing fibres was found to be $E_F = 29 \pm 4$ GPa. This value may initially appear low when compared to the reported modulus of an individual SWNT, on the order of 1 TPa.[391] However, the SWNT-networks in this work are comprised of nanotube ropes or fibres, where the individual SWNTs are now weakly bound

to each other through van der Waals forces.[392] It has been shown that the Young's modulus of a given nanotube fibre strongly decreases with its diameter, with values in the literature ranging from 20 - 100 GPa for SWNT ropes having a diameter of $\sim$ 15 nm.[393,394] Though the fitted value of $\sim$ 29 GPa lies within this range, it is worth noting that this model is thought to potentially underestimate the true fibre modulus.[395] The SWNT-only data point sits close to the fitted line in Fig. 6.7, as would be expected for a model describing fibre-networks. The measured modulus of 6.1 $\pm$ 0.7 GPa for this free-standing P3-SWNT buckypaper is in strong agreement with similarly prepared buckypapers by *Wang et al.*[396] Interestingly, the graphene:MoS_2 2D:2D composite modulus was similar to the SWNT:MoS_2 value at a similar additive level.

6.5.2 Tensile Strength, σ_c

The tensile strength is a key performance indicator for composite materials that will experience tensile loads or stretching. The 1D:2D nano:nano composite ultimate tensile strength (UTS) is plotted as a function of φ in Fig. 6.8. The composites with the lowest additive levels display modest tensile strengths, on the order of $\sim$ 0.5 MPa. However, the composite tensile strength improved with each increase in φ, reaching a value of $\sim$ 5.5 MPa for the 9.4 vol % sample. The measured tensile strength of $\sim$ 35 MPa for the SWNT-only film is well in-line with published SWNT buckypapers.[397] However, the fact that this value doesn't lie on the composite trend is quite interesting. When compared to a buckypaper, the presence of the nanosheet matrix likely increases the mean inter-nanotube distance and reduces both the selection of available nanotube-nanotube interactions and the total inter-fibre bonded area. Finally, it is interesting that the tensile strength of the 2D:2D graphene:MoS_2 composite is notably inferior to its 1D:2D equivalent in Fig. 6.8. This is attributed to geometric effects, whereby SWNT entanglement in the 1D:2D composite dominates its mechanical response.

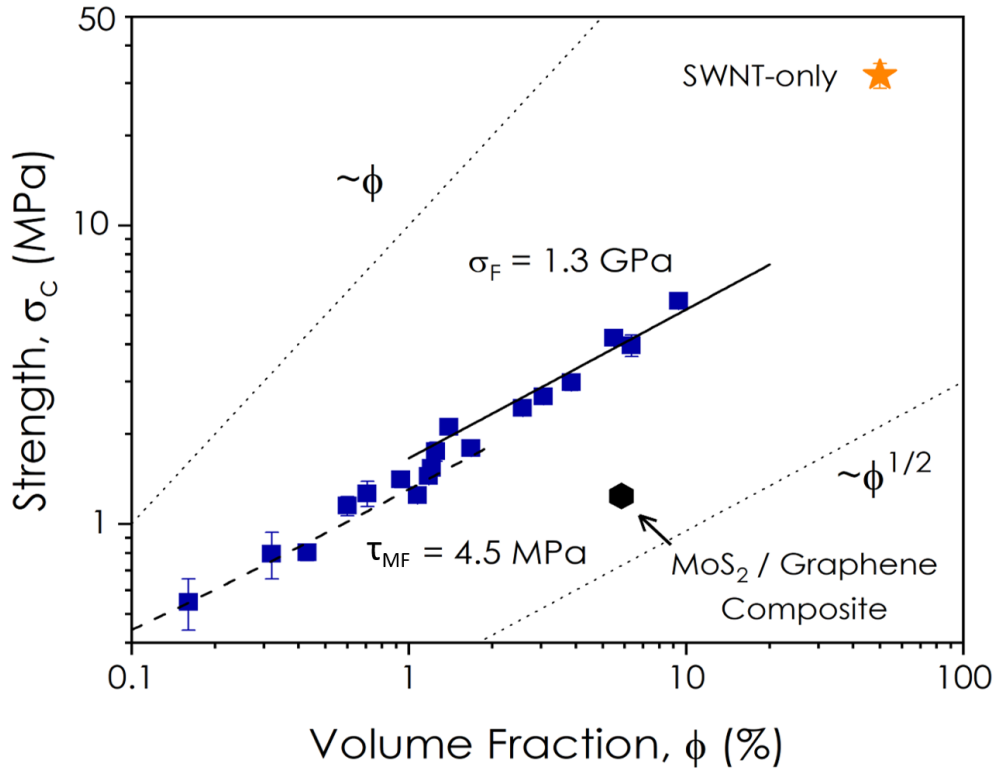

Figure 6.8: Composite Tensile Strength: Plot of the 1D:2D nano:nano composite tensile strength as a function of φ. The black octagon represents a graphene:MoS_2 composite, while a SWNT buckypaper is denoted by an orange star. The dashed black line is a fit of Eqn. 6.15 to the strength data for $\varphi < \varphi_{c,m}$, which yields a matrix:fibre interfacial shear strength of $\tau_{MF} = 4.5 \pm 0.2$ MPa. The solid black line is a fit of Eqn. 6.16 to the strength data above $\varphi_{c,m}$ and provides a value of $\sigma_F = 1.3 \pm 0.1$ GPa for the strength of the reinforcing nanotube fibres.

While the composite strength data in Fig. 6.8 demonstrates a slight kink at $\varphi \sim 1$ vol %, what is equally unusual is the well-defined sublinear dependence on φ. In continuous-matrix nanocomposites one would expect to see the tensile strength increase linearly with φ for well-dispersed fillers, or decrease with additive content if they are poorly dispersed.[398] Alternatively, the strength of fibrous networks is usually described using models developed by Page.[399] However, the Page equation implies a near-linear $\sigma_c - \varphi$ dependence and so is inconsistent with the strength data presented in Fig. 6.8.

Following a comprehensive survey of the literature, a family of models that predict a sub-linear

$\sigma_c - \varphi$ for fibre-reinforced composites were found.[400,401] Within this framework composite failure can occur via three distinct processes, with each process being dominant for a given angular range, θ, between the reinforcing fibre and the applied load. These are: (i) fibre failure for low-θ, (ii) interfacial shear failure for intermediate-θ and (iii) transverse matrix failure in a plane parallel to the fibre axis at high-θ. To obtain an expression that provided a good fit to the data in Fig. 6.8, the approach of *Lees et al.*[402] was modified to initially consider only two failure mechanisms. The fibre failure, σ_{FB}, and transverse matrix failure, σ_{MF}, components were considered, while the shear failure component was introduced in an alternative manner. The two strength expressions considered are associated with failure stresses of

$$\sigma_{FB} = \frac{\sigma_{\parallel}}{cos^2\theta} \qquad\qquad \sigma_{TF} = \frac{\sigma_{\perp}}{sin^2\theta}$$

where $\sigma_{\parallel}$ is the strength of a fibre-reinforced composite containing only fibres aligned parallel to the direction of the applied stress and $\sigma_{\perp}$ is the strength of that composite in the transverse direction. The composite strength, σ_c, can then be found by averaging these contributions over the appropriate θ-range to arrive at Eqn. 6.11

$$\sigma_c = \frac{4\sqrt{\sigma_{\parallel}\sigma_{\perp}}}{\pi} \tag{6.11}$$

This expression can be made experimentally testable by approximating that the composite strength in the transverse, or high-θ, direction is equal to the matrix strength, $\sigma_{\perp} \sim \sigma_M$. Furthermore, for an aligned-fibre composite the in-plane, or low-θ, tensile strength is described by Eqn. 6.12[386]

$$\sigma_{\parallel} = \eta_{L,S}\sigma_F\varphi + (1-\varphi)\sigma_M \tag{6.12}$$

Here, σ_F is the nanotube bundle strength and $\eta_{L,S}$ is the strength efficiency factor. The efficiency factor takes one of two values, depending on whether the fibre length is above or below a critical value, L_c. The critical length is given by $L_c = \sigma_F D_F / 2\tau_{MF}$,[403] where D_F is the fibre diameter and τ_{MF} is the shear strength of the matrix-fibre interface. Fibre lengths where $L_F < L_c$ will not carry the maximum load and will result in a reduced value of $\eta_{L,S}$. Thus, we arrive at two separate expressions for $\eta_{L,S}$, depending on the length of the fibres in the nano:nano composite.[404] It is expected that both of the $\eta_{L,S}$ regimes will be relevant for 1D:2D nano:nano composites due to the φ-dependent evolution of the nanotube network and they are described by Eqns. 6.13 - 6.14

$$\eta_{L,S}\left(L_F < L_c\right) = \frac{L_F}{2L_c} \qquad (6.13) \qquad\qquad \eta_{L,S}\left(L_F \geqslant L_c\right) = 1 - \frac{L_c}{2L_F} \qquad (6.14)$$

Low-φ Tensile Strength: $\varphi < \varphi_{c,m}$

According to Fig. 6.6B, when the composite volume fraction is below 1 vol % the fibres comprising the network are nanotube bundles of length $\sim$ 1 μm. This length is equivalent to the length of the individual SWNTs, meaning that the constituent nanotubes span the entire bundle. These bundles would be exceptionally strong, likely having strengths comparable to individual SWNTs. The critical length for such fibres would then be enormous and the fibre length would be expected to fall far below this value, such that $L_F \ll L_c$ for $\varphi < 1$ vol %. By combining the appropriate form for the length efficiency factor, given by Eqn. 6.13, with Eqns. 6.11 & 6.12, we arrive at an expression that describes the tensile strength of 1D:2D nano:nano composites in the low-φ regime

$$\sigma_c\left(L_F < L_c\right) = \frac{4}{\pi}\left[\sigma_M \tau_{MF} \varphi \left(\frac{L_F}{D_F}\right) + \sigma_M^2 \left(1 - \varphi\right)\right]^{1/2} \qquad (6.15)$$

This model is fitted to the composite tensile strength data in Fig. 6.8 for $\varphi < 1.2$ vol % and finds

reasonable agreement. It is notable that Eqn. 6.15 now incorporates the initially omitted interfacial failure strength component through τ_{MF}, the shear strength of the matrix-fibre interface. By fixing the filler aspect ratio to the value of $L_F / D_F = 175$ found in Fig. 6.6B, a value for the interfacial shear strength of $\tau_{MF} = 4.1 \pm 0.2$ MPa can be extracted from the fit. While this is in the reported range for matrix-filler shear strengths,[405] it is considerably lower than values of 20 - 60 MPa normally found in polymer-nanotube composites. This is not wholly unexpected for a discontinuous nanosheet matrix. The reduced intimacy between bundle and nanosheet surfaces would be anticipated to result in a weaker matrix-fibre shear strength.[406] Indeed, the τ_{MF} presented here is more comparable to the value of ~ 2 MPa reported for the interfacial shear strength of a MWCNT sliding on a graphite surface.[407] The extracted value of $\sigma_M = 0.14 \pm 0.05$ MPa is also reasonably consistent with previous work that measured the tensile strength of a MoS_2 network to be 0.24 ± 0.06 MPa.[347]

High-φ Tensile Strength: $\varphi > \varphi_{c,m}$

Based on the evidence in Fig. 6.6B, the reinforcing network is now expected to comprise long ropes of entwined bundles. These ropes will have much lower tensile strengths than individual nanotubes,[408] and the fibre length is proposed to greatly exceed its critical value for $\varphi > 1$ vol %. In this scenario, $\eta_{L,S} \sim 1$, which leads to an expression for the tensile strength of a 1D:2D nano:nano composite in the high-φ regime

$$\sigma_c \left(L_F > L_c\right) \approx \frac{4}{\pi} \left[\sigma_M \sigma_F \varphi + {\sigma_M}^2 \left(1 - \varphi\right)\right]^{1/2} \tag{6.16}$$

Eqn. 6.16 was fitted to the composite strength data in Fig. 6.8 for $\varphi > 1.2$ vol %. This yields a matrix strength value of $\sigma_M = 0.13 \pm 0.05$ MPa, consistent with the value of 0.14 ± 0.05 MPa found

by fitting Eqn 6.15 to the low-φ data. Furthermore, a value of $\sigma_F = 1.2 \pm 0.1$ GPa was determined for the fibre tensile strength. This value is in line with literature reports that show SWNT bundles to have tensile strengths of a few GPa.[409] Combining the fitted values for the fibre strength and matrix-fibre shear strength shows that the nanotube ropes found in the composite for $\varphi > 1$ vol % have critical aspect ratios of ~ 200. With reference to the data in Fig. 6.6B, this implies that composite failure will begin to occur via fibre failure once the volume fraction exceeds 1 vol % and ropes where $L_F/D_F > 200$ are formed. Furthermore, the credibility of the fitted σ_F value can be tested by using it to calculate the nanotube-nanotube interfacial shear strength, τ_{NT}. This was performed following a method developed by Vilatela *et al.*[410] Due to the strength of its constituent nanotubes, a nanotube bundle tends to fail by nanotube pullout or interfacial frictional sliding. Here, under an applied axial load individual nanotubes will be pulled from their sockets inside a bundle until the bundle fails. By considering this failure mechanism for a nanotube bundle, a simple expression can be used to relate its strength, σ_F, to the nanotube-nanotube interfacial shear strength, τ_{NT}. This is given in Eqn. 6.17

$$\sigma_F = \frac{\tau_{NT} L_{NT}}{4 D_{NT}} \tag{6.17}$$

Taking $\sigma_F = 1.2 \pm 0.1$ GPa, $L_{NT} \sim 1$ μm and $D_{NT} \sim 1$ nm yields an interfacial shear strength of $\tau_{NT} \sim 4.8$ MPa. This value agrees well with the results of Vilatela's literature review, finding values centered on ~ 5 MPa for graphitic systems.[410]

6.5.3 Strain-at-Break, ε_c

The data for strain-at-break as a function of φ is given in Fig. 6.9 and offers compelling evidence for a change in the nanotube network architecture at $\varphi \sim 1$ vol %. Initially the composite breaking strain

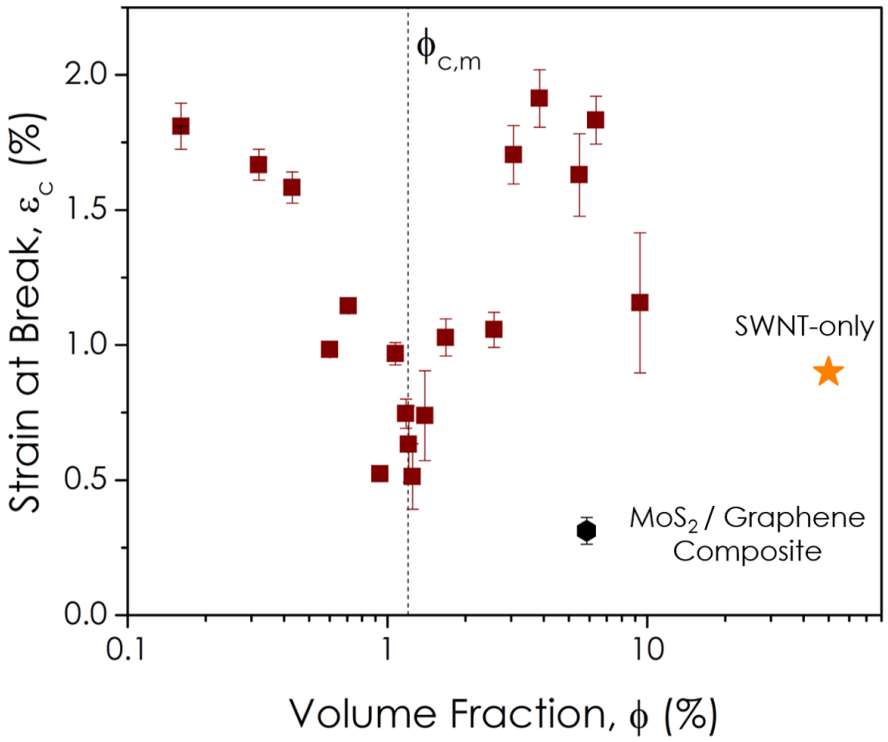

Figure 6.9: Composite Strain-at-Break: Plot of the 1D:2D nano:nano composite breaking strain as a function of φ. The black octagon represents a graphene:MoS_2 composite, while a SWNT buckypaper is denoted by an orange star.

is seen to fall-off with φ, decreasing from $\sim$ 2 % at low-φ to $\sim$ 0.5 % at $\varphi = 1$ vol %. The composite strain-at-break is then observed to rise again above $\varphi = 1$ vol %, reaching $\sim$ 2 % for the samples in the 4 - 8 vol % range. Interestingly, the composite breaking strain may fall-off above this nanotube loading level, with the breaking strain of the SWNT-only film having a value of $\sim$ 1 %, in line with published values. [397]

It is difficult to develop quantitative models for the breaking strain in composites, however, some points can be made based on the data. In the low-φ regime, where the nanotube network is expected to be weak and poorly connected, a clear falloff in ε_c is observed with increasing φ. Such behaviour is typical of polymer-nanotube composites and has been attributed to a number of mechanisms. [101]

As an example, the presence of stiff filler particles can constrain the matrix and significantly reduce its ability to deform.[340] This has been demonstrated especially well in the case of soft matrixes, where the breaking strain of SWNT-elastomer composites has been observed to fall exponentially with increasing nanotube addition.[411,412] It is proposed that a similar mechanism is occurring in 1D:2D nano:nano composites for $\varphi < 1$ vol %. As the fraction of rigid nanotube bundles suspended in the disordered matrix increases, it increasingly constrains its ability to deform.

On the other hand, the increasing breaking strain observed for $\varphi > 1$ vol % is extremely unusual in composite systems. Such behaviour is more commonly observed in networks of one-dimensional fibres, such as the cellulose fibres found in paper.[413] A review of the mechanical properties of cellulose fibre networks reveals that the most dense networks, analogous to the highest filler volume fractions here, exhibit the largest breaking strains.[414] This has been shown to be a general phenomenon and is linked to an increase in the total inter-fibre bonded area with increasing φ.[415] Taken together, this interpretation of the strain-at-break data strongly supports the narrative of a transition between a short-fibre reinforced composite at low-φ, to a robust and entangled fibrous network at high-φ.

6.5.4 Tensile Toughness, T_c

The composite tensile toughness is the volumetric work done in stretching a sample to failure. The majority of this work goes towards increasing the elastic potential energy of the stretched sample, and upon fracture a portion of this energy is used to create a fracture surface. For brittle materials most of this energy is recoverable if the material is unloaded prior to failure. However, for materials like the composites studied here, inelastic deformation can occur through irreversible nanotube reorientation or viscoelastic dissipation.[364] In this regime, the work of fracture per unit area, W/A, can be related to the composite toughness via the sample gauge length, L_0, as $W/A = f(\varphi, L_0)\, T_c L_0$. The sample

gauge length represents the initial sample length between the clamps of the tensile tester, before any stress is applied. The fraction of the elastic energy used to create the fracture surface, $f(\varphi, L_0)$, is expected to depend on both φ and L_0, as well as the structural properties of the composite.

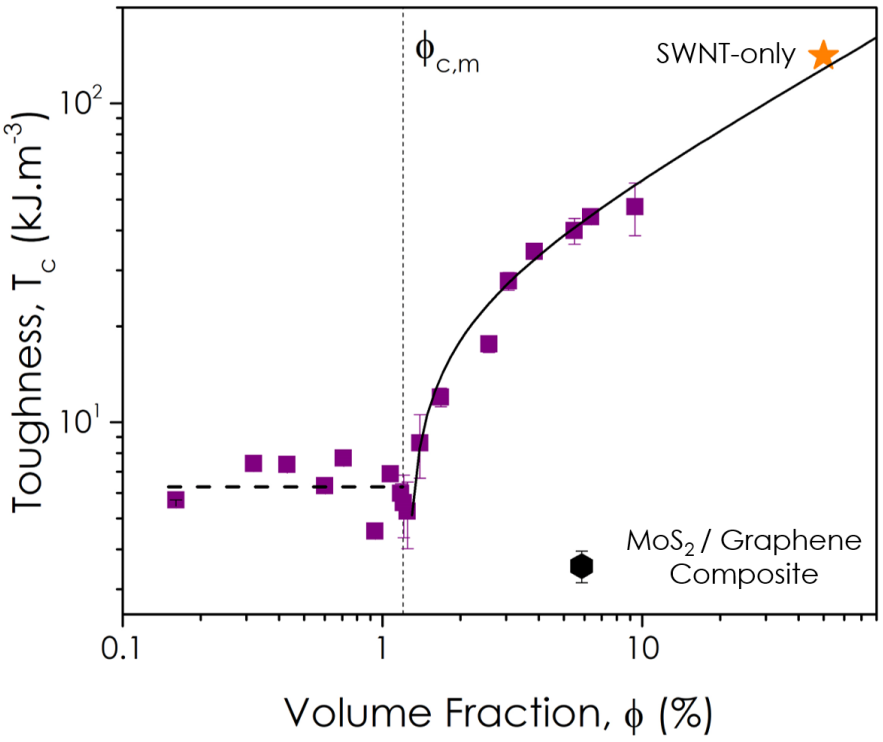

Figure 6.10: Composite Tensile Toughness: Plot of the 1D:2D nano:nano composite toughness as a function of φ. The black octagon represents a graphene:MoS_2 composite, while a SWNT buckypaper is denoted by an orange star. The dashed black line below $\varphi_{c,m}$ is the average tensile toughness for $\varphi < \varphi_{c,m}$. The solid black line is a fit of Eqn. 6.22 to the tensile toughness data for $\varphi > 1$ vol %.

The macroscopic composite toughness is plotted as a function of φ in Fig. 6.10. The low-φ data is roughly invariant with nanotube loading, showing values of ~ 5 kJ m^{-3}. This is interesting as it suggests that any increases in W/A associated with increasing nanotube content for $\varphi < 1$ vol % are balanced by changes in $f(\varphi, L_0)$. However, above 1 vol % the toughness increases rapidly, reaching a value of ~ 45 kJ m^{-3} for the 9.4 vol % sample. It is proposed that W/A increases much faster than $f(\varphi, L_0)$ in the $\varphi > 1$ vol % regime. This is of considerable importance from an applications

standpoint, where improvements in tensile toughness have been linked to enhanced cycling stability in 1D:2D battery electrodes.[347] While the primary failure mechanism in nanosheet-based electrodes is crack formation driven by repeated expansion / contraction from charging / discharging cycles, the tensile toughness is proposed as a reasonable descriptor of the overall durability of these systems.

From the fracture surface images shown in Fig. 6.5D, it is clear that composite failure occurs via failure of nanotube ropes for $\varphi > \varphi_{c,m}$. The most likely mechanism is the pullout of individual nanotubes from their bundles through a mechanism similar to that described in Eqn. 6.17.[416] To describe the composite toughness, T_c, a model that considers the total energy associated with frictional sliding of nanotubes from their sockets in bundles is presented. This follows the method of Wagner *et al.*[417] and is fully developed in Appendix A.4, but the key points will be discussed here. The work of fracture for nanotubes pulling out from a single bundle can be given by Eqn. 6.18

$$W_{Bun} = \frac{\pi D_F^2 L_{NT}^2 \tau_{NT}}{96 D_{NT}} \left[1 - \frac{D_{NT}}{D_F}\left(1 - \frac{\tau_{MF}}{\tau_{NT}}\right)\right] \tag{6.18}$$

where τ_{MF} and τ_{NT} are the shear stresses at the matrix-nanotube and nanotube-nanotube interfaces. The total work of fracture can usually be found by multiplying this quantity by the number of bundles crossing the fracture surface, N/A. However, in the vicinity of $\varphi_{c,m}$ not all of these bundles will be connected to the global nanotube network. These unconnected nanotubes will not fully contribute to the work of fracture. Accounting for this, the work of fracture for the network, $(W/A)_{Net}$, can be expressed as

$$\left(\frac{W}{A}\right)_{Net} = P(\varphi)\left(\frac{N}{A}\right) W_{Bun} \tag{6.19}$$

where $P(\varphi)$ is the fraction of all nanotube bundles connected to the global network. $P(\varphi)$ is known

as the percolation probability and scales from $P(\varphi) = 0$ at low-φ to $P(\varphi) = 1$ at $\varphi = 1$. An expression for the number of bundles crossing the fracture surface is derived in Appendix A.4 as $(N/A) = (4\varphi) / \left(\pi D_F^2\right)$ and when combined with Eqns. 6.18 and 6.19, yields the exact expression given in Eqn. 6.20

$$\left(\frac{W}{A}\right)_{Net} = P(\varphi)\,\varphi\frac{L_{NT}^2\tau_{NT}}{24D_{NT}}\left[1-\frac{D_{NT}}{D_F}\left(1-\frac{\tau_{MF}}{\tau_{NT}}\right)\right] \approx P(\varphi)\,\varphi\frac{L_{NT}^2\tau_{NT}}{24D_{NT}} \tag{6.20}$$

However, from the strength data in Section 6.5.2 it was found that $\tau_{MF} \approx \tau_{NT}$, while the nanotube fibre diameter is expected to exceed the diameter of single nanotubes such that $D_F >> D_{NT}$. This allows $(W/A)_{Net}$ to be approximated in the form shown to the right of Eqn. 6.20. Though there is no analytical expression for $P(\varphi)$ within the percolation theory framework, it can be approximated as $P(\varphi) = ((\varphi - \varphi_{c,m})/(1-\varphi_{c,m}))^k$,[418] where k is taken as the mechanical percolation exponent. This form fulfils the boundary conditions on $P(\varphi)$ mentioned above and allows the composite tensile toughness to be expressed by Eqn. 6.21

$$T_c \approx \frac{\varphi}{f(\varphi, L_0)}\left(\frac{\varphi-\varphi_{c,m}}{1-\varphi_{c,m}}\right)^k \frac{L_{NT}^2\,\tau_{NT}}{24D_{NT}L_0} \tag{6.21}$$

By fitting the toughness data in Fig. 6.10 for $\varphi > 1$ vol %, T_c was found to be directly proportional to $(\varphi - \varphi_{c,m})^k$. This implies that the fraction of elastic potential energy used to create the fracture surface is dependent only on φ, at least over the examined φ-range. This produces $f(\varphi, L_0) = C\varphi$, where C is a dimensionless constant. Substituting into Eqn. 6.21, a final expression for the composite

tensile toughness can be derived

$$T_c \approx \frac{1}{C}\left(\frac{\varphi - \varphi_{c,m}}{1-\varphi_{c,m}}\right)^k \frac{L_{NT}^2\,\tau_{NT}}{24 D_{NT} L_0} \tag{6.22}$$

Eqn. 6.22 is fitted to the 1D:2D composite toughness data in Fig. 6.10 for $\varphi > 1$ vol % and finds strong agreement. Notably, the tensile toughness of the SWNT-only sample is in-line with the $\varphi >$ 1 vol % trend, as would be expected for a model describing fibre-networks. Taking $L_{NT} \sim 1$ µm and $D_{NT} \sim 1$ nm, the fitted line yields values of $k = 0.47$ and $\varphi_{c,m} = 1.2$ vol % respectively. By substituting the τ_{NT} value of ~ 4.8 MPa found in Section 6.5.2, it is possible to estimate $C \sim 0.22$. As an example, this implies that at $\varphi = 10$ vol %, only 2.2 % of the stored elastic energy is used to create a fracture surface. Indeed, repeated zipping and unzipping of van der Waals bonds at nanotube-nanotube interaction sites, as well as reorientation of entangled nanotubes as the sample is strained has been linked to strong energy dissipation in nanotube buckypapers.[419] Both the toughness data and model described above are particularly interesting from an applications standpoint. The data in Fig 6.10 clearly exhibits percolation-like behaviour whereby the composite tensile toughness only increases once the nanotube volume fraction exceeds 1.2 vol %. Thus, meaningful increases in toughness can only be achieved once this percolation threshold is surpassed. Crucially, this value is quite low for 1D:2D nano:nano composites. This means that in applications such as battery electrodes where toughness is known to be a key parameter,[347] very little active material must be sacrificed to dramatically enhance the composite mechanical properties.

6.6 Conclusions

The electrical, mechanical and morphological properties of a SWNT:MoS_2 nano:nano composite have been studied as a function of SWNT volume fraction, φ, in this chapter. These composites were found to comprise interpenetrating disordered networks of nanosheets and nanotubes, with φ-invariant porosities of $\sim$ 56 %. When coupled with the remarkably low percolation threshold for conduction of $\varphi_{c,e} = 0.16$ vol %, this primes these composites for energy storage and catalytic applications. Comprehensive SEM analysis revealed the reinforcing nanotube network to undergo a φ-dependent morphological evolution. For nanotube volume fractions below 1 vol %, the nanotube network was found to comprise small bundles with aspect ratios of $\sim$ 200. However, for $\varphi > 1$ vol % a transformation to a more continuous network dominated by extremely long ropes with aspect ratios of up to 4700 occurs. This transition was found to significantly affect the mechanical response of the composites. The composite modulus and failure-strain exhibited short-fibre composite behavior for $\varphi < 1$ vol %, while both increased in a manner consistent with fibrous networks for $\varphi > 1$ vol %. The composite tensile strength similarly evolved from a regime limited by the matrix-fibre interface at low-φ, to one limited by the strength of the nanotube ropes for $\varphi > 1$ vol %. Significantly, while the composite tensile toughness was constant at low-φ, it was found to increase rapidly for $\varphi > 1$ vol %, consistent with percolation theory. Compared to the nanosheet matrix, addition of 5 wt % (9.4 vol %) nanotubes leads to increases in modulus, strength, and toughness by factors of $\sim$ 55, 70, and 10, respectively. These increases transform the properties of the material, rendering it robust and suitable for a range of applications.

Life is full of doors that don't open when you knock, equally spaced amid those that open when you don't want them to.

Roger Zelazny

7

Electrical Transport in Printed Nanosheet Networks

The explosion in demand for wearable and low-cost consumer electronics has catalysed research into thin-film electronics at a frenetic pace.[420] Fortunately, this has coincided with notable developments in both the solution-phase production of 2D materials and a suite of printing techniques to deposit them.[421] Owing to their unique geometry, processability and diverse electronic properties, networks of 2D nanomaterials are particularly well-placed to play a central role.[298] Indeed, an array of printed nanosheet devices have already been demonstrated including capacitors, thin-film transistors and solar cells.[422,423] However, despite significant advances the field is still in its nascent phase and considerable challenges remain before a printed 2D hegemony can be established. Chief among these is that the re-

markable properties of the constituent nanosheets do not naturally confer to the network, with carrier mobilities in printed networks often lagging their constituent nanosheets by factors of 10^2 - 10^3.[191] This dichotomy has been primarily attributed to presence of interfacial junctions between adjacent nanosheets. Here, charge carriers must tunnel or hop across the vdW gap, stifling their progression through the network.[424] Potential routes towards engineering and optimising these interfaces were discussed in Section 5.1.2, while a means to augment the electrical conductivity of nanosheet networks with SWNT additives was demonstrated in Chapter 6. However, fundamental information on these interfacial junctions in purely 2D networks remains a significant gap in the literature.

The electrical properties of spray-coated LPE nanosheet networks are investigated as a function their constituent nanosheet length in this chapter. The prevailing narrative is that conductive pathways comprised of larger nanosheets will exhibit fewer junctions and increased network conductivities. However, any dependence of conductivity on nanosheet length has only been reported in a limited number of papers and the underlying mechanisms are not quantitatively understood at present.[213,425] This work aims to characterise the electrical conductivity of semiconducting WSe_2, semi-metallic graphene and metallic silver nanoplatelet networks as a function nanosheet length. Networks with diverse electrical properties were chosen with the expectation that intersheet interactions would vary as the electronic structure of their nanosheets was altered. Any length-dependent effects would be of great interest from an applications standpoint, but also to inform future network optimisation. Further, a simple, yet quantitative model is presented to describe the conductivity response of such networks in terms of both intrinsic nanosheet and global network properties.

7.1 Materials & Methods

All bulk powders used were commercially sourced. Graphite powder was purchased from Asbury (Grade 3763) and WSe_2 powder from Alfa Aesar (10 - 20 μm, 99.8 %). Silver nanoplatelets (AgNP) were bought from Tokusen Nano (N300 and M13). HPLC grade isopropanol, sodium cholate hydrate (> 99 %) and a silver nanoparticle dispersion (< 50 nm diameter, 30 - 35 wt % in methyltriglycol) were purchased from Sigma Aldrich. Deionised (DI) water was produced in-house (18.3 MΩ.cm).

2D inks were prepared using liquid phase exfoliation, as outlined in Section 3.1. For each material, the bulk powder was dispersed in 80 ml of deionised water at a concentration of 35 gl^{-1}. This initial dispersion was then tip sonicated for 1 h using a Sonics Vibra-cell VCX-750 ultrasonic processor at 60 % amplitude. The process temperature was maintained at 7 °C using a chiller and the tip action was pulsed at a 6 - 2 on / off ratio to prevent solvent evaporation and overheating of the horn probe. The resultant dispersion was then centrifuged for 1 h at 4900 rpm and decanted to remove any potential contaminants from the starting powder.[221] The retained sediment was redispersed in 80 ml of DI water and sodium cholate at a concentration of 2 gl^{-1}. This dispersion was then sonicated for 8 h at 60 % amplitude, with a 4 - 4 pulsing action. Exfoliation was performed in water-surfactant as it has been reported to produce smaller and thinner nanosheets than solvent exfoliated dispersions.[212]

Each stock dispersion of nanosheets was then size-selected using liquid cascade centrifugation, as outlined in Section 3.3, using a Hettich Mikro 220R centrifuge (fixed angle rotor). The parent polydispersion was first centrifuged at 500 rpm for 2 h to isolate any unexfoliated material in the sediment. Crucially, this can be subjected to a second exfoliation step to produce more nanosheets. The retained supernatant was decanted and subjected to a second centrifugation at 1000 rpm for 2 h. The trapped sediment, comprising the largest nanosheets from the dispersion, was then collected and redispersed

in fresh DI water and sodium cholate (2 gl^{-1}). As these nanosheets were trapped between 0.5 and 1 krpm, the central rpm of this nanosheet fraction was 0.75 krpm. The supernatant was then subjected to iterative centrifuge cascades, removing the sediment at each step, to isolate the other size fractions. Nanosheet fractions were trapped at central rpm values of 0.75, 1.25, 1.75, 2.25, 2.75, 3.5, 4.75 and 7.75 krpm. Each size-selected fraction was then redispersed in a reduced volume of DI water and sodium cholate (2 gl^{-1}). These inks were then transferred to IPA for spraying. To remove the sodium cholate, each dispersion was centrifuged for 2 h at 6 krpm (or 15 krpm for nanosheet fractions trapped above 3 krpm). The supernatant was discarded and the sediment redispersed in fresh IPA. This step was repeated twice. Extinction spectra were recorded post-transfer to determine the ink concentration for each size using previously developed metrics.[125] These measurements were performed using a Varian Cary 50 UV-Vis spectrophotometer in 1 nm increments using a 4 mm quartz cuvette. The mean nanosheet length for each size-selected ink was determined using TEM measurements performed on a JEOL 2100 TEM system operating at 200 kV.

Inks were spray coated onto ultrasonically cleaned glass slides at temperature of 70 °C using a Harder and Steenbeck Infinity Airbrush attached to a Janome JR2300N mobile gantry. A N_2 back pressure of 45 psi, nozzle diameter of 0.4 mm and stand-off distance of 100 mm were used. Each sprayed trace was patterned into 1 × 4.5 mm bars using stainless steel masks and annealed overnight under vacuum at 80 °C to remove residual solvent. Silver nanoparticle top electrodes were patterned onto each printed trace using an aerosol jet printer (Optomec AJP300). The samples were again annealed overnight at 80 °C to sinter the silver nanoparticle electrodes. Electrical characterisation was performed under ambient conditions using a Keithley 2612A source meter connected to a probe station. Two-terminal measurements were used on all samples, except the printed AgNPs, where 4-probe measurements were employed. Trace thicknesses were measured using a Bruker Dektak stylus pro-

filometer (19.6 μN force). To ensure stylus contact was not damaging the printed networks, thickness measurements were repeated over the same trace to ensure successive values were comparable and rule out stylus burrowing. Raman spectroscopy was performed on the deposited traces using a Horiba LabRAM spectrometer with a 532 nm wavelength under ambient conditions. SEM was performed using a Zeiss Ultra Plus SEM at an accelerating voltage of 2 - 3 kV.

7.2 Ink Preparation & Characterisation

Solution processed inks for each of the materials studied in this work are shown in Fig. 7.1A-C. An initial TEM survey was performed on each 2D ink, with representative images shown below their parent ink in Fig. 7.1. The nanosheets, indicated by regions of darker contrast, were found to be well exfoliated two-dimensional objects in all cases. The AgNPs shown in Fig. 7.1C were synthesised, rather than delaminated from a parent crystal. This confers a triangular shape and increased thickness when compared with the more thin and rectangular WSe_2 and graphene nanosheets in Fig. 7.1A-B.[426]

An intrinsic feature of the liquid phase exfoliation (LPE) process is that the produced dispersions are highly polydisperse, with broad distributions in both lateral size, l_{NS}, and thickness, t_{NS}.[330] To characterise the influence of nanosheet dimension on the electrical properties of their printed networks, it is necessary to sort the nanosheet fractions into tightly selected bands in both length and thickness. For each material, the stock dispersion was subjected to liquid centrifugation cascades (LCC) to produce a subset of size-selected inks. As nanosheet length and thickness are intrinsically coupled in LPE through nanosheet mechanics, nanosheets that are smaller in lateral dimension will also be more thin.[223] This is important from a printed electronics standpoint as the electronic bandgap scales with layer number in semiconducting TMDs.[427] Here, any distribution in nanosheet thickness will lead to local spatial variations in bandgap, which can cause charge carrier trapping and

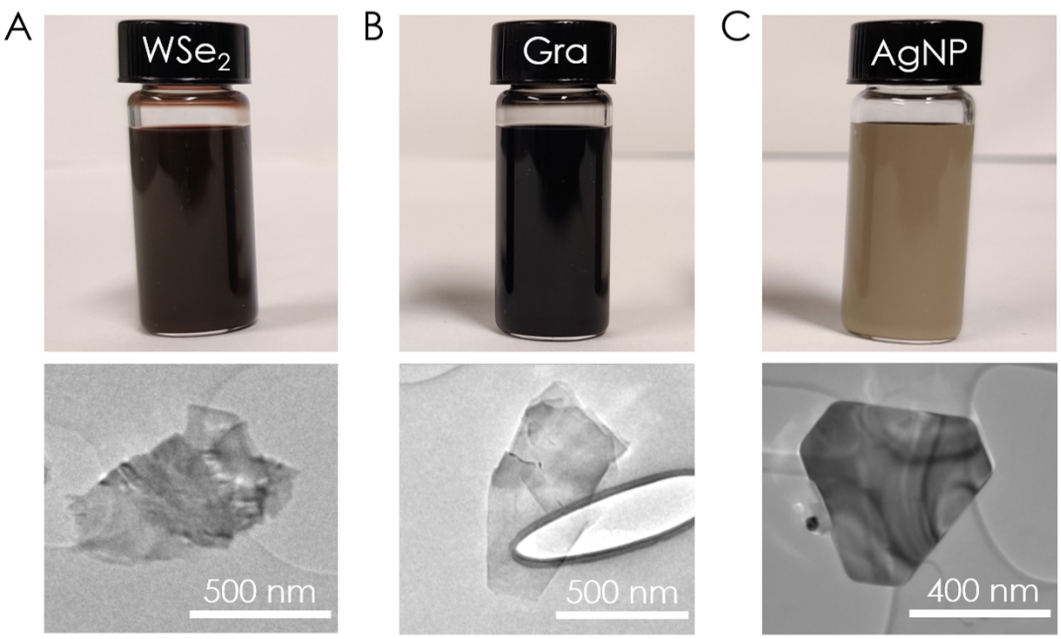

Figure 7.1: Solution-Processed 2D Inks: Photographs and representative TEM images of **A)** WSe_2, **B)** Graphene and **C)** Silver nanoplatelet inks and nanosheets respectively.

adversely affect reproducibility.[428] Thus, it is essential to trap nanosheet sizes into tightly confined bands. Extinction spectra were recorded for each size-selected ink to assess both the nanosheet dimensions and ink concentrations. As shown in Fig. 7.2, the effect of nanosheet size has a considerable effect on its electronic properties.

TMDs are rich in excitonic features, as can be seen for the size-selected WSe_2 inks in Fig. 7.2A. As nanosheet edges and basal planes are electronically distinct, they exhibit different absorbance coefficients at a given wavelength. This allows the nanosheet length, l_{NS}, to be inferred from different peak intensity ratios.[429] Furthermore, the mean nanosheet thickness in a given ink, t_{NS}, can be correlated to energetic shifts in excitonic transitions. This arises from quantum confinement and screening effects as the number of layers is reduced.[430] The lowest energy energy transition, known as the A-exciton, is of particular relevance in this work and is seen to blue-shift with decreasing nanosheet size in Fig.

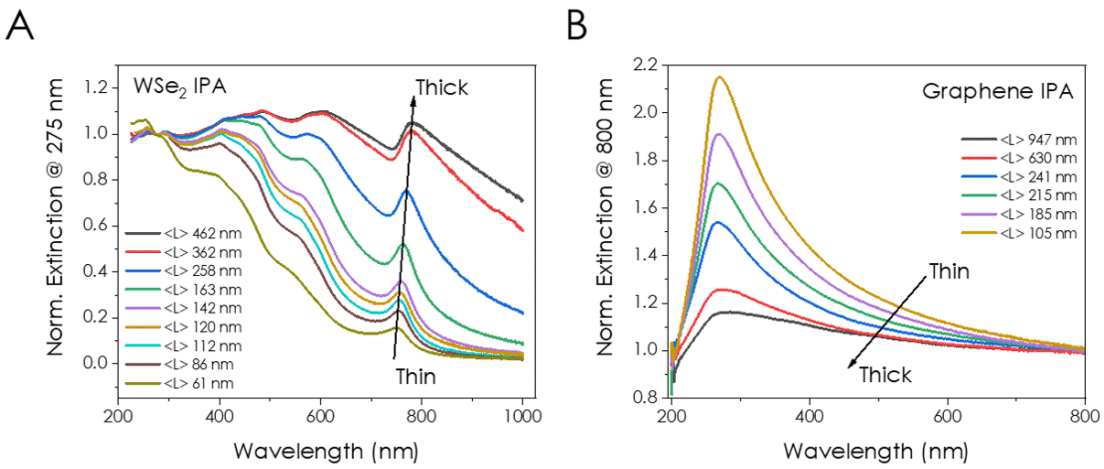

Figure 7.2: Size-selected Extinction Spectra: UV-vis extinction spectra for size-selected inks of **A)** WSe_2 nanosheets, normalised to the local minimum at 275 nm and **B)** Graphene nanosheets normalised to the dimension independent plateau at 800 nm

7.2A. In graphene, the absorption response in the long wavelength region ($>$ 550 nm) is independent of nanosheet dimension, depending only on the mass of graphene present.[431] However, at higher energies the $\pi - \pi^*$ peak appears and it is well-reported that the ratio of this peak to the long wavelength plateau increases with decreasing nanosheet thickness, as shown in Fig. 7.2B.[125] While the UV-vis data in Fig. 7.2 is indicative of families of size-selected inks for each material, the nanosheet length for graphene cannot be determined without Raman measurements. Furthermore, though spectroscopic metrics for WSe_2 have recently been published, they are only applicable for nanosheet thicknesses $\leq$ 10 monolayers.[432] Thus, statistical TEM was used to determine the mean lateral nanosheet dimension in each size selected ink, with the results for WSe_2 and graphene given in Fig. 7.2.

A set of size-selected WSe_2 inks is shown in Fig. 7.3A, where the rich colour is indicative of the formation of relatively thin, semiconducting nanosheets.[259] The concentration of each of these inks was determined from its extinction spectrum using the Beer-Lambert law and metrics developed by Harvey *et al.*[433] Both the nanosheet length and yield for each trapping band is plotted as a function of central rpm in Fig. 7.3B. Here, the total nanosheet mass sedimented at each step of the LCC process is

seen to fall approximately with rpm^{-1}. A similar trend is shown for nanosheet length, l_{NS}, as predicted by theory.[219] This demonstrates the LCC process to facilitate selective production of 2D inks with nanosheet lengths spanning an order of magnitude: WSe_2 inks exhibited l_{NS} values of ~ 450 - 50 nm, while the graphene nanosheet fractions were ~ 950 - 100 nm in lateral dimension.

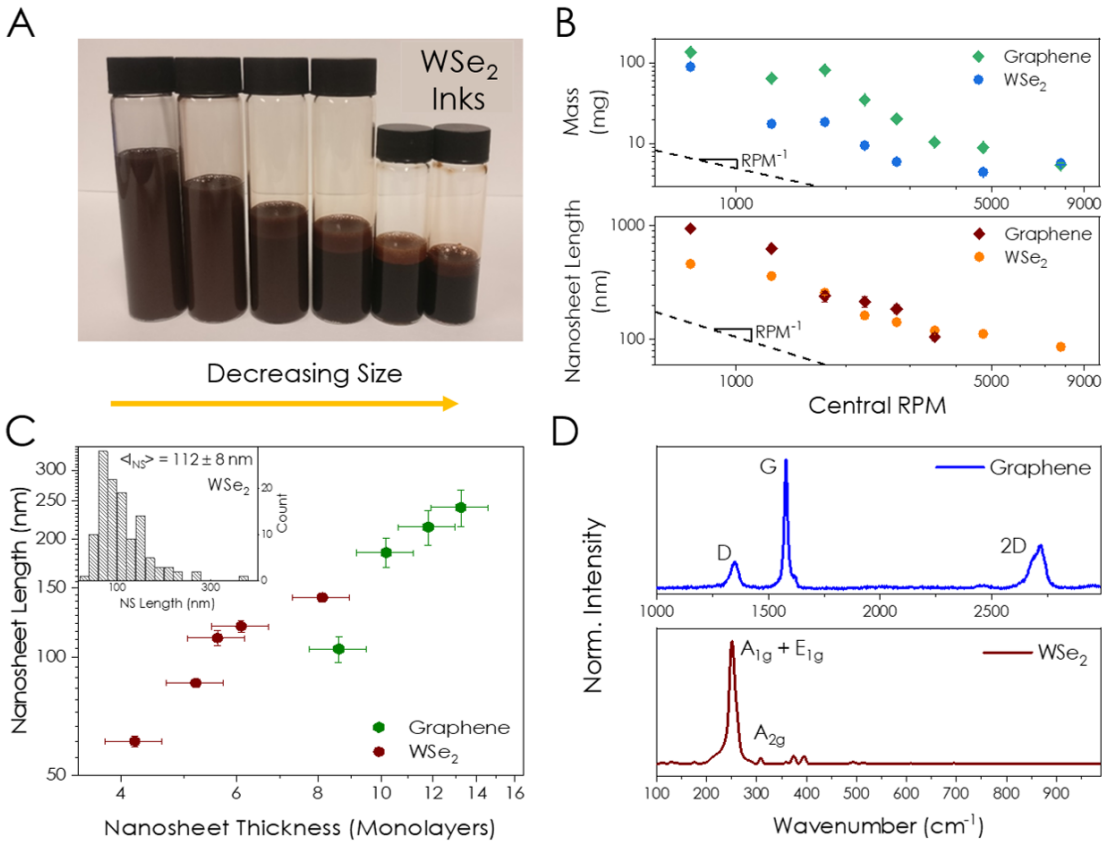

Figure 7.3: Ink Properties: A) Photograph of a family of size-selected WSe_2 inks. **B)** Plots of the mean nanosheet yield and length for each size-selected ink as a function of trapping speed. **C)** Plot of nanosheet length, l_{NS}, and thickness, t_{NS}. Inset: TEM-measured lateral size-distribution for a WSe_2 ink. **D)** Representative Raman spectra for sprayed traces of WSe_2 and graphene.

As centrifugation separates by mass, graphene will generally demonstrate larger nanosheet lengths than TMDs at a given trapping speed. Graphene sheets have a lower density than WSe_2 and will be thinner for a given length. Furthermore, the conjugated C-C bonds along the graphene basal plane

reduce sonication-induced scission.[223,434] The data in Fig. 7.3B is important from an applications standpoint as it serves to inform ink formulation for two of the most commonly used 2D materials (assuming 2.4 g of bulk powder). The nanosheet thickness, t_{NS}, was inferred for a subset of the graphene and WSe_2 inks using spectroscopic metrics.[125,432] A number of the nanosheet fractions used in this work had thicknesses that exceeded 10 monolayers, which is beyond the scope of the metrics. The nanosheet thickness is plotted against its length for the samples within the range of the metrics in Fig. 7.3C. Here, a well-defined relationship between nanosheet length and thickness can be seen across the size-selected inks, as predicted for LPE nanosheets through nanosheet mechanics.[223] This implies that the nanosheet aspect ratio, $k = l_{NS}/t_{NS}$, is well-defined for both graphene and WSe_2, demonstrating values of $\sim$ 50 and $\sim$ 30 respectively. A representative distribution of TEM measured lengths for a size-selected WSe_2 ink is shown in the inset of Fig. 7.3C. Raman spectroscopy was performed on sprayed traces of each ink for compositional and environmental analysis. The Raman peaks for each material, shown in Fig. 7.3D, were as expected and exhibited minimal oxidation effects or degradation. With the properties of the inks and their constituent nanosheets characterised, each sample was then prepared for deposition. To ensure dispersion stability and consistent deposition, each ink was diluted to a concentration of 0.35 gl^{-1}. This concentration was found to prevent aggregation within the ink while facilitating repeatable and homogeneous trace deposition.[435,436]

7.3 Network Deposition & Optimisation

With an optimised set of size-selected inks for each material, nanosheet traces could then be deposited. Spray coating was used due to the reduced procedural complexity when compared with other prevalent techniques, such as inkjet (IJP) and aerosol jet printing (AJP). Crucially, this allowed each ink to be deposited under identical process parameters; IJP is limited to smaller nanosheet sizes to prevent

nozzle clogging,[251] while AJP is a multifaceted process where it is difficult to ensure a constant process environment across samples.[239] By optimising the deposition process, uniform traces were printed for each ink, as shown for a sprayed WSe_2 network in Fig. 7.4A. Each of the printed films were found to be homogeneous and continuous on a macroscopic length scale.

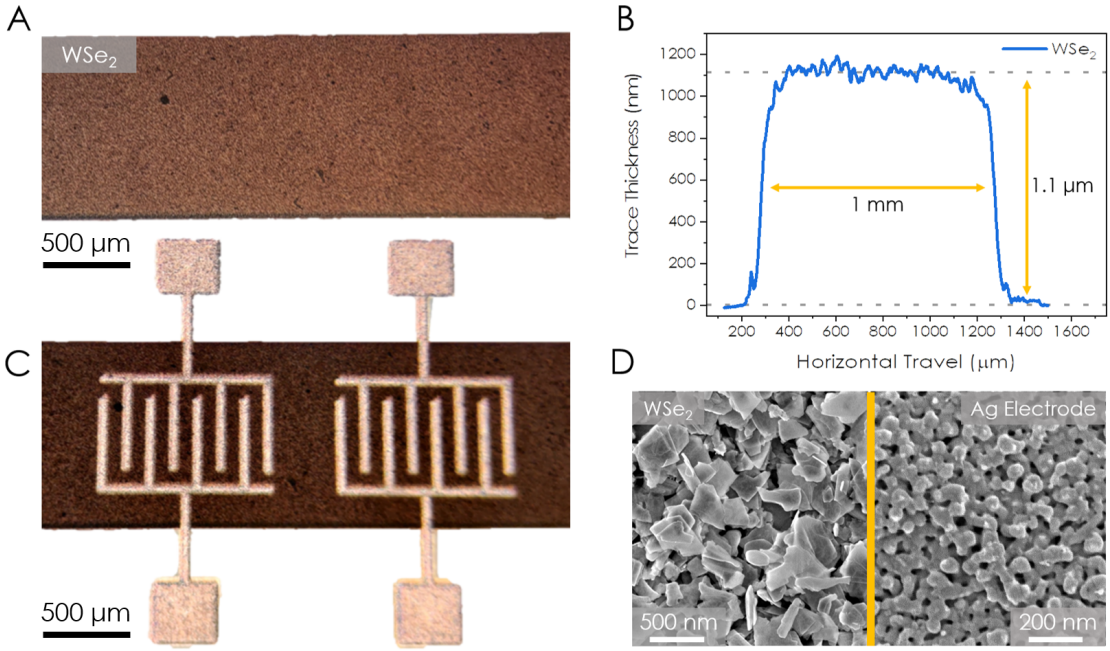

Figure 7.4: Sprayed Nanosheet Networks: A) Optical microscope image of a sprayed WSe_2 nanosheet network. **B)** Representative profilometry scan across the printed trace showing a trace height of 1.1 µm and width of 1 mm **C)** Silver nanoparticle electrodes, aerosol jet printed onto the WSe_2 network. **D)** SEM images of a printed WSe_2 network and a sintered Ag nanoparticle electrode.

It is important to note that despite this macroscopic uniformity, printed nanosheet networks are well-reported to exhibit local disorder and porosities on the order of 50 %.[191] Following deposition, each trace was annealed under vacuum at 80 °C to remove any residual solvent from the network. Glass was chosen over flexible substrates, such as PVA / Al_2O_3-coated polyethylene terephthalate (PET), as part of an attempt to alleviate the contribution of substrate roughness to the network morphology. Furthermore, a rigid substrate facilitated more accurate profilometry measurements on the sprayed

traces. This is reflected in Fig. 7.4B, were a representative profilometry trace is shown for a 1.1 μm thick WSe_2 network.

To assess the in-plane conductivity, silver nanoparticle electrodes were aerosol jet printed onto each of the 2D traces, as shown in Fig. 7.4C. This facilitated *in situ* control over the electrode dimensions for each sample. Top electrodes were employed to closely follow the surface topography and improve the contact interface, as interfacial effects are known to influence the performance of printed heterostacks.[437] By optimising the deposition parameters and ink viscosity, the printed silver linewidth was reduced to $\sim$ 15 μm for electrode thicknesses of $\sim$ 1 μm. This enabled interdigitated silver nanoparticle electrodes (IDEs) of varying channel dimensions to be designed and printed on demand. For the WSe_2 trace shown in Fig. 7.4C, a channel length of 70 μm was used. SEM images of a printed WSe_2 network and silver nanoparticle electrodes are shown in Fig. 7.4D. The 2D network is seen to comprise nanosheets primarily aligned in the plane of the film, and exhibits significant porosity. The effect of electrode annealing is also clearly shown, where at temperatures as low as 80 °C the individual Ag nanoparticles are seen to coalesce. This enhances the electrode conductivity by a factor of $\sim$ 50, towards values of $\sim 10^6$ Sm^{-1}, but also improves the network-electrode interface.

7.4 Conductivity Scaling with Nanosheet length, l_{NS}

To fully optimise the electrical properties of solution-processed 2D networks, it will be necessary to characterise the influence of both the constituent nanosheets and global network. While these are distinct sources, their contributions are likely intertwined. Changing the nanosheet dimensions will alter the number of interfacial junctions along a given path, and likely the morphology of the network as a whole. Further, as nanosheet thickness and length are intrinsically coupled in LPE nanosheets, any changes in l_{NS} will also modify t_{NS}.[223] Thus, characterising the conductivity response as a function

of nanosheet length represents an initial, but required, step towards understanding these complex disordered systems. Crucially, any dependence on nanosheet length would open immediate avenues for network optimisation, owing to the ease with which nanosheets can be size-selected through LCC. The coming sections will briefly describe the length-dependent conductivity response in printed WSe_2, graphene and silver nanoplatelet networks. This will be followed by the development of a conductivity model and a more detailed discussion of the electrical transport in these 2D networks.

7.4.1 Semiconducting Networks: WSe_2

WSe_2 was chosen as the initial material as it is among the most conductive of the layered TMDs and has demonstrated promise in device applications.[438] Traces on the order of 1 μm thick were printed for each size-selected ink and patterned with silver electrodes as shown in Fig. 7.4A & C. Representative I-V curves for a subset of the sprayed WSe_2 networks are shown in Fig. 7.5A. The in-plane electrical conductivity of sprayed WSe_2 networks is plotted as a function of nanosheet length, l_{NS}, in Fig. 7.5B. The data is striking, showing the network conductivity to fall significantly as the length of the constituent nanosheets is reduced. Indeed, as l_{NS} is reduced from 462 nm to 62 nm, the conductivity of the printed network is seen to decrease by a factor of ~ 10 from $\sim 1 \times 10^{-3}$ Sm^{-1} to 2×10^{-4} Sm^{-1}.

Notably, the conductivity data for the largest nanosheet sizes is in agreement with values on the order of $\sim 10^{-3}$ Sm^{-1} reported for similarly prepared films.[191] In this work, the authors removed all but the largest WSe_2 nanosheets such that the mean dimensions were $l_{NS} \sim 330$ nm and $t_{NS} \sim 13$ layers. Though no directly comparable data is available for smaller WSe_2 nanosheets, Higgins *et al.* reported transport in similar semiconducting WS_2 networks to become impaired as nanosheet size is reduced.[73] To ensure that the trend exhibited by the sprayed data was not an artefact of the deposition process, the study was repeated by aerosol jet printing the WSe_2 traces. As shown in Fig. 7.5B, networks deposited

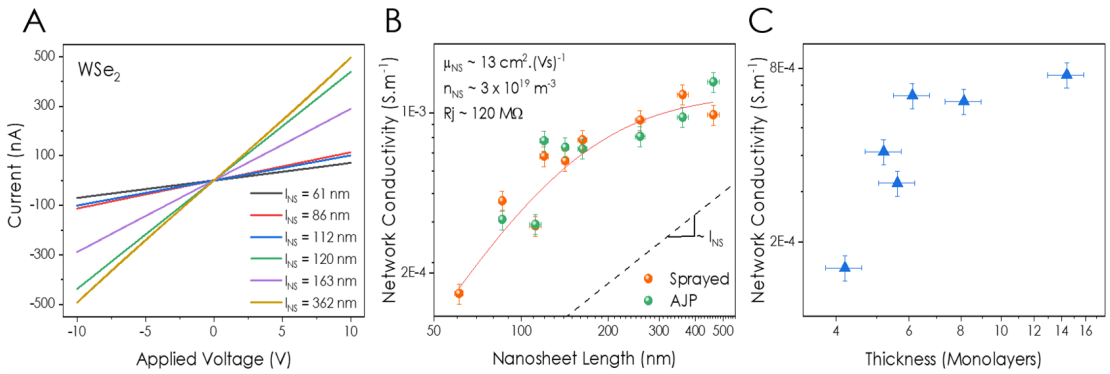

Figure 7.5: Printed WSe_2 Networks: A) Representative I-V curves for a subset of sprayed WSe_2 traces. **B)** Plot of the in-plane conductivity of printed WSe_2 networks as a function of mean nanosheet length, l_{NS}. The red line is a fit to Eqn. 7.2. **C)** Plot of the in-plane conductivity as a function of mean nanosheet thickness, t_{NS}.

from the same inks show reasonable agreement between the two deposition techniques, suggesting the dependence to be material-driven. As mentioned, l_{NS} and t_{NS} are intrinsically coupled for LPE nanosheets through an equipartition of the energies required to peel nanosheets from a parent crystal and to induce nanosheet scission by breaking intralayer bonds.[223] Thus, the conductivity data shows a similar trend with nanosheet thickness, t_{NS}, in Fig. 7.5C.

Interestingly, the data in Fig. 7.5B falls in line with the axiom that a reasonably well-aligned network of large nanosheets will be more conductive than a similar network comprised of smaller nanosheets. This is generally attributed to the reduced number of interfacial junctions that a charge carrier will experience when crossing the network.[331] However, it has also been reported that the WSe_2 nanosheet mobility increases by over three orders of magnitude as the nanosheet thickness increases from 1 to 10 monolayers.[439] Indeed, a degree of scatter in Fig. 7.5B & C can likely be attributed to thickness-driven mobility and bandgap scaling.[427] The LCC process traps a distribution of nanosheet sizes in each fraction, meaning inks comprised of few-layer nanosheets will demonstrate a distribution of nanosheet thicknesses and correspondingly, bandgaps. This can lead to spatial variations in bandgap across a printed trace, which has been linked to charge trapping and increased interfacial energy barriers.[440]

Crucially, this suggests that the dimension-dependent conductivity scaling in Fig. 7.5B & C is driven by both intrinsic and interfacial effects.

7.4.2 Semi-Metallic Networks: Graphene

Following WSe_2, the length-dependent conductivity of printed graphene networks was investigated. An initial SEM survey was performed on each sample to assess the character of both the interfacial junctions and global network as a function of nanosheet length, l_{NS}.

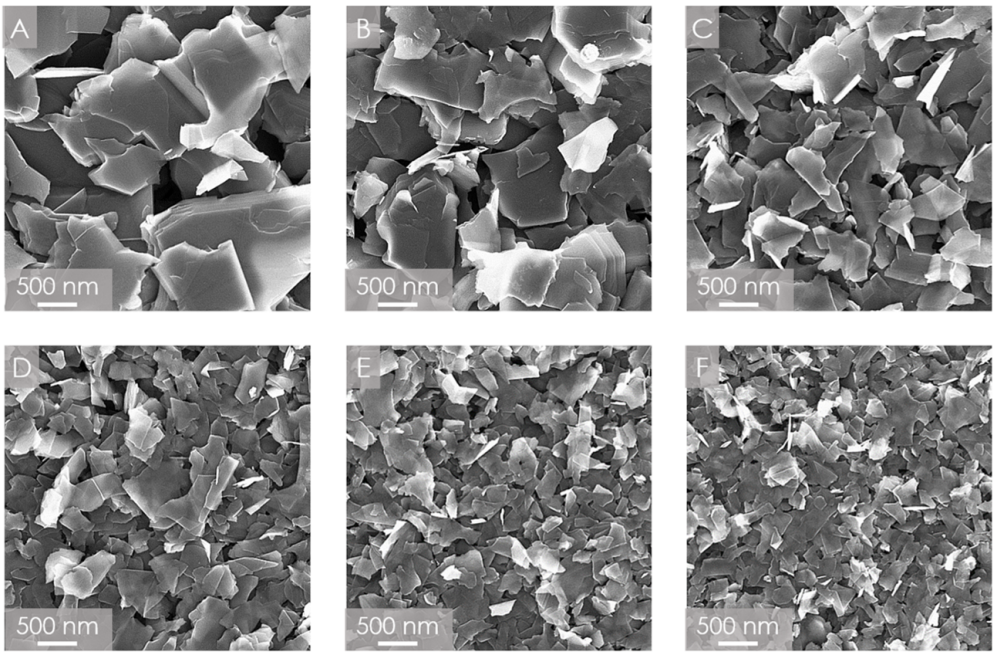

Figure 7.6: Graphene Network SEM: High resolution images of spray coated graphene nanosheet networks comprised of **A)** 947 nm, **B)** 630 nm, **C)** 241 nm, **D)** 215 nm, **E)** 185 nm and **F)** 105 nm long nanosheets.

As shown in Fig. 7.6, printed nanosheet networks exhibit a disordered morphology with considerable porosity. This leads to an array of different nanosheet / nanosheet interfaces and a broad range of junction resistances. Each image in Fig. 7.6A - F was captured at the same scale to give a qualitative idea of how the network changes as the nanosheet dimension is changed from large to small.

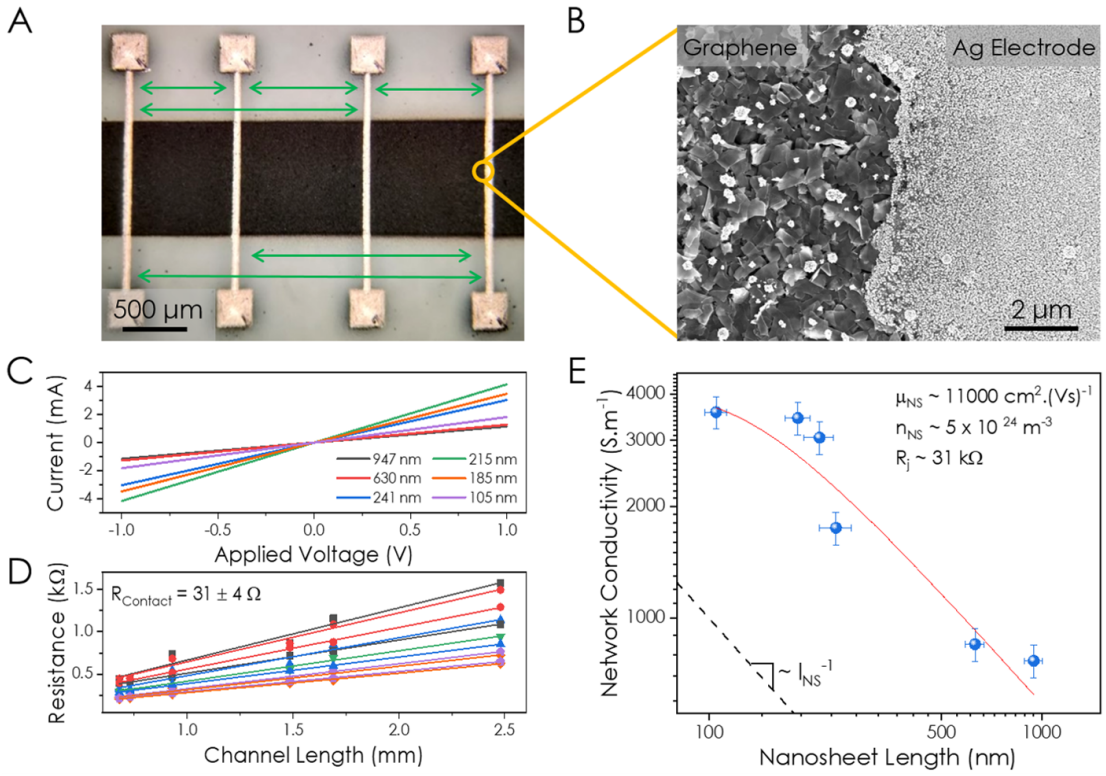

Figure 7.7: Printed Graphene Networks: A) Sprayed graphene trace with AJP silver nanoparticle top electrodes. The various channel lengths used to measure the network conductivity are denoted by green arrows. **B)** SEM image of the network / electrode interface. **C)** Representative I-V curves for printed graphene networks of each nanosheet size. **D)** Plot of the network resistance as a function of channel length, where the network / electrode contact resistance, R_C, is given by the *y*-intercept. **E)** Plot of the in-plane conductivity of printed graphene networks as a function of mean nanosheet length, l_{NS}. The red line is a fit to Eqn. 7.2.

For electrical measurements on graphene networks the interdigitated electrodes used for WSe_2 were replaced by parallel electrodes spaced over a few millimetres, as shown in Fig. 7.7A. This stems from the inherently higher conductivity of graphene.[441] A high resolution SEM image of the electrode / network interface is shown in Fig. 7.7B to highlight both the intimacy of the interface and resolution of the printed silver lines. Representative I-V curves for each of the size-selected graphene networks are shown in Fig. 7.7C. The measured network resistance at each inter-electrode separation, or channel length, was found from its I-V curve for each sample. This is plotted in Fig. 7.7D, where the sample resistance is seen to decrease linearly as the channel length is reduced. From the *y*-intercept a mean

contact resistance value of $R_C = 31 \pm 4\ \Omega$ is extracted. When normalised to the area of the electrode / network interface, this translates to a specific contact resistance of $14 \pm 2\ \text{m}\Omega.\text{cm}^2$. This suggests that the AJP silver nanoparticle electrodes are in intimate contact with the graphene network. The length-dependent in-plane conductivity for sprayed graphene networks is plotted in Fig. 7.7E. Crucially, this data appears to refute the narrative that longer nanosheets lead to fewer junctions and an increased network conductivity - at least for LPE nanosheets over the considered length range.

The conductivity data in Fig. 7.7E exhibits a clear trend with ${l_{NS}}^{-1}$, increasing from $\sim 767\ \text{Sm}^{-1}$ to $\sim 3574\ \text{Sm}^{-1}$ as the nanosheet length is reduced from 947 to 105 nm. Though the conductivity data in Fig. 7.7E may initially seem counterintuitive, a number of physical mechanisms are likely contributing to this ${l_{NS}}^{-1}$ scaling. The conductivity of graphene nanosheets is known to fall with increasing nanosheet thickness,[442] while the inter-nanosheet junction resistance has been observed to increase with t_{NS}.[443] Indeed, the carrier mobility in printed networks of electrochemically exfoliated (EE) graphene nanosheets has been reported to scale inversely with the constituent nanosheet thickness.[444] Here, the increased network mobility is attributed to superior flexibility in thinner nanosheets. As the nanosheet bending modulus scales with t_{NS},[445,446] thin nanosheets are more supple and will facilitate conformal overlap with neighbouring nanosheets and improved junction quality. Notably, while sprayed networks of LPE graphene exhibit a ${l_{NS}}^{-1}$ conductivity scaling in this work, the inverse has been reported for printed networks of electrochemically exfoliated r-GO, where l_{NS} and t_{NS} are not intrinsically coupled.[425] Similarly, screen printed networks of LPE graphene have demonstrated both behaviours as the nanosheet length is changed.[213] This suggests that though nanosheet length is an important parameter, the aspect ratio and junction quality also hold considerable influence over charge transport through the network.

7.4.3 Metallic Networks: Silver Nanoplatelets (AgNP)

Finally, an initial study on the length-dependent conductivity in printed silver nanoplatelet networks was performed. Silver nanoplatelets (AgNPs) have emerged as a more economical and device-friendly alternative to silver nanoparticles for printed conductors.[447] This arises from their 2D geometry, which facilitates both reduced printing passes and annealing temperatures ($\sim$ 150°C) to form a conductive trace. Two stock AgNP dispersions were commercially sourced from Tokusen nano (N300, $l_{NP} \sim$ 300 - 500 nm and M13, $l_{NP} \sim$ 1 - 3 µm). These stock samples were redispersed in DI water and size-selected using a shortened centrifugation cascade. The size-selected inks are shown in Fig. 7.8A, where a clear colour change can be seen as the size of the constituent nanoplatelets is reduced due to light scattering.[264]

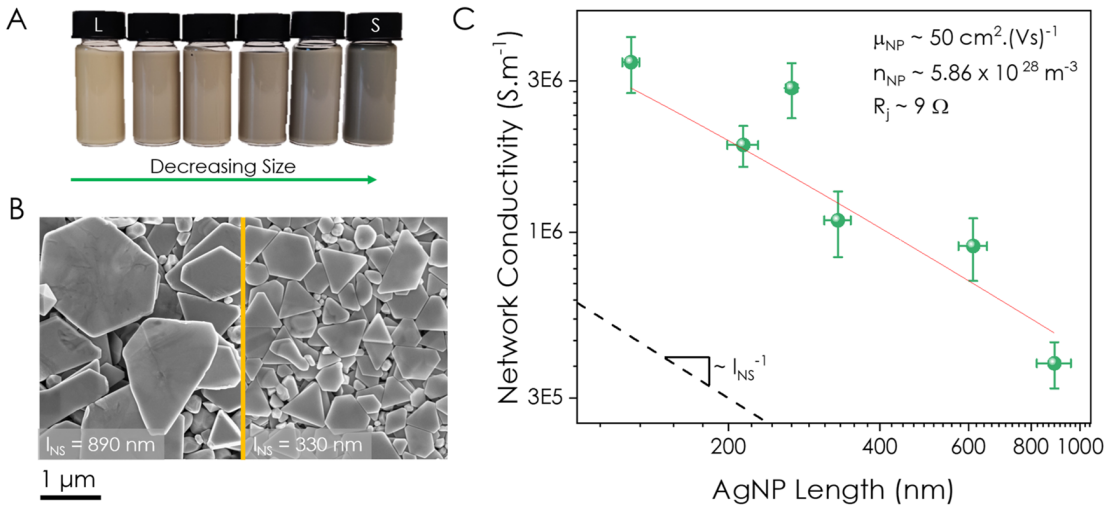

Figure 7.8: Printed Silver Nanoplatelet Networks: A) Size-selected vials of AgNP inks. **B)** SEM images of two size-selected networks (l_{NP} = 890 nm and 330 nm) taken at same scale. **C)** Plot of the in-plane conductivity of printed AgNP networks as a function of mean nanoplatelet length, l_{NP}. The red line is a fit to Eqn. 7.2.

Each size-selected AgNP ink was diluted to a concentration of 5 gl^{-1} for spraying and owing to the unsuitability of glass substrates for water-based dispersions, PET was used. Here, the substrate

temperature was increased to 90 °C to expedite solvent evaporation. To compensate for the increased substrate roughness, each trace was printed ~ 3 μm thick to improve the signal-to-noise ratio in profilometry measurements. Comparative SEM images of sprayed AgNP networks for nanoplatelets of different lengths are shown in Fig. 7.8B. The images were captured at the same scale to highlight the changes in both the average nanoplatelet size and network character. In both cases the AgNPs are seen to be primarily aligned in the plane of the film. However, both networks display a significant degree of porosity and a broad range of junction types, in line with the WSe_2 and graphene networks.

As with graphene, the AgNP data in Fig. 7.8C exhibits a clear scaling with ${l_{NP}}^{-1}$, increasing from $\sim 4 \times 10^5$ Sm^{-1} to $\sim 3 \times 10^6$ Sm^{-1} as the average AgNP length was reduced from 880 nm to 128 nm. While the AgNPs used here are not layered materials, initial AFM data suggests that the AgNP aspect ratio remains broadly constant as their length is reduced. This may suggest that the nanoplatelets conform to each other more favourably as they are thinned or that the packing uniformity increases with decreasing l_{NP}. Thus, while the WSe_2 networks conform to the narrative that longer nanosheets will result in fewer interfacial junctions and produce higher network conductivities, the conductive graphene and AgNP networks diverge from this. To address this, a simple yet quantitative model was developed to describe the dimension-dependent scaling in terms of both nanosheet and network properties. This model is fully derived in Appendix A.5 but the key points will be discussed here.

7.4.4 Nanosheet Network Conductivity Model

It is first assumed that charge carriers flow along well-defined conductive paths through the nanosheet network, as shown in Fig. 7.9A. Such a path can be considered as a series of voltage drops across both nanosheets and their interfacial junctions. Thus, the fundamental unit of this current path is the nanosheet / junction pair, where for every nanosheet that an electron traversing the network crosses,

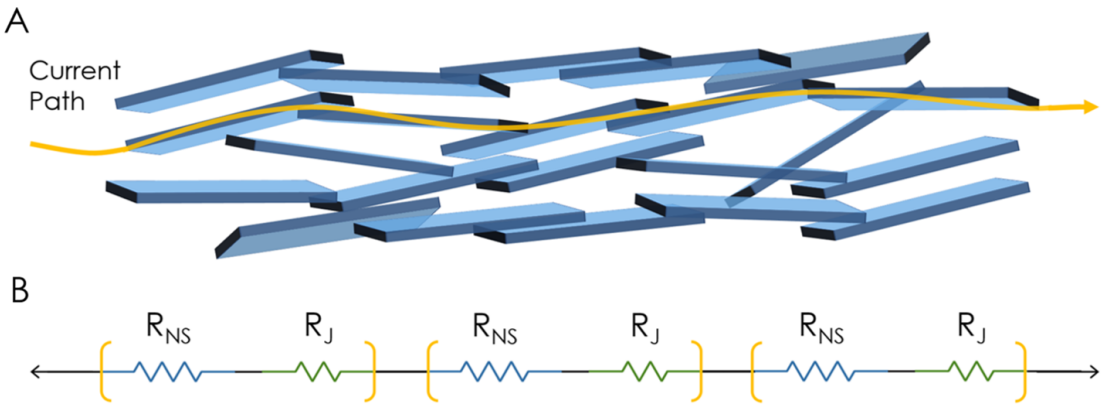

Figure 7.9: Nanosheet Network Model: A) Schematic of a current path through a nanosheet network. **B)** This path represented as a series of of voltage drops across nanosheet / junction pairs. Each pair consists of a nanosheet and interfacial junction, each with a resistance of R_{NS} and R_J respectively.

it must also pass through a junction. A current path through the network will be comprised of many of these nanosheet / junction pairs in series, as shown in Fig. 7.9B. Here, a voltage is dropped across both the nanosheet and junction, each having resistances of R_{NS} and R_J respectively. Thus, the network conductivity, σ_{Net}, is limited by both the conductivity of individual nanosheets, σ_{NS}, and by parasitic junction resistances as the electrons tunnel or hop across the vdW gap between nanosheets.[312] By equating the time taken for an electron to traverse the entire network with the time taken for it to cross every nanosheet / junction pair in a current path that spans it, a simple model for σ_{Net} can be derived. This is shown explicitly in Appendix A.5 and its form is given by Eqn. 7.1

$$\sigma_{Net} \approx \frac{\sigma_{NS}\,\varphi^{\beta}}{\left[1+\frac{R_J}{R_{NS}}\right]\left[1+\frac{k}{{l_{NS}}^3\,n_{NS}}\left(\frac{R_J}{R_{NS}}\right)^{\alpha}\right]} \tag{7.1}$$

where φ is the nanosheet volume fraction, β is a percolation exponent, $k = l_{NS}/t_{NS}$ is the nanosheet aspect ratio and n_{NS} is the nanosheet carrier density. The term $\left(k\,/\,n_{NS}\,{l_{NS}}^3\right)^{-1}$ represents the average number of charge carriers per nanosheet. Crucially, this model describes the conductivity response

of a LPE nanosheet network in terms of both material and network properties. While the network conductivity will clearly exhibit a dependence on the conductivity of the constituent nanosheets, σ_{NS}, it will similarly depend on the volume fraction of nanosheets in the network, φ. Printed nanosheet networks are well-reported to contain significant porosity, which will affect the nature of the junctions in a network.[191] For low-φ values the network is likely to be disordered and exhibit a wide range of different junction types. However, as φ approaches $\sim$ 1 the network will tend towards well-aligned nanosheets with large-area and conformal basal plane junctions. Such a transition would likely reduce the junction resistance, R_J, and increase the network mobility, μ_{Net}. Indeed, this effect was recently demonstrated by Lin *et al.* where a highly-aligned network of MoS_2 nanosheets was shown to exhibit carrier mobilities approaching the nanosheet value, μ_{NS}.[308]

The interplay of the nanosheet and junction resistances, R_{NS} and R_J, plays a similarly significant role. For highly conductive materials, such as graphene, the junction resistance is proposed to greatly exceed the nanosheet resistance such that $R_J \gg R_{NS}$. Networks from the TMD family may exhibit different behaviours, depending on the doping level and intrinsic resistance of the nanosheets. The exponent α determines the degree of influence that the ratio R_J/R_{NS} has on the network. Crucially, nanosheet-specific properties such as nanosheet length, l_{NS}, carrier density, n_{NS}, and aspect ratio, k, are used. The nanosheet resistance, R_{NS}, is a difficult quantity to find published values for. However, by approximating the nanosheets as squares, R_{NS} can be expressed in terms of intrinsic nanosheet properties as $R_{NS} = k/\left(n_{NS} e \mu_{NS} l_{NS}\right)$. This allows Eqn. 7.1 to be expressed as

$$\sigma_{Net} \approx \frac{n_{NS} e \mu_{NS} \varphi^{\beta}}{\left[1 + \frac{R_J n_{NS} e \mu_{NS} l_{NS}}{k}\right]\left[1 + \frac{k}{{l_{NS}}^3 n_{NS}}\left(\frac{R_J n_{NS} e \mu_{NS} l_{NS}}{k}\right)^{\alpha}\right]} \tag{7.2}$$

It must be noted that this model is currently an approximation as it only considers a single current

path through the nanosheet network. Charge carriers in disordered 2D networks will likely travel through a number of different current paths simultaneously in parallel. This more complex network topology is neglected by Eqn. 7.2 in its present form. However, in the absence of quantitative data on the internal morphology of these 2D architectures, it is hoped this simplified approximation can be used to provide insight into the mechanism of conduction.

Conductivity Model: WSe_2

This model is fit to the sprayed WSe_2 data in Fig. 7.5B and finds reasonable agreement. Significantly, given the just the mean nanosheet length, l_{NS}, thickness, t_{NS}, and network conductivity, σ_{Net}, estimates for the nanosheet mobility, carrier density or junction resistance can be extracted. To fit the data the nanosheet carrier density was fixed at $n_{NS} = 3 \times 10^{19}$ m^{-3}, which is well within the range of reported values of 10^{18} - 10^{22} m^{-3} for WSe_2.[448,449] Furthermore, the nanosheet aspect ratio was set to be $k = 30$ based on the data in Fig. 7.3C. Finally, the nanosheet volume fraction was fixed to be $\varphi = 0.5$, in line with values generally reported for nanosheet networks.[349] The fitted nanosheet mobility of $\mu_{NS} = 13 \pm 2$ $cm^2\,(Vs)^{-1}$ is in line with published values for few-layer WSe_2 of $\sim$ 5 - 100 $cm^2\,(Vs)^{-1}$.[450–453] However, experiments to both expand the dataset and assess this fitted value directly using independent techniques are underway.

To this point there have been very few reports on the interfacial barriers between TMD nanosheets, which represents a significant gap in the literature. The fitted value of 100 ± 20 MΩ for the inter-nanosheet junction resistance in WSe_2 is clearly a limiting factor in these networks (*cf.* s-SWNT $R_J \sim$ 500 kΩ.[323]) Interfacial barriers of this magnitude likely contribute to the large variance in reported σ_{Net} values for a similar TMD, MoS_2. Here, published values span a range of 10^{-6} Sm^{-1} – 1 Sm^{-1} as the network morphology, and nature of the nanosheet junctions, is changed.[308,454] This clearly

demonstrates the scope for optimisation in these networks. Interestingly, Eqn. 7.1 predicts similar behaviours across the semiconducting members of the TMD family, which are expected to exhibit large junction resistances and low carrier densities. This is shown explicitly in Appendix A.5A. In the limit of this scenario where $R_J/R_{NS} \gg 1$ and $\left(\left(k/n_{NS}{l_{NS}}^3\right)^{\alpha}(R_J/R_{NS})\right) \gg 1$, the network conductivity can be approximated as

$$\sigma_{Net,SC} \approx \frac{\varphi^{\beta} l_{NS} k}{e\mu_{NS}{R_J}^2} \tag{7.3}$$

Using values reported by Kelly *et al.* for printed LPE WSe_2 networks ($\mu_{NS} \sim 91$ cm^2 (Vs)$^{-1}$, $l_{NS} \sim 320$ nm, $\varphi \sim 0.4$ and $k \sim 38$) produces $R_J \sim 600$ MΩ.[191] While this is a simple approximation, it is interesting that it is both comparable to the fitted R_J value of ~ 120 MΩ in this work and presents such a large resistance. Furthermore, this simplification of the conductivity model would suggest that semiconducting materials such as MoS_2, $MoSe_2$ and WS_2 will show a similar dependence with l_{NS}. While temperature-dependent conductivity data is limited, carrier transport in nanosheet networks has been reported to occur via variable range hopping at low-temperatures with a transition to thermally-activated behaviour as temperature is increased.[455] The activation energy, E_A, in these networks appears to scale with increasing material bandgap, E_g, ranging from ~ 0.15 eV for graphene to ~ 0.85 eV for BiOCl.[456,457] While data for 2D TMDs is more scattered, E_A is seen to increase from 0.21 eV for WSe_2 ($E_g \sim 1.64$ eV) to 0.32 eV for MoS_2 ($E_g \sim 1.85$ eV).[191] Drawing an analogy with the nanocrystal networks discussed in Chapter 5.1, E_A can be decomposed into an intrinsic component based on the nanosheet carrier density, n_{NS}, and a mobility activation energy associated with inter-sheet hopping. Thus, increases in E_A with E_g in 2D networks are likely driven by changes in both n_{NS} and the magnitude of the interfacial barrier, R_J. These parameters are accounted for in Eqn.

7.2 and while distinct for a given material, they are expected to be similar across the group VI TMDs.

Conductivity Model: Graphene

When the network conductivity model is applied to the graphene data, as shown in Fig. 7.7E, it again finds broad agreement. Interestingly, α was again found to be ~ 1, which suggests that the relative magnitude of R_J/R_{NS} has a comparable effect across both semiconducting and conductive nanosheet networks. Owing to the increased number of reports on graphene, the fitted parameters can be readily compared with published values. As LPE graphene nanosheets exhibit enhanced aspect ratios when compared to LPE TMDs,[223] the nanosheet aspect ratio was fixed to be $k = 50$, in agreement with the data in Fig. 7.3C. Furthermore, the nanosheet volume fraction was again fixed at $\varphi = 0.5$, while the nanosheet carrier density was set as 5×10^{24} m^{-3}.[458,459] By fitting Eqn. 7.2 to the graphene data in Fig. 7.7E values for the nanosheet mobility of $\mu_{NS} = 11000 \pm 6000$ cm^2 (Vs)$^{-1}$ and junction resistance $R_J = 31 \pm 4$ kΩ can be extracted from the data. The former is well within the range of 5000 - 18000 cm^2 (Vs)$^{-1}$ predicted by Fang *et al.* for multi-layer graphene nanosheets at room temperature.[442] Similarly, the extracted value of $R_J \sim 31$ kΩ agrees well with values of ~ 10 kΩ reported for CVD-grown graphene nanosheets.[443] The variation in R_J likely arises from a range of junction types in solution-processed nanosheet networks, compared with vertical stacking in the CVD work. Significantly, even in this unoptimised system R_J compares favourably to values of ~ 250 kΩ reported for metallic - metallic carbon nanotube junctions due to the increased interfacial area.[323]

While the ${l_{NS}}^{-1}$ scaling in the conductivity data in Fig. 7.7E may seem counterintuitive, such a dependence is again predicted by the conductivity model in Eqn. 7.1. This is shown explicitly in Appendix A.5B. For materials that are junction limited and exhibit large carrier densities such that, $R_J/R_{NS} \gg 1$ and $\left(\left(k\,/\,n_{NS}{l_{NS}}^3\right)^{\alpha}(R_J/R_{NS})\right) \ll 1$, the network conductivity model in Eqn. 7.1 can

be approximated to scale as

$$\sigma_{Net} \approx \frac{k\,\varphi^{\beta}}{R_J\,l_{NS}} \tag{7.4}$$

This form predicts the ${l_{NS}}^{-1}$ scaling seen for graphene in Fig. 7.7E, and would be expected to apply to similar networks of highly conductive nanosheets. Applying Eqn. 7.4 to published data on printed graphene networks produces junction resistance values in the range of $R_J \sim 5$ - 100 kΩ.[454,460,461] This is in strong agreement with the fitted value of $R_J \sim 31$ kΩ. An estimated value for the resistance of a graphene nanosheet, R_{NS}, can be found by approximating that $R_{NS} \approx (l_{NS}) / (\sigma_{NS}\,l_{NS}\,t_{NS}) = (\sigma_{NS}\,t_{NS})^{-1}$. Using values of $\sigma_{NS} \sim 8 \times 10^6$ Sm^{-1} and $t_{NS} \sim 5$ nm,[442] produces a nanosheet resistance of $R_{NS} \sim 25$ Ω. The corresponding ratio of (R_J/R_{NS}) is in the 200 - 1000 range, showing these networks to be heavily junction limited.

Conductivity Model: AgNPs

The ${l_{NS}}^{-1}$ conductivity scaling for silver nanoplatelets shown in Fig. 7.8C may seem counterintuitive at first - charge transport in these networks can reasonably be expected to be limited by inter-sheet junctions, and smaller platelets would lead to more junctions along a given current path. However, when this $R_J \gg R_{NS}$ behaviour is combined with the large carrier density of silver $\sim 5 \times 10^{28}$ m^{-3}, the network conductivity model again predicts a ${l_{NS}}^{-1}$ conductivity scaling through

$$\sigma_{Net} \approx \frac{k\,\varphi^{\beta}}{R_J\,l_{NS}} \tag{7.5}$$

As the data points in Fig. 7.8C are preliminary results, the fit of Eqn. 7.2 is intended to be a qualitative demonstration until more data is added. However, a reasonable value for the inter-platelet

junction resistance of $R_J = 9 \pm 2\ \Omega$ can be extracted by fixing μ_{NP} and n_{NP} to their bulk values of $\mu_{NP} = 50\ \mathrm{cm}^2\ (\mathrm{Vs})^{-1}$ and $n_{NP} = 5.86 \times 10^{28}\ \mathrm{m}^{-3}$ respectively.[462,463] The exponent α was fixed at $\alpha = 1$, while initial AFM results suggest the AgNP aspect ratio to be ~ 15. However, as the AgNPs are synthesised and not constrained by LPE mechanics, a thorough AFM study is required to verify this across each size fraction. Calculating the AgNP resistance using $R_{NP} \approx (\sigma_{NP} t_{NP})^{-1}$ yields $R_{NP} \sim 0.3\ \Omega$. This demonstrates these networks to be heavily junction-limited through the ratio of their junction and nanoplatelet resistances of $(R_J/R_{NP}) \sim 30$. Though these initial results are promising, significant work remains to complete this study and quantitatively fit the data. Furthermore, the effect of annealing at sub-sintering temperatures on the conductivity response is of interest. This would offer a simple means to modulate R_J and characterise the length dependent response.

The conductivity model presented in this chapter will hopefully inform routes to optimise solution-processed printed 2D networks going forward. It would seem that to maximise electrical performance it will be necessary to engineer the network morphology so that it is limited by the material itself. In the regime where $R_J \ll R_{NS}$, the network conductivity model given by Eqn. 7.2 simplifies to predict a material limited conductivity of $\sigma_{Net,M} \approx \sigma_{NS}\varphi$. By reducing the network porosity and increasing the nanosheet alignment the quality of these interfaces can be improved to reduce R_J, while simultaneously increasing φ towards its optimal value of 1. This is likely the case in the highly-aligned MoS_2 networks demonstrated by Lin *et al.*[308] Here, the improved nanosheet interfaces and near-perfect alignment combine to create a regime where the network mobility approaches that of its constituent nanosheets.

7.5 Conclusions

The electrical properties of printed WSe_2, graphene and AgNP networks have been investigated as a function of constituent nanosheet length, l_{NS}, in this chapter. A family of size-selected 2D inks, each spanning an order of magnitude in l_{NS}, were produced using liquid cascade centrifugation. The resultant inks were then spray coated and electrically characterised. The in-plane conductivity of spray-coated WSe_2 networks was observed to decrease by an order of magnitude as the length of the constituent nanosheets was reduced from 462 nm to 62 nm. Interestingly, the conductivity of both graphene and silver nanoplatelet networks was found to exhibit the opposite response, scaling with ${l_{NS}}^{-1}$. Here, the printed network conductivity was found to increase by a factor of $\sim$ 10 as l_{NS} was reduced from $\sim$ 1 μm to 100 nm for both materials. While these results are interesting in their own right, they are also of immediate relevance for device optimisation and demonstrate a route to tune the electrical properties of solution-processed 2D networks.

Perhaps more significantly, a model is presented to describe the conductivity response of the printed networks in terms of both nanosheet and network properties. Crucially, this model predicts the diverse electrical behaviours observed experimentally by considering the interplay of the intra- and inter-nanosheet resistances in each network. However, though the model capability has been initially demonstrated using three electronically diverse 2D materials, much work remains. Additional data for each of the studied materials would enable improved fitting accuracy, while verifying the fitted values independently using THz spectroscopy or TFT measurements will be important. By considering additional materials, such as MoS_2 and WS_2, the model can be further tested and improved. It is hoped that this work may provide insight into the electrical properties of printed 2D networks, while illuminating pathways to optimise their device performance.

What sane person could live in this world and not be crazy?

Ursula K. Le Guin

8

FIB-SEM Tomography of Nanosheet Networks

As the field of nanoscience matures it is becoming increasingly clear that the morphology of a 2D network plays a dominant role in determining its resultant properties.[424] This has led to a shift in focus towards assessing and optimising network attributes including porosity, pore tortuosity, nanosheet alignment and connectivity. It is well-reported that the mechanical properties of aligned nanosheet networks greatly eclipse their more disordered analogues,[464] and in Chapter 7 the morphology of a 2D network was shown to have a dominant effect on its electrical transport characteristics. Thus, in order to capitalise on the superlative properties of the constituent nanosheets and ensure they confer to the ensemble, methods to quantitatively analyse the morphology of these systems will be essential.

Important properties such as porosity are rarely reported for 2D networks in the literature. When reported, methods such as mercury intrusion porisometry (MIP),[465] Brunauer–Emmett–Teller (BET) nitrogen adsorption / desorption analysis,[466] and sample weighing are employed.[352] However, each of these techniques have well-documented limitations and do not provide information on network alignment or morphology. This has led to the emergence of FIB-SEM nanotomography (FIB-SEM NT) for the assessment of nanostructured networks. Single FIB-SEM cross-sections are routinely used to probe the internal character of such networks.[467] However, individual cross-sections may not be representative of the global network and do not provide any 3D information. In FIB-SEM NT, the slice and image process is automated whereby a sequence of interpolated cross-sectional slices through a network can be compiled into a high-fidelity 3D reconstruction. For a standard FIB-SEM NT run this can include hundreds to thousands of cross-sectional images, encompassing volumes of tens to hundreds of μm^3. The generated sample volumes are similar in nature to those produced by x-ray computed tomography and although the FIB-SEM NT process is destructive it offers significantly higher resolutions on the order of ~ 5 nm (*cf.* x-ray CT resolution > 500 nm).[468]

FIB-SEM NT has been utilised to characterise the morphology and composition of fuel cells,[469] the pore shape and connectivity in oil shale,[470] and even joints in acorn barnacles.[471] However, to this point disordered networks of nanosheets have not been considered. This is addressed in the coming chapter, where spray-coated graphene networks are characterised as a function of constituent nanosheet length, l_{NS}. Graphene networks were chosen due to their inherently high conductivity and to build upon the length-dependent electrical study in Chapter 7. While a preliminary length-dependent investigation is performed, the principal aim of this chapter is to demonstrate the viability of the FIB-SEM NT technique and to lay the foundations for more comprehensive studies.

8.1 Materials & Methods

Graphene inks were synthesised using graphite powder purchased from Asbury (Grade 3763). HPLC grade isopropanol and sodium cholate hydrate (> 99%) were purchased from Sigma Aldrich. Deionised water (18.3 MΩ.cm) was produced in-house. The silver nanoparticle dispersion was purchased from Sigma Aldrich (< 50 nm diameter, 30 - 35 wt % in methyltriglycol).

Graphite powder was added to 80 ml of DI water at a concentration of 30 gl^{-1}. This dispersion was initially probe-sonicated for 1 h using a Sonics Vibra-cell VCX-750 ultrasonic processor at 60 % amplitude. The process temperature was maintained at 7 °C using a chiller and the tip action was pulsed at 6 s on and 2 s off to prevent solvent evaporation and overheating of the horn probe. This initial dispersion was then centrifuged for 1 h at 4900 rpm using a Hettich Mikro 220R centrifuge (fixed angle rotor) to isolate purified graphite in the sediment. The supernatant was discarded and the graphite redispersed in 80 gl^{-1} of DI water and sodium cholate at a concentration of 2 gl^{-1}. This dispersion was then sonicated for a further 8 h at 60 % amplitude, with the tip pulsed 4 s on and 4 s off. The resultant dispersion was then centrifuged at 500 rpm for 2 h to remove any unexfoliated material, leaving a stock polydispersion of exfoliated graphite.

The stock dispersion was size-selected using the liquid cascade centrifugation technique described in Section 3.3 and employed in Chapter 7. The nanosheet size fractions isolated in this work were trapped using 500 - 1000 rpm, 1000 - 1500 rpm and 1500 - 2000 rpm bands to isolate the largest (L), intermediate (M) and smallest (S) flakes in the sediment, respectively. In each case the sediment was redispersed in fresh DI water and sodium cholate (2 gl^{-1}). These inks were then transferred to IPA for spraying. To remove the sodium cholate, each dispersion was centrifuged for 2 h at 6 krpm. The supernatant was discarded and the sediment redispersed in fresh IPA. This step was repeated twice.

Extinction spectra were recorded post-transfer to determine the ink concentration for each size using previously developed metrics.[125] These measurements were performed using a Varian Cary 50 UV-Vis spectrophotometer in 1 nm increments using a 4 mm quartz cuvette. The mean nanosheet length for each of the dispersions, L, M and S, was determined using TEM measurements performed on a JEOL 2100 TEM system operating at a 200 kV accelerating voltage. Each ink was diluted and drop-cast onto holey carbon grids for TEM analysis. The nanosheet lengths were found by measuring the longest axis of each sheet in an image. Each ink was then diluted to a concentration of 0.35 gl^{-1} for spraying.

Inks were spray coated onto ultrasonically cleaned glass slides at temperature of 70 °C using a Harder and Steenbeck Infinity Airbrush attached to a Janome JR2300N mobile gantry. A N_2 back pressure of 45 psi, nozzle diameter of 0.4 mm and stand-off distance of 100 mm were used. Each of the sprayed traces were patterned into 1×4.5 mm bars using stainless steel masks. The FIB-SEM measurements in this work were performed using a dual beam Zeiss Auriga FIB-SEM. Each printed trace was mounted on a SEM stub using conductive carbon tabs (PELCO®, 12 mm diameter). To ensure system stability when imaging / milling, a conductive path to ground from the sample was added using silver paint purchased from Ted Pella Inc. To render three-dimensional image stacks from a sample, commercial software was used (Zeiss ATLAS 5). All SEM imaging was performed in both SE2 and Inlens mode at an accelerating voltage of 2 kV.

8.2 Sample Preparation & Characterisation

Each of the size-selected graphene inks used in this work are shown in Fig. 8.1A. The inks were first characterised in the UV-Vis spectrometer. As before, the nanosheet thickness in a given fraction is seen to decrease as the trapping rpm is increased. The change in nanosheet size is shown in Fig. 8.1B, where the relative intensity of the $\pi - \pi^*$ peaks can be used as a marker of the nanosheet dimensions. This

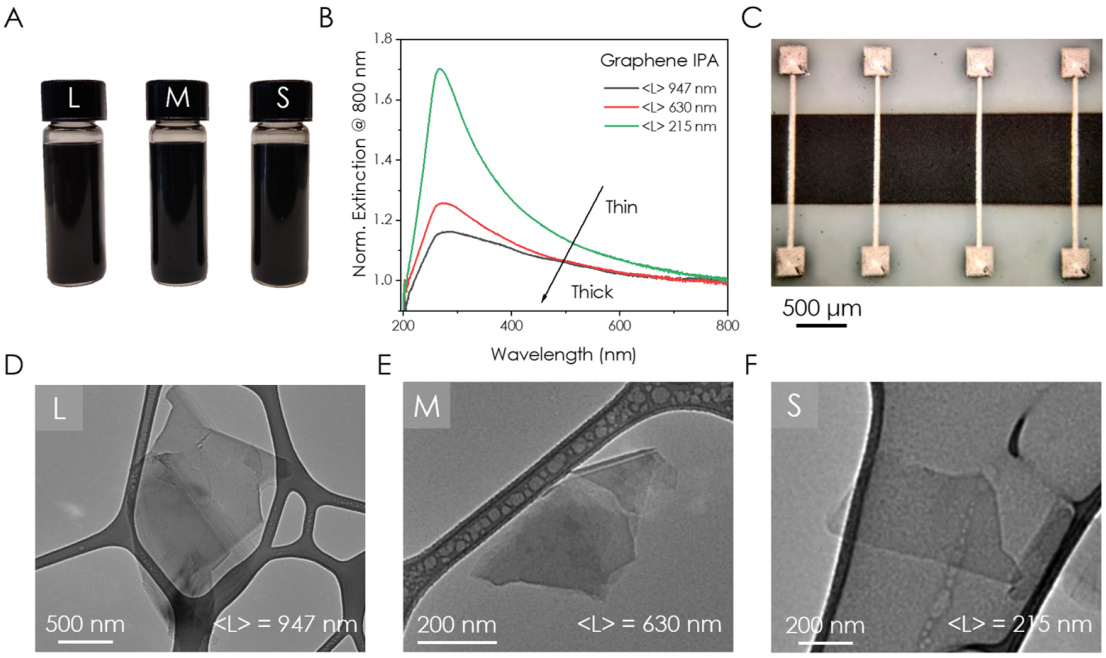

Figure 8.1: Ink Characterisation: A) Image of the size selected graphene inks. **B)** Extinction spectra of the inks showing the changing nanosheet thickness with centrifugation speed. **C)** A spray coated network of graphene nanosheets for FIB-SEM tomography. **D-F)** Representative TEM images of nanosheets from each of the 3 size-selected fractions on holey carbon grids.

shift in nanosheet thickness corresponds to changes in the nanosheet length, as length and thickness are intrinsically coupled through nanosheet formation mechanics for LPE samples.[223]

A representative printed graphene trace is shown in Fig. 8.1C. The 4.5 × 1 mm bars were spray coated onto glass slides with thicknesses of 1 - 2 µm. These sample thicknesses were chosen to provide as much of a cross-sectional area as possible for FIB-SEM analysis. Glass substrates were used due to their surface flatness, to remove substrate contributions to the network morphology. A TEM survey was performed on each of the inks to assess both the degree of exfoliation and to measure the nanosheet dimensions. Representative TEM images of the large, medium and small size-selected nanosheets are shown on holey carbon grids in Fig. 8.1D-F. In all cases the nanosheets were found to be well-exfoliated two-dimensional objects and their lengths were measured by statistical counting. The size-selection

parameters and nanosheet dimensions for each of the graphene inks studied are given in Table. 8.1.

Ink	Trapping Band (krpm)	Nanosheet Length (nm)
Large	0.5 - 1	947 ± 58
Medium	1 - 1.5	630 ± 40
Small	1.5 - 2	215 ± 22

Table 8.1: Size-selected Nanosheet Dimensions: Centrifugation trapping speeds and their corresponding nanosheet lengths for each of the inks used. The nanosheet lengths were measured in the TEM.

8.3 FIB-SEM Tomography of Printed Nanosheet Networks

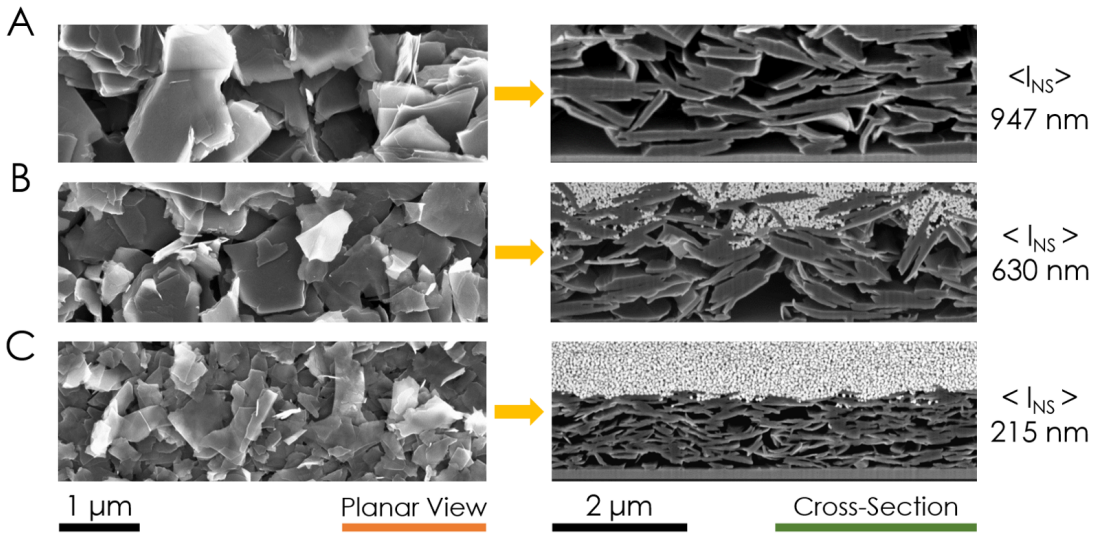

Figure 8.2: Length-dependent SEM & FIB Characterisation: Planar SEM and FIB-SEM cross-sectional images of sprayed graphene networks with average nanosheet lengths of **A)** 947 nm, **B)** 630 nm and **C)** 215 nm.

While SEM is a versatile method to characterise the morphology of 2D networks, it is generally limited to surface regions. Similarly, while FIB microscopy facilitates imaging of the internal network structure, it is limited in scope to single or multiple isolated cross-sections. As a reference, planar SEM and FIB-SEM cross-sections for each graphene network studied are shown in Fig. 8.2A-C. Each of the

images were recorded at the same scale to highlight differences in the network character as the length of the constituent nanosheets is changed. While the nanosheets in each FIB-SEM cross-section appear to be quite thick, each of these fractions were size-selected at the lowest rpms and so will be comprised of the thickest sheets in the parent dispersion. Additionally, these nanosheets have been subjected to two high speed centrifugation steps to transfer them from H_2O / SC to IPA, potentially inducing a degree of aggregation. It has also been proposed that aggregation occurs during film formation, with a $\sim$ 5-fold decrease in the mean nanosheet aspect ratio reported pre- and post-deposition.[472] While some qualitative observations can be made from the images in Fig. 8.2, it is difficult to assess if this picture is representative of the network as a whole or extract meaningful quantitative information. FIB-SEM nanotomography provides a means to assess the character of these networks on a more representative scale in three-dimensions, while retaining the the resolution of these 2D techniques.

Sample preparation for FIB-SEM tomography is broadly similar to the standard FIB-SEM process. However, as sample processing times can exceed 12 hours and span volumes of hundreds of μm^3 some additional steps are required. The sample is mounted on the stage and tilted to 54 ° so that the FIB and SEM probes are coincident at the 5 mm working distance. The gas injection system (GIS) is then introduced in close proximity to the sample. An initial protective platinum deposit is formed on the sample region of interest through electron beam induced deposition (120 µm aperture and an accelerating voltage of 2 kV). This step is crucial for printed nanosheet networks, which display increased roughness when compared to crystalline samples. Here, the platinum deposit both reduces the potential for ion beam damage and decreases the sample roughness to alleviate beam interaction effects such as curtaining.[289]

A schematic overview of a printed graphene network with the regions relevant to the FIB-SEM NT process is shown in Fig. 8.3A. The region of interest for imaging is the volume directly below the pro-

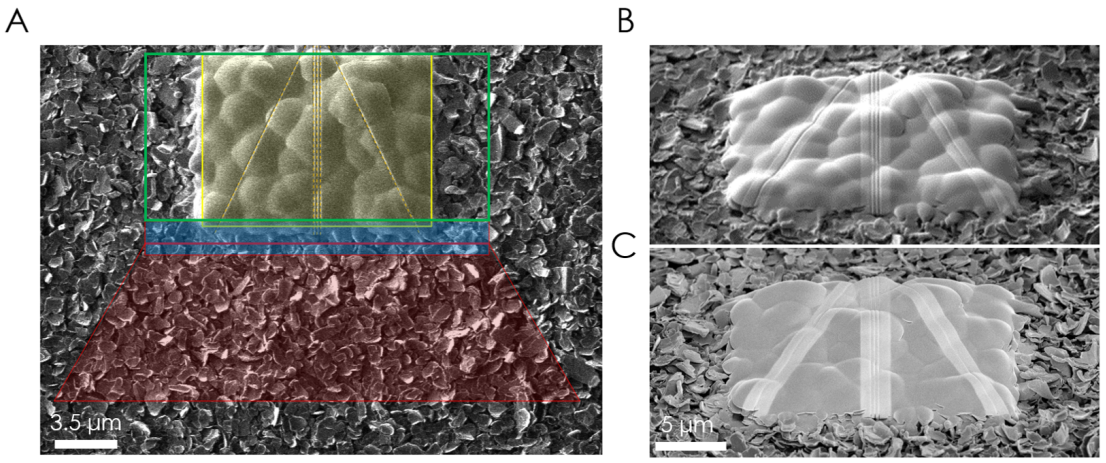

Figure 8.3: Nanotomography Setup: A) Schematic showing the relevant regions of the nanosheet network including the region of interest (yellow), sputtering area (green) and viewing trench (red). **B)** Milling of the 3D tracking and Auto-tune lines in the platinum protective pad and **C)** the deposition of high-contrast tungsten to fill the etched marks.

tective platinum pad, highlighted yellow in Fig. 8.3A. The region of interest was on the order of $\sim 15 \times 20$ µm for each of the printed networks studied. A second platinum pad has already been deposited on top of the initial deposit here, this time through ion-beam induced deposition (1 nA beam current and an accelerating voltage of 30 kV). The area to be milled is represented by the green box and is larger than the region of interest to increase the field of view. The red-shaded trapezoid represents the trench, which is region of the sample that is sputtered to allow the network cross-sections to be imaged by the SEM. This region is generally milled at larger currents, $\sim$ 10 nA, while the blue region in the vicinity of the sample is sputtered at $\sim$ 240 pA to protect the region of interest.

SEM Auto-Tune and 3D Tracking

The critical step in preparing a sample for nanotomography is the addition of the SEM auto-tune and 3D tracking marks. These are milled into the platinum deposit using a highly-focused 50 pA beam, as shown in Fig. 8.3B. These etched traces are then filled in or highlighted using a different metal, in this

case tungsten, that will offer contrast when imaged in the SEM, shown in Fig. 8.3C. Following this, an additional layer of platinum is deposited onto the protective pad to enclose the tungsten tracking in the ion beam deposited platinum.

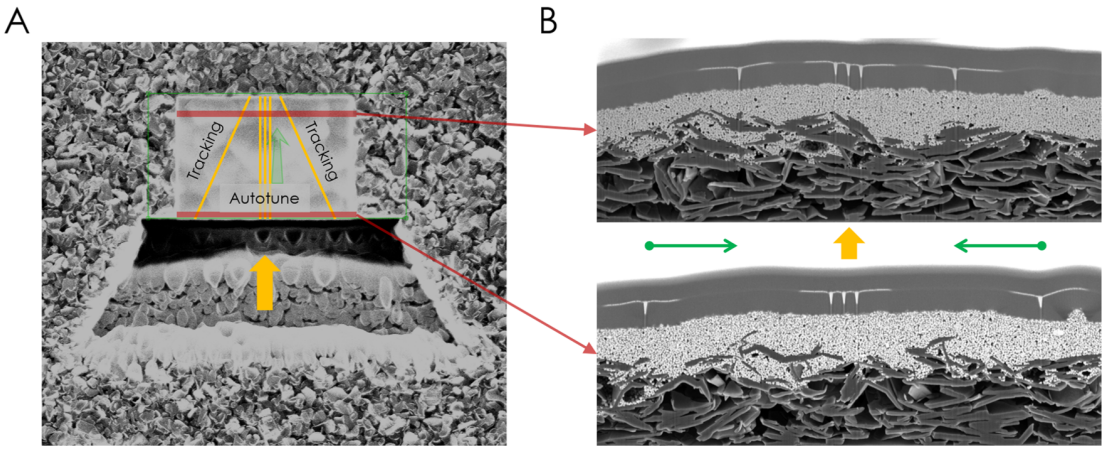

Figure 8.4: SEM Autotune & 3D Tracking: A) FIB image showing the 3 parallel SEM autotune reference marks and angled 3D tracking lines. **B)** SEM view of the calibration marks demonstrating the approach of the 3D tracking marks as the sample is milled.

The ATLAS system stays focused and calibrated throughout the milling and imaging by using SEM auto-tune reference marks. These are the three parallel lines shown in Figs. 8.3 and 8.4. At regular intervals the SEM system will attempt to find the tungsten autotune marks shown in Fig. 8.4B and will then adjust both the focus and stigmation of the SEM probe until they are in sharp focus. This ensures that the cross-sectional images of the nanosheet networks remain in focus throughout the milling / imaging process as the sample working distance increases and the system drifts. The autotune marks were used to calibrate the system between each frame in this work.

3D tracking is performed using the diagonal lines shown in Figs. 8.3 and 8.4. These lines are milled and highlighted at a well-defined angle with respect to the system coordinates. As each cross-section is milled the tungsten tracking marks will approach each other when imaged by the SEM. This is shown in Fig. 8.4B, where two slices have been selected from the milled stack, one 10 nm into the

sample and the other 3 μm into the milling. As the approach angle is known, the horizontal shift of these lines towards each other between each frame can be used to determine the depth of the mill and slice thickness. This value is essential to interpolate the image stack and reconstruct a high-fidelity 3D volume. The slice thickness chosen in this work was 10 nm. The system uses the first few slices to calibrate a 10 nm milling depth and then uses the approach of the 3D tracking lines to measure the thickness of each subsequent slice and correct any system drifts during the process. Once the calibration marks have been established, the primary viewing trench is sputtered from the 2D network. Network cross-sections at the region of interest can now be imaged and the system is ready for a run, as shown in Fig. 8.4A. Cross-sectional images of the nanosheet networks are acquired using both SE2 and Inlens detectors with a pixel size of 5 nm to extract as much spatial information as possible.

Reconstruction of Nanosheet Networks

Following a completed FIB-SEM NT run, a stack of images is interpolated using the thickness value measured for each slice and aligned using the SEM autotune calibration marks. A network volume can then be reconstructed by stitching the image stack together, as shown in Fig. 8.5A. Sample volumes of 22, 31 and 127 μm^3 were milled, sliced and generated for networks comprised of nanosheets with lengths of 215, 630 and 947 nm respectively. The reconstructed volumes are limited in size by both the printed trace thickness, which at $\sim$ 1 μm is characteristic of the dimensions used in printed thin film electronics, and the feature sizes for each network. A representative volume for the intermediate $l_{NS} = 630$ nm network is shown in Fig. 8.5B.

Crucially, the volumes shown in Fig. 8.5B-D are entirely reconstructed from 10 nm thick slices in the *xy*-plane as shown in Fig. 8.5A. Thus, the *yz*- and *xz*-planes of the generated volumes were not directly imaged and are entirely reconstructed. As can be seen in Fig. 8.5B, when the slices have been

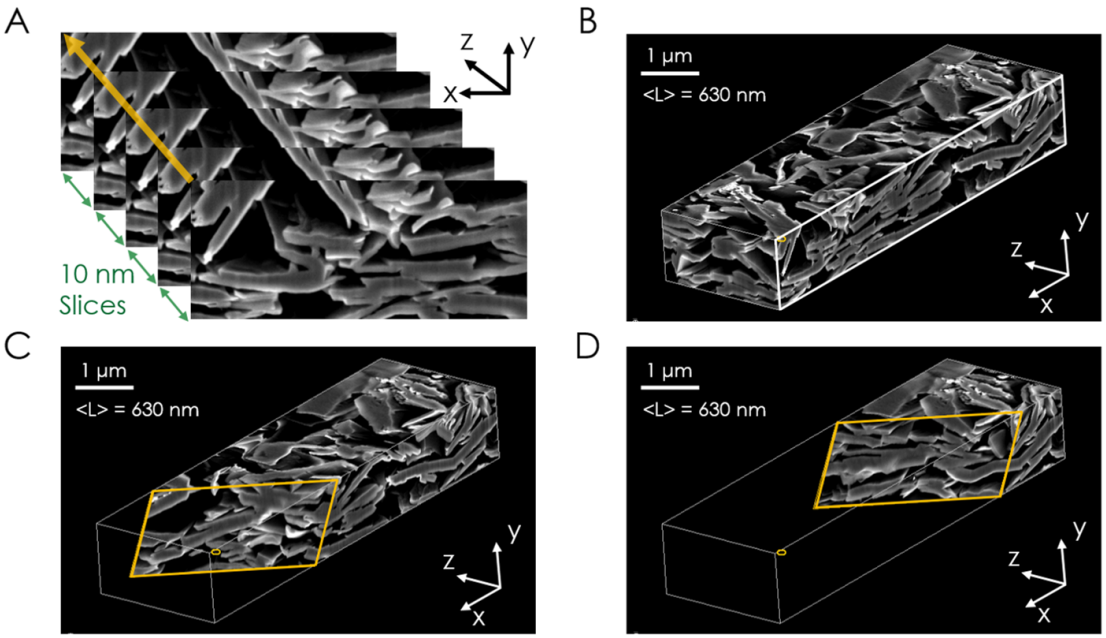

Figure 8.5: 3D Network Reconstruction: A) Demonstration of how the image slices are interpolated and stitched together in the *z*-direction to generate a 3D volume. **B-D)** Representative volumes of the $l_{NS} = 630$ nm sprayed graphene network. Cross-sectional planes, highlighted by yellow boxes, are passed through the volume at different depths to reveal the internal structure.

correctly interpolated and aligned, high-fidelity reconstruction of the real nanosheet network is possible through the FIB-SEM NT technique. To highlight this, a cross-sectional plane was passed through the network to reveal the internal character at different distances into the reconstructed volume. This plane is outlined by a yellow box in Fig. 8.5C-D. Though the internal network structure it reveals is entirely reconstructed, the morphology of individual nanosheets and pores can be clearly observed.

The rich morphological information provided by FIB-SEM NT is comparable in nature to x-ray computed tomography. However, FIB-SEM tomography offers vastly superior resolution, with pixel sizes of 5 nm (*cf.* x-ray CT pixel size $\gg$ 50 nm).[473] Network volumes like those shown in Fig. 8.5B-D can be used to qualitatively assess the network character or pore tortuosity. For example, it is clear that this 2D network is comprised of nanosheets primarily aligned in the plane of the film. However, a

considerable degree of disorder is also apparent. This leads to the formation of a large number of pores as shown in Fig. 8.5B - D. To extract quantitative information on key parameters such as porosity, network connectivity and alignment, it is necessary to process the image stacks and separate the pore and nanosheet volumes.

8.4 Morphological Properties of Nanosheet Networks

Segmentation

Image segmentation represents a pivotal step in the analysis pipeline by replacing pixel intensity values with region labels, in this case pore volume and nanosheets. Traditional classification techniques are based on the intensity and spatial relationships of pixels. However, a researcher performing manual segmentation will use many additional factors such as previous knowledge. This has precipitated the emergence of trainable machine learning techniques for image segmentation, whereby the algorithm can first be taught what constitutes a pore / nanosheet to aid the classification process. Segmentation of the nanosheet networks was performed using the *WEKA* trainable segmentation module in *FIJI*.[474] Wherever possible, published and open-source methods such as *WEKA* segmentation were used. This was due to the added control that could be exerted over the procedure, as it was found that many commercial softwares employed overly-simple or "black-box" processes. The segmentation pipeline is demonstrated using cross-sectional images from the $l_{NS} = 215$ nm network in Fig. 8.6A-C.

The WEKA classifier is initially trained on a representative cross-sectional image of the nanosheet network. Regions of the image are manually assigned as either pore volume or nanosheets to train the model, as shown in Fig. 8.6A. Once these initial definitions have been made by the operator, the algorithm then attempts to classify the image using both the manual definitions and the selected classification features. Three different classes of feature were chosen to classify the nanosheet networks:

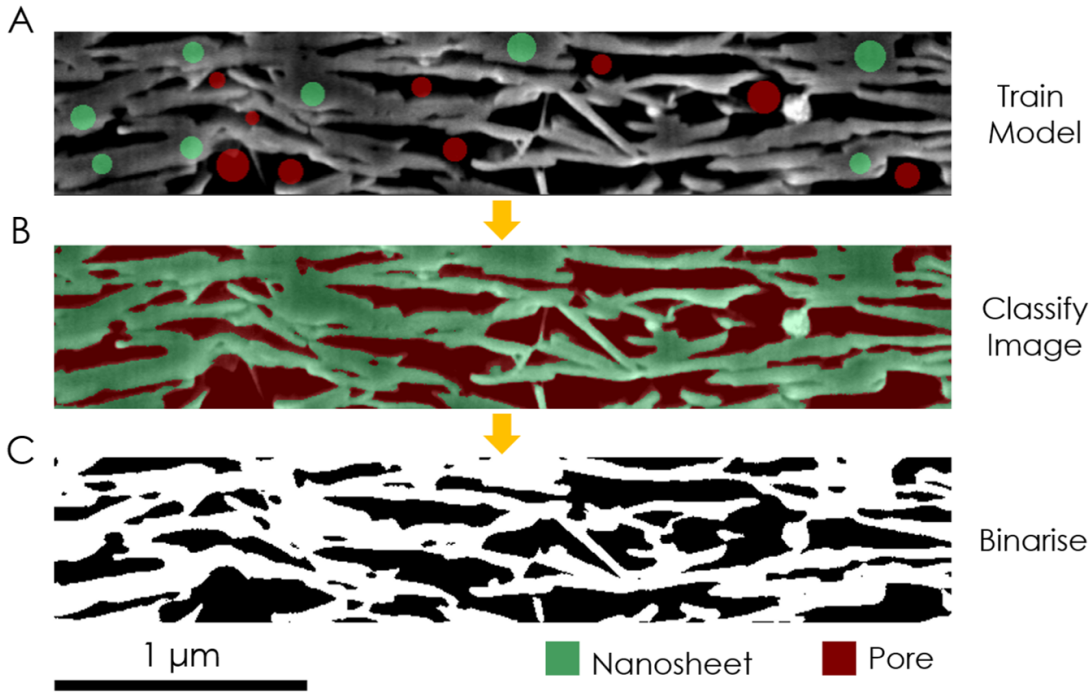

Figure 8.6: Image Classification: Segmentation of a printed graphene network into its nanosheet and pore volume components using trainable machine learning. The cross-section shown is from the $l_{NS} = 215$ nm network.

edge detectors, texture filters and noise reduction filters. As nanosheet-pore boundaries were crucial to the classification process a number of edge-detecting filters were employed, including Laplacian and Sobel filters, Hessian matrix eigenvalues and the difference of Gaussians.[475,476] Textural features were used to calculate the mean, variance and maxima of pixels within a given radius of a target pixel and set the pixel to that value. Finally, noise reduction filters such as Gaussian blurs serve to reduce imaging artefacts and local intensity variations in the image. By appropriate selection of training features, the classifier can be fed training information with 10^5 different features for segmentation.

The classification algorithm is a multi-threaded random forest classifier with 200 decision trees and two random features per node.[477] Each decision tree is comprised of a series of binary nodes, which are essentially points where the decision tree splits in two to try and segment the image. Each of the

200 decision trees in the random forest will then make a prediction on whether the region in question is a nanosheet or a pore. The class with the most predictions out of the 200 becomes the model's prediction. Each decision tree is trained on a different, random dataset and classified using a random subset of training features, thus the forest of decision trees are uncorrelated and protect each other from individual error.[478] A classified cross-section of the $l_{NS} = 215$ nm network is shown in Fig. 8.6B.

To quantitatively assess the reconstructed nanosheet volumes, correct segmentation is the decisive step. A poorly trained model can significantly skew the analysis that follows. Thus, it is crucial to help the model by first capturing images that are suitable, with as much contrast between the pores and nanosheets as possible. Further, it is essential to repeatedly train and assess the model before applying it to the image stack. Only regions of the nanosheet network that are at the cross-section face should be assigned as "nanosheet" by the model, otherwise the network porosity will be underestimated. While the classifier performance can be visually inspected by the operator, the validity of the random forest model is numerically assessed through the out-of-bag (OOB) score. Here, a subset of the training data known as the OOB sample is passed through each decision tree in the random forest that did not contain the OOB sample data. Each of these decision trees will then make a prediction and the OOB score is the percentage of correct predictions made. The out-of-bag error was used to assess the model performance in this work, where the OOB error is simply (100 − OOB score) %. In each case the model was run and training features were added until the OOB error was reduced below 8 %. Finally, for comparative FIB-SEM NT as in this work, it is crucial that each sample is classified using the same features. Though image classification is a non-trivial process, with sufficient training images can be classified and binarised with a spatial resolution approaching that of the original image ($\sim$ 5 nm), as shown in Fig. 8.6B-C.

8.4.1 Porosity

The porosity of 2D networks is a significant quantity across many potential applications including printed electronics, energy storage and catalysis.[352] The total network volume in these systems, V_T, is comprised of both nanosheet, V_{NS}, and pore volume, V_P, contributions such that $V_T = V_{NS} + V_P$. As before, the nanosheet volume fraction is given by $\varphi = V_{NS}/V_T$ and the network porosity is simply (1 - φ). While sample-weighing has been used to determine the porosity of printed and vacuum filtered networks, this does not provide any information on the nature of the pores.[191] Brunauer–Emmett–Teller (BET) nitrogen adsorption / desorption analysis and mercury intrusion porosimetry (MIP) have been used to determine the pore volume, size-distribution and specific surface area of 2D networks.[424] However, both of these techniques require restrictively large samples ($\sim$ 0.5 g or $>$ 100 μm thick) and considerable sample preparation.[479] These sample dimensions are prohibitively large for the characterisation of most printed devices, which display thicknesses $<$ 10 μm. Here, FIB-SEM tomography presents an *in-situ* means to identify and characterise each pore in the network. This means properties such as porosity, specific surface area and pore connectivity can be directly measured on a voxel-by-voxel basis using segmented network volumes. A $l_{NS} = 215$ nm network that has been classified into its nanosheet and pore volume components is shown in Fig. 8.7.

The pore volume of the reconstructed networks was characterised using 2-pass "connexity" analysis.[480] For each voxel in the network the neighbourhood of its 26 nearest neighbours is inspected (those sharing a common face, edge or point). All adjacent voxels with intensities above the threshold limit are considered to be a part of the same pore. As each image stack was binarised, this threshold is any voxel with a non-zero value. This is shown for the reconstructed network pore volume in Fig. 8.7, where any volume that hasn't been classified as pore volume has been removed from the network.

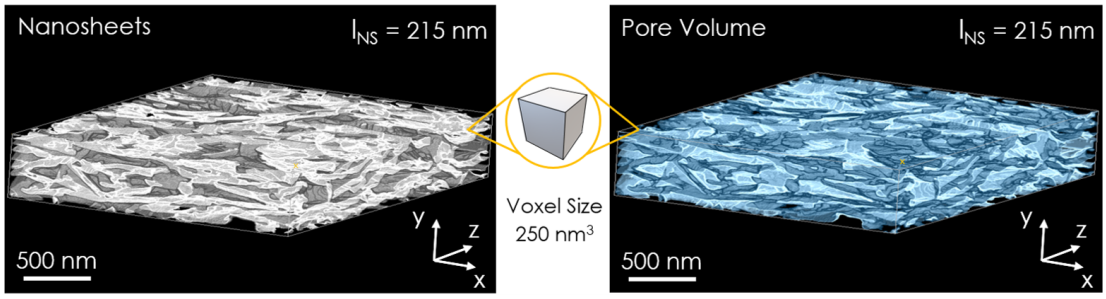

Figure 8.7: Segmented Nanosheet & Pore Volumes: Reconstructed volumes of the l_{NS} = 215 nm network following classification showing the segmented nanosheet (white) and pore volume (blue) contributions. The voxel size in each classified volume is 250 nm^3.

Each voxel in this volume is then tagged with a number, with all of the voxels in a given pore having the same tag. Any voxel missing at least one of its nearest neighbours is defined to be at the edge of a pore. Crucially, this requires no *a-priori* knowledge of the pore dimensions and unlike techniques such as BET is scale invariant. Once this operation is completed the pore dimensions can be measured by counting the constituent or edge voxels for each of the tagged pores. As this is performed on a voxel-by-voxel basis, this process theoretically has a resolution on the order of $\sim$ 250 nm^3, however, this is contingent on accurate segmentation and binarisation.

The porosity was found for each sample by summing every voxel in the network volume that was tagged as a pore and dividing it by the total number of voxels. This is plotted as a function of l_{NS} for each of the graphene networks in Fig. 8.8A. The porosity values of 40 - 50 % found here are in broad agreement with values of 40 - 70 % reported for vacuum filtered and printed nanosheet networks using weighing, BET and MIP. [191,352,424] Though primarily intended as demonstration of the FIB-SEM NT technique, the nanosheet length in a sprayed coated network can be seen to have a clear effect on its porosity in Fig. 8.8A. The network porosity is seen to fall with decreasing nanosheet size, from 49 $\pm$ 2 % for the network of 947 nm long nanosheets to 40 $\pm$ 2 % for the l_{NS} = 215 nm network (the error estimates are based on the OOB error from the segmentation process).

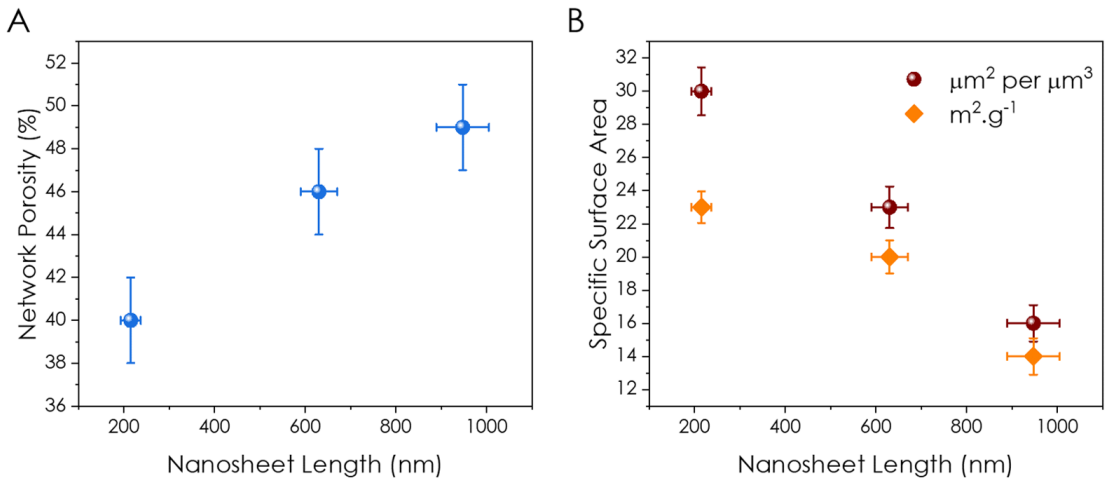

Figure 8.8: Network Porosity & Specific Surface Area: Plots of the **A)** Porosity and **B)** Specific surface area of the printed nanosheet networks as a function of nanosheet length, l_{NS}.

Significantly, this decrease in porosity as l_{NS} is reduced correlates to an increase in the in-plane conductivity from $\sim$ 800 to 3000 Sm^{-1} over the same l_{NS} range, as measured in Chapter 7. This may be due to packing effects, whereby larger and thicker nanosheets are more rigid and jam when packed. Smaller and more thin nanosheets are more mechanically flexible and may conform to each other more favourably.[481] This would both reduce the porosity and improve the nanosheet interface quality.

That the network porosity can be tailored by altering the size of the constituent nanosheets may not seem surprising, however, it has not been reported to this point. Indeed, the network porosity is rarely quoted in many of the available publications. This preliminary data suggests that size-selecting nanosheets prior to deposition offers a potential means to tailor the porosity of printed 2D networks. When compared with techniques such as phase inversion or post-deposition mechanical treatments, this could offer drastically reduced procedural complexity.[213,482] A reduction in porosity with decreasing l_{NS} would be expected to have implications for printed 2D networks beyond conductivity enhancement. Decreases in network porosity would potentially reduce the prevalence of pinholes in

vertically stacked devices, which will be discussed in a coming section. While it would be premature to describe any trends based off such a limited dataset, these initial results both demonstrate the viability of FIB-SEM NT for porosity measurements on 2D networks, while outlining a potential means to tune their morphological properties.

8.4.2 Specific Surface Area

The specific surface area of the printed networks is plotted as a function of nanosheet length in Fig. 8.8B. The total pore surface area is measured by summing the number of voxels that have at least one of its nearest neighbours in contact with the background (i.e. nanosheets). This can then be related to the volume or mass of the network to calculate the specific surface area, as shown in Fig. 8.8B. Again, though the dataset is limited, it is clear that the network specific surface area increases as the constituent nanosheet dimensions are reduced, growing from 14 ± 1 $m^2\,g^{-1}$ for the network of largest nanosheets to 23 ± 1 $m^2\,g^{-1}$ for the $l_{NS} = 215$ nm network (*cf.* graphite ~ 0.6 $m^2\,g^{-1}$).[483] The data is also represented geometrically in Fig. 8.8B, where the accessible nanosheet area is given as a function of sample volume, showing a similar length dependence. This is in agreement with reports that propose the specific surface area of a nanosheet network will scale inversely with nanosheet thickness.[484] Furthermore, a reduction in nanosheet thickness can reduce its rigidity, leading to phenomena such as nanosheet bending or crumpling, which are known to increase the network specific surface area.[484]

Reported values for the specific surface area of printed nanosheet networks are limited. However, a range of specific surface areas in the region of 10 - 10^2 $m^2\,g^{-1}$ have been published for networks created through a variety of other deposition techniques. Vacuum filtered networks of LPE graphene ($l_{NS} = 260$ nm, $t_{NS} \sim 8$ monolayers) have been recently reported with specific surface areas in the 30 - 60 $m^2\,g^{-1}$ range, as measured by both BET and MIP.[424] Nicolosi *et al.* measured the specific surface

area of a sprayed film of LPE vanadium oxide nanosheets to be 25 $m^2\ g^{-1}$, which is in close agreement with the values for sprayed graphene networks presented here.[485] This reduction in available surface area from theoretical values of 2600 $m^2\ g^{-1}$ for graphene is likely due to severe restacking of nanosheets when deposited, reducing the accessible surface area of the network.[486]

8.4.3 Pore Connectivity

Though porosity is an important network parameter, the nature of the pore volume is equally, if not more, significant. The pore connectivity determines the amount of nanosheet surface area that is accessible for gas sensing or catalysis,[487] while for battery and supercapacitor applications it can determine the degree of electrolyte infiltration and ion kinetics.[488] In excess of 1000 pores were identified and characterised in each of the three samples studied. Interestingly, it was found that the pore volume in each network was dominated by a single, contiguous macropore spanning the entire volume. While it has been reported that the pore volume in 2D networks is dominated by such open pores,[424] more than 99 % of the entire pore volume was found to be contained in a single pore for each of the studied networks. Considering an isolated cross-section, as in Fig. 8.2, it is clear that isolated pores exist independently of each other. This suggests that there is a minimum sample depth (number of interpolated network slices) or volume at which the individual pore chambers connect to each other.

To investigate this, each network was broken down into distinct sections and analysed. Starting with a single network cross-section the sampled volume was increased in 10 nm increments by adding sequential slices, given by the sample depth, z. The dominant pore fraction, γ_p, was then measured for each volume. This parameter represents the fraction of the total pore volume contained in the largest pore. The process is shown schematically in Fig. 8.9 using the $l_{NS} = 215$ nm network, where each isolated pore is assigned a different colour. As the network volume is increased by adding network slices

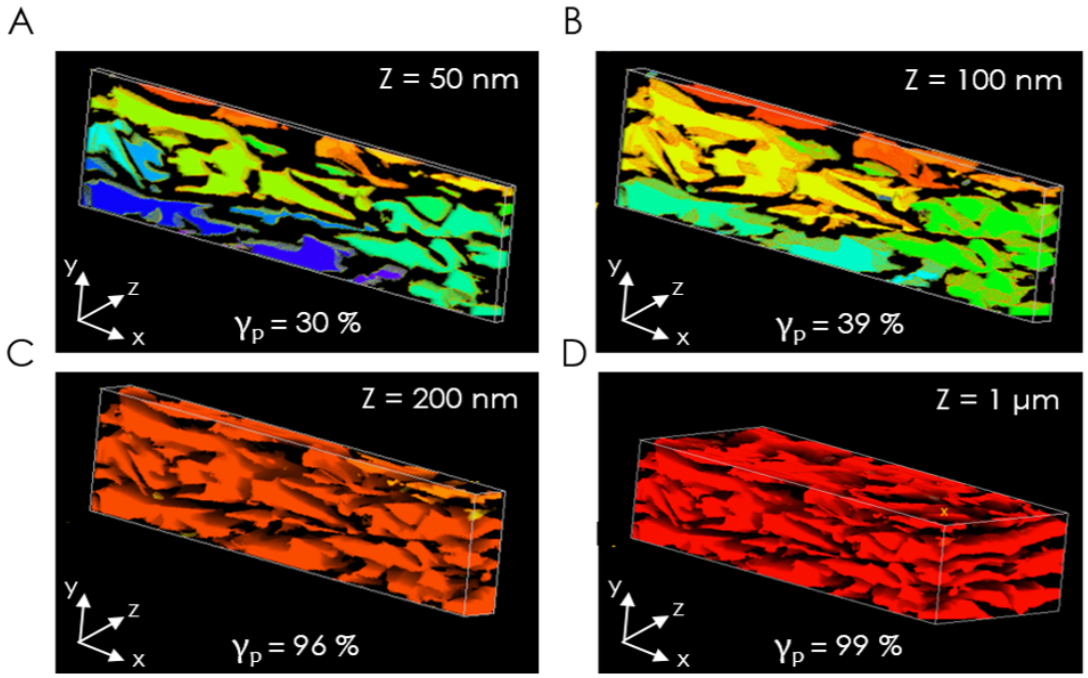

Figure 8.9: Pore Connectivity: Reconstructed pore volume for the $l_{NS} = 215$ nm network at depths of **A)** 50 nm, **B)** 100 nm, **C)** 200 nm and **D)** 1 μm. In each image the sampled volume is increased by adding 10 nm thick cross-sections in the z-direction. Each individual pore is marked by a different colour and for each network volume the fraction of the total pore volume contained within the largest pore is given by the dominant pore fraction, γ_p.

in the z-direction, isolated pores are seen to coalesce into a single contiguous monochrome volume. This corresponds to an increase in dominant pore fraction γ_p from 30 % for a 50 nm thick section to 96 % for a 200 nm deep network section. At a depth of $z = 1$ μm the network pore volume is clearly dominated by a single continuous red pore, shown in Fig. 8.9D. As the network cross-sectional area was kept fixed in the xy-plane, this implies that there is a sample depth where the individual pores coalesce and connect to each other.

To quantify this "connectivity length", the dominant pore fraction was plotted as a function of sample depth for each network in 20 nm increments. This is shown for the $l_{NS} = 215$ nm network in Fig. 8.10A, where each line (A-D) is taken from a different region in the sample. Here, γ_p is seen to

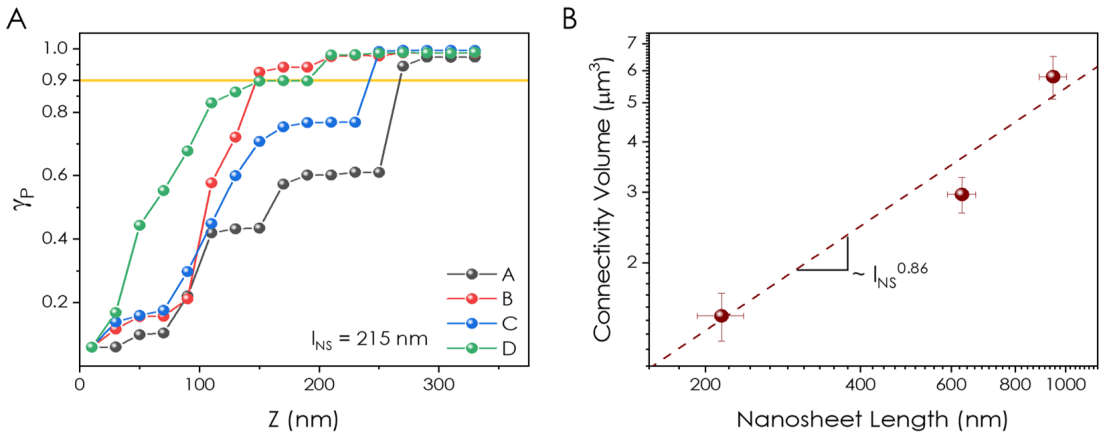

Figure 8.10: Dominant Pore Fraction, γ_P: A) Plot of the dominant pore fraction, γ_P, as a function of network depth for the $l_{NS} = 215$ nm network. The solid line marks where γ_P first reaches 90 % for each sample. **B)** Plot of the connectivity volume for each network. This is the average minimum sample volume for each network where 90 % of the total pore volume is contained in the dominant pore.

increase asymptotically towards 1 as the sample depth is increased. However, the difference between the trends across the sample would suggest that these networks are not homogeneous. This is an important result. Further, the plateaus in γ_P followed by significant increases are interesting. This implies that in these network sections the pore volume is dominated by 2 distinct macropores, which at some depth combine to give the huge increases in γ_P shown in Fig. 8.10A.

The depth at which 90 % of the total pore volume was found to be contained in this dominant pore is marked by the solid line in Fig. 8.10A, and was in the region of 200 - 400 nm for each of the networks studied. More generally, this can be expressed as a minimum connectivity volume, which is plotted as a function of nanosheet length in Fig. 8.10B. This was found to be on the order of a few μm^3 for each of the networks measured, increasing from $\sim$ 1.5 μm^3 to $\sim$ 6 μm^3 going from the $l_{NS} = 215$ nm network to the $l_{NS} = 947$ nm network. Again, while this is primarily a demonstration of the morphological insight FIB-SEM NT can provide, this initial data suggests that the pore volume in printed 2D networks exhibits some dependence on nanosheet dimensions. Furthermore, the pore volume is

found to dominated by an accessible and contiguous macropore comprised of many interconnected chambers. Work to assess the validity of these findings, and build upon them, will hopefully further contribute to our understanding of these networks.

8.4.4 Pore Size and Shape

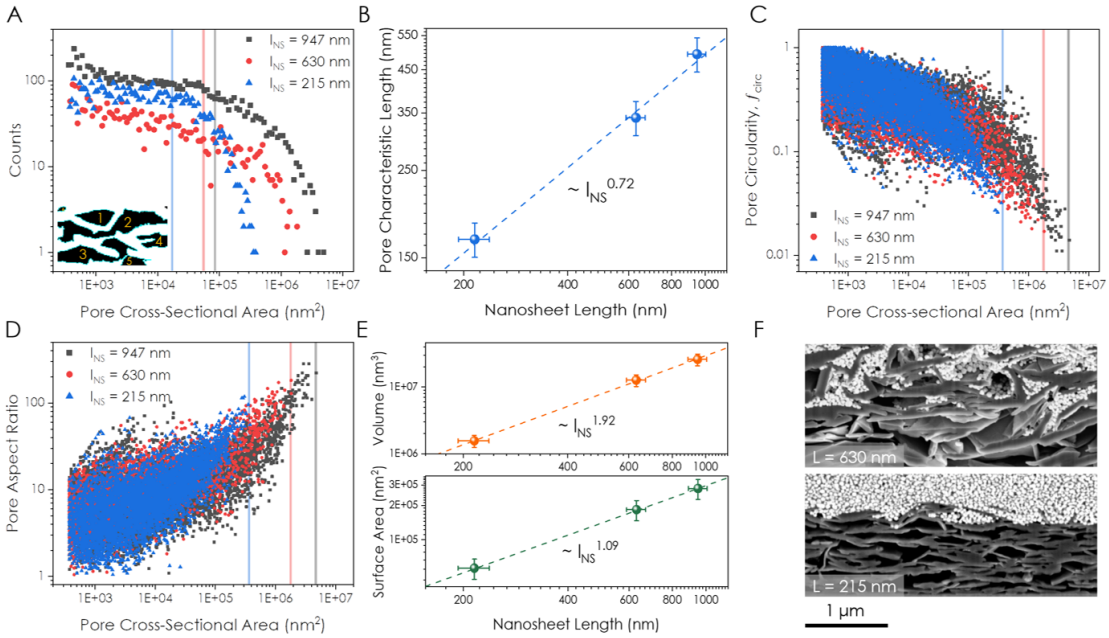

Figure 8.11: Length Dependent Pore Morphology: A) Pore cross-sectional area distributions for each network. The mean area for each is marked by a solid coloured line. Inset: Pore identification. **B)** Plot of the characteristic pore length for each network. **C)** Pore circularity and **D)** Pore aspect ratio versus pore cross-sectional area for each network. The solid vertical lines mark the largest pore area measured for each network. **E)** Approximated mean pore volume and surface area as a function of nanosheet length. **F)** SEM images showing the infiltration of silver nanoparticle top electrodes for the $l_{NS} =$ 630 nm and 215 nm networks.

Due to the contiguous nature of the network pore volume, 3D pore size and shape distributions would be unrepresentative as most of the volumetric information is contained in a single data point. However, this open pore is comprised of thousands of interconnected chambers of different size and shape. By breaking the network up into its 2D cross-sections, it is possible to assess the geometric properties of these chambers and evaluate how they change with nanosheet size. For each network,

a cross-section was taken every 100 nm through the volume and the pore chambers were analysed in two-dimensions. As with the volumetric analysis, this was done on a pixel-by-pixel basis to measure the cross-sectional area, perimeter and shape of each pore chamber in a network slice. Individual pores were found, numbered and outlined, as shown in the inset of Fig. 8.11A. This allows the connected nature of the pores to be circumvented and the properties of the pore chambers can be assessed.

The frequency distributions of pore cross-sectional area are shown for each network in Fig. 8.11A and exhibit a decrease in frequency as the pore size is increased. This suggests that the network pore volume is comprised of a large number of reasonably small pore chambers, with the dominant contribution being made by a few extensive caverns. The mean pore cross-sectional area for each network is marked by a solid line in Fig. 8.11A and can be seen to fall as l_{NS} is reduced. This is likely due to a combination of packing effects and scaling with nanosheet dimension.[481] Such a decrease in the mean chamber cross-sectional area, from ~ 86000 nm^2 for the $l_{NS} = 947$ nm network to ~ 17000 nm^2 for the $l_{NS} = 215$ nm network, would be expected to have significant implications for the network as a whole. To highlight this length dependent effect, the average pore characteristic length is plotted as a function of nanosheet length in Fig. 8.11B. This parameter is given by the square root of the pore cross-sectional area and is seen to increase with nanosheet length to the power of ~ 0.72. That this parameter increases from ~ 167 nm for the $l_{NS} = 215$ nm network to ~ 493 nm for the $l_{NS} = 947$ nm sample is an interesting result. While more data is clearly needed to draw any meaningful conclusions, this further adds to the narrative that the network morphology is dependent on nanosheet dimension.

The shape of the pore chambers is another quantity of interest. The pore circularity, f_{circ}, is a dimensionless parameter that measures how close in form a given pore is to a circle, and is plotted as a function of its cross-sectional area in Fig. 8.11C. Circularity is defined by $f_{circ} = (4\pi A) \,/\, \left(P^2\right)$, where A and P are the measured area and perimeter of the pore. As a perfect circle is defined by $f_{circ} = 1$,

any values below this suggest that the pore shape is deviating into irregular geometries. The general trend shown by each network in Fig 8.11C is that as the pore size increases, the pore chamber cross-section deviates from circular to irregular and extended shapes. While the circularity can be directly calculated from the images, a less abstract parameter is the pore aspect ratio, k. By approximating each pore as a rectangle, the pore aspect ratio can be calculated using only the circularity where $k = (-2f_{circ} + \pi + \sqrt{\pi^2 - 4\pi f_{circ}})/2f_{circ}$. The approximated pore aspect ratio is plotted against its cross-sectional area in Fig. 8.11D and shows k to increase with the size of the pore chamber. This is simply the inverted trend shown for circularity in Fig. 8.11C, but shows that as the pore size is increased the chambers become more elongated. Furthermore, the majority of pores in Fig. 8.11D exhibit aspect ratios larger than 1, which suggests that the chamber cross-sections have slit-like openings. This is in agreement with BET measurements on vacuum filtered graphene networks.[424] To emphasise the effect of nanosheet length on the network properties, the largest pore for each network is marked by a solid line in Fig. 8.11C & D. This shows that the maximum pore size decreases as nanosheet length is reduced. Furthermore, it can be seen that the shape of the most extreme pores in each network become more irregular as nanosheet length is increased.

By taking each individual pore and rotating it about one of its axes, this two-dimensional data can be used to approximate how the volume and surface area of these chambers may scale with nanosheet size. This is described in detail in Appendix A.6, but briefly, each pore is modelled as an ellipse of equivalent surface area to the measured value from Fig. 8.11A. The major and minor axes of the equivalent ellipse are also forced to match the measured height and width of the pore as closely as possible. By then rotating each ellipse about its major-axis both the surface area and volume of revolution for each pore chamber can be approximated, as shown in Fig. 8.11E. Here, both the average volume and surface area of the modelled pore chambers exhibit power law increases with nanosheet length, scaling with

l_{NS} to the power of ~ 1.92 and ~ 1.09 respectively. This corresponds to $\sim 16\times$ and $\sim 5\times$ increases in both chamber volume and surface area with a corresponding ~ 4-fold increase in l_{NS}. While further data is needed, this again shows the pore dimensions to scale with l_{NS} in these networks.

These length-dependent changes in the network pore volume are of particular relevance to printed heterostacks. A significant problem in printed nanosheet networks is the presence of pinholes, which lead to electrical shorting in vertically printed devices.[489] The porosity data in Fig. 8.8A, coupled with the results in Fig. 8.11A-E, suggests that printed networks comprised of larger nanosheets are more open. To test this from a device perspective, silver nanoparticle ($\sim$ 50 nm diameter) top electrodes were aerosol jet printed onto the 630 nm and 215 nm networks. As shown in Fig. 8.11F, the nanoparticles penetrate up to 1.3 μm into the $l_{NS} = 630$ nm sample. This is clearly an issue for printed vertical heterostacks where the benchmark thickness for discrete layers is 100 - 500 nm. By using nanosheets or nanoplatelets in place of nanoparticles the potential for electrical shorting can be mitigated.[489] However, even in purely 2D systems shorting between conductive layers remains a major issue for intermediate layers that are $\leq$ 500 nm thick.[422] Interestingly, the network comprised of 215 nm long nanosheets shows minimal incorporation of Ag nanoparticles. Coupled with the data in Fig. 8.11A-E, this suggests that printed networks of smaller nanosheets form more densely packed and pinhole-free networks, which presents a simple and effective means to improve printed device performance.

8.4.5 Nanosheet Alignment

The alignment of nanosheets within a network influences many of its resultant properties. It is known that well-aligned networks lead to enhanced basal plane overlap between nanosheets, which improves the network conductivity,[308] mechanical properties,[490] and lithium storage capabilities.[491] To this point, the alignment of these disordered networks has been evaluated using techniques such as small-

angle x-ray scattering (SAXS) and single FIB-SEM cross-sections. These techniques assess either the ensemble or a single image, respectively.[492] However, by applying fast Fourier transforms (FFT) to slices throughout the image stack, the network alignment can be assessed both locally and globally.

The FFT process works by taking the spatial pattern represented by grey values in each pixel of a network cross-section, $f(i,j)$, and converts them into direction-dependent frequency components in the Fourier domain, $F(k,l)$. This technique was initially employed to measure the alignment of electrospun biological fibres,[493] but has recently been applied to mechanically compressed graphene networks.[213] Each 2D slice in the network is initially divided into square sections of $N \times N$ pixels. The Fourier power spectrum for each is then calculated by transforming to the spatial frequency domain according to Eqn. 8.1. This is performed using the *Directionality* module in *ImageJ*. Representative cross-sectional images of each of the analysed network volumes are shown in Fig. 8.12A-C.

$$F(k,l) = \frac{1}{N^2} \sum_{i=0}^{N-1} \sum_{j=0}^{N-1} f\left(i,j\right) e^{-i2\pi(ki/N + li/N)} \tag{8.1}$$

The generated frequency plot can be used to assess the directionality and alignment of objects in the spatial domain image. A representative FFT frequency plot for the $l_{NS} = 947$ nm network is shown in Fig. 8.12D. Low frequency pixels are placed at the centre of the plot and correspond to domains in the real image that contain pixels of similar intensity values. The majority of this information originates from the overall shape and background of the spatial domain image and is known as the DC component, $F(0,0)$.[494] High-frequency pixels are radially distant from the centre and correspond to regions in the spatial domain that exhibit abrupt changes in pixel intensity, such as edges and features. Structures with a preferred orientation in the original image generate high intensity values that are clustered along the highest degree of directional anisotropy in the FFT power spectrum. This results

in lines of increased intensity through the origin in the frequency plot. The direction of these intensity bands are shifted by 90 ° with respect to the original image.

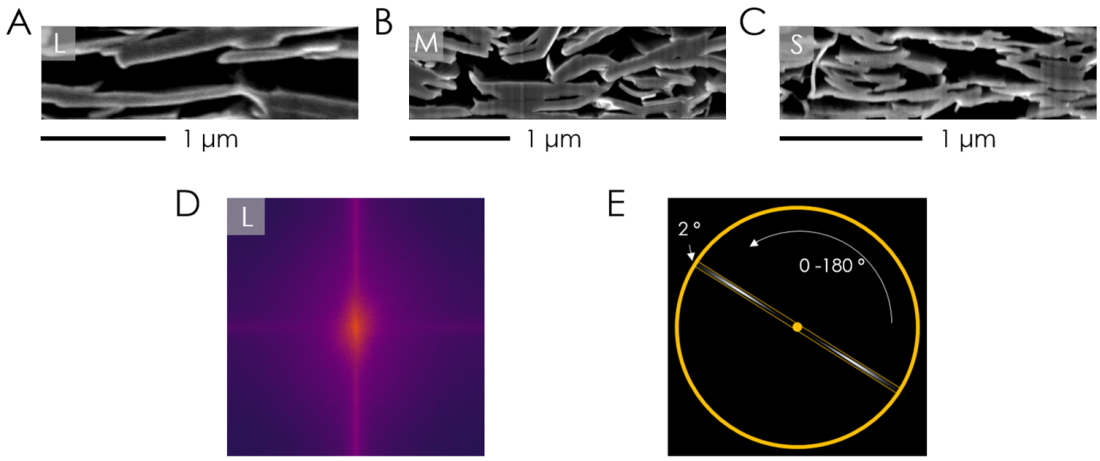

Figure 8.12: FFTs of Network Cross-sections: A-C) Representative SEM cross-sections of the l_{NS} = 947, 630 and 215 nm networks. **D)** FFT frequency plot of a cross-sectional image from the l_{NS} = 947 nm network. **E)** Schematic showing the principle of the angular filter used to assess the nanosheet alignment in each network cross-section.

The frequency spectrum shown in Fig. 8.12D demonstrates a clear vertical band of intensity, which suggests that the nanosheets are primarily aligned in the plane of the film. This corresponds to 0 ° or the horizontal direction in the SEM images. An angular filter can be applied to the generated frequency plot to quantitatively assess the directionality of objects in the spatial domain image.[495] This filter is comprised of a circular projection on the frequency plot, as shown in Fig. 8.12E. Here, the entire image is covered except a 2 ° wide band that spans its diameter. The total pixel intensity contained in this 2 ° slice is found in each instance as it is swept from 0 – 180 ° in 2 ° increments. The process is shown schematically in Fig. 8.12E. By plotting the total intensity measured for each 2 ° band as a function of angle from 0 - 180 ° an alignment plot can be generated for each network cross-section. Areas of increased intensity in the frequency domain image will have a greater summed intensity when compared to the background. These regions will appear as peaks in the 2D FFT alignment plot. A

tall and narrow peak (reduced FWHM) represents a more uniform degree of alignment about a given angle, while a broad peak or shoulder indicates that more than one axis of alignment may be present. FFT alignment plots for each of the networks are shown in Fig. 8.13A - C. The distributions were generated by calculating the directionality of network cross-sections in 50 nm increments, or every 5 slices, through the volume. The angular intensity values for each individual slice are shown (grey squares), while the average intensity across the entire network for each angle is denoted by the red spheres. The averaged intensity distribution for each network was then fitted with a Cauchy-Lorentz distribution of the form

$$y = y_0 + \frac{2A}{\pi}\left(\frac{w}{4\left(x - x_0\right)^2 + w^2}\right) \tag{8.2}$$

where x_0 represents the angle corresponding to the peak of the distribution or primary axis of alignment and w is the FWHM of the peak. The networks in Fig. 8.13A - C were found to be primarily oriented in the plane of the film, with each distribution centered on ~ 0 °. However, by using the FWHM of each peak to quantify the network alignment, these initial measurements imply that the size of the constituent nanosheets plays a role. The results are summarised in Fig. 8.13D where spray-coated networks of larger nanosheets are seen to exhibit enhanced alignment in the plane of the film. The $l_{NS} = 947$ nm network displays a FWHM about its primary axis of alignment of 33 ± 1 °, while the dispersion of the $l_{NS} = 215$ nm network is 125 % this value with a FWHM of 41 ± 1 °. Though the network of $l_{NS} = 630$ nm nanosheets broadly agrees with this trend of increased alignment with nanosheet size, the distribution is not as clean as reflected by the increased fitting error.

A trend of enhanced alignment with increasing nanosheet length has been reported for solution-processed networks of graphene oxide (GO). GO sheets with increased aspect ratios are known to pref-

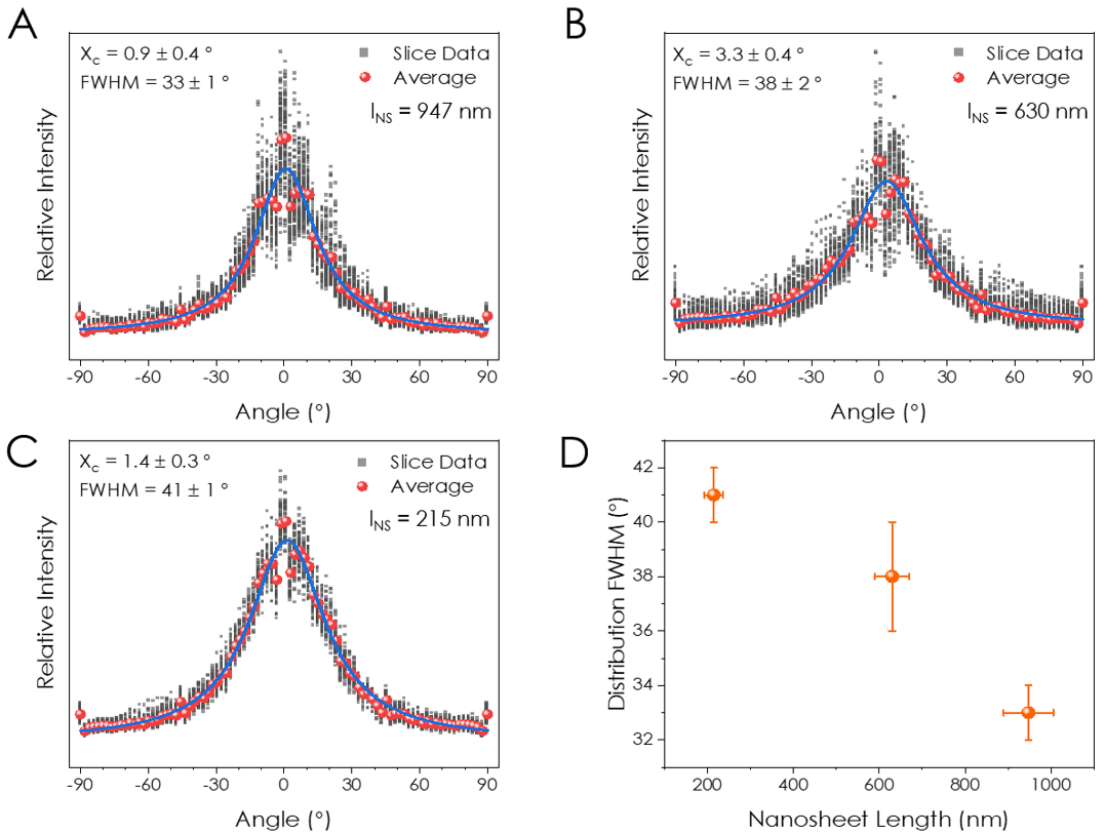

Figure 8.13: Length Dependent Network Alignment: A-C) FFT angular intensity distributions for the $l_{NS} =$ **A)** 947 nm, **B)** 630 nm and **C)** 215 nm nanosheet networks. The grey squares represent the data for each slice in the network. The red spheres represent the average intensity across the entire network for each angle. The blue line is a fit of Eqn. 8.2 to the average intensity data. **D)** Plot of the distribution FWHM as a function of constituent nanosheet length to quantify the network alignment.

erentially align parallel to the GO basal plane in solution, leading to enhanced alignment in prepared GO papers.[496] Furthermore, Lin *et al.* propose that the alignment and stacking behaviour of GO sheets of different sizes is driven by their aspect ratio, which facilitates improved alignment through excluded volume interactions as it is increased.[464] Indeed, the authors employed the FFT technique described here on vacuum filtered GO papers of different nanosheet sizes, finding the network alignment to increase with GO nanosheet size. However, this analysis was performed using only a single image from each network. As shown in Fig. 8.13A - C, there is considerable variability in the align-

ment data from slice to slice (grey squares) in a given network. This alludes to the inhomogeneity of these networks and suggests that single cross-sectional images may not be sufficient to characterise the alignment of a network. Furthermore, both of these studies were performed on ultra-large GO nanosheets that were either vacuum filtered or drop-cast. Spray coating is a more dynamic process and the nanosheets used in this work are an order of magnitude smaller. Though it is almost a truism that larger nanosheets lead to improved network alignment, when the porosity data is factored in this is an interesting result. The $l_{NS} = 215$ nm network exhibits the lowest network porosity, but the largest dispersion about its primary axis of alignment. This may be attributed to the increased conformity of the smaller and thinner nanosheets,[481] which leads to a reduction in the network porosity while increasing their angular dispersion. However, the results presented here are only preliminary and subsequent measurements will need to be made. Most importantly, this work serves to demonstrate the potential of FIB-SEM NT for the quantitative characterisation of nanosheet networks.

8.5 Conclusions

In this chapter, FIB-SEM NT has been presented as novel means to characterise the morphology of nanostructured networks. Nanosheet network volumes of 22, 31 and 127 μm^3 were reconstructed by serial milling and imaging of 10 nm thick network cross-sections in a FIB-SEM microscope. These volumes were then segmented into their nanosheet and pore components for quantitative analysis using trainable machine learning. Methods to comprehensively assess network properties such as porosity, specific surface area and nanosheet alignment were then presented and applied to the reconstructed volumes. This was demonstrated through an initial study of three printed graphene networks, each comprised of nanosheets of different dimensions ($l_{NS} = 947$, 630 and 215 nm).

The porosity of the printed graphene networks was found to steadily decrease from 49 $\pm$ 2 % to 40 $\pm$ 2 % as the constituent nanosheet length was reduced from 947 nm to 215 nm. Notably, the pore volume in these networks was found to be highly contiguous, with $>$ 99 % of the total pore volume contained in a single open pore. A reduction in nanosheet size was seen to increase the specific surface area of the printed networks from 14 $\pm$ 1 $m^2 g^{-1}$ to 23 $\pm$ 1 $m^2 g^{-1}$ going from the largest to smallest nanosheets. Interestingly, both pore shape and size were found to be a function of nanosheet length. Here, a network of $l_{NS} = 947$ nm nanosheets exhibited a mean pore cross-sectional area that was $\sim 5\times$ as large as the value found for the $l_{NS} = 215$ nm network. Finally, the directionality and alignment of each nanosheet network was evaluated using fast Fourier transforms, where it was found that networks comprised of larger nanosheets demonstrated enhanced alignment.

This chapter is primarily a demonstration of the FIB-SEM NT technique for characterisation of 2D networks, with a focus on developing quantitative methods to assess the network morphology. Crucially, the results presented here are only a prelude to the morphological information this approach may provide going forward. Though preliminary, some of the initial length-dependent findings are of considerable interest from a network optimisation and applications standpoint, which attests to the significant potential of this technique.

And following our will and wind

We may just go where no one's been

We'll ride the spiral to the end

And may just go where no one's been

Spiral out, keep going.

9

Conclusions & Future Work

While the stratospheric rise of 2D materials has catalysed research at a frenetic pace, the remarkable properties of nanosheets and their networks remain largely restricted to the lab at present. To make the transition to widespread device applications the ability to characterise and tailor the properties of these networks will be prerequisite. This is no small-undertaking. However, if the pace of progress over the last decade is any indicator, it is conceivable that 2D networks will begin to deliver state-of-the-art applications in the coming years. This work hopes to make a small contribution by investigating some of the fundamental properties of these systems.

While 2D networks are promising materials for electrochemical applications, their performance is limited by mechanical instabilities. Enhanced electrical and mechanical performance has been realised through nanotube addition. However, a quantitative study of reinforcement with nanotube volume fraction, φ, had yet to be performed. In this work, the mechanical and morphological properties of 1D:2D nanocomposites were investigated using a model SWNT:MoS_2 system. These composites were found to comprise disordered networks of nanotubes and nanosheets, exhibiting φ-invariant porosities of $\sim$ 56 %. The reinforcing 1D network was found to evolve from loosely connected bundles at low-φ, to an entangled and fibrous architecture for $\varphi > 1$ vol %. This morphological transition transforms the mechanical properties of the composites. Below 1 vol % the composite modulus and failure-strain exhibited short-fibre composite behavior, while both increased in a manner consistent with fibrous networks for $\varphi > 1$ vol %. The composite tensile strength similarly evolved from a regime limited by the matrix-fibre interface at low-φ, to one limited by the strength of the nanotube ropes for $\varphi > 1$ vol %. Significantly, while the composite tensile toughness was constant at low-φ, it was found to increase rapidly for $\varphi > 1$ vol % consistent with percolation theory. Compared to the 2D matrix, addition of 5 wt % SWNTs led to increases in the composite modulus, strength, and toughness by factors of $\sim$ 55, 70, and 10, respectively. These increases transform the properties of the material, rendering it mechanically robust and suitable for a range of applications.

Owing to the unique geometry and diverse electronic properties of their constituent nanosheets, 2D networks are similarly well-placed to feature in the field of printed electronics. Although it is known that electrical performance in 2D networks is limited by inter-nanosheet junctions, work to characterise this effect has been limited. To begin to address this, the electrical conductivity of an array of printed nanosheet networks was investigated as a function of constituent nanosheet length, l_{NS}. By modulating l_{NS} the character and quantity of interfacial junctions, as well as intrinsic nanosheet

properties, can be altered. A family of size-selected WSe_2, graphene and silver 2D inks, each spanning an order of magnitude in l_{NS}, were produced using liquid cascade centrifugation and characterised. The in-plane conductivity of spray-coated WSe_2 networks was observed to decrease by an order of magnitude as l_{NS} was reduced from 462 nm to 62 nm. Interestingly, the conductivity of both graphene and silver nanoplatelet networks was found to exhibit the opposite response, scaling with ${l_{NS}}^{-1}$. As l_{NS} was reduced from $\sim$ 1 µm to 100 nm the printed network conductivity was found to increase by a factor of $\sim$ 10 for both materials. While these trends are of considerable interest in their own right, a model to describe this length-dependent conductivity scaling in printed 2D networks was developed. By considering the interplay of the intra- and inter-nanosheet resistances in each network, this model predicts the diverse electrical behaviours observed experimentally. Crucially, it also presents a framework for network optimisation. Inter-nanosheet resistances of $\sim$ 9 Ω, 31 kΩ and 120 MΩ were approximated for silver, graphene and WSe_2 nanosheets, respectively.

By studying charge transport in printed 2D networks the influence of morphology on network performance became highly apparent. If these systems are to deliver on their applications potential the ability to characterise and tailor their morphological properties will be essential. A possible means to address this is provided though FIB-SEM nanotomography. By milling and imaging huge numbers of consecutive network cross-sections a 2D image stack can be reconstructed into a high-fidelity 3D volume for analysis. The viability of this technique was demonstrated through an initial length-dependent investigation of printed graphene networks for $l_{NS} = 947$, 630 and 215 nm. The network porosity was found to steadily decrease from $\sim$ 49 % to $\sim$ 40 % as the constituent nanosheet length was reduced from 947 nm to 215 nm. Interestingly, the pore volume in each network was found to be highly contiguous, with $>$ 99 % of the total pore volume contained in a single open pore. As l_{NS} was reduced from 947 to 215 nm the specific surface area of the printed networks was seen to increase

from $\sim 14\ m^2\ g^{-1}$ to $\sim 23\ m^2\ g^{-1}$. Notably, both pore shape and size were found to be a function of nanosheet length. The network of $l_{NS} = 947$ nm nanosheets exhibited a mean pore cross-sectional area that was $\sim 5\times$ as large as the value found for the $l_{NS} = 215$ nm network. Finally, the alignment of each nanosheet network was evaluated using fast Fourier transforms, where printed traces comprised of larger nanosheets demonstrated enhanced alignment.

Mechanical Reinforcement of Nanosheet Networks

The work presented in Chapter 6 demonstrated reinforcement of 2D networks at SWNT additive levels as low as 2 - 5 wt %. This compares favourably with polymer binders, which are often required in larger amounts and have been shown to have a deleterious effect on both electrical transport and storage capability. Indeed, 1D:2D battery electrodes comprised of SWNTs and GeS nanosheets have recently displayed state-of-the-art lithium storage capacities of 1523 mAh g^{-1} (*cf.* Graphite $\sim$ 370 mAh g^{-1}).[270] Crucially, this mechanical enhancement is not limited to conducting SWNTs. Vacuum filtered 1D:2D nanocomposites comprised of insulating 1D boron nitride nanotubes (BNNTs) and 2D BiOCl nanosheets have demonstrated similar reinforcement effects, though this work is ongoing. An interesting study would be to investigate composite 1D:2D BNNT:BiOCl inks for printed traces. Any reinforcement similar to the vacuum filtered nanocomposites would be significant. More robust networks would likely prevent redispersion in thin BiOCl layers and reduce the minimum required thickness for printed dielectric layers. This would translate to immediate improvements in vertically printed devices, such as 2D capacitors. Furthermore, the effect of these fibrous networks on the 2D network morphology could be observed using a conductive 2D material and BNNTs. By performing electrical tests and FIB-SEM NT on comparable networks with and without BNNTs, the effect of these 1D binders on the network conductivity and morphology could be discerned.

As the era of the "internet of things" descends, the ability to selectively engineer and optimise printed 2D networks will be vital. The conductivity data and model presented in Chapter 7 aims to contribute to our understanding of printed LPE nanosheets. However, considerable work remains to be done. Experiments to expand the data set for both graphene and AgNPs are currently underway. Further, it will be necessary to perform measurements on additional materials to both expand the scope of the study and further evaluate the model. Work to address this is currently ongoing with printed WS_2 networks. This would extend the study to encompass a range of network conductivities that spans from $\sim 10^{-5}$ Sm^{-1} for WS_2 to $\sim 10^{6}$ Sm^{-1} for AgNPs.

It will be important to independently verify network properties predicted by the model. Terra-Hertz (THz) spectroscopy on sprayed traces will allow the nanosheet mobility to be directly measured. Similarly, thin-film transistor measurements will enable both the network mobility and carrier density to be extracted as a function of nanosheet length for the semiconducting networks. Recent work by collaborators and Yanase *et al.*[497] has shown that annealing 2D TMDs in the presence of selenium / sulfur leads to improved network conductivity and vacancy healing. Thus, it would be interesting to determine the effect of doping on the length-dependent conductivity in semiconducting networks. Finally, with an optimised method to produce size-selected 2D inks established, a study on the out-of-plane conductivity of these printed networks would be of significant interest. This would further inform our understanding of charge transport in these systems, while being of immediate relevance to printed device applications.

Morphology of Nanosheet Networks

The work presented in Chapter 8 is in its nascent phase and additional experiments are underway to build upon it. The values for network porosity, pore-connectivity and nanosheet alignment are in broad agreement with published values for similar networks analysed using independent techniques. However, it will be crucial to provide a direct comparison. This will be performed through a comparative porosity study using mercury intrusion porosimetry (MIP). As MIP requires sample volumes far beyond the scope of printed traces (> 100 μm thick), this will be achieved using filtered graphene networks. Similarly, it will be important to test and compare FIB-SEM NT to other techniques such as x-ray computed tomography and scanning confocal microscopy. These large-area characterisation techniques may compliment the high-resolution information provided by FIB-SEM NT.

Experiments are underway to bolster the length-dependent graphene data presented in Chapter 8. Any trend in properties such as porosity or nanosheet alignment with l_{NS} would make a significant contribution to our understanding of these systems and illuminate pathways to optimisation. Printed graphene networks of different nanosheet length are in preparation to build upon the initial results presented. This will also compliment the length-dependent conductivity study in Chapter 7 and inform the network conductivity model. In addition, it will be interesting to assess deposition-driven morphological effects. Such an investigation would involve characterising thin-films deposited from the same ink using an array of printing techniques including AJP, IJP, spray-coating and screen-printing. Finally, it will be essential to expand the scope of this technique beyond conductive materials to assess semiconducting nanosheets and their devices. While this is a non-trivial problem, protocols for FIB–SEM NT of soft, porous, and poorly conducting materials have recently been reported.[498]

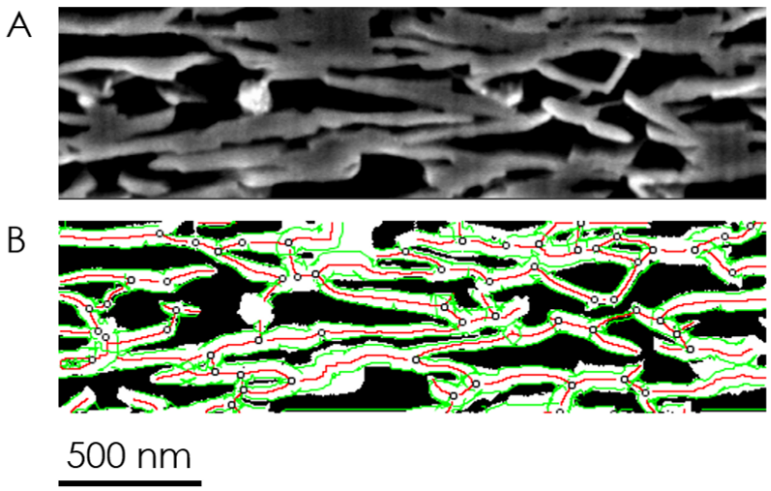

Figure 9.1: Ridge Detection Algorithm: A) Cross-sectional SEM image of the $l_{NS} = 215$ nm network. **B)** Binarised image with a ridge detection algorithm applied. Junction nodes are given by circles, nanosheet contours are marked by red lines, while their thicknesses are estimated by the green lines.

Future work will focus on nanosheet connectivity in 2D networks. This would allow current paths and their junctions to be both visualised and quantified. A simple example of this is shown in Fig. 9.1, where a ridge detection algorithm is applied to a 2D network cross-section.[499] These algorithms are generally used to identify roads and their junctions in aerial photographs. However, as shown in Fig. 9.1B, they can be applied in a similar manner to nanosheet network cross-sections. While more elegant and elaborate three-dimensional models are in development, the simple 2D approximation in Fig. 9.1B displays reasonable performance in identifying nanosheets (red contours), their thicknesses (green lines) and their junctions (hollow circles). Applying this algorithm to each image in a stack would allow a 3D model of the nanosheets and their junctions to be generated by interpolation. While this is currently a crude approximation, information of this kind would significantly contribute to our understanding of these complex systems. Crucially, though the network properties assessed in this work are already of considerable interest, they are only a prelude to the capabilities of this technique in the near future.

A

Appendix

A.1 Porosity in 1D:2D Nanocomposites

The 1D:2D composites used in this work differ from more commonly studied systems in that they contain significant porosity. This, combined with the density variation across different materials, means that the filler mass fraction is not the most informative metric for such networks. The mass fraction can be converted to the more useful volume fraction by first considering that the total volume of the film is the sum of its components such that

$$V_T = V_{NT} + V_{NS} + V_P \tag{A.1}$$

where V_T is the total volume and V_{NT}, V_{NS} and V_P are the volumes of the nanotubes, nanosheets and pores respectively. The volume fraction is thus

$$\varphi_i = \frac{V_i}{V_T} = \frac{M_i}{M_T}\frac{\rho_T}{\rho_i} = M_{f,i}\frac{\rho_T}{\rho_i} \tag{A.2}$$

where $i = $ NT, NS, P and $M_{f,i}$ is the corresponding mass fraction. We can now restate Eqn. A.1 as

$$\varphi_{NT} + \varphi_{NS} + \varphi_P = 1 \tag{A.3}$$

By substituting in for the φ_{NS} term through Eqn. A.2 we attain

$$\varphi_{NT} + M_{f,NS}\frac{\rho_T}{\rho_{NS}} + \varphi_P = 1 \tag{A.4}$$

By then considering individual components of the film mass fraction $M_{f,NS} + M_{f,NT} = 1$ we can alter Eqn. A.4 such that

$$\varphi_{NT} + (1 - M_{f,NT})\frac{\rho_T}{\rho_{NS}} + \varphi_P = 1 \tag{A.5}$$

By rearranging Eqn. A.2 in terms of the total film density, ρ_T, we arrive at

$$\rho_T = \frac{\varphi_{NT}\rho_{NT}}{M_{f,NT}} \tag{A.6}$$

which can then be substituted into Eqn. A.5 to derive

$$\varphi_{NT} + \varphi_{NT}\frac{(1 - M_{f,NT})}{M_{f,NT}}\frac{\rho_{NT}}{\rho_{NS}} + \varphi_P = 1 \tag{A.7}$$

Rearranged in terms of the nanotube filler volume fraction, φ_{NT}

$$\varphi_{NT} = \frac{(1 - \varphi_P)}{1 + \left(\left({M_{f,NT}}^{-1} - 1 \right) \left(\frac{\rho_{NT}}{\rho_{NS}} \right) \right)} \tag{A.8}$$

Furthermore we can express the film porosity as a function of known and experimentally measurable quantities as

$$\varphi_P = 1 - \varphi_{NT} \left(\left({M_{f,NT}}^{-1} - 1 \right) \left(\frac{\rho_{NT}}{\rho_{NS}} \right) \right) \tag{A.9}$$

A.2 SEM Fibre-Length Analysis

The length of a fibre in a network, L_F, can be related to the number of observable ends, N_{Ends}. For a network of rods on a surface it is self-evident that the areal density of rod ends is equivalent to twice the areal density of rods

$$\frac{N_{Ends}}{A} = 2\frac{N_{Rods}}{A} \tag{A.10}$$

However, the rod number density is unknown. To find an expression for it we note that for a given SEM image, the total length of all visible rods, L_T, is an experimentally measurable parameter. The total length of visible rods per unit area can then be related to the rod number density and the true rod / fibre length, L_F, as

$$\frac{L_T}{A} = L_F\left(\frac{N_{Rods}}{A}\right) \tag{A.11}$$

Combining the two above expressions gives an expression for the true length of a rod / fibre on the composite surface, L_F, in terms of experimentally measurable parameters from SEM images

$$L_F = 2\left(\frac{L_T}{A}\right)\left(\frac{N_{Ends}}{A}\right)^{-1} \tag{A.12}$$

Thus, by counting both the number of visible rod ends and the total visible rod length per unit area, a value for the true rope length can be found using SEM images of the composite surface. While the measurement of the number of rod ends visible per unit area is a matter of counting as shown in Fig. A.1C, determining the length of all visible rods per unit area in a heavily entangled network is non-trivial. This can be simplified by limiting the field of view to a circle as shown in Fig. A.1A.

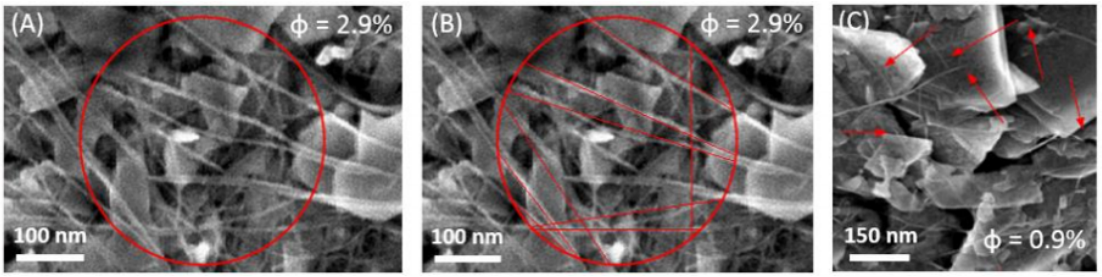

Figure A.1: Nanotube Bundle Length Analysis: A-B) Demonstration of the circular field of view approximation on a 2.9 vol % composite, where the visible chords are marked in **B). C)** Representative image of a $\varphi < 1$ vol % composite where the individual bundle character is apparent and bundle ends can be seen.

If the bundles are roughly straight, the length of visible rods per unit area can be given by summing the individual rod lengths enclosed in the circle

$$\frac{L_T}{A} = \frac{\sum L_{Rod}}{A_{Circ}} \tag{A.13}$$

However, if there are many straight rods crossing the circle, we can use the result that the average length of a chord to a circle of radius r is $4r/\pi$. Thus, by simply counting the number of rods acting as chords to the circle, as shown in Fig. A.1B, and multiplying by the average length we can find a value for the length of all visible rods per unit area

$$\frac{L_T}{A} = No.Chords \times \left(\frac{4r}{\pi}\right)\left(\frac{1}{\pi r^2}\right) \tag{A.14}$$

To build a representative statistical distribution, each SEM image for a given composite volume fraction was split into a 3×4 grid, with each grid containing one circular field of view. This was repeated for 4 images for each studied volume fraction.

A.3 Elastic Modulus Derivation: High-φ

A number of publications have reported that the modulus of a 2D fibre network can be described by an equation having the following form [500]

$$E_{2D} = \eta_0 E_F w^2 (q - Kq_c) \tag{A.15}$$

where E_F is the fibre modulus, w^2 is the cross-sectional area of the fibre, q is the total fibre length per unit area of composite (in a 2D plane) and Kq_c is a constant parameter analogous to a mechanical percolation threshold, $\varphi_{c,m}$. [501] η_0 is once again the filler orientation factor, which is $3/8$ for fibres orientated randomly in-plane. By recognising that the above equation describes the 2D modulus, relating the applied force per unit film width, w, to the strain, ε, we can create an analogous expression for the 3D case by dividing the 2D modulus by the film thickness, t.

$$2D : \frac{F}{w} = E_{2D}\varepsilon \qquad 3D : \frac{F}{wt} = E_{3D}\varepsilon$$

giving

$$E_{3D} = \frac{E_{2D}}{t} \tag{A.16}$$

The total fibre length per unit area, q, can also be re-expressed for the nanotube fibres used in our case. We can simply relate the total length per unit area to the nanotube length, l, multiplied by the areal density of nanotubes, N/A, such that $q = Nl/A$. By considering a film cross-sectional area of A and thickness, t, and using the definition of the fibre volume fraction, φ, we can get an expression for q as follows

$$\varphi = \left(\frac{N}{A}\right)\frac{w^2 l}{t} \qquad where: \qquad \left(\frac{N}{A}\right) = \frac{q}{l}$$

giving

$$q = \frac{\varphi t}{w^2} \qquad \& \qquad q_c = \frac{\varphi_{c,m} t}{w^2} \tag{A.17}$$

By now converting the 2D modulus to a 3D modulus using Eqn. A.16 and substituting in our derived expressions for the total and critical fibre lengths per unit area, q and $q_{c,m}$, we arrive at the final modulus equation for our high-φ composites

$$E_c = \eta_0 E_F(\varphi - \varphi_{c,m}) \qquad for: \qquad \varphi > \varphi_{c,m}$$

A.4 Nanotube Pull-out Model for Composite Toughness

The following derivation is based on a model developed by *Wagner et al.*[417] For a single nanotube pulling out of a matrix, the work of pull-out is given by[340]

$$W_{NT} = \pi R_{NT} L_{Emb}^2 \tau_{eff}$$

where R_{NT} is the radius of the nanotube, L_{Emb} is the initial embedded length of the nanotube and τ_{eff} is the effective interfacial shear stress. If above $\varphi_{c,m}$, an applied load is predominantly carried by a continuous network of entangled bundles and failure can only occur by bundle failure. This is most likely to occur via pullout of the nanotubes from their sockets within bundles as shown in Fig. A.2.

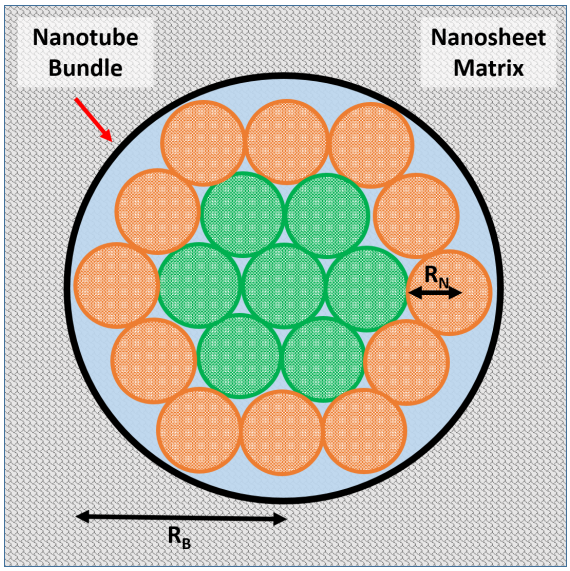

Figure A.2: Nanotube Bundle Cross-Section: Composite cross-section showing a nanotube bundle and its individual nanotube components. The green nanotubes have only nanotube neighbours, while those coloured orange have interfaces with the nanosheet matrix.

We consider those tubes in the centre of nanotube bundles as having only nanotube neighbours

while those at the bundle edge have interfaces with the nanosheet matrix. This infers that τ_{eff} is the weighted mean of the shear stresses associated with both nanotube-nanotube and nanotube-matrix interfaces, given by τ_{NT} and τ_{MF} respectively. Thus, the effective shear-stress can be broken down into components as follows

$$\tau_{eff} = F_s\,\tau_{MF} + (1 - F_s)\,\tau_{NT} \tag{A.18}$$

where F_s is the fraction of the total number of interfaces associated with the bundle surface. This can be found by expressing the circumference of a nanotube bundle as a fraction of sum of the circumferences of each of the nanotubes contained within it. The number of nanotubes in a bundle, n, can be simply found by dividing the bundle cross-sectional area by the cross-sectional area of a single nanotube.

$$F_s = \frac{2\,\pi\,R_F}{n\,2\,\pi\,R_{NT}} \qquad \textit{where}: \qquad n = \left(\frac{R_F}{R_{NT}}\right)^2$$

By subbing this expression for F_s into Eqn. A.18 and factorising we get an expression for the weighted mean of shear stresses, τ_{eff}, in terms of the radii of the nanotubes and bundles / fibres, R_{NT} and R_F

$$\tau_{eff} = \tau_{NT}\left(1 - \frac{R_{NT}}{R_F}\left(1 - \frac{\tau_{MF}}{\tau_{NT}}\right)\right) \tag{A.19}$$

On fracture, the nanotubes that get pulled out from the matrix are displaced from a range of initial embedded lengths ranging from 0 to some maximum length, $L_{Emb,max}$. The mean work of pull-out per nanotube is then given by

$$\langle W_{NT} \rangle = \frac{\int_0^{L_{Emb,Max}} W_{NT}\, d\left(L_{Emb}\right)}{\int_0^{L_{Emb,Max}} d\left(L_{Emb}\right)} = \frac{\pi R_{NT} L_{Emb,Max}^2 \tau_{eff}}{3} \qquad where: L_{Emb,Max} = \frac{L_{NT}}{2}$$

By now multiplying the work of pull-out for a single nanotube by the number of nanotubes in a bundle we can derive an expression for the work of pull-out of a single nanotube bundle, W_B. We must also account for double counting of nanotube-nanotube interfaces. The second factor of 2 takes into account that on average, only half of the nanotube neighbours of a nanotube undergoing pullout are associated with the other side of the fracture and so contribute to the frictional sliding.

$$W_B = \frac{n}{2 \times 2} \langle W_{NT} \rangle = \frac{\pi R_F^2 L_{NT}^2 \tau_{NT}}{48} \left(1 - \frac{R_{NT}}{R_F}\left(1 - \frac{\tau_{MF}}{\tau_{NT}}\right)\right) \tag{A.20}$$

In order to work out the number of bundles crossing the fracture surface, we consider a slice of composite having an area equal to the composite cross-section and of depth equal to that of the nanotube length. Now consider a fracture plane running through the centre of this slice and approximate all nanotubes as being perpendicular to this plane. Thus, all nanotubes with centre points in this slice will intersect the fracture plane and will be involved in the pull-out mechanics. By taking N to be the number of bundles crossing the fracture surface, we can get a simple expression the nanotube volume fraction, which can also be rearranged to give the number of nanotubes per unit area

$$\varphi = \frac{N \pi R_F^2 L_{NT}}{L_{NT} A} \qquad rearranging: \qquad \frac{N}{A} = \frac{\varphi}{\pi R_F^2} \tag{A.21}$$

However, not all of these bundles will be connected to the network in the bulk sample and so will not contribute to the mechanical reinforcement. We introduce a term which expresses the probability

that a given bundle is connected to the network, $P(\varphi)$. An expression for the number of bundles per unit area crossing the fracture plane, that are connected to the network, is given by Eqn. A.22

$$\left(\frac{N}{A}\right)_{Net} = P(\varphi)\frac{N}{A} = P(\varphi)\frac{\varphi}{\pi R_F^2} \tag{A.22}$$

This is readily converted to the work of fracture per unit area by multiplying Eqn. A.22 by the work of pull-out for each bundle, W_B, as given by Eqn. A.20.

$$\left(\frac{W}{A}\right)_{Net} = \varphi P(\varphi)\frac{L_{NT}^2 \tau_{NT}}{24 D_{NT}}\left[1 - \frac{R_{NT}}{R_F}\left(1 - \frac{\tau_{MF}}{\tau_{NT}}\right)\right]$$

We can now use percolation theory in order to derive an expression for the percolation probability. $P(\varphi)$ behaves as follows: $P(\varphi) = 0$ at low-φ and $P(\varphi) = 1$ at $\varphi = 1$. While the analytical form is still unknown, we can use the ansantz that a function such as the one presented in Eqn. A.23 is of the correct form, where k is an exponent

$$P(\varphi) = \left(\frac{\varphi - \varphi_{c,m}}{1 - \varphi}\right)^k \tag{A.23}$$

Subbing in our ansantz for the percolation probability $P(\varphi)$ gives the complete expression for the work of fracture for a network of bundles

$$\left(\frac{W}{A}\right)_{Net} = \varphi\left(\frac{\varphi - \varphi_{c,m}}{1 - \varphi_{c,m}}\right)^k \frac{L_{NT}^2 \tau_{NT}}{24 D_{NT}}\left[1 - \frac{R_{NT}}{R_F}\left(1 - \frac{\tau_{MF}}{\tau_{NT}}\right)\right] \tag{A.24}$$

A final approximation allows us to vastly simplify this expression. If the radius of the bundle of nanotubes is much greater than the radius of a single nanotube, which was observed to be the case using scanning electron microscopy, then the term in square brackets in Eqn. A.24 tends to unity.

Thus, the final expression for the work of fracture for a network of nanotube bundles failing by pull-out is given by

$$\left(\frac{W}{A}\right)_{Net} = \varphi \left(\frac{\varphi - \varphi_{c,m}}{1 - \varphi_{c,m}}\right)^{k} \frac{L_{NT}^{2} \tau_{NT}}{24 D_{NT}} \qquad for: \qquad R_F \gg R_{NT} \qquad \text{(A.25)}$$

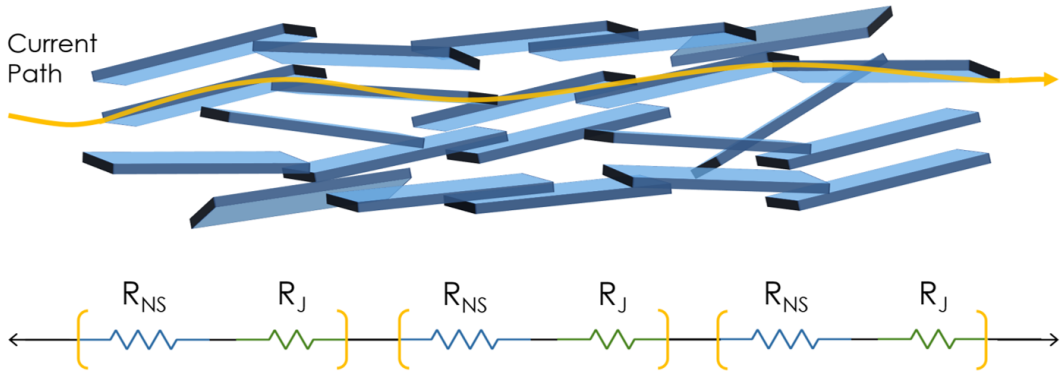

Figure A.3: Nanosheet Network Model: A) Schematic of a current path through a nanosheet network. **B)** This path represented as a series of of voltage drops across nanosheet / junction pairs. Each pair consists of a nanosheet and interfacial junction, each with a resistance of R_{NS} and R_J respectively.

Consider a current path through a reasonably aligned nanosheet network, as shown schematically in Fig. A.3. By representing such a path as a series of voltage drops across both nanosheets and their interfacial junctions, a simple, but robust, transport model can be developed. In the simplest case, the time taken for an electron to cross a nanosheet network, τ_{Net}, is given by the quotient of the distance travelled and electron velocity. These are given by the sample length, L, and drift velocity, v_d, respectively. This transit time can also be expressed in terms of the network mobility, μ_{Net}, and applied potential, V, as

$$\tau_{Net} = \frac{L}{v_d} = \frac{L^2}{\mu_{Net} V} \tag{A.26}$$

An equivalent expression to Eqn. A.26 can be derived in terms of the fundamental unit of the current path through the network, the nanosheet-junction pair. That is, every time an electron passes through a nanosheet, it must also pass through a junction in order to reach the next nanosheet. It is

proposed that a current path is made up of many of these pairs in series, as shown in Fig. A.3. The minimum number of nanosheet-junction pairs in a conductive path, N, is simply given by

$$N = \frac{L}{(l_{NS} + l_J)} \tag{A.27}$$

where l_{NS} and l_J are the average nanosheet and junction lengths respectively. Assuming conduction is dominated by such minimised path lengths, the overall transit time for an electron through the network can be related to the time taken to traverse a nanosheet, τ_{NS}, and junction, τ_J, as

$$\tau_{Net} \approx N(\tau_{NS} + \tau_J) = \frac{L}{(l_{NS} + l_J)} (\tau_{NS} + \tau_J) \tag{A.28}$$

This reduces the problem to one of estimating τ_{NS} and τ_J. To do this, it is necessary to consider how the applied voltage, V, is divided among voltage drops across both nanosheets and junctions. In a given path, the applied voltage will be dropped over the set of contributing NS / junction pairs. Then, in a current path of minimum length, the voltage drop across a single NS / junction pair is

$$V_P = \frac{V(l_{NS} + l_J)}{L} \tag{A.29}$$

However, the voltage drop across the NS / junction pair can be decomposed into its nanosheet and junction components. The voltage drop across a junction, V_J, and nanosheet, V_{NS}, can be given by

$$V_P = \underbrace{\frac{R_{NS}}{(R_J + R_{NS})} V_{Net} \frac{(l_{NS} + l_J)}{L}}_{\mathrm{V_{NS}}} + \underbrace{\frac{R_J}{(R_J + R_{NS})} V_{Net} \frac{(l_{NS} + l_J)}{L}}_{\mathrm{V_J}} \tag{A.30}$$

The time taken for an electron to traverse a nanosheet, τ_{NS}, can now be expressed as

$$\tau_{NS} = \frac{l_{NS}^2}{\mu_{NS} V_{NS}} = \frac{{l_{NS}}^2}{\mu_{NS}} \frac{(R_J + R_{NS})}{R_{NS}} \frac{L}{V(l_{NS} + l_J)} \tag{A.31}$$

The time taken for an electron to traverse an inter-nanosheet junction, τ_J, can be crudely estimated from the current flowing across the junction, I_J. The time interval between charges passing through the junction is given by $\tau_{interval} = \frac{e}{I_J}$. This interval has contributions from both the actual time to pass through the junction, τ_J, and the waiting time between a charge exiting the junction and the next charge arriving, τ_w. The interval time can then be written in the form $\tau_{interval} = \tau_w + \frac{\tau_J}{m}$, where $m > 1$ only when, on average, more than one charge passes through the junction at the same time. This can only be the case when the wait time, τ_w, is much shorter than the time to cross the junction, τ_J. The interval can now be written in the form

$$\tau_{interval} = \tau_w + \frac{\tau_J}{m} = \frac{e}{I_J} = \frac{eR_J}{V_J} \tag{A.32}$$

Rearranging Eqn. A.32 in terms of the time to cross the junction, τ_J

$$\tau_j = \frac{peR_J}{V_J} \qquad where: \qquad \frac{1}{p} = \frac{\tau_w}{\tau_J} + \frac{1}{m} \tag{A.33}$$

Here, p is a parameter that reflects whether the rate-limiting step is the junction or not. For $\tau_w > \tau_J$, the junction is not limiting and $m = 1$ and $p < 1$. However, if the wait time is less than the time taken to traverse the junction, such that $\tau_w < \tau_J$, electrons are delivered to the junction effectively and their progression is limited by transport across the junction. In the case that more than one charge carrier can pass through the junction in parallel, where $m > 1$, this will generally result in $p > 1$,

which defines the junction limiting regime. While it is non-trivial to directly calculate p, its form can reasonably be assumed to depend to the relative magnitudes of both the nanosheet and junction resistances. Junction limited networks exhibit $p > 1$, while those that aren't have $p < 1$. Transport in these networks would be expected to be limited by either the nanosheets themselves, or a combination of nanosheets and junctions. With this in mind, an ansantz can be made that $p = \left(\frac{R_J}{R_{NS}}\right)^{\alpha}$, where $\alpha > 0$. Finally, the time taken for a charge carrier to cross an interfacial junction can be written as

$$\tau_J = \left(\frac{R_J}{R_{NS}}\right)^{\alpha} \frac{eR_J}{V_J} = \left(\frac{R_J}{R_{NS}}\right)^{\alpha} eR_J \frac{R_J + R_{NS}}{R_J} \frac{L}{(l_{NS} + l_J)\, V} \tag{A.34}$$

By combining the equations for τ_{NS} and τ_J, given by Eqns. A.31 and A.34 respectively, and comparing it with the time taken to cross the nanosheet network, τ_{Net}, yields

$$\frac{L^2}{\mu_{Net} V} \approx \frac{L}{(l_{NS} + l_J)} \left[\frac{l_{NS}^2}{\mu_{NS}} \frac{R_J + R_{NS}}{R_J} \frac{L}{(l_{NS} + l_J)\, V} + \left(\frac{R_J}{R_{NS}}\right)^{\alpha} eR_J \frac{R_J + R_{NS}}{R_J} \frac{L}{(l_{NS} + l_J)\, V}\right] \tag{A.35}$$

This can be rearranged in terms of the mobility of the nanosheet network, μ_{Net}

$$\mu_{Net} \approx \frac{(l_{NS} + l_J)^2 \left(\frac{\mu_{NS}}{l_{NS}^2}\right)}{\left[1 + \frac{R_J}{R_{NS}}\right] \left[1 + \frac{eR_{NS}\mu_{NS}}{l_{NS}^2} \left(\frac{R_J}{R_{NS}}\right)^{\alpha}\right]} \tag{A.36}$$

Thankfully, this equation can be simplified by reasonably assuming that $l_{NS} \gg l_J$. Furthermore, it has been shown that the network carrier density approximately scales with nanosheet carrier density according to percolation theory, whereby $n_{Net} = n_{NS}\varphi^{\beta}$.[310] Here, φ represents the nanosheet volume fraction in the network while β is the percolation exponent. Using $\sigma = ne\mu$, both sides of Eqn. A.36

can be converted into expressions for conductivity

$$\sigma_{Net} \approx \frac{\sigma_{NS}\phi^{\beta}}{\left[1+\frac{R_J}{R_{NS}}\right]\left[1+\frac{eR_{NS}\mu_{NS}}{l_{NS}^2}\left(\frac{R_J}{R_{NS}}\right)^{\alpha}\right]} \tag{A.37}$$

The derived expression in Eqn. A.37 describes the conductivity of a network of objects that contains porosity, without specifying their geometry. To apply this equation specifically to nanosheets, we can approximate their shape to be squares of side l_{NS} and thickness, t_{NS}. This allows the nanosheet resistance to be defined as $R_{NS} = (l_{NS}/\sigma_{NS} l_{NS} t_{NS})$. Combining this expression with the definition of nanosheet aspect ratio $k = (l_{NS}/t_{NS})$ and subbing in for σ_{NS}, the nanosheet resistance term can be expressed as $R_{NS} = \left(k/e\, n_{NS}\mu_{NS} l_{NS}\right)$. This allows a final expression, specific to nanosheets, to be derived

$$\sigma_{Net} \approx \frac{n_{NS} e \mu_{NS} \phi^{\beta}}{\left[1+\frac{R_J n_{NS} e \mu_{NS} l_{NS}}{k}\right]\left[1+\frac{k}{l_{NS}^3 n_{NS}}\left(\frac{R_J n_{NS} e \mu_{NS} l_{NS}}{k}\right)^{\alpha}\right]} \tag{A.38}$$

The term $\left(k\,/\,n_{NS}{l_{NS}}^3\right)^{-1}$ represents the average number of charge carriers per nanosheet. Crucially, when the junction resistance is set to zero and the volume fraction is set to 1, this equation returns the nanosheet conductivity. This model aims to approximately describe the conductivity response of a nanosheet network in terms experimentally known and measurable parameters. Interestingly, the network conductivity expression given by Eqn. A.37 can be simplified to give approximate versions that apply under limited circumstances.

A) Semiconducting TMD Networks

In networks where the junction resistance is predicted to be large while the carrier density of the nanosheets is relatively low, it is expected that

$$\frac{R_J}{R_{NS}} \gg 1 \quad \& \quad \left(\frac{k}{{l_{NS}}^3 n_{NS}}\right)^{\alpha} \left(\frac{R_J}{R_{NS}}\right) \gg 1$$

This would be anticipated to be the case for many networks of semiconducting TMDs, such as WSe_2 in the main text. In this scenario, Eqn. A.37 can be simplified to give

$$\sigma_{Net} \approx \frac{\sigma_{NS}\,\varphi^{\beta}}{\left[\left(\frac{k}{{l_{NS}}^3 n_{NS}}\right)\left(\frac{R_J}{R_{NS}}\right)^{\alpha+1}\right]} \xrightarrow{\text{For } \alpha = 1} \approx \frac{\varphi^{\beta}\, l_{NS}\, k}{e\,\mu_{NS}\,{R_J}^2} \tag{A.39}$$

By fitting the WSe_2, graphene and AgNP data in the main text α was found to be equal to 1. This allows the equation to be simplified as shown in Eqn. A.39 to the form used in the main text.

B) Semi-metallic and Metallic Networks

In networks where the junction resistance is again predicted to be large but the carrier density of the nanosheets is now also sizable, it is expected that

$$\frac{R_J}{R_{NS}} \gg 1 \quad \& \quad \left(\frac{k}{{l_{NS}}^3 n_{NS}}\right)^{\alpha} \left(\frac{R_J}{R_{NS}}\right) \ll 1$$

This is anticipated to be the case for the silver and graphene networks in the main text, which are likely to be junction limited but also exhibit carrier densities $> 10^{24}$ m^{-3}. Here, the average carriers per nanosheet term $\left(k \,/\, n_{NS}\, {l_{NS}}^3\right)^{-1}$ will be huge, which will satisfy the above conditions. In this

scenario, Eqn. A.37 can be simplified to give the form used in the main text

$$\sigma_{Net} \approx \frac{k\,\varphi^{\beta}}{R_J\, l_{NS}} \tag{A.40}$$

C) Highly-aligned Networks

Finally, in the case where the junction resistance is dramatically reduced and the network conductivity is limited solely by the material

$$\frac{R_J}{R_{NS}} \ll 1 \quad \& \quad \left(\frac{k}{{l_{NS}}^3\, n_{NS}}\right)^{\alpha} \left(\frac{R_J}{R_{NS}}\right) \ll 1$$

This is expected to be the case for highly-aligned 2D networks, where large-area junctions are facilitated by the conformal overlap of nanosheet basal planes. In this scenario, Eqn. A.37 can be simplified to give

$$\sigma_{Net} \approx \sigma_{NS}\, \varphi^{\beta} \tag{A.41}$$

Here, the network conductivity is equal to the conductivity of the constituent nanosheets scaled by the network volume fraction (which will likely be approaching ~ 1 in these aligned networks).

A.6 Pore-Ellipse Approximation

In this approximation, each individual pore in a 2D cross-section is modelled as an ellipse of equivalent surface area. This is shown schematically in Fig. A.4A. When each pore is first characterised using the 2-pass "connexity" analysis, its longest dimension is designated as the width, w, while the largest dimension perpendicular to this is designated the height, h. To convert each pore into an equivalent ellipse, the ellipse area is forced to match the measured pore area, while the ellipse major and minor axes, $2a$ and $2b$, are fixed to be as close to w and h as possible. Furthermore, the direction of w is used to inform the ellipse orientation, as shown in Fig. A.4A.

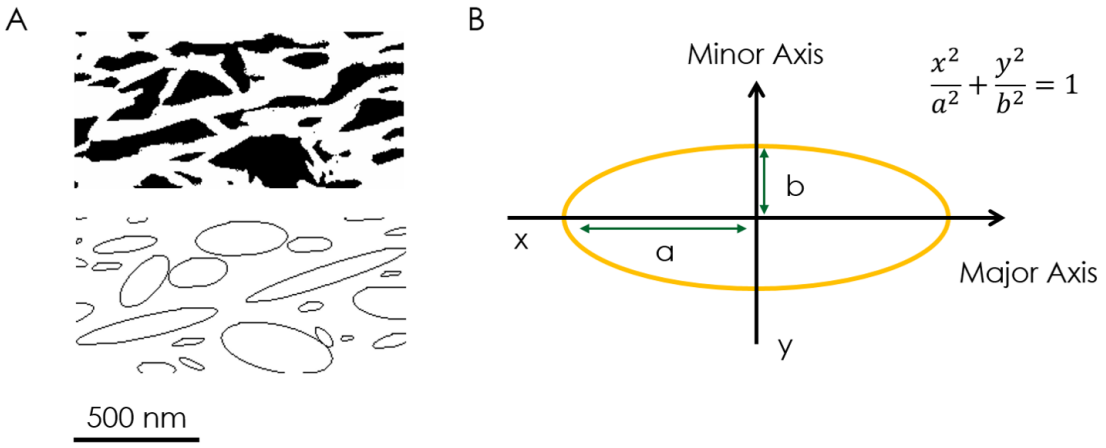

Figure A.4: Equivalent Ellipse Approximation: A) Schematic showing a 2D network cross-section and an approximation where each pore is modelled as an ellipse. **B)** Equation of an ellipse and diagram showing the semi-major and semi-minor axes.

The volume of revolution for each ellipse can then be found by rotating its cross-sectional area about its semi-major axis from zero to π. For an ellipse of the form shown in Fig. A.4B, its volume of revolution when rotated about the x-axis is given by

$$V_{Rev} = \frac{4}{3}\pi a b^2 \tag{A.42}$$

In a similar manner, the surface area of revolution for an ellipse about its semi-major axis can be shown to be

$$A_{Rev} = 2\pi b^2 \left(1 + \frac{a}{b}\frac{arcsin(\varepsilon)}{\varepsilon}\right) \qquad where: \qquad \varepsilon = \sqrt{1 - \left(\frac{b}{a}\right)^2} \tag{A.43}$$

where ε is the eccentricity of the ellipse. Though the ellipses shown in Fig. A.4A are reasonably accurate representations of their corresponding pores, this approximation loses accuracy as the shape the pore becomes more irregular. To check this, the measured 2D surface area and perimeter of every pore in each network was divided by the area and perimeter of its equivalent ellipse (EE). As shown in Fig. A.5A, the measured and EE surface areas are essentially identical, as reflected by their ratio being 1. Due to the nature of the EE approximation, the measured and EE perimeters are not expected to be as close. However, as shown in Fig. A.5B, the majority of pores in each network have similar perimeter lengths to their equivalent ellipses. That the measured perimeter exceeds the ellipse approximation in many cases is no surprise due to the irregular nature of the pores.

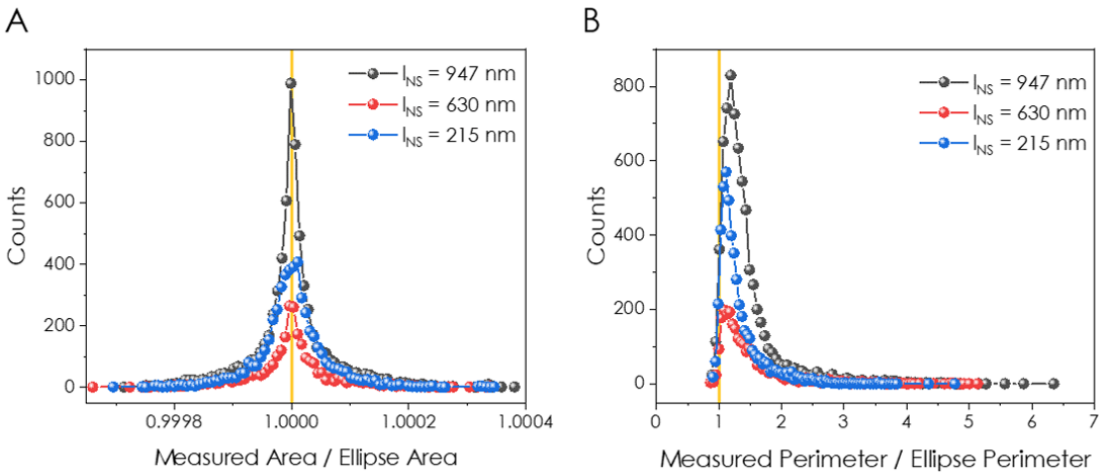

Figure A.5: Equivalent Ellipse Area and Perimeter Distributions: A) Ratio of measured cross-sectional area to the area of its equivalent ellipse and **B)** measured perimeter to the perimeter of its equivalent ellipse for each pore in each network.

References

[1] L. E. Murr, *Handbook of materials structures, properties, processing and performance*. Springer, 2015.

[2] D. Schaming and H. Remita, "Nanotechnology: from the ancient time to nowadays," *Foundations of Chemistry*, vol. 17, no. 3, pp. 187–205, 2015.

[3] P. Walter, E. Welcomme, P. Hallégot, N. J. Zaluzec, C. Deeb, J. Castaing, P. Veyssière, R. Bréniaux, J.-L. Lévêque, and G. Tsoucaris, "Early use of pbs nanotechnology for an ancient hair dyeing formula," *Nano letters*, vol. 6, no. 10, pp. 2215–2219, 2006.

[4] G. Artioli, I. Angelini, and A. Polla, "Crystals and phase transitions in protohistoric glass materials," *Phase Transitions*, vol. 81, no. 2-3, pp. 233–252, 2008.

[5] E. Fois, A. Gamba, and A. Tilocca, "On the unusual stability of maya blue paint: molecular dynamics simulations," *Microporous and Mesoporous Materials*, vol. 57, no. 3, pp. 263–272, 2003.

[6] M. Faraday, "Experimental relations of gold (and other metals) to light," *Philosophical Transactions of the Royal Society of London*, no. 147, pp. 145–181, 1857.

[7] C. Granqvist, R. Buhrman, J. Wyns, and A. Sievers, "Far-infrared absorption in ultrafine al particles," *Physical Review Letters*, vol. 37, no. 10, p. 625, 1976.

[8] H. W. Kroto, J. R. Heath, S. C. O'Brien, R. F. Curl, and R. E. Smalley, "C60: Buckminsterfullerene," *Nature*, vol. 318, no. 6042, pp. 162–163, 1985.

[9] K. S. Novoselov, A. K. Geim, S. V. Morozov, D. Jiang, Y. Zhang, S. V. Dubonos, I. V. Grigorieva, and A. A. Firsov, "Electric field effect in atomically thin carbon films," *science*, vol. 306, no. 5696, pp. 666–669, 2004.

[10] G. Cheon, K.-A. N. Duerloo, A. D. Sendek, C. Porter, Y. Chen, and E. J. Reed, "Data mining for new two-and one-dimensional weakly bonded solids and lattice-commensurate heterostructures," *Nano letters*, vol. 17, no. 3, pp. 1915–1923, 2017.

[11] P. Avouris, T. F. Heinz, and T. Low, *2D Materials*. Cambridge University Press, 2017.

[12] A. K. Geim and K. S. Novoselov, "The rise of graphene," in *Nanoscience and technology: a collection of reviews from nature journals*, pp. 11–19, World Scientific, 2010.

[13] C. Soldano, A. Mahmood, and E. Dujardin, "Production, properties and potential of graphene," *Carbon*, vol. 48, no. 8, pp. 2127–2150, 2010.

[14] S. Iijima, "Helical microtubules of graphitic carbon," *Nature*, vol. 354, no. 6348, pp. 56–58, 1991.

[15] L. Radushkevich and V. á. Lukyanovich, "O strukture ugleroda, obrazujucegosja pri termiceskom razlozenii okisi ugleroda na zeleznom kontakte," *Zurn Fisic Chim*, vol. 26, no. 1, pp. 88–95, 1952.

[16] W. Choi, N. Choudhary, G. H. Han, J. Park, D. Akinwande, and Y. H. Lee, "Recent development of two-dimensional transition metal dichalcogenides and their applications," *Materials Today*, vol. 20, no. 3, pp. 116–130, 2017.

[17] B. Brodie, "About the atomic weight of graphite," *Justus Liebigs Annalen der Chemie*, vol. 114, no. 1, pp. 6–24, 1860.

[18] P. Debye and P. Scherrer, "Interferences on randomly oriented particles in x-ray light. i.," *News from the Society of Sciences in G ”o ttingen, Mathematical-Physical Class*, vol. 1916, pp. 1–15, 1916.

[19] A. W. Hull, "A new method of x-ray crystal analysis," *Physical Review*, vol. 10, no. 6, p. 661, 1917.

[20] J. D. Bernal, "The structure of graphite," *Proceedings of the Royal Society of London. Series A, Containing Papers of a Mathematical and Physical Character*, vol. 106, no. 740, pp. 749–773, 1924.

[21] P. R. Wallace, "The band theory of graphite," *Physical review*, vol. 71, no. 9, p. 622, 1947.

[22] J. McClure, "Diamagnetism of graphite," *Physical Review*, vol. 104, no. 3, p. 666, 1956.

[23] L. Landau and E. Lifshitz, "Statistical physics part i, pergamon press," 1980.

[24] J. Venable, G. Spiller, and M. Hanbucken, "Nucleation and growth of thin film," *Rep. Prog. Phys.*, vol. 47, no. 4, pp. 399–459, 1984.

[25] J. C. Meyer, A. K. Geim, M. I. Katsnelson, K. S. Novoselov, T. J. Booth, and S. Roth, "The structure of suspended graphene sheets," *Nature*, vol. 446, no. 7131, pp. 60–63, 2007.

[26] N. David, P. Tsvi, and W. Steven, *Statistical mechanics of membranes and surfaces*. World Scientific, 2004.

[27] A. K. Geim, "Graphene: status and prospects," *science*, vol. 324, no. 5934, pp. 1530–1534, 2009.

[28] C. M. Hussain, *Handbook of environmental materials management*. Springer, 2019.

[29] A. Hernández-Mínguez, Y. Liou, and P. Santos, "Interaction of surface acoustic waves with electronic excitations in graphene," *Journal of Physics D: Applied Physics*, vol. 51, no. 38, p. 383001, 2018.

[30] A. C. Neto, F. Guinea, N. M. Peres, K. S. Novoselov, and A. K. Geim, "The electronic properties of graphene," *Reviews of modern physics*, vol. 81, no. 1, p. 109, 2009.

[31] J.-C. Charlier, P. Eklund, J. Zhu, and A. Ferrari, "Electron and phonon properties of graphene: their relationship with carbon nanotubes," in *Carbon nanotubes*, pp. 673–709, Springer, 2007.

[32] M. Katsnelson, K. Novoselov, and A. Geim, "Chiral tunnelling and the klein paradox in graphene," *Nature physics*, vol. 2, no. 9, pp. 620–625, 2006.

[33] M. S. Fuhrer, C. N. Lau, and A. H. MacDonald, "Graphene: materially better carbon," *MRS bulletin*, vol. 35, no. 4, pp. 289–295, 2010.

[34] A. S. Mayorov, R. V. Gorbachev, S. V. Morozov, L. Britnell, R. Jalil, L. A. Ponomarenko, P. Blake, K. S. Novoselov, K. Watanabe, T. Taniguchi, *et al.*, "Micrometer-scale ballistic transport in encapsulated graphene at room temperature," *Nano letters*, vol. 11, no. 6, pp. 2396–2399, 2011.

[35] P. Zomer, S. Dash, N. Tombros, and B. Van Wees, "A transfer technique for high mobility graphene devices on commercially available hexagonal boron nitride," *Applied Physics Letters*, vol. 99, no. 23, p. 232104, 2011.

[36] C. Lee, X. Wei, J. W. Kysar, and J. Hone, "Measurement of the elastic properties and intrinsic strength of monolayer graphene," *science*, vol. 321, no. 5887, pp. 385–388, 2008.

[37] M. Montes-Morán, W. Gauthier, A. Martínez-Alonso, and J. Tascón, "Mechanical properties of high-strength carbon fibres. validation of an end-effect model for describing experimental data," *Carbon*, vol. 42, no. 7, pp. 1275–1278, 2004.

[38] W. Liu, J. Ma, X. Yao, and R. Fang, "Inorganic fibers for biomedical engineering applications," in *Materials for Biomedical Engineering*, pp. 1–32, Elsevier, 2019.

[39] F. Bonaccorso, L. Colombo, G. Yu, M. Stoller, V. Tozzini, A. C. Ferrari, R. S. Ruoff, and V. Pellegrini, "Graphene, related two-dimensional crystals, and hybrid systems for energy conversion and storage," *Science*, vol. 347, no. 6217, 2015.

[40] J. Du and H.-M. Cheng, "The fabrication, properties, and uses of graphene/polymer composites," *Macromolecular Chemistry and Physics*, vol. 213, no. 10-11, pp. 1060–1077, 2012.

[41] W. Bao, F. Miao, Z. Chen, H. Zhang, W. Jang, C. Dames, and C. N. Lau, "Controlled ripple texturing of suspended graphene and ultrathin graphite membranes," *Nature nanotechnology*, vol. 4, no. 9, p. 562, 2009.

[42] F. Guinea, M. Katsnelson, and M. Vozmediano, "Midgap states and charge inhomogeneities in corrugated graphene," *Physical Review B*, vol. 77, no. 7, p. 075422, 2008.

[43] K. S. Novoselov and A. Geim, "Scientific background on the nobel prize in physics 2010: Graphene," *The Royal Swedish Academy of Sciences*, 2010.

[44] M. Aliofkhazraei, N. Ali, W. I. Milne, C. S. Ozkan, S. Mitura, and J. L. Gervasoni, *Graphene science handbook: Applications and industrialization*. Crc Press, 2016.

[45] R. G. Dickinson and L. Pauling, "The crystal structure of molybdenite," *Journal of the American Chemical Society*, vol. 45, no. 6, pp. 1466–1471, 1923.

[46] J. A. Wilson and A. Yoffe, "The transition metal dichalcogenides discussion and interpretation of the observed optical, electrical and structural properties," *Advances in Physics*, vol. 18, no. 73, pp. 193–335, 1969.

[47] R. Frindt, "Single crystals of mos2 several molecular layers thick," *Journal of Applied Physics*, vol. 37, no. 4, pp. 1928–1929, 1966.

[48] R. Frindt, "Optical absorption of a few unit-cell layers of mo s 2," *Physical Review*, vol. 140, no. 2A, p. A536, 1965.

[49] P. Joensen, R. Frindt, and S. R. Morrison, "Single-layer mos2," *Materials research bulletin*, vol. 21, no. 4, pp. 457–461, 1986.

[50] H. Zhou, C. Wang, J. C. Shaw, R. Cheng, Y. Chen, X. Huang, Y. Liu, N. O. Weiss, Z. Lin, Y. Huang, *et al.*, "Large area growth and electrical properties of p-type wse2 atomic layers," *Nano letters*, vol. 15, no. 1, pp. 709–713, 2015.

[51] Z. Sun, A. Martinez, and F. Wang, "Optical modulators with 2d layered materials," *Nature Photonics*, vol. 10, no. 4, p. 227, 2016.

[52] H. Huang, Y. Cui, Q. Li, C. Dun, W. Zhou, W. Huang, L. Chen, C. A. Hewitt, and D. L. Carroll, "Metallic 1t phase mos2 nanosheets for high-performance thermoelectric energy harvesting," *Nano Energy*, vol. 26, pp. 172–179, 2016.

[53] Q. Yue, J. Kang, Z. Shao, X. Zhang, S. Chang, G. Wang, S. Qin, and J. Li, "Mechanical and electronic properties of monolayer mos2 under elastic strain," *Physics Letters A*, vol. 376, no. 12-13, pp. 1166–1170, 2012.

[54] T. Polcar and A. Cavaleiro, "Review on self-lubricant transition metal dichalcogenide nanocomposite coatings alloyed with carbon," *Surface and Coatings Technology*, vol. 206, no. 4, pp. 686–695, 2011.

[55] M. Chhowalla, H. S. Shin, G. Eda, L.-J. Li, K. P. Loh, and H. Zhang, "The chemistry of two-dimensional layered transition metal dichalcogenide nanosheets," *Nature chemistry*, vol. 5, no. 4, p. 263, 2013.

[56] Y. Yoon, K. Ganapathi, and S. Salahuddin, "How good can monolayer mos2 transistors be?," *Nano letters*, vol. 11, no. 9, pp. 3768–3773, 2011.

[57] S. Bertolazzi, J. Brivio, and A. Kis, "Stretching and breaking of ultrathin mos2," *ACS nano*, vol. 5, no. 12, pp. 9703–9709, 2011.

[58] J. Brivio, D. T. Alexander, and A. Kis, "Ripples and layers in ultrathin mos2 membranes," *Nano letters*, vol. 11, no. 12, pp. 5148–5153, 2011.

[59] B. Radisavljevic, A. Radenovic, J. Brivio, V. Giacometti, and A. Kis, "Single-layer mos 2 transistors," *Nature nanotechnology*, vol. 6, no. 3, p. 147, 2011.

[60] H. Schmidt, F. Giustiniano, and G. Eda, "Electronic transport properties of transition metal dichalcogenide field-effect devices: surface and interface effects," *Chemical Society Reviews*, vol. 44, no. 21, pp. 7715–7736, 2015.

[61] R. Kappera, D. Voiry, S. E. Yalcin, W. Jen, M. Acerce, S. Torrel, B. Branch, S. Lei, W. Chen, S. Najmaei, *et al.*, "Metallic 1t phase source/drain electrodes for field effect transistors from chemical vapor deposited mos2," *Apl Materials*, vol. 2, no. 9, p. 092516, 2014.

[62] M. Kertesz and R. Hoffmann, "Octahedral vs. trigonal-prismatic coordination and clustering in transition-metal dichalcogenides," *Journal of the American Chemical Society*, vol. 106, no. 12, pp. 3453–3460, 1984.

[63] M. Py and R. Haering, "Structural destabilization induced by lithium intercalation in mos2 and related compounds," *Canadian Journal of Physics*, vol. 61, no. 1, pp. 76–84, 1983.

[64] T. Lorenz, D. Teich, J.-O. Joswig, and G. Seifert, "Theoretical study of the mechanical behavior of individual tis2 and mos2 nanotubes," *The Journal of Physical Chemistry C*, vol. 116, no. 21, pp. 11714–11721, 2012.

[65] J. Kang, S. Tongay, J. Zhou, J. Li, and J. Wu, "Band offsets and heterostructures of two-dimensional semiconductors," *Applied Physics Letters*, vol. 102, no. 1, p. 012111, 2013.

[66] A. Kuc, N. Zibouche, and T. Heine, "Influence of quantum confinement on the electronic structure of the transition metal sulfide t s 2," *Physical Review B*, vol. 83, no. 24, p. 245213, 2011.

[67] Q. H. Wang, K. Kalantar-Zadeh, A. Kis, J. N. Coleman, and M. S. Strano, "Electronics and optoelectronics of two-dimensional transition metal dichalcogenides," *Nature nanotechnology*, vol. 7, no. 11, p. 699, 2012.

[68] A. Splendiani, L. Sun, Y. Zhang, T. Li, J. Kim, C.-Y. Chim, G. Galli, and F. Wang, "Emerging photoluminescence in monolayer mos2," *Nano letters*, vol. 10, no. 4, pp. 1271–1275, 2010.

[69] K. F. Mak, C. Lee, J. Hone, J. Shan, and T. F. Heinz, "Atomically thin mos 2: a new direct-gap semiconductor," *Physical review letters*, vol. 105, no. 13, p. 136805, 2010.

[70] S. Mukherjee, J. Turnley, E. Mansfield, J. Holm, D. Soares, L. David, and G. Singh, "Exfoliated transition metal dichalcogenide nanosheets for supercapacitor and sodium ion battery applications," *Royal Society open science*, vol. 6, no. 8, p. 190437, 2019.

[71] L. Lin, W. Lei, S. Zhang, Y. Liu, G. G. Wallace, and J. Chen, "Two-dimensional transition metal dichalcogenides in supercapacitors and secondary batteries," *Energy Storage Materials*, vol. 19, pp. 408–423, 2019.

[72] S.-H. Park, P. J. King, R. Tian, C. S. Boland, J. Coelho, C. J. Zhang, P. McBean, N. McEvoy, M. P. Kremer, D. Daly, *et al.*, "High areal capacity battery electrodes enabled by segregated nanotube networks," *Nature Energy*, vol. 4, no. 7, pp. 560–567, 2019.

[73] T. M. Higgins, S. Finn, M. Matthiesen, S. Grieger, K. Synnatschke, M. Brohmann, M. Rother, C. Backes, and J. Zaumseil, "Electrolyte-gated n-type transistors produced from aqueous inks of ws2 nanosheets," *Advanced Functional Materials*, vol. 29, no. 4, p. 1804387, 2019.

[74] D. McManus, A. Dal Santo, P. Selvasundaram, R. Krupke, A. LiBassi, and C. Casiraghi, "Photocurrent study of all-printed photodetectors on paper made of different transition metal dichalcogenide nanosheets," *Flexible and Printed Electronics*, vol. 3, no. 3, p. 034005, 2018.

[75] M. C. Hersam, "Progress towards monodisperse single-walled carbon nanotubes," *Nature nanotechnology*, vol. 3, no. 7, p. 387, 2008.

[76] M. Rahmandoust and A. Öchsner, "Buckling behaviour and natural frequency of zigzag and armchair single-walled carbon nanotubes," in *Journal of Nano Research*, vol. 16, pp. 153–160, Trans Tech Publ, 2011.

[77] R. Saito, G. Dresselhaus, and M. Dresselhaus, "Physical properties of carbon nanotubes. 1998," *Imperial College, London*, 1991.

[78] M. Reibold, P. Paufler, A. Levin, W. Kochmann, N. Pätzke, and D. Meyer, "Carbon nanotubes in an ancient damascus sabre," *Nature*, vol. 444, no. 7117, pp. 286–286, 2006.

[79] R. Zhang, Y. Zhang, Q. Zhang, H. Xie, W. Qian, and F. Wei, "Growth of half-meter long carbon nanotubes based on schulz–flory distribution," *Acs Nano*, vol. 7, no. 7, pp. 6156–6161, 2013.

[80] M.-F. Yu, O. Lourie, M. J. Dyer, K. Moloni, T. F. Kelly, and R. S. Ruoff, "Strength and breaking mechanism of multiwalled carbon nanotubes under tensile load," *Science*, vol. 287, no. 5453, pp. 637–640, 2000.

[81] T. Ebbesen and P. Ajayan, "Large-scale synthesis of carbon nanotubes," *Nature*, vol. 358, no. 6383, pp. 220–222, 1992.

[82] T. Guo, P. Nikolaev, A. Thess, D. T. Colbert, and R. E. Smalley, "Catalytic growth of single-walled manotubes by laser vaporization," *Chemical physics letters*, vol. 243, no. 1-2, pp. 49–54, 1995.

[83] M. Endo, K. Takeuchi, S. Igarashi, K. Kobori, M. Shiraishi, and H. W. Kroto, "The production and structure of pyrolytic carbon nanotubes (pcnts)," *Journal of Physics and Chemistry of Solids*, vol. 54, no. 12, pp. 1841–1848, 1993.

[84] W. Zhou, Y. Ooi, R. a. a. Russo, P. Papanek, D. Luzzi, J. Fischer, M. Bronikowski, P. Willis, and R. Smalley, "Structural characterization and diameter-dependent oxidative stability of single wall carbon nanotubes synthesized by the catalytic decomposition of co," *Chemical Physics Letters*, vol. 350, no. 1-2, pp. 6–14, 2001.

[85] S. Reich, C. Thomsen, and J. Maultzsch, *Carbon nanotubes: basic concepts and physical properties*. John Wiley & Sons, 2008.

[86] M. Damnjanović, I. Milošević, T. Vuković, and R. Sredanović, "Full symmetry, optical activity, and potentials of single-wall and multiwall nanotubes," *Physical Review B*, vol. 60, no. 4, p. 2728, 1999.

[87] P. G. Collins and P. Avouris, "The electronic properties of carbon nanotubes," *Contemporary Concepts of Condensed Matter Science*, vol. 3, pp. 49–81, 2008.

[88] P. L. McEuen, M. Bockrath, D. H. Cobden, Y.-G. Yoon, and S. G. Louie, "Disorder, pseudospins, and backscattering in carbon nanotubes," *Physical Review Letters*, vol. 83, no. 24, p. 5098, 1999.

[89] J. Kong, C. Zhou, A. Morpurgo, H. Soh, C. Quate, C. Marcus, and H. Dai, "Synthesis, integration, and electrical properties of individual single-walled carbon nanotubes," *Applied Physics A*, vol. 69, no. 3, pp. 305–308, 1999.

[90] Y. Wang and G. J. Weng, "Electrical conductivity of carbon nanotube-and graphene-based nanocomposites," in *Micromechanics and Nanomechanics of Composite Solids*, pp. 123–156, Springer, 2018.

[91] R. A. Matula, "Electrical resistivity of copper, gold, palladium, and silver," *Journal of Physical and Chemical Reference Data*, vol. 8, no. 4, pp. 1147–1298, 1979.

[92] S. Hong and S. Myung, "A flexible approach to mobility," *Nature nanotechnology*, vol. 2, no. 4, pp. 207–208, 2007.

[93] G. Pennington and N. Goldsman, "Semiclassical transport and phonon scattering of electrons in semiconducting carbon nanotubes," *Physical Review B*, vol. 68, no. 4, p. 045426, 2003.

[94] M. Ouyang, J.-L. Huang, C. L. Cheung, and C. M. Lieber, "Energy gaps in" metallic" single-walled carbon nanotubes," *Science*, vol. 292, no. 5517, pp. 702–705, 2001.

[95] R. H. Baughman, A. A. Zakhidov, and W. A. De Heer, "Carbon nanotubes–the route toward applications," *science*, vol. 297, no. 5582, pp. 787–792, 2002.

[96] M. S. Arnold, A. A. Green, J. F. Hulvat, S. I. Stupp, and M. C. Hersam, "Sorting carbon nanotubes by electronic structure using density differentiation," *Nature nanotechnology*, vol. 1, no. 1, pp. 60–65, 2006.

[97] A. Kelly and N. H. Macmillan, "Strong solids.," *Oxford University Press, Walton Street, Oxford OX 2 6 DP, UK, 1986.*, 1986.

[98] G. Overney, W. Zhong, and D. Tomanek, "Structural rigidity and low frequency vibrational modes of long carbon tubules," *Zeitschrift für Physik D Atoms, Molecules and Clusters*, vol. 27, no. 1, pp. 93–96, 1993.

[99] E. W. Wong, P. E. Sheehan, and C. M. Lieber, "Nanobeam mechanics: elasticity, strength, and toughness of nanorods and nanotubes," *science*, vol. 277, no. 5334, pp. 1971–1975, 1997.

[100] B. Peng, M. Locascio, P. Zapol, S. Li, S. L. Mielke, G. C. Schatz, and H. D. Espinosa, "Measurements of near-ultimate strength for multiwalled carbon nanotubes and irradiation-induced crosslinking improvements," *Nature nanotechnology*, vol. 3, no. 10, p. 626, 2008.

[101] J. N. Coleman, U. Khan, W. J. Blau, and Y. K. Gun'ko, "Small but strong: a review of the mechanical properties of carbon nanotube–polymer composites," *Carbon*, vol. 44, no. 9, pp. 1624–1652, 2006.

[102] S.-H. Kim, H. Kim, and N. J. Kim, "Brittle intermetallic compound makes ultrastrong low-density steel with large ductility," *Nature*, vol. 518, no. 7537, pp. 77–79, 2015.

[103] L. Yu, C. Shearer, and J. Shapter, "Recent development of carbon nanotube transparent conductive films," *Chemical reviews*, vol. 116, no. 22, pp. 13413–13453, 2016.

[104] T. Han, A. Nag, S. C. Mukhopadhyay, and Y. Xu, "Carbon nanotubes and its gas-sensing applications: A review," *Sensors and Actuators A: Physical*, vol. 291, pp. 107–143, 2019.

[105] Z. Ling, A. Harvey, D. McAteer, I. J. Godwin, B. Szydłowska, A. Griffin, V. Vega-Mayoral, Y. Song, A. Seral-Ascaso, V. Nicolosi, *et al.*, "Quantifying the role of nanotubes in nano: nano composite supercapacitor electrodes," *Advanced Energy Materials*, vol. 8, no. 8, p. 1702364, 2018.

[106] M. Zhu, R. Outlaw, M. Bagge-Hansen, H. Chen, and D. Manos, "Enhanced field emission of vertically oriented carbon nanosheets synthesized by c2h2/h2 plasma enhanced cvd," *Carbon*, vol. 49, no. 7, pp. 2526–2531, 2011.

[107] W. Ren, W. Zhou, H. Zhang, and C. Cheng, "Ald tio2-coated flower-like mos2 nanosheets on carbon cloth as sodium ion battery anode with enhanced cycling stability and rate capability," *ACS applied materials & interfaces*, vol. 9, no. 1, pp. 487–495, 2017.

[108] M. Dresselhaus and G. Dresselhaus, "Intercalation compounds of graphite," *Advances in Physics*, vol. 30, no. 2, pp. 139–326, 1981.

[109] L. Zhang, J. Liang, Y. Huang, Y. Ma, Y. Wang, and Y. Chen, "Size-controlled synthesis of graphene oxide sheets on a large scale using chemical exfoliation," *Carbon*, vol. 47, no. 14, pp. 3365–3368, 2009.

[110] Y. Hernandez, V. Nicolosi, M. Lotya, F. M. Blighe, Z. Sun, S. De, I. McGovern, B. Holland, M. Byrne, Y. K. Gun'Ko, *et al.*, "High-yield production of graphene by liquid-phase exfoliation of graphite," *Nature nanotechnology*, vol. 3, no. 9, p. 563, 2008.

[111] A. J. Mannix, B. Kiraly, M. C. Hersam, and N. P. Guisinger, "Synthesis and chemistry of elemental 2d materials," *Nature Reviews Chemistry*, vol. 1, no. 2, pp. 1–14, 2017.

[112] R. A. Schultz, M. C. Jensen, and R. C. Bradt, "Single crystal cleavage of brittle materials," *International journal of fracture*, vol. 65, no. 4, pp. 291–312, 1994.

[113] R. Frindt and A. Yoffe, "Physical properties of layer structures: optical properties and photoconductivity of thin crystals of molybdenum disulphide," *Proceedings of the Royal Society of London. Series A. Mathematical and Physical Sciences*, vol. 273, no. 1352, pp. 69–83, 1963.

[114] X. Lu, M. Yu, H. Huang, and R. S. Ruoff, "Tailoring graphite with the goal of achieving single sheets," *Nanotechnology*, vol. 10, no. 3, p. 269, 1999.

[115] D. Pacile, J. Meyer, Ç. Girit, and A. Zettl, "The two-dimensional phase of boron nitride: Few-atomic-layer sheets and suspended membranes," *Applied Physics Letters*, vol. 92, no. 13, p. 133107, 2008.

[116] K. S. Novoselov, D. Jiang, F. Schedin, T. Booth, V. Khotkevich, S. Morozov, and A. K. Geim, "Two-dimensional atomic crystals," *Proceedings of the National Academy of Sciences*, vol. 102, no. 30, pp. 10451–10453, 2005.

[117] W. Kern and G. L. Schnable, "Low-pressure chemical vapor deposition for very large-scale integration processing—a review," *IEEE Transactions on Electron Devices*, vol. 26, no. 4, pp. 647–657, 1979.

[118] X. Li, W. Cai, J. An, S. Kim, J. Nah, D. Yang, R. Piner, A. Velamakanni, I. Jung, E. Tutuc, *et al.*, "Large-area synthesis of high-quality and uniform graphene films on copper foils," *science*, vol. 324, no. 5932, pp. 1312–1314, 2009.

[119] L. Tao, K. Chen, Z. Chen, W. Chen, X. Gui, H. Chen, X. Li, and J.-B. Xu, "Centimeter-scale cvd growth of highly crystalline single-layer mos2 film with spatial homogeneity and the visualization of grain boundaries," *ACS applied materials & interfaces*, vol. 9, no. 13, pp. 12073–12081, 2017.

[120] S. Li, S. Wang, D.-M. Tang, W. Zhao, H. Xu, L. Chu, Y. Bando, D. Golberg, and G. Eda, "Halide-assisted atmospheric pressure growth of large wse2 and ws2 monolayer crystals," *Applied Materials Today*, vol. 1, no. 1, pp. 60–66, 2015.

[121] N. Kholin, E. Rut'kov, and A. Y. Tontegode, "The nature of the adsorption bond between graphite islands and iridium surface," *Surface science*, vol. 139, no. 1, pp. 155–172, 1984.

[122] G. Deokar, J. Avila, I. Razado-Colambo, J.-L. Codron, C. Boyaval, E. Galopin, M.-C. Asensio, and D. Vignaud, "Towards high quality cvd graphene growth and transfer," *Carbon*, vol. 89, pp. 82–92, 2015.

[123] S. Hofmann, P. Braeuninger-Weimer, and R. S. Weatherup, "Cvd-enabled graphene manufacture and technology," *The journal of physical chemistry letters*, vol. 6, no. 14, pp. 2714–2721, 2015.

[124] C.-M. Seah, S.-P. Chai, and A. R. Mohamed, "Mechanisms of graphene growth by chemical vapour deposition on transition metals," *Carbon*, vol. 70, pp. 1–21, 2014.

[125] C. Backes, K. R. Paton, D. Hanlon, S. Yuan, M. I. Katsnelson, J. Houston, R. J. Smith, D. McCloskey, J. F. Donegan, and J. N. Coleman, "Spectroscopic metrics allow in situ measurement of mean size and thickness of liquid-exfoliated few-layer graphene nanosheets," *Nanoscale*, vol. 8, no. 7, pp. 4311–4323, 2016.

[126] J. Chen, B. Yao, C. Li, and G. Shi, "An improved hummers method for eco-friendly synthesis of graphene oxide," *Carbon*, vol. 64, pp. 225–229, 2013.

[127] W. Gao, "The chemistry of graphene oxide," in *Graphene oxide*, pp. 61–95, Springer, 2015.

[128] S. Stankovich, D. A. Dikin, G. H. Dommett, K. M. Kohlhaas, E. J. Zimney, E. A. Stach, R. D. Piner, S. T. Nguyen, and R. S. Ruoff, "Graphene-based composite materials," *nature*, vol. 442, no. 7100, pp. 282–286, 2006.

[129] H. Boehm, A. Clauss, G. Fischer, and U. Hofmann, "Surface properties of extremely thin graphite lamellae," in *Proceedings of the fifth conference on carbon*, vol. 1, pp. 73–80, Pergamon Press New York, 1962.

[130] H. P. Boehm, R. Setton, and E. Stumpp, "Nomenclature and terminology of graphite intercalation compounds (iupac recommendations 1994)," *Pure and Applied Chemistry*, vol. 66, no. 9, pp. 1893–1901, 1994.

[131] R. Nair, H. Wu, P. Jayaram, I. Grigorieva, and A. Geim, "Unimpeded permeation of water through helium-leak–tight graphene-based membranes," *Science*, vol. 335, no. 6067, pp. 442–444, 2012.

[132] D. A. Dikin, S. Stankovich, E. J. Zimney, R. D. Piner, G. H. Dommett, G. Evmenenko, S. T. Nguyen, and R. S. Ruoff, "Preparation and characterization of graphene oxide paper," *Nature*, vol. 448, no. 7152, pp. 457–460, 2007.

[133] G. Lagaly and K. Beneke, "Intercalation and exchange reactions of clay minerals and non-clay layer compounds," *Colloid and Polymer Science*, vol. 269, no. 12, pp. 1198–1211, 1991.

[134] C.-J. Shih, A. Vijayaraghavan, R. Krishnan, R. Sharma, J.-H. Han, M.-H. Ham, Z. Jin, S. Lin, G. L. Paulus, N. F. Reuel, *et al.*, "Bi-and trilayer graphene solutions," *Nature Nanotechnology*, vol. 6, no. 7, p. 439, 2011.

[135] G. Eda, H. Yamaguchi, D. Voiry, T. Fujita, M. Chen, and M. Chhowalla, "Photoluminescence from chemically exfoliated mos2," *Nano letters*, vol. 11, no. 12, pp. 5111–5116, 2011.

[136] A. S. Golub, Y. V. Zubavichus, Y. L. Slovokhotov, and Y. N. Novikov, "Single-layer dispersions of transition metal dichalcogenides in the synthesis of intercalation compounds," *Russian chemical reviews*, vol. 72, no. 2, pp. 123–141, 2003.

[137] A. Takagaki, D. Lu, J. N. Kondo, M. Hara, S. Hayashi, and K. Domen, "Exfoliated hnb308 nanosheets as a strong protonic solid acid," *Chemistry of materials*, vol. 17, no. 10, pp. 2487–2489, 2005.

[138] T. J. Pinnavaia, "Intercalated clay catalysts," *Science*, vol. 220, no. 4595, pp. 365–371, 1983.

[139] D.-M. Hwang, G. Kirczenow, P. Lagrange, A. Magerl, R. Moret, S. Moss, S. Setton, S. Solin, and H. Zabel, *Graphite intercalation compounds I: Structure and dynamics*, vol. 14. Springer Science & Business Media, 2013.

[140] R. Joensen, "Frindt, and sr morrison," *Mater. Res. Bull*, vol. 21, p. 457, 1986.

[141] Y. Matsuo, T. Niwa, and Y. Sugie, "Preparation and characterization of cationic surfactant-intercalated graphite oxide," *Carbon*, vol. 37, no. 6, pp. 897–901, 1999.

[142] B. Zhang, L. Luan, R. Gao, F. Li, Y. Li, and T. Wu, "Rapid and effective removal of cr (vi) from aqueous solution using exfoliated ldh nanosheets," *Colloids and Surfaces A: Physicochemical and Engineering Aspects*, vol. 520, pp. 399–408, 2017.

[143] P. Meneghetti and S. Qutubuddin, "Synthesis, thermal properties and applications of polymer-clay nanocomposites," *Thermochimica Acta*, vol. 442, no. 1-2, pp. 74–77, 2006.

[144] Y. Ebina, T. Sasaki, and M. Watanabe, "Study on exfoliation of layered perovskite-type niobates," *Solid State Ionics*, vol. 151, no. 1-4, pp. 177–182, 2002.

[145] T. Tanaka, Y. Ebina, K. Takada, K. Kurashima, and T. Sasaki, "Oversized titania nanosheet crystallites derived from flux-grown layered titanate single crystals," *Chemistry of materials*, vol. 15, no. 18, pp. 3564–3568, 2003.

[146] G. Eda, T. Fujita, H. Yamaguchi, D. Voiry, M. Chen, and M. Chhowalla, "Coherent atomic and electronic heterostructures of single-layer mos2," *ACS nano*, vol. 6, no. 8, pp. 7311–7317, 2012.

[147] T. M. Suter, T. S. Miller, J. K. Cockcroft, A. E. Aliev, M. C. Wilding, A. Sella, F. Corà, C. A. Howard, and P. F. McMillan, "Formation of an ion-free crystalline carbon nitride and its reversible intercalation with ionic species and molecular water," *Chemical science*, vol. 10, no. 8, pp. 2519–2528, 2019.

[148] M. El Garah, S. Bertolazzi, S. Ippolito, M. Eredia, I. Janica, G. Melinte, O. Ersen, G. Marletta, A. Ciesielski, and P. Samorì, "Mos2 nanosheets via electrochemical lithium-ion intercalation under ambient conditions," *FlatChem*, vol. 9, pp. 33–39, 2018.

[149] J. N. Coleman, M. Lotya, A. O'Neill, S. D. Bergin, P. J. King, U. Khan, K. Young, A. Gaucher, S. De, R. J. Smith, *et al.*, "Two-dimensional nanosheets produced by liquid exfoliation of layered materials," *Science*, vol. 331, no. 6017, pp. 568–571, 2011.

[150] A. Harvey, J. B. Boland, I. Godwin, A. G. Kelly, B. M. Szydłowska, G. Murtaza, A. Thomas, D. J. Lewis, P. O'Brien, and J. N. Coleman, "Exploring the versatility of liquid phase exfoliation: producing 2d nanosheets from talcum powder, cat litter and beach sand," *2D Materials*, vol. 4, no. 2, p. 025054, 2017.

[151] J. Gallego-Juarez, "Piezoelectric ceramics and ultrasonic transducers," *Journal of Physics E: Scientific Instruments*, vol. 22, no. 10, p. 804, 1989.

[152] S. Ippolito, A. Ciesielski, and P. Samorì, "Tailoring the physicochemical properties of solution-processed transition metal dichalcogenides via molecular approaches," *Chemical Communications*, vol. 55, no. 61, pp. 8900–8914, 2019.

[153] T. J. Mason and J. P. Lorimer, *Applied sonochemistry: the uses of power ultrasound in chemistry and processing*. Wiley-Vch Weinheim, 2002.

[154] P. Turner, M. Hodnett, R. Dorey, and J. D. Carey, "Controlled sonication as a route to in-situ graphene flake size control," *Scientific reports*, vol. 9, no. 1, pp. 1–8, 2019.

[155] J. N. Coleman, "Liquid exfoliation of defect-free graphene," *Accounts of chemical research*, vol. 46, no. 1, pp. 14–22, 2013.

[156] M. Yi and Z. Shen, "A review on mechanical exfoliation for the scalable production of graphene," *Journal of Materials Chemistry A*, vol. 3, no. 22, pp. 11700–11715, 2015.

[157] F. Hennrich, R. Krupke, K. Arnold, J. A. Rojas Stütz, S. Lebedkin, T. Koch, T. Schimmel, and M. M. Kappes, "The mechanism of cavitation-induced scission of single-walled carbon nanotubes," *The Journal of Physical Chemistry B*, vol. 111, no. 8, pp. 1932–1937, 2007.

[158] R. N. Muthu, S. Rajashabala, and R. Kannan, "Hexagonal boron nitride (h-bn) nanoparticles decorated multi-walled carbon nanotubes (mwcnt) for hydrogen storage," *Renewable Energy*, vol. 85, pp. 387–394, 2016.

[159] C. C. Mayorga-Martinez, A. Ambrosi, A. Y. S. Eng, Z. Sofer, and M. Pumera, "Transition metal dichalcogenides (mos2, mose2, ws2 and wse2) exfoliation technique has strong influence upon their capacitance," *Electrochemistry Communications*, vol. 56, pp. 24–28, 2015.

[160] H. Santos and C. Lodeiro, "Ultrasound in chemistry: Analytical applications, ed. j.-l. capelo-martinez," 2009.

[161] K. Kouroupis-Agalou, A. Liscio, E. Treossi, L. Ortolani, V. Morandi, N. M. Pugno, and V. Palermo, "Fragmentation and exfoliation of 2-dimensional materials: a statistical approach," *Nanoscale*, vol. 6, no. 11, pp. 5926–5933, 2014.

[162] F. Bonaccorso, A. Bartolotta, J. N. Coleman, and C. Backes, "2d-crystal-based functional inks," *Advanced Materials*, vol. 28, no. 29, pp. 6136–6166, 2016.

[163] K. R. Paton, E. Varrla, C. Backes, R. J. Smith, U. Khan, A. O'Neill, C. Boland, M. Lotya, O. M. Istrate, P. King, *et al.*, "Scalable production of large quantities of defect-free few-layer graphene by shear exfoliation in liquids," *Nature materials*, vol. 13, no. 6, p. 624, 2014.

[164] E. Varrla, K. R. Paton, C. Backes, A. Harvey, R. J. Smith, J. McCauley, and J. N. Coleman, "Turbulence-assisted shear exfoliation of graphene using household detergent and a kitchen blender," *Nanoscale*, vol. 6, no. 20, pp. 11810–11819, 2014.

[165] S. Biccai, S. Barwich, D. Boland, A. Harvey, D. Hanlon, N. McEvoy, and J. N. Coleman, "Exfoliation of 2d materials by high shear mixing," *2D Materials*, vol. 6, no. 1, p. 015008, 2018.

[166] Y. Tominaga, K. Sato, D. Shimamoto, Y. Imai, and Y. Hotta, "Wet-jet milling-assisted exfoliation of h-bn particles with lamination structure," *Ceramics International*, vol. 41, no. 9, pp. 10512–10519, 2015.

[167] N. Rasenack and B. W. Müller, "Micron-size drug particles: common and novel micronization techniques," *Pharmaceutical development and technology*, vol. 9, no. 1, pp. 1–13, 2004.

[168] N. Omura, Y. Hotta, K. Sato, Y. Kinemuchi, S. Kume, and K. Watari, "Fabrication of stable al2o3 slurries and dense green bodies using wet jet milling," *Journal of the American Ceramic Society*, vol. 89, no. 9, pp. 2738–2743, 2006.

[169] A. T. Seyhan, Y. Göncü, O. Durukan, A. Akay, and N. Ay, "Silanization of boron nitride nanosheets (bnnss) through microfluidization and their use for producing thermally conductive and electrically insulating polymer nanocomposites," *Journal of Solid State Chemistry*, vol. 249, pp. 98–107, 2017.

[170] P. G. Karagiannidis, S. A. Hodge, L. Lombardi, F. Tomarchio, N. Decorde, S. Milana, I. Goykhman, Y. Su, S. V. Mesite, D. N. Johnstone, *et al.*, "Microfluidization of graphite and formulation of graphene-based conductive inks," *ACS nano*, vol. 11, no. 3, pp. 2742–2755, 2017.

[171] S. Bellani, E. Petroni, A. E. Del Rio Castillo, N. Curreli, B. Martín-García, R. Oropesa-Nuñez, M. Prato, and F. Bonaccorso, "Scalable production of graphene inks via wet-jet milling exfoliation for screen-printed micro-supercapacitors," *Advanced Functional Materials*, vol. 29, no. 14, p. 1807659, 2019.

[172] A. D. R. Castillo, V. Pellegrini, A. Ansaldo, F. Ricciardella, H. Sun, L. Marasco, J. Buha, Z. Dang, L. Gagliani, E. Lago, *et al.*, "High-yield production of 2d crystals by wet-jet milling," *Materials Horizons*, vol. 5, no. 5, pp. 890–904, 2018.

[173] D. Hanlon, C. Backes, E. Doherty, C. S. Cucinotta, N. C. Berner, C. Boland, K. Lee, A. Harvey, P. Lynch, Z. Gholamvand, *et al.*, "Liquid exfoliation of solvent-stabilized few-layer black phosphorus for applications beyond electronics," *Nature communications*, vol. 6, no. 1, pp. 1–11, 2015.

[174] J. R. Brent, A. K. Ganguli, V. Kumar, D. J. Lewis, P. D. McNaughter, P. O'Brien, P. Sabherwal, and A. A. Tedstone, "On the stability of surfactant-stabilised few-layer black phosphorus in aqueous media," *RSC advances*, vol. 6, no. 90, pp. 86955–86958, 2016.

[175] J.-W. T. Seo, A. A. Green, A. L. Antaris, and M. C. Hersam, "High-concentration aqueous dispersions of graphene using nonionic, biocompatible block copolymers," *The Journal of Physical Chemistry Letters*, vol. 2, no. 9, pp. 1004–1008, 2011.

[176] A. F. Barton, *CRC handbook of solubility parameters and other cohesion parameters*. CRC press, 1991.

[177] S. D. Bergin, V. Nicolosi, P. V. Streich, S. Giordani, Z. Sun, A. H. Windle, P. Ryan, N. P. P. Niraj, Z.-T. T. Wang, L. Carpenter, *et al.*, "Towards solutions of single-walled carbon nanotubes in common solvents," *Advanced Materials*, vol. 20, no. 10, pp. 1876–1881, 2008.

[178] Y. Hernandez, M. Lotya, D. Rickard, S. D. Bergin, and J. N. Coleman, "Measurement of multicomponent solubility parameters for graphene facilitates solvent discovery," *Langmuir*, vol. 26, no. 5, pp. 3208–3213, 2010.

[179] S. D. Bergin, Z. Sun, D. Rickard, P. V. Streich, J. P. Hamilton, and J. N. Coleman, "Multicomponent solubility parameters for single-walled carbon nanotube- solvent mixtures," *ACS nano*, vol. 3, no. 8, pp. 2340–2350, 2009.

[180] E. Liebermann and V. Fried, "Estimation of the excess gibbs free energy and enthalpy of mixing of binary nonassociated mixtures," *Industrial & Engineering Chemistry Fundamentals*, vol. 11, no. 3, pp. 350–354, 1972.

[181] J. N. Coleman, "Liquid-phase exfoliation of nanotubes and graphene," *Advanced Functional Materials*, vol. 19, no. 23, pp. 3680–3695, 2009.

[182] M. Rubinstein, "Polymer physics—the ugly duckling story: Will polymer physics ever become a part of "proper" physics?," *Journal of Polymer Science Part B: Polymer Physics*, vol. 48, no. 24, pp. 2548–2551, 2010.

[183] J. H. Hildebrand *et al.*, "Solubility of non-electrolytes," 1936.

[184] J. H. Hildebrand, J. M. Prausnitz, and R. Lane Scott, *Regular and related solutions: the solubility of gases, liquids, and solids*. Chapman and Hall, 1970.

[185] C. Hansen, "Three dimensional solubility parameter and solvent diffusion coefficient. importance in surface coating formulation," *Doctoral Dissertation*, 1967.

[186] T. Lindvig, M. L. Michelsen, and G. M. Kontogeorgis, "A flory–huggins model based on the hansen solubility parameters," *Fluid Phase Equilibria*, vol. 203, no. 1-2, pp. 247–260, 2002.

[187] J. Shen, Y. He, J. Wu, C. Gao, K. Keyshar, X. Zhang, Y. Yang, M. Ye, R. Vajtai, J. Lou, *et al.*, "Liquid phase exfoliation of two-dimensional materials by directly probing and matching surface tension components," *Nano letters*, vol. 15, no. 8, pp. 5449–5454, 2015.

[188] H. C. Yau, M. K. Bayazit, J. H. Steinke, and M. S. Shaffer, "Sonochemical degradation of n-methylpyrrolidone and its influence on single walled carbon nanotube dispersion," *Chemical Communications*, vol. 51, no. 93, pp. 16621–16624, 2015.

[189] A. Jawaid, D. Nepal, K. Park, M. Jespersen, A. Qualley, P. Mirau, L. F. Drummy, and R. A. Vaia, "Mechanism for liquid phase exfoliation of mos2," *Chemistry of Materials*, vol. 28, no. 1, pp. 337–348, 2016.

[190] S. P. Ogilvie, M. J. Large, G. Fratta, M. Meloni, R. Canton-Vitoria, N. Tagmatarchis, F. Massuyeau, C. P. Ewels, A. A. King, and A. B. Dalton, "Considerations for spectroscopy of liquid-exfoliated 2d materials: emerging photoluminescence of n-methyl-2-pyrrolidone," *Scientific reports*, vol. 7, no. 1, pp. 1–7, 2017.

[191] A. G. Kelly, T. Hallam, C. Backes, A. Harvey, A. S. Esmaeily, I. Godwin, J. Coelho, V. Nicolosi, J. Lauth, A. Kulkarni, *et al.*, "All-printed thin-film transistors from networks of liquid-exfoliated nanosheets," *Science*, vol. 356, no. 6333, pp. 69–73, 2017.

[192] E. C. Agency, "Candidate list of substances of very high concern for authorisation," 2016.

[193] A. Capasso, A. D. R. Castillo, H. Sun, A. Ansaldo, V. Pellegrini, and F. Bonaccorso, "Ink-jet printing of graphene for flexible electronics: an environmentally-friendly approach," *Solid State Communications*, vol. 224, pp. 53–63, 2015.

[194] J. Kim, S. Kwon, D.-H. Cho, B. Kang, H. Kwon, Y. Kim, S. O. Park, G. Y. Jung, E. Shin, W.-G. Kim, *et al.*, "Direct exfoliation and dispersion of two-dimensional materials in pure water via temperature control," *Nature communications*, vol. 6, no. 1, pp. 1–9, 2015.

[195] K.-G. Zhou, N.-N. Mao, H.-X. Wang, Y. Peng, and H.-L. Zhang, "A mixed-solvent strategy for efficient exfoliation of inorganic graphene analogues," *Angewandte Chemie International Edition*, vol. 50, no. 46, pp. 10839–10842, 2011.

[196] C. Backes, T. M. Higgins, A. Kelly, C. Boland, A. Harvey, D. Hanlon, and J. N. Coleman, "Guidelines for exfoliation, characterization and processing of layered materials produced by liquid exfoliation," *Chemistry of materials*, vol. 29, no. 1, pp. 243–255, 2017.

[197] L. Vaisman, H. D. Wagner, and G. Marom, "The role of surfactants in dispersion of carbon nanotubes," *Advances in colloid and interface science*, vol. 128, pp. 37–46, 2006.

[198] M. J. Rosen and J. T. Kunjappu, *Surfactants and interfacial phenomena*. John Wiley & Sons, 2012.

[199] W. Wenseleers, I. I. Vlasov, E. Goovaerts, E. D. Obraztsova, A. S. Lobach, and A. Bouwen, "Efficient isolation and solubilization of pristine single-walled nanotubes in bile salt micelles," *Advanced Functional Materials*, vol. 14, no. 11, pp. 1105–1112, 2004.

[200] M. Fang, K. Wang, H. Lu, Y. Yang, and S. Nutt, "Single-layer graphene nanosheets with controlled grafting of polymer chains," *Journal of Materials Chemistry*, vol. 20, no. 10, pp. 1982–1992, 2010.

[201] S. Lin and D. Blankschtein, "Role of the bile salt surfactant sodium cholate in enhancing the aqueous dispersion stability of single-walled carbon nanotubes: a molecular dynamics simulation study," *The Journal of Physical Chemistry B*, vol. 114, no. 47, pp. 15616–15625, 2010.

[202] S. Biccai, *Exfoliation and sensing Application of 2D Materials*. PhD thesis, Trinity College Dublin, 2020.

[203] A. Griffin, A. Harvey, B. Cunningham, D. Scullion, T. Tian, C.-J. Shih, M. Gruening, J. F. Donegan, E. J. Santos, C. Backes, *et al.*, "Spectroscopic size and thickness metrics for liquid-exfoliated h-bn," *Chemistry of Materials*, vol. 30, no. 6, pp. 1998–2005, 2018.

[204] B. Derjaguin and L. LD, "Theory of the stability of strongly charged lyophobic sols and of the adhesion of strongly charged particles in solutions of electrolytes," *Acta Physicochimica U.R.S.S*, vol. 14, pp. 633–662, 1941.

[205] E. J. W. Verwey, J. T. G. Overbeek, and K. Van Nes, *Theory of the stability of lyophobic colloids: the interaction of sol particles having an electric double layer*. Elsevier Publishing Company, 1948.

[206] H. Ohshima, "The derjaguin–landau–verwey–overbeek (dlvo) theory of colloid stability," *Electrical Phenomena at Interfaces and Biointerfaces: Fundamentals and Applications in Nano-, Bio-, and Environmental Sciences*, p. 27, 2012.

[207] J. N. Israelachvili, *Intermolecular and surface forces*. Academic press, 2015.

[208] B. White, S. Banerjee, S. O'Brien, N. J. Turro, and I. P. Herman, "Zeta-potential measurements of surfactant-wrapped individual single-walled carbon nanotubes," *The Journal of Physical Chemistry C*, vol. 111, no. 37, pp. 13684–13690, 2007.

[209] H. C. Hamaker, "The london—van der waals attraction between spherical particles," *physica*, vol. 4, no. 10, pp. 1058–1072, 1937.

[210] W. B. Russel, W. Russel, D. A. Saville, and W. R. Schowalter, *Colloidal dispersions*. Cambridge university press, 1991.

[211] A. Kumar and C. K. Dixit, "Methods for characterization of nanoparticles," in *Advances in Nanomedicine for the Delivery of Therapeutic Nucleic Acids*, pp. 43–58, Elsevier, 2017.

[212] C. Backes, R. J. Smith, N. McEvoy, N. C. Berner, D. McCloskey, H. C. Nerl, A. O'Neill, P. J. King, T. Higgins, D. Hanlon, *et al.*, "Edge and confinement effects allow in situ measurement of size and thickness of liquid-exfoliated nanosheets," *Nature communications*, vol. 5, no. 1, pp. 1–10, 2014.

[213] M. J. Large, S. P. Ogilvie, A. Amorim Graf, P. J. Lynch, M. A. O'Mara, T. Waters, I. Jurewicz, J. P. Salvage, and A. B. Dalton, "Large-scale surfactant exfoliation of graphene and conductivity-optimized graphite enabling wireless connectivity," *Advanced Materials Technologies*, p. 2000284, 2020.

[214] M. V. Bracamonte, G. I. Lacconi, S. E. Urreta, and L. E. F. Foa Torres, "On the nature of defects in liquid-phase exfoliated graphene," *The Journal of Physical Chemistry C*, vol. 118, no. 28, pp. 15455–15459, 2014.

[215] P. May, U. Khan, A. O'Neill, and J. N. Coleman, "Approaching the theoretical limit for reinforcing polymers with graphene," *Journal of Materials Chemistry*, vol. 22, no. 4, pp. 1278–1282, 2012.

[216] T. F. Jaramillo, K. P. Jørgensen, J. Bonde, J. H. Nielsen, S. Horch, and I. Chorkendorff, "Identification of active edge sites for electrochemical h2 evolution from mos2 nanocatalysts," *science*, vol. 317, no. 5834, pp. 100–102, 2007.

[217] A. A. Green and M. C. Hersam, "Ultracentrifugation of single-walled nanotubes," *Materials Today*, vol. 10, no. 12, pp. 59–60, 2007.

[218] X. Zhang, Z. Lai, C. Tan, and H. Zhang, "Solution-processed two-dimensional mos2 nanosheets: preparation, hybridization, and applications," *Angewandte Chemie International Edition*, vol. 55, no. 31, pp. 8816–8838, 2016.

[219] T. Svedberg and K. Pederson, "The ultracentrifuge," *Oxford*, 1940.

[220] C. Backes, B. M. Szydłowska, A. Harvey, S. Yuan, V. Vega-Mayoral, B. R. Davies, P.-l. Zhao, D. Hanlon, E. J. Santos, M. I. Katsnelson, *et al.*, "Production of highly monolayer enriched dispersions of liquid-exfoliated nanosheets by liquid cascade centrifugation," *Acs Nano*, vol. 10, no. 1, pp. 1589–1601, 2016.

[221] S. Barwich, U. Khan, and J. N. Coleman, "A technique to pretreat graphite which allows the rapid dispersion of defect-free graphene in solvents at high concentration," *The Journal of Physical Chemistry C*, vol. 117, no. 37, pp. 19212–19218, 2013.

[222] J. Kang, J.-W. T. Seo, D. Alducin, A. Ponce, M. J. Yacaman, and M. C. Hersam, "Thickness sorting of two-dimensional transition metal dichalcogenides via copolymer-assisted density gradient ultracentrifugation," *Nature communications*, vol. 5, p. 5478, 2014.

[223] C. Backes, D. Campi, B. M. Szydlowska, K. Synnatschke, E. Ojala, F. Rashvand, A. Harvey, A. Griffin, Z. Sofer, N. Marzari, *et al.*, "Equipartition of energy defines the size–thickness relationship in liquid-exfoliated nanosheets," *ACS nano*, vol. 13, no. 6, pp. 7050–7061, 2019.

[224] M. A. A. Soltan, *An investigation into the history of the airbrush and the impact of the conservation treatment of airbrushed canvas paintings*. PhD thesis, Northumbria University, 2015.

[225] N. Ferrer-Anglada, M. Kaempgen, V. Skákalová, U. Dettlaf-Weglikowska, and S. Roth, "Synthesis and characterization of carbon nanotube-conducting polymer thin films," *Diamond and Related Materials*, vol. 13, no. 2, pp. 256–260, 2004.

[226] M. Kaempgen, G. Duesberg, and S. Roth, "Transparent carbon nanotube coatings," *Applied surface science*, vol. 252, no. 2, pp. 425–429, 2005.

[227] V. Scardaci, R. Coull, P. E. Lyons, D. Rickard, and J. N. Coleman, "Spray deposition of highly transparent, low-resistance networks of silver nanowires over large areas," *Small*, vol. 7, no. 18, pp. 2621–2628, 2011.

[228] M. Chen, H. Yu, S. V. Kershaw, H. Xu, S. Gupta, F. Hetsch, A. L. Rogach, and N. Zhao, "Fast, air-stable infrared photodetectors based on spray-deposited aqueous hgte quantum dots," *Advanced Functional Materials*, vol. 24, no. 1, pp. 53–59, 2014.

[229] P. Blake, P. D. Brimicombe, R. R. Nair, T. J. Booth, D. Jiang, F. Schedin, L. A. Ponomarenko, S. V. Morozov, H. F. Gleeson, E. W. Hill, *et al.*, "Graphene-based liquid crystal device," *Nano letters*, vol. 8, no. 6, pp. 1704–1708, 2008.

[230] Y. Dong and B. Pan, "A review of speckle pattern fabrication and assessment for digital image correlation," *Experimental Mechanics*, vol. 57, no. 8, pp. 1161–1181, 2017.

[231] J. W. Owen, N. A. Azarova, M. A. Loth, M. Paradinas, M. Coll, C. Ocal, J. E. Anthony, and O. D. Jurchescu, "Effect of processing parameters on performance of spray-deposited organic thin-film transistors," *Journal of Nanotechnology*, vol. 2011, 2011.

[232] F. F. Vidor, T. Meyers, G. I. Wirth, and U. Hilleringmann, "Zno nanoparticle thin-film transistors on flexible substrate using spray-coating technique," *Microelectronic Engineering*, vol. 159, pp. 155–158, 2016.

[233] A. Friederich, J. R. Binder, and W. Bauer, "Rheological control of the coffee stain effect for inkjet printing of ceramics," *Journal of the American Ceramic Society*, vol. 96, no. 7, pp. 2093–2099, 2013.

[234] H. Shi and C. Kleinstreuer, "Simulation and analysis of high-speed droplet spray dynamics," *Journal of Fluids Engineering*, vol. 129, no. 5, pp. 621–633, 2007.

[235] X. Shen, C.-M. Ho, and T.-S. Wong, "Minimal size of coffee ring structure," *The Journal of Physical Chemistry B*, vol. 114, no. 16, pp. 5269–5274, 2010.

[236] M. Majumder, C. Rendall, M. Li, N. Behabtu, J. A. Eukel, R. H. Hauge, H. K. Schmidt, and M. Pasquali, "Insights into the physics of spray coating of swnt films," *Chemical Engineering Science*, vol. 65, no. 6, pp. 2000–2008, 2010.

[237] G. V. Kaliyannan, S. V. Palanisamy, M. Palanisamy, M. Chinnasamy, S. Somasundaram, N. Nagarajan, and R. Rathanasamy, "Utilization of 2d gahnite nanosheets as highly conductive, transparent and light trapping front contact for silicon solar cells," *Applied Nanoscience*, vol. 9, no. 7, pp. 1427–1437, 2019.

[238] B. E. Kahn, "The m3d aerosol jet system, an alternative to inkjet printing for printed electronics," *Organic and Printed Electronics*, vol. 1, no. 1, pp. 14–17, 2007.

[239] N. Wilkinson, M. Smith, R. Kay, and R. Harris, "A review of aerosol jet printing—a non-traditional hybrid process for micro-manufacturing," *The International Journal of Advanced Manufacturing Technology*, vol. 105, no. 11, pp. 4599–4619, 2019.

[240] M. Smith, Y. S. Choi, C. Boughey, and S. Kar-Narayan, "Controlling and assessing the quality of aerosol jet printed features for large area and flexible electronics," *Flexible and Printed Electronics*, vol. 2, no. 1, p. 015004, 2017.

[241] Q. Huang and Y. Zhu, "Printing conductive nanomaterials for flexible and stretchable electronics: A review of materials, processes, and applications," *Advanced Materials Technologies*, vol. 4, no. 5, p. 1800546, 2019.

[242] C. Rodes, T. Smith, R. Crouse, and G. Ramachandran, "Measurements of the size distribution of aerosols produced by ultrasonic humidification," *Aerosol science and technology*, vol. 13, no. 2, pp. 220–229, 1990.

[243] T. D. Donnelly, J. Hogan, A. Mugler, M. Schubmehl, N. Schommer, A. Bernoff, S. Dasnurkar, and T. Ditmire, "Using ultrasonic atomization to produce an aerosol of micron-scale particles," *Review of scientific instruments*, vol. 76, no. 11, p. 113301, 2005.

[244] M. Ha, W. Zhang, D. Braga, M. J. Renn, C. H. Kim, and C. D. Frisbie, "Aerosol-jet-printed, 1 volt h-bridge drive circuit on plastic with integrated electrochromic pixel," *ACS applied materials & interfaces*, vol. 5, no. 24, pp. 13198–13206, 2013.

[245] E. B. Secor, "Principles of aerosol jet printing," *Flexible and Printed Electronics*, vol. 3, no. 3, p. 035002, 2018.

[246] G. W. Israel and S. Friedlander, "High-speed beams of small particles," *Journal of Colloid and Interface Science*, vol. 24, no. 3, pp. 330–337, 1967.

[247] S. Li, J. G. Park, S. Wang, R. Liang, C. Zhang, and B. Wang, "Working mechanisms of strain sensors utilizing aligned carbon nanotube network and aerosol jet printed electrodes," *Carbon*, vol. 73, pp. 303–309, 2014.

[248] A. Mahajan, C. D. Frisbie, and L. F. Francis, "Optimization of aerosol jet printing for high-resolution, high-aspect ratio silver lines," *ACS applied materials & interfaces*, vol. 5, no. 11, pp. 4856–4864, 2013.

[249] J. Q. Feng, "Sessile drop deformations under an impinging jet," *Theoretical and Computational Fluid Dynamics*, vol. 29, no. 4, pp. 277–290, 2015.

[250] B. Derby, "Inkjet printing of functional and structural materials: fluid property requirements, feature stability, and resolution," *Annual Review of Materials Research*, vol. 40, pp. 395–414, 2010.

[251] T. Seifert, E. Sowade, F. Roscher, M. Wiemer, T. Gessner, and R. R. Baumann, "Additive manufacturing technologies compared: morphology of deposits of silver ink using inkjet and aerosol jet printing," *Industrial & Engineering Chemistry Research*, vol. 54, no. 2, pp. 769–779, 2015.

[252] A. A. Gupta, A. Bolduc, S. G. Cloutier, and R. Izquierdo, "Aerosol jet printing for printed electronics rapid prototyping," in *2016 IEEE International Symposium on Circuits and systems (ISCAS)*, pp. 866–869, IEEE, 2016.

[253] L. J. Deiner and T. L. Reitz, "Inkjet and aerosol jet printing of electrochemical devices for energy conversion and storage," *Advanced Engineering Materials*, vol. 19, no. 7, p. 1600878, 2017.

[254] R. Liu, H. Ding, J. Lin, F. Shen, Z. Cui, and T. Zhang, "Fabrication of platinum-decorated single-walled carbon nanotube based hydrogen sensors by aerosol jet printing," *Nanotechnology*, vol. 23, no. 50, p. 505301, 2012.

[255] S. Lu, J. A. Cardenas, R. Worsley, N. X. Williams, J. B. Andrews, C. Casiraghi, and A. D. Franklin, "Flexible, print-in-place 1d–2d thin-film transistors using aerosol jet printing," *ACS nano*, vol. 13, no. 10, pp. 11263–11272, 2019.

[256] H.-H. Perkampus, *UV-VIS Spectroscopy and its Applications*. Springer Science & Business Media, 2013.

[257] F. S. Rocha, A. J. Gomes, C. N. Lunardi, S. Kaliaguine, and G. S. Patience, "Experimental methods in chemical engineering: Ultraviolet visible spectroscopy—uv-vis," *The Canadian Journal of Chemical Engineering*, vol. 96, no. 12, pp. 2512–2517, 2018.

[258] Varian Inc, *Cary 6000i Preliminary performance Data*.

[259] A. O'Neill, U. Khan, and J. N. Coleman, "Preparation of high concentration dispersions of exfoliated mos2 with increased flake size," *Chemistry of Materials*, vol. 24, no. 12, pp. 2414–2421, 2012.

[260] G. F. Bassani and G. P. Parravicini, *Electronic states and optical transitions in solids*, vol. 8. Pergamon, 1975.

[261] P. Bouguer, *Optical test on the dimming of the light*. Claude Jombert's, ruë S. Jacques, at the corner of the Mathurins ruë, at Image Notre Dame, 1729.

[262] J. H. Lambert, *Photometria sive de mensura et gradibus luminis, colorum et umbrae*. Klett, 1760.

[263] A. Beer, "Determination of the absorption of red light in colored liquids," *Ann. Physics*, vol. 162, pp. 78–88, 1852.

[264] A. Harvey, C. Backes, J. B. Boland, X. He, A. Griffin, B. Szydlowska, C. Gabbett, J. F. Donegan, and J. N. Coleman, "Non-resonant light scattering in dispersions of 2d nanosheets," *Nature communications*, vol. 9, no. 1, pp. 1–11, 2018.

[265] C. V. Raman and K. S. Krishnan, "A new type of secondary radiation," *Nature*, vol. 121, no. 3048, pp. 501–502, 1928.

[266] H. A. Szymanski, *Raman spectroscopy: theory and practice*. Springer Science & Business Media, 2012.

[267] K. J. Ember, M. A. Hoeve, S. L. McAughtrie, M. S. Bergholt, B. J. Dwyer, M. M. Stevens, K. Faulds, S. J. Forbes, and C. J. Campbell, "Raman spectroscopy and regenerative medicine: a review," *NPJ Regenerative medicine*, vol. 2, no. 1, pp. 1–10, 2017.

[268] A. Jorio, M. S. Dresselhaus, R. Saito, and G. Dresselhaus, *Raman spectroscopy in graphene related systems*. John Wiley & Sons, 2011.

[269] G. Keresztury, "R aman spectroscopy: Theory," *Handbook of vibrational spectroscopy*, 2006.

[270] J. B. Boland, R. Tian, A. Harvey, V. Vega-Mayoral, A. Griffin, D. V. Horvath, C. Gabbett, M. Breshears, J. Pepper, Y. Li, *et al.*, "Liquid phase exfoliation of ges nanosheets in ambient conditions for lithium ion battery applications," *2D Materials*, vol. 7, no. 3, p. 035015, 2020.

[271] J. Laudenbach, D. Schmid, F. Herziger, F. Hennrich, M. Kappes, M. Muoth, M. Haluska, F. Hof, C. Backes, F. Hauke, *et al.*, "Diameter dependence of the defect-induced raman modes in functionalized carbon nanotubes," *Carbon*, vol. 112, pp. 1–7, 2017.

[272] B. Inkson, "Scanning electron microscopy (sem) and transmission electron microscopy (tem) for materials characterization," in *Materials characterization using nondestructive evaluation (NDE) methods*, pp. 17–43, Elsevier, 2016.

[273] L. d. Broglie, "Xxxv. a tentative theory of light quanta," *The London, Edinburgh, and Dublin Philosophical Magazine and Journal of Science*, vol. 47, no. 278, pp. 446–458, 1924.

[274] J. C. Spence, *High-resolution electron microscopy*. OUP Oxford, 2013.

[275] H. Kohl and L. Reimer, *Transmission electron microscopy: physics of image formation*. Springer, 2008.

[276] A. Bogner, P.-H. Jouneau, G. Thollet, D. Basset, and C. Gauthier, "A history of scanning electron microscopy developments: towards "wet-stem" imaging," *Micron*, vol. 38, no. 4, pp. 390–401, 2007.

[277] T. H. Maugh II, "James hillier, 91; designed first practical electron microscope," *LA Times*, Jan 2007.

[278] L. Reimer, "Scanning electron microscopy: physics of image formation and microanalysis," 2000.

[279] W. Zhou, R. Apkarian, Z. L. Wang, and D. Joy, "Fundamentals of scanning electron microscopy (sem)," in *Scanning microscopy for nanotechnology*, pp. 1–40, Springer, 2006.

[280] P. J. Goodhew and J. Humphreys, *Electron microscopy and analysis*. CRC Press, 2000.

[281] M. Knoll and E. Ruska, "Das elektronenmikroskop," *Zeitschrift für physik*, vol. 78, no. 5-6, pp. 318–339, 1932.

[282] D. J. Smith, "Ultimate resolution in the electron microscope?," *Materials Today*, vol. 11, pp. 30–38, 2008.

[283] D. B. Williams and C. B. Carter, "Transmission electron microscopy: a textbook for materials science. 2009."

[284] W. Escovitz, T. Fox, and R. Levi-Setti, "Scanning transmission ion microscope with a field ion source," *Proceedings of the National Academy of Sciences*, vol. 72, no. 5, pp. 1826–1828, 1975.

[285] S. Reyntjens and R. Puers, "A review of focused ion beam applications in microsystem technology," *Journal of micromechanics and microengineering*, vol. 11, no. 4, p. 287, 2001.

[286] A. Rigort and J. M. Plitzko, "Cryo-focused-ion-beam applications in structural biology," *Archives of biochemistry and biophysics*, vol. 581, pp. 122–130, 2015.

[287] L. A. Giannuzzi *et al.*, *Introduction to focused ion beams: instrumentation, theory, techniques and practice*. Springer Science & Business Media, 2004.

[288] J. Orloff, L. Swanson, and M. Utlaut, *High resolution focused ion beams: FIB and its applications: Fib and its applications: the physics of liquid metal ion sources and ion optics and their application to focused ion beam technology*. Springer Science & Business Media, 2003.

[289] P. R. Munroe, "The application of focused ion beam microscopy in the material sciences," *Materials characterization*, vol. 60, no. 1, pp. 2–13, 2009.

[290] L. Frey, C. Lehrer, and H. Ryssel, "Nanoscale effects in focused ion beam processing," *Applied physics A*, vol. 76, no. 7, pp. 1017–1023, 2003.

[291] M. Nastasi, N. Michael, J. Mayer, J. K. Hirvonen, and M. James, *Ion-solid interactions: fundamentals and applications*. Cambridge University Press, 1996.

[292] S. Matteson, "Atomic mixing in ion impact: A collision cascade model," *Applied Physics Letters*, vol. 39, no. 3, pp. 288–290, 1981.

[293] C. A. Volkert and A. M. Minor, "Focused ion beam microscopy and micromachining," *MRS bulletin*, vol. 32, no. 5, pp. 389–399, 2007.

[294] S. Peng, L. Li, X. Han, W. Sun, M. Srinivasan, S. G. Mhaisalkar, F. Cheng, Q. Yan, J. Chen, and S. Ramakrishna, "Cobalt sulfide nanosheet/graphene/carbon nanotube nanocomposites as flexible electrodes for hydrogen evolution," *Angewandte Chemie*, vol. 126, no. 46, pp. 12802–12807, 2014.

[295] J. B. Boland, A. Harvey, R. Tian, D. Hanlon, V. Vega-Mayoral, B. Szydlowska, A. Griffin, T. Stimpel-Lindner, S. Jaskaniec, V. Nicolosi, *et al.*, "Liquid phase exfoliation of moo 2 nanosheets for lithium ion battery applications," *Nanoscale Advances*, vol. 1, no. 4, pp. 1560–1570, 2019.

[296] R. J. Young, I. A. Kinloch, L. Gong, and K. S. Novoselov, "The mechanics of graphene nanocomposites: a review," *Composites Science and Technology*, vol. 72, no. 12, pp. 1459–1476, 2012.

[297] F. Torrisi and J. N. Coleman, "Electrifying inks with 2d materials," *Nature nanotechnology*, vol. 9, no. 10, pp. 738–739, 2014.

[298] Z. Lin, Y. Huang, and X. Duan, "Van der waals thin-film electronics," *Nature Electronics*, vol. 2, no. 9, pp. 378–388, 2019.

[299] R. Karthick and F. Chen, "Free-standing graphene paper for energy application: Progress and future scenarios," *Carbon*, vol. 150, pp. 292–310, 2019.

[300] Y. Yuan, G. Giri, A. L. Ayzner, A. P. Zoombelt, S. C. Mannsfeld, J. Chen, D. Nordlund, M. F. Toney, J. Huang, and Z. Bao, "Ultra-high mobility transparent organic thin film transistors grown by an off-centre spin-coating method," *Nature communications*, vol. 5, no. 1, pp. 1–9, 2014.

[301] C. R. Newman, C. D. Frisbie, D. A. da Silva Filho, J.-L. Brédas, P. C. Ewbank, and K. R. Mann, "Introduction to organic thin film transistors and design of n-channel organic semiconductors," *Chemistry of materials*, vol. 16, no. 23, pp. 4436–4451, 2004.

[302] D. V. Talapin, J.-S. Lee, M. V. Kovalenko, and E. V. Shevchenko, "Prospects of colloidal nanocrystals for electronic and optoelectronic applications," *Chemical reviews*, vol. 110, no. 1, pp. 389–458, 2010.

[303] L. Hu, H. S. Kim, J.-Y. Lee, P. Peumans, and Y. Cui, "Scalable coating and properties of transparent, flexible, silver nanowire electrodes," *ACS nano*, vol. 4, no. 5, pp. 2955–2963, 2010.

[304] L. Xiang, H. Zhang, G. Dong, D. Zhong, J. Han, X. Liang, Z. Zhang, L.-M. Peng, and Y. Hu, "Low-power carbon nanotube-based integrated circuits that can be transferred to biological surfaces," *Nature Electronics*, vol. 1, no. 4, pp. 237–245, 2018.

[305] Z. Lin, Y. Chen, A. Yin, Q. He, X. Huang, Y. Xu, Y. Liu, X. Zhong, Y. Huang, and X. Duan, "Solution processable colloidal nanoplates as building blocks for high-performance electronic thin films on flexible substrates," *Nano letters*, vol. 14, no. 11, pp. 6547–6553, 2014.

[306] A. K. Geim and I. V. Grigorieva, "Van der waals heterostructures," *Nature*, vol. 499, no. 7459, pp. 419–425, 2013.

[307] S. Haigh, A. Gholinia, R. Jalil, S. Romani, L. Britnell, D. Elias, K. Novoselov, L. Ponomarenko, A. Geim, and R. Gorbachev, "Cross-sectional imaging of individual layers and buried interfaces of graphene-based heterostructures and superlattices," *Nature materials*, vol. 11, no. 9, pp. 764–767, 2012.

[308] Z. Lin, Y. Liu, U. Halim, M. Ding, Y. Liu, Y. Wang, C. Jia, P. Chen, X. Duan, C. Wang, *et al.*, "Solution-processable 2d semiconductors for high-performance large-area electronics," *Nature*, vol. 562, no. 7726, pp. 254–258, 2018.

[309] K. Lee, H.-Y. Kim, M. Lotya, J. N. Coleman, G.-T. Kim, and G. S. Duesberg, "Electrical characteristics of molybdenum disulfide flakes produced by liquid exfoliation," *Advanced materials*, vol. 23, no. 36, pp. 4178–4182, 2011.

[310] D. O'Suilleabhain, V. Vega-Mayoral, A. G. Kelly, A. Harvey, and J. N. Coleman, "Percolation effects in electrolytically gated ws2/graphene nano: Nano composites," *ACS applied materials & interfaces*, vol. 11, no. 8, pp. 8545–8555, 2019.

[311] F. Torrisi, T. Hasan, W. Wu, Z. Sun, A. Lombardo, T. S. Kulmala, G.-W. Hsieh, S. Jung, F. Bonaccorso, P. J. Paul, *et al.*, "Inkjet-printed graphene electronics," *ACS nano*, vol. 6, no. 4, pp. 2992–3006, 2012.

[312] J.-Y. Kim and N. A. Kotov, "Charge transport dilemma of solution-processed nanomaterials," *Chemistry of Materials*, vol. 26, no. 1, pp. 134–152, 2014.

[313] Y.-M. Niquet, V.-H. Nguyen, F. Triozon, I. Duchemin, O. Nier, and D. Rideau, "Quantum calculations of the carrier mobility: Methodology, matthiessen's rule, and comparison with semi-classical approaches," *Journal of Applied Physics*, vol. 115, no. 5, p. 054512, 2014.

[314] A. Griffin, K. Nisi, J. Pepper, A. Harvey, B. M. Szydłowska, J. N. Coleman, and C. Backes, "Effect of surfactant choice and concentration on the dimensions and yield of liquid-phase-exfoliated nanosheets," *Chemistry of Materials*, vol. 32, no. 7, pp. 2852–2862, 2020.

[315] S. Barwich, J. N. Coleman, and M. E. Möbius, "Yielding and flow of highly concentrated, few-layer graphene suspensions," *Soft Matter*, vol. 11, no. 16, pp. 3159–3164, 2015.

[316] S. Biccai, C. S. Boland, D. P. O'Driscoll, A. Harvey, C. Gabbett, D. R. O'Suilleabhain, A. J. Griffin, Z. Li, R. J. Young, and J. N. Coleman, "Negative gauge factor piezoresistive composites based on polymers filled with mos2 nanosheets," *ACS nano*, vol. 13, no. 6, pp. 6845–6855, 2019.

[317] N. Rouhi, D. Jain, and P. J. Burke, "High-performance semiconducting nanotube inks: Progress and prospects," *ACS nano*, vol. 5, no. 11, pp. 8471–8487, 2011.

[318] S. P. Schießl, X. de Vries, M. Rother, A. Massé, M. Brohmann, P. A. Bobbert, and J. Zaumseil, "Modeling carrier density dependent charge transport in semiconducting carbon nanotube networks," *Physical Review Materials*, vol. 1, no. 4, p. 046003, 2017.

[319] M. Brohmann, M. Rother, S. P. Schießl, E. Preis, S. Allard, U. Scherf, and J. Zaumseil, "Temperature-dependent charge transport in polymer-sorted semiconducting carbon nanotube networks with different diameter distributions," *The Journal of Physical Chemistry C*, vol. 122, no. 34, pp. 19886–19896, 2018.

[320] A. Malhofer, M. Rother, Y. Zakharko, A. Graf, S. P. Schießl, and J. Zaumseil, "Direct visualization of percolation paths in carbon nanotube/polymer composites," *Organic Electronics*, vol. 45, pp. 151–158, 2017.

[321] M. Brohmann, F. J. Berger, M. Matthiesen, S. P. Schießl, S. Schneider, and J. Zaumseil, "Charge transport in mixed semiconducting carbon nanotube networks with tailored mixing ratios," *ACS nano*, vol. 13, no. 6, pp. 7323–7332, 2019.

[322] D.-m. Sun, M. Y. Timmermans, Y. Tian, A. G. Nasibulin, E. I. Kauppinen, S. Kishimoto, T. Mizutani, and Y. Ohno, "Flexible high-performance carbon nanotube integrated circuits," *Nature nanotechnology*, vol. 6, no. 3, pp. 156–161, 2011.

[323] S. Colasanti, V. D. Bhatt, A. Abdelhalim, and P. Lugli, "3-d percolative model-based multiscale simulation of randomly aligned networks of carbon nanotubes," *IEEE Transactions on Electron Devices*, vol. 63, no. 3, pp. 1346–1351, 2016.

[324] G. Calabrese, L. Pimpolari, S. Conti, F. Mavier, S. Majee, R. Worsley, Z. Wang, F. Pieri, G. Basso, G. Pennelli, *et al.*, "Inkjet-printed graphene hall mobility measurements and low-frequency noise characterization," *Nanoscale*, vol. 12, no. 12, pp. 6708–6716, 2020.

[325] T. Chen, B. Skinner, W. Xie, B. Shklovskii, and U. R. Kortshagen, "Carrier transport in films of alkyl-ligand-terminated silicon nanocrystals," *The Journal of Physical Chemistry C*, vol. 118, no. 34, pp. 19580–19588, 2014.

[326] D. Lanigan and E. Thimsen, "Contact radius and the insulator–metal transition in films comprised of touching semiconductor nanocrystals," *ACS nano*, vol. 10, no. 7, pp. 6744–6752, 2016.

[327] R. Lechner, A. R. Stegner, R. N. Pereira, R. Dietmueller, M. S. Brandt, A. Ebbers, M. Trocha, H. Wiggers, and M. Stutzmann, "Electronic properties of doped silicon nanocrystal films," *Journal of Applied Physics*, vol. 104, no. 5, p. 053701, 2008.

[328] W. Aigner, O. Bienek, B. P. Falcão, S. U. Ahmed, H. Wiggers, M. Stutzmann, and R. N. Pereira, "Intra-and inter-nanocrystal charge transport in nanocrystal films," *Nanoscale*, vol. 10, no. 17, pp. 8042–8057, 2018.

[329] E. B. Secor, M. H. Dos Santos, S. G. Wallace, N. P. Bradshaw, and M. C. Hersam, "Tailoring the porosity and microstructure of printed graphene electrodes via polymer phase inversion," *The Journal of Physical Chemistry C*, vol. 122, no. 25, pp. 13745–13750, 2018.

[330] J. R. Dunklin, P. Lafargue, T. M. Higgins, G. T. Forcherio, M. Benamara, N. McEvoy, D. K. Roper, J. N. Coleman, Y. Vaynzof, and C. Backes, "Production of monolayer-rich gold-decorated 2h–ws 2 nanosheets by defect engineering," *npj 2D Materials and Applications*, vol. 1, no. 1, pp. 1–9, 2018.

[331] K. Parvez, R. Worsley, A. Alieva, A. Felten, and C. Casiraghi, "Water-based and inkjet printable inks made by electrochemically exfoliated graphene," *Carbon*, vol. 149, pp. 213–221, 2019.

[332] M. Singh, H. M. Haverinen, P. Dhagat, and G. E. Jabbour, "Inkjet printing—process and its applications," *Advanced materials*, vol. 22, no. 6, pp. 673–685, 2010.

[333] J. Zhou, G. Xu, Z. Zhang, and H. Wang, "Facile synthesis of cu 2 mos 4 nanosheet/multi-walled carbon nanotube composites as a high-efficiency electrocatalyst for hydrogen evolution," *New Journal of Chemistry*, vol. 43, no. 24, pp. 9574–9582, 2019.

[334] I. Freestone, N. Meeks, M. Sax, and C. Higgitt, "The lycurgus cup—a roman nanotechnology," *Gold bulletin*, vol. 40, no. 4, pp. 270–277, 2007.

[335] C. S. Boland, U. Khan, G. Ryan, S. Barwich, R. Charifou, A. Harvey, C. Backes, Z. Li, M. S. Ferreira, M. E. Möbius, *et al.*, "Sensitive electromechanical sensors using viscoelastic graphene-polymer nanocomposites," *Science*, vol. 354, no. 6317, pp. 1257–1260, 2016.

[336] Q. Zhang, J.-Q. Huang, W.-Z. Qian, Y.-Y. Zhang, and F. Wei, "The road for nanomaterials industry: a review of carbon nanotube production, post-treatment, and bulk applications for composites and energy storage," *Small*, vol. 9, no. 8, pp. 1237–1265, 2013.

[337] J. Sandler, J. Kirk, I. Kinloch, M. Shaffer, and A. Windle, "Ultra-low electrical percolation threshold in carbon-nanotube-epoxy composites," *Polymer*, vol. 44, no. 19, pp. 5893–5899, 2003.

[338] Z. Spitalsky, D. Tasis, K. Papagelis, and C. Galiotis, "Carbon nanotube–polymer composites: chemistry, processing, mechanical and electrical properties," *Progress in polymer science*, vol. 35, no. 3, pp. 357–401, 2010.

[339] M. Biercuk, M. C. Llaguno, M. Radosavljevic, J. Hyun, A. T. Johnson, and J. E. Fischer, "Carbon nanotube composites for thermal management," *Applied physics letters*, vol. 80, no. 15, pp. 2767–2769, 2002.

[340] T. Clyne and D. Hull, *An introduction to composite materials*. Cambridge university press, 2019.

[341] G. Lota, K. Fic, and E. Frackowiak, "Carbon nanotubes and their composites in electrochemical applications," *Energy & Environmental Science*, vol. 4, no. 5, pp. 1592–1605, 2011.

[342] W.-J. Kwak, K. C. Lau, C.-D. Shin, K. Amine, L. A. Curtiss, and Y.-K. Sun, "A mo2c/carbon nanotube composite cathode for lithium–oxygen batteries with high energy efficiency and long cycle life," *Acs Nano*, vol. 9, no. 4, pp. 4129–4137, 2015.

[343] D. Wang, X. Li, J. Yang, J. Wang, D. Geng, R. Li, M. Cai, T.-K. Sham, and X. Sun, "Hierarchical nanostructured core–shell sn@ c nanoparticles embedded in graphene nanosheets: spectroscopic view and their application in lithium ion batteries," *Physical Chemistry Chemical Physics*, vol. 15, no. 10, pp. 3535–3542, 2013.

[344] S. Zhang, L. Zhu, H. Song, X. Chen, and J. Zhou, "Enhanced electrochemical performance of mno nanowire/graphene composite during cycling as the anode material for lithium-ion batteries," *Nano Energy*, vol. 10, pp. 172–180, 2014.

[345] L. David, R. Bhandavat, and G. Singh, "Mos2/graphene composite paper for sodium-ion battery electrodes," *ACS nano*, vol. 8, no. 2, pp. 1759–1770, 2014.

[346] C. Zhu, X. Mu, P. A. van Aken, J. Maier, and Y. Yu, "Fast li storage in mos2-graphene-carbon nanotube nanocomposites: advantageous functional integration of 0d, 1d, and 2d nanostructures," *Advanced Energy Materials*, vol. 5, no. 4, p. 1401170, 2015.

[347] Y. Liu, X. He, D. Hanlon, A. Harvey, U. Khan, Y. Li, and J. N. Coleman, "Electrical, mechanical, and capacity percolation leads to high-performance mos2/nanotube composite lithium ion battery electrodes," *ACS nano*, vol. 10, no. 6, pp. 5980–5990, 2016.

[348] T. M. Higgins, D. McAteer, J. C. M. Coelho, B. M. Sanchez, Z. Gholamvand, G. Moriarty, N. McEvoy, N. C. Berner, G. S. Duesberg, V. Nicolosi, *et al.*, "Effect of percolation on the capacitance of supercapacitor electrodes prepared from composites of manganese dioxide nanoplatelets and carbon nanotubes," *ACS nano*, vol. 8, no. 9, pp. 9567–9579, 2014.

[349] D. McAteer, Z. Gholamvand, N. McEvoy, A. Harvey, E. O'Malley, G. S. Duesberg, and J. N. Coleman, "Thickness dependence and percolation scaling of hydrogen production rate in mos2 nanosheet and nanosheet–carbon nanotube composite catalytic electrodes," *ACS nano*, vol. 10, no. 1, pp. 672–683, 2016.

[350] B. Writer, "Anode materials, sei, carbon, graphite, conductivity, graphene, reversible, formation," in *Lithium-Ion Batteries*, pp. 1–71, Springer, 2019.

[351] J. Xiao, X. Wang, X.-Q. Yang, S. Xun, G. Liu, P. K. Koech, J. Liu, and J. P. Lemmon, "Electrochemically induced high capacity displacement reaction of peo/mos2/graphene nanocomposites with lithium," *Advanced Functional Materials*, vol. 21, no. 15, pp. 2840–2846, 2011.

[352] C. Gabbett, C. S. Boland, A. Harvey, V. Vega-Mayoral, R. J. Young, and J. N. Coleman, "The effect of network formation on the mechanical properties of 1d: 2d nano: nano composites," *Chemistry of Materials*, vol. 30, no. 15, pp. 5245–5255, 2018.

[353] R. Wang, C. Xu, J. Sun, Y. Liu, L. Gao, H. Yao, and C. Lin, "Heat-induced formation of porous and free-standing mos2/gs hybrid electrodes for binder-free and ultralong-life lithium ion batteries," *Nano Energy*, vol. 8, pp. 183–195, 2014.

[354] K. B. Singh and M. S. Tirumkudulu, "Cracking in drying colloidal films," *Physical review letters*, vol. 98, no. 21, p. 218302, 2007.

[355] M. S. Tirumkudulu and W. B. Russel, "Cracking in drying latex films," *Langmuir*, vol. 21, no. 11, pp. 4938–4948, 2005.

[356] H. Zheng, J. Li, X. Song, G. Liu, and V. S. Battaglia, "A comprehensive understanding of electrode thickness effects on the electrochemical performances of li-ion battery cathodes," *Electrochimica Acta*, vol. 71, pp. 258–265, 2012.

[357] D. McAteer, I. J. Godwin, Z. Ling, A. Harvey, L. He, C. S. Boland, V. Vega-Mayoral, B. Szydłowska, A. A. Rovetta, C. Backes, *et al.*, "Liquid exfoliated co (oh) 2 nanosheets as low-cost, yet high-performance, catalysts for the oxygen evolution reaction," *Advanced Energy Materials*, vol. 8, no. 15, p. 1702965, 2018.

[358] J. Huang, Z. Wang, M. Hou, X. Dong, Y. Liu, Y. Wang, and Y. Xia, "Polyaniline-intercalated manganese dioxide nanolayers as a high-performance cathode material for an aqueous zinc-ion battery," *Nature communications*, vol. 9, no. 1, pp. 1–8, 2018.

[359] Z. Xiong, Y. S. Yun, and H.-J. Jin, "Applications of carbon nanotubes for lithium ion battery anodes," *Materials*, vol. 6, no. 3, pp. 1138–1158, 2013.

[360] J. Stallard, W. Tan, F. Smail, T. Gspann, A. Boies, and N. Fleck, "The mechanical and electrical properties of direct-spun carbon nanotube mats," *Extreme Mechanics Letters*, vol. 21, pp. 65–75, 2018.

[361] A. Barhoum, P. Samyn, T. Öhlund, and A. Dufresne, "Review of recent research on flexible multifunctional nanopapers," *Nanoscale*, vol. 9, no. 40, pp. 15181–15205, 2017.

[362] Q. Cheng, J. Bao, J. Park, Z. Liang, C. Zhang, and B. Wang, "High mechanical performance composite conductor: multi-walled carbon nanotube sheet/bismaleimide nanocomposites," *Advanced Functional Materials*, vol. 19, no. 20, pp. 3219–3225, 2009.

[363] Y. Bai, R. Zhang, X. Ye, Z. Zhu, H. Xie, B. Shen, D. Cai, B. Liu, C. Zhang, Z. Jia, *et al.*, "Carbon nanotube bundles with tensile strength over 80 gpa," *Nature nanotechnology*, vol. 13, no. 7, pp. 589–595, 2018.

[364] H. Chen, L. Zhang, J. Chen, M. Becton, X. Wang, and H. Nie, "Effect of cnt length and structural density on viscoelasticity of buckypaper: A coarse-grained molecular dynamics study," *Carbon*, vol. 109, pp. 19–29, 2016.

[365] A. Moropoulou, A. Bakolas, and S. Anagnostopoulou, "Composite materials in ancient structures," *Cement and concrete composites*, vol. 27, no. 2, pp. 295–300, 2005.

[366] X. Cao, C. Tan, X. Zhang, W. Zhao, and H. Zhang, "Solution-processed two-dimensional metal dichalcogenide-based nanomaterials for energy storage and conversion," *Advanced Materials*, vol. 28, no. 29, pp. 6167–6196, 2016.

[367] C. Feng, J. Ma, H. Li, R. Zeng, Z. Guo, and H. Liu, "Synthesis of molybdenum disulfide (mos2) for lithium ion battery applications," *Materials Research Bulletin*, vol. 44, no. 9, pp. 1811–1815, 2009.

[368] V. N. Popov, "Carbon nanotubes: properties and application," *Materials Science and Engineering: R: Reports*, vol. 43, no. 3, pp. 61–102, 2004.

[369] F. Du, R. C. Scogna, W. Zhou, S. Brand, J. E. Fischer, and K. I. Winey, "Nanotube networks in polymer nanocomposites: rheology and electrical conductivity," *Macromolecules*, vol. 37, no. 24, pp. 9048–9055, 2004.

[370] Y. Li and M. Kröger, "A theoretical evaluation of the effects of carbon nanotube entanglement and bundling on the structural and mechanical properties of buckypaper," *Carbon*, vol. 50, no. 5, pp. 1793–1806, 2012.

[371] G. Cunningham, M. Lotya, N. McEvoy, G. S. Duesberg, P. van der Schoot, and J. N. Coleman, "Percolation scaling in composites of exfoliated mos 2 filled with nanotubes and graphene," *Nanoscale*, vol. 4, no. 20, pp. 6260–6264, 2012.

[372] D. R. Lide, *CRC handbook of chemistry and physics*, vol. 85. CRC press, 2004.

[373] F. M. Blighe, P. E. Lyons, S. De, W. J. Blau, and J. N. Coleman, "On the factors controlling the mechanical properties of nanotube films," *Carbon*, vol. 46, no. 1, pp. 41–47, 2008.

[374] W. Bauhofer and J. Z. Kovacs, "A review and analysis of electrical percolation in carbon nanotube polymer composites," *Composites Science and Technology*, vol. 69, no. 10, pp. 1486–1498, 2009.

[375] D. Stauffer and A. Aharony, *Introduction to percolation theory*. Taylor & Francis, 2018.

[376] I. Balberg, "Limits on the continuum-percolation transport exponents," *Physical Review B*, vol. 57, no. 21, p. 13351, 1998.

[377] N. Johner, C. Grimaldi, I. Balberg, and P. Ryser, "Transport exponent in a three-dimensional continuum tunneling-percolation model," *Physical Review B*, vol. 77, no. 17, p. 174204, 2008.

[378] S. Giordani, S. D. Bergin, V. Nicolosi, S. Lebedkin, M. M. Kappes, W. J. Blau, and J. N. Coleman, "Debundling of single-walled nanotubes by dilution: observation of large populations of individual nanotubes in amide solvent dispersions," *The journal of physical chemistry B*, vol. 110, no. 32, pp. 15708–15718, 2006.

[379] M. van Hecke, "Jamming of soft particles: geometry, mechanics, scaling and isostaticity," *Journal of Physics: Condensed Matter*, vol. 22, no. 3, p. 033101, 2009.

[380] Y. I. Song, J. W. Lee, T. Y. Kim, H. J. Jung, Y. C. Jung, S. J. Suh, and C.-M. Yang, "Performance-determining factors in flexible transparent conducting single-wall carbon nanotube film," *Carbon Letters (Carbon Lett.)*, vol. 14, no. 4, pp. 255–258, 2013.

[381] X. Ma, Y. Zare, and K. Y. Rhee, "A two-step methodology to study the influence of aggregation/agglomeration of nanoparticles on young's modulus of polymer nanocomposites," *Nanoscale research letters*, vol. 12, no. 1, p. 621, 2017.

[382] D. G. Papageorgiou, Z. Li, M. Liu, I. A. Kinloch, and R. J. Young, "Mechanisms of mechanical reinforcement by graphene and carbon nanotubes in polymer nanocomposites," *Nanoscale*, 2020.

[383] R. J. Young, M. Liu, I. A. Kinloch, S. Li, X. Zhao, C. Vallés, and D. G. Papageorgiou, "The mechanics of reinforcement of polymers by graphene nanoplatelets," *Composites Science and Technology*, vol. 154, pp. 110–116, 2018.

[384] R. J. Young and P. A. Lovell, *Introduction to polymers*. CRC press, 2011.

[385] E. Guth, "Theory of filler reinforcement," *Rubber Chemistry and Technology*, vol. 18, no. 3, pp. 596–604, 1945.

[386] J. Rosenthal, "A model for determining fiber reinforcement efficiencies and fiber orientation in polymer composites," *Polymer composites*, vol. 13, no. 6, pp. 462–466, 1992.

[387] H. Cox, "The elasticity and strength of paper and other fibrous materials," *British journal of applied physics*, vol. 3, no. 3, p. 72, 1952.

[388] L. A. Carlsson and T. Lindstrom, "A shear-lag approach to the tensile strength of paper," *Composites Science and Technology*, vol. 65, no. 2, pp. 183–189, 2005.

[389] M. Rubinstein, R. H. Colby, *et al.*, *Polymer physics*, vol. 23. Oxford university press New York, 2003.

[390] D. P. O'Driscoll, V. Vega-Mayoral, I. Harley, C. S. Boland, and J. N. Coleman, "Optimising composite viscosity leads to high sensitivity electromechancial sensors," *2D Materials*, vol. 5, no. 3, p. 035042, 2018.

[391] J. P. Lu, "Elastic properties of carbon nanotubes and nanoropes," *Physical Review Letters*, vol. 79, no. 7, p. 1297, 1997.

[392] J.-P. Salvetat, G. A. D. Briggs, J.-M. Bonard, R. R. Bacsa, A. J. Kulik, T. Stöckli, N. A. Burnham, and L. Forró, "Elastic and shear moduli of single-walled carbon nanotube ropes," *Physical review letters*, vol. 82, no. 5, p. 944, 1999.

[393] A. Kis, G. Csanyi, J.-P. Salvetat, T.-N. Lee, E. Couteau, A. Kulik, W. Benoit, J. Brugger, and L. Forro, "Reinforcement of single-walled carbon nanotube bundles by intertube bridging," *Nature materials*, vol. 3, no. 3, pp. 153–157, 2004.

[394] A. B. Dalton, S. Collins, E. Munoz, J. M. Razal, V. H. Ebron, J. P. Ferraris, J. N. Coleman, B. G. Kim, and R. H. Baughman, "Super-tough carbon-nanotube fibres," *Nature*, vol. 423, no. 6941, pp. 703–703, 2003.

[395] V. Räisänen, M. Alava, K. Niskanen, and R. Nieminen, "Does the shear-lag model apply to random fiber networks?," *Journal of materials research*, vol. 12, no. 10, pp. 2725–2732, 1997.

[396] G. T. Pham, Y.-B. Park, S. Wang, Z. Liang, B. Wang, C. Zhang, P. Funchess, and L. Kramer, "Mechanical and electrical properties of polycarbonate nanotube buckypaper composite sheets," *Nanotechnology*, vol. 19, no. 32, p. 325705, 2008.

[397] L. Berhan, Y. Yi, A. Sastry, E. Munoz, M. Selvidge, and R. Baughman, "Mechanical properties of nanotube sheets: Alterations in joint morphology and achievable moduli in manufacturable materials," *Journal of Applied Physics*, vol. 95, no. 8, pp. 4335–4345, 2004.

[398] M. L. Manchado, L. Valentini, J. Biagiotti, and J. Kenny, "Thermal and mechanical properties of single-walled carbon nanotubes–polypropylene composites prepared by melt processing," *Carbon*, vol. 43, no. 7, pp. 1499–1505, 2005.

[399] W. Sampson, "Materials properties of paper as influenced by its fibrous architecture," *International materials reviews*, vol. 54, no. 3, pp. 134–156, 2009.

[400] J. Lees, "A study of the tensile strength of short fiber reinforced plastics," *Polymer Engineering & Science*, vol. 8, no. 3, pp. 195–201, 1968.

[401] P. E. Chen, "Strength properties of discontinuous fiber composites," *Polymer Engineering & Science*, vol. 11, no. 1, pp. 51–56, 1971.

[402] R. F. Gibson, *principles of composite material mechanics 2nd Ed*. Taylor & Francis, 2007.

[403] A. Kelly and a. W. Tyson, "Tensile properties of fibre-reinforced metals: copper/tungsten and copper/molybdenum," *Journal of the Mechanics and Physics of Solids*, vol. 13, no. 6, pp. 329–350, 1965.

[404] D. Shah, "Developing plant fibre composites for structural applications by optimising composite parameters: a critical review," *Journal of Materials Science*, vol. 48, no. 18, pp. 6083–6107, 2013.

[405] T. Tsuda, T. Ogasawara, F. Deng, and N. Takeda, "Direct measurements of interfacial shear strength of multi-walled carbon nanotube/peek composite using a nano-pullout method," *Composites Science and Technology*, vol. 71, no. 10, pp. 1295–1300, 2011.

[406] M. Nie, D. M. Kalyon, K. Pochiraju, and F. T. Fisher, "A controllable way to measure the interfacial strength between carbon nanotube and polymer using a nanobridge structure," *Carbon*, vol. 116, pp. 510–517, 2017.

[407] M. Falvo, R. Taylor Ii, A. Helser, V. Chi, F. P. Brooks Jr, S. Washburn, and R. Superfine, "Nanometre-scale rolling and sliding of carbon nanotubes," *Nature*, vol. 397, no. 6716, pp. 236–238, 1999.

[408] T. Xiao, Y. Ren, K. Liao, P. Wu, F. Li, and H. Cheng, "Determination of tensile strength distribution of nanotubes from testing of nanotube bundles," *Composites science and technology*, vol. 68, no. 14, pp. 2937–2942, 2008.

[409] F. Li, H. Cheng, S. Bai, G. Su, and M. Dresselhaus, "Tensile strength of single-walled carbon nanotubes directly measured from their macroscopic ropes," *Applied physics letters*, vol. 77, no. 20, pp. 3161–3163, 2000.

[410] J. J. Vilatela, J. A. Elliott, and A. H. Windle, "A model for the strength of yarn-like carbon nanotube fibers," *Acs Nano*, vol. 5, no. 3, pp. 1921–1927, 2011.

[411] U. Khan, P. May, A. O'Neill, J. J. Vilatela, A. H. Windle, and J. N. Coleman, "Tuning the mechanical properties of composites from elastomeric to rigid thermoplastic by controlled addition of carbon nanotubes," *Small*, vol. 7, no. 11, pp. 1579–1586, 2011.

[412] F. M. Blighe, W. J. Blau, and J. N. Coleman, "Towards tough, yet stiff, composites by filling an elastomer with single-walled nanotubes at very high loading levels," *Nanotechnology*, vol. 19, no. 41, p. 415709, 2008.

[413] S. Borodulina, A. Kulachenko, M. Nygårds, and S. Galland, "Stress-strain curve of paper revisited," *Nordic pulp & paper research journal*, vol. 27, no. 2, pp. 318–328, 2012.

[414] B. Malmberg, "Relationships between properties of laboratory handsheets pressed with different wet pressures," *SVENSK PAPPERSTIDNING-NORDISK CELLULOSA*, vol. 73, no. 10, p. 334, 1970.

[415] R. Seth and D. Page, "The stress-strain curve of paper," *The role of fundamental research in paper making, mechanical engineering publication*, pp. 421–45, 1981.

[416] P. M. Ajayan, L. S. Schadler, C. Giannaris, and A. Rubio, "Single-walled carbon nanotube–polymer composites: strength and weakness," *Advanced materials*, vol. 12, no. 10, pp. 750–753, 2000.

[417] H. D. Wagner, P. M. Ajayan, and K. Schulte, "Nanocomposite toughness from a pull-out mechanism," *Composites Science and Technology*, vol. 83, pp. 27–31, 2013.

[418] J. Wu and D. McLachlan, "Percolation exponents and thresholds obtained from the nearly ideal continuum percolation system graphite-boron nitride," *Physical review B*, vol. 56, no. 3, p. 1236, 1997.

[419] Y. Li and M. Kröger, "Viscoelasticity of carbon nanotube buckypaper: zipping–unzipping mechanism and entanglement effects," *Soft Matter*, vol. 8, no. 30, pp. 7822–7830, 2012.

[420] X. Gao, G. Bian, and J. Zhu, "Electronics from solution-processed 2d semiconductors," *Journal of Materials Chemistry C*, vol. 7, no. 41, pp. 12835–12861, 2019.

[421] C. Backes, A. M. Abdelkader, C. Alonso, A. Andrieux-Ledier, R. Arenal, J. Azpeitia, N. Balakrishnan, L. Banszerus, J. Barjon, R. Bartali, *et al.*, "Production and processing of graphene and related materials," *2D Materials*, vol. 7, no. 2, p. 022001, 2020.

[422] Y. Nalawade, J. Pepper, A. Harvey, A. Griffin, D. Caffrey, A. G. Kelly, and J. N. Coleman, "All-printed dielectric capacitors from high permittivity, liquid-exfoliated biocl nanosheets," *ACS Applied Electronic Materials*, 2020.

[423] A. G. Kelly, V. Vega-Mayoral, J. B. Boland, and J. N. Coleman, "Whiskey-phase exfoliation: exfoliation and printing of nanosheets using irish whiskey," *2D Materials*, vol. 6, no. 4, p. 045036, 2019.

[424] S. Barwich, J. M. de Araújo, A. Rafferty, C. G. da Rocha, M. S. Ferreira, and J. N. Coleman, "On the relationship between morphology and conductivity in nanosheet networks," *Carbon*, 2020.

[425] P. He and B. Derby, "Inkjet printing ultra-large graphene oxide flakes," *2D Materials*, vol. 4, no. 2, p. 021021, 2017.

[426] Q. Lu, K.-J. Lee, K.-B. Lee, H.-T. Kim, J. Lee, N. V. Myung, and Y.-H. Choa, "Investigation of shape controlled silver nanoplates by a solvothermal process," *Journal of colloid and interface science*, vol. 342, no. 1, pp. 8–17, 2010.

[427] A. Prakash and J. Appenzeller, "Bandgap extraction and device analysis of ionic liquid gated wse2 schottky barrier transistors," *Acs Nano*, vol. 11, no. 2, pp. 1626–1632, 2017.

[428] J. Zhu, J. Wu, Y. Sun, J. Huang, Y. Xia, H. Wang, H. Wang, Y. Wang, Q. Yi, and G. Zou, "Thickness-dependent bandgap tunable molybdenum disulfide films for optoelectronics," *RSC advances*, vol. 6, no. 112, pp. 110604–110609, 2016.

[429] L. Ueberricke, J. N. Coleman, and C. Backes, "Robustness of size selection and spectroscopic size, thickness and monolayer metrics of liquid-exfoliated ws2," *physica status solidi (b)*, vol. 254, no. 11, p. 1700443, 2017.

[430] A. Raja, A. Chaves, J. Yu, G. Arefe, H. M. Hill, A. F. Rigosi, T. C. Berkelbach, P. Nagler, C. Schüller, T. Korn, *et al.*, "Coulomb engineering of the bandgap and excitons in two-dimensional materials," *Nature communications*, vol. 8, no. 1, pp. 1–7, 2017.

[431] R. R. Nair, P. Blake, A. N. Grigorenko, K. S. Novoselov, T. J. Booth, T. Stauber, N. M. Peres, and A. K. Geim, "Fine structure constant defines visual transparency of graphene," *Science*, vol. 320, no. 5881, pp. 1308–1308, 2008.

[432] K. Synnatschke, P. A. Cieslik, A. Harvey, A. Castellanos-Gomez, T. Tian, C.-J. Shih, A. Chernikov, E. J. Santos, J. N. Coleman, and C. Backes, "Length-and thickness-dependent optical response of liquid-exfoliated transition metal dichalcogenides," *Chemistry of Materials*, vol. 31, no. 24, pp. 10049–10062, 2019.

[433] A. Harvey, *Liquid-Phase Exfoliation and Characterisation of Novel Layered Materials*. PhD thesis, Trinity College Dublin, 2017.

[434] P. Hess, "Predictive modeling of intrinsic strengths for several groups of chemically related monolayers by a reference model," *Physical Chemistry Chemical Physics*, vol. 20, no. 11, pp. 7604–7611, 2018.

[435] I. M. Hutchings and G. D. Martin, *Inkjet technology for digital fabrication*. John Wiley & Sons, 2012.

[436] V. Bianchi, T. Carey, L. Viti, L. Li, E. H. Linfield, A. G. Davies, A. Tredicucci, D. Yoon, P. G. Karagiannidis, L. Lombardi, *et al.*, "Terahertz saturable absorbers from liquid phase exfoliation of graphite," *Nature communications*, vol. 8, no. 1, pp. 1–9, 2017.

[437] A. M. Gaikwad, Y. Khan, A. E. Ostfeld, S. Pandya, S. Abraham, and A. C. Arias, "Identifying orthogonal solvents for solution processed organic transistors," *Organic Electronics*, vol. 30, pp. 18–29, 2016.

[438] G. Xian, J. Zhang, L. Liu, J. Zhou, H. Liu, L. Bao, C. Shen, Y. Li, Z. Qin, and H. Yang, "Scalable preparation of water-soluble ink of few-layered wse 2 nanosheets for large-area electronics," *Chinese Physics B*, 2020.

[439] Z. Wang, Q. Li, Y. Chen, B. Cui, Y. Li, F. Besenbacher, and M. Dong, "The ambipolar transport behavior of wse 2 transistors and its analogue circuits," *NPG Asia Materials*, vol. 10, no. 8, pp. 703–712, 2018.

[440] G. Cunningham, D. Hanlon, N. McEvoy, G. S. Duesberg, and J. N. Coleman, "Large variations in both dark-and photoconductivity in nanosheet networks as nanomaterial is varied from mos 2 to wte 2," *Nanoscale*, vol. 7, no. 1, pp. 198–208, 2015.

[441] B. Marinho, M. Ghislandi, E. Tkalya, C. E. Koning, and G. de With, "Electrical conductivity of compacts of graphene, multi-wall carbon nanotubes, carbon black, and graphite powder," *Powder Technology*, vol. 221, pp. 351–358, 2012.

[442] X.-Y. Fang, X.-X. Yu, H.-M. Zheng, H.-B. Jin, L. Wang, and M.-S. Cao, "Temperature-and thickness-dependent electrical conductivity of few-layer graphene and graphene nanosheets," *Physics Letters A*, vol. 379, no. 37, pp. 2245–2251, 2015.

[443] P. N. Nirmalraj, T. Lutz, S. Kumar, G. S. Duesberg, and J. J. Boland, "Nanoscale mapping of electrical resistivity and connectivity in graphene strips and networks," *Nano letters*, vol. 11, no. 1, pp. 16–22, 2011.

[444] E. Yakimchuk, R. Soots, I. Kotin, and I. Antonova, "2d printed graphene conductive layers with high carrier mobility," *Current Applied Physics*, vol. 17, no. 12, pp. 1655–1661, 2017.

[445] Q. Lu, M. Arroyo, and R. Huang, "Elastic bending modulus of monolayer graphene," *Journal of Physics D: Applied Physics*, vol. 42, no. 10, p. 102002, 2009.

[446] Y. Shen and H. Wu, "Interlayer shear effect on multilayer graphene subjected to bending," *Applied Physics Letters*, vol. 100, no. 10, p. 101909, 2012.

[447] D.-Y. Wang, Y. Chang, Y.-X. Wang, Q. Zhang, and Z.-G. Yang, "Green water-based silver nanoplate conductive ink for flexible printed circuit," *Materials Technology*, vol. 31, no. 1, pp. 32–37, 2016.

[448] A. Klein, P. Dolatzoglou, M. Lux-Steiner, and E. Bucher, "Influence of material synthesis and doping on the transport properties of wse2 single crystals grown by selenium transport," *Solar energy materials and solar cells*, vol. 46, no. 3, pp. 175–186, 1997.

[449] A. G. Kelly, *Printed Electronics from Solution-Processed 2D Materials*. PhD thesis, Trinity College Dublin, 2018.

[450] J. H. Park, A. Rai, J. Hwang, C. Zhang, I. Kwak, S. F. Wolf, S. Vishwanath, X. Liu, M. Dobrowolska, J. Furdyna, *et al.*, "Band structure engineering of layered wse2 via one-step chemical functionalization," *ACS nano*, vol. 13, no. 7, pp. 7545–7555, 2019.

[451] J. Sun, Y. Wang, S. Guo, B. Wan, L. Dong, Y. Gu, C. Song, C. Pan, Q. Zhang, L. Gu, *et al.*, "Lateral 2d wse2 p–n homojunction formed by efficient charge-carrier-type modulation for high-performance optoelectronics," *Advanced Materials*, vol. 32, no. 9, p. 1906499, 2020.

[452] L. Yu, A. Zubair, E. J. Santos, X. Zhang, Y. Lin, Y. Zhang, and T. Palacios, "High-performance wse2 complementary metal oxide semiconductor technology and integrated circuits," *Nano letters*, vol. 15, no. 8, pp. 4928–4934, 2015.

[453] Q. Cheng, J. Pang, D. Sun, J. Wang, S. Zhang, F. Liu, Y. Chen, R. Yang, N. Liang, X. Lu, *et al.*, "Wse2 2d p-type semiconductor-based electronic devices for information technology: Design, preparation, and applications," *InfoMat*, vol. 2, no. 4, pp. 656–697, 2020.

[454] D. J. Finn, M. Lotya, G. Cunningham, R. J. Smith, D. McCloskey, J. F. Donegan, and J. N. Coleman, "Inkjet deposition of liquid-exfoliated graphene and mos 2 nanosheets for printed device applications," *Journal of Materials Chemistry C*, vol. 2, no. 5, pp. 925–932, 2014.

[455] J. Halim, E. J. Moon, P. Eklund, J. Rosen, M. W. Barsoum, and T. Ouisse, "Variable range hopping and thermally activated transport in molybdenum-based mxenes," *Physical Review B*, vol. 98, no. 10, p. 104202, 2018.

[456] D. Kong, L. T. Le, Y. Li, J. L. Zunino, and W. Lee, "Temperature-dependent electrical properties of graphene inkjet-printed on flexible materials," *Langmuir*, vol. 28, no. 37, pp. 13467–13472, 2012.

[457] Y. Myung, F. Wu, S. Banerjee, J. Park, and P. Banerjee, "Electrical conductivity of p-type biocl nanosheets," *Chemical Communications*, vol. 51, no. 13, pp. 2629–2632, 2015.

[458] M. Michel, C. Biswas, and A. B. Kaul, "High-performance ink-jet printed graphene resistors formed with environmentally-friendly surfactant-free inks for extreme thermal environments," *Applied Materials Today*, vol. 6, pp. 16–21, 2017.

[459] T. Juntunen, H. Jussila, M. Ruoho, S. Liu, G. Hu, T. Albrow-Owen, L. W. Ng, R. C. Howe, T. Hasan, Z. Sun, *et al.*, "Inkjet printed large-area flexible few-layer graphene thermoelectrics," *Advanced Functional Materials*, vol. 28, no. 22, p. 1800480, 2018.

[460] T. Carey, S. Cacovich, G. Divitini, J. Ren, A. Mansouri, J. M. Kim, C. Wang, C. Ducati, R. Sordan, and F. Torrisi, "Fully inkjet-printed two-dimensional material field-effect heterojunctions for wearable and textile electronics," *Nature communications*, vol. 8, no. 1, pp. 1–11, 2017.

[461] R. Soots, E. Yakimchuk, N. Nebogatikova, I. Kotin, and I. Antonova, "Graphene suspensions for 2d printing," *Technical Physics Letters*, vol. 42, no. 4, pp. 438–441, 2016.

[462] V. Palenskis, "Drift mobility, diffusion coefficient of randomly moving charge carriers in metals and other materials with degenerated electron gas," *World Journal of Condensed Matter Physics*, vol. 3, no. 1, 2013.

[463] C. K. Ullal, J. Shi, and R. Sundararaman, "Electron mobility in graphene without invoking the dirac equation," *American Journal of Physics*, vol. 87, no. 4, pp. 291–295, 2019.

[464] X. Lin, X. Shen, Q. Zheng, N. Yousefi, L. Ye, Y.-W. Mai, and J.-K. Kim, "Fabrication of highly-aligned, conductive, and strong graphene papers using ultralarge graphene oxide sheets," *ACS nano*, vol. 6, no. 12, pp. 10708–10719, 2012.

[465] Y. Wang, J. Wang, C. Ma, W. Qiao, and L. Ling, "Fabrication of hierarchical carbon nanosheet-based networks for physical and chemical adsorption of co2," *Journal of colloid and interface science*, vol. 534, pp. 72–80, 2019.

[466] C. Wang, Y. Zhou, M. Ge, X. Xu, Z. Zhang, and J. Jiang, "Large-scale synthesis of sno2 nanosheets with high lithium storage capacity," *Journal of the American Chemical Society*, vol. 132, no. 1, pp. 46–47, 2010.

[467] Y. Yue, N. Liu, W. Liu, M. Li, Y. Ma, C. Luo, S. Wang, J. Rao, X. Hu, J. Su, *et al.*, "3d hybrid porous mxene-sponge network and its application in piezoresistive sensor," *Nano Energy*, vol. 50, pp. 79–87, 2018.

[468] M. Farhadian, K. Raeissi, M. Golozar, S. Labbaf, T. Hajilou, and A. Barnoush, "3d-focused ion beam tomography and quantitative porosity evaluation of zro2-sio2 composite coating; amorphous sio2 as a porosity tailoring agent," *Applied Surface Science*, vol. 511, p. 145567, 2020.

[469] J. A. Taillon, C. Pellegrinelli, Y.-L. Huang, E. D. Wachsman, and L. G. Salamanca-Riba, "Improving microstructural quantification in fib/sem nanotomography," *Ultramicroscopy*, vol. 184, pp. 24–38, 2018.

[470] T. Saif, Q. Lin, A. R. Butcher, B. Bijeljic, and M. J. Blunt, "Multi-scale multi-dimensional microstructure imaging of oil shale pyrolysis using x-ray micro-tomography, automated ultra-high resolution sem, maps mineralogy and fib-sem," *Applied energy*, vol. 202, pp. 628–647, 2017.

[471] R. L. Mitchell, M. Coleman, P. Davies, L. North, E. Pope, C. Pleydell-Pearce, W. Harris, and R. Johnston, "Macro-to-nanoscale investigation of wall-plate joints in the acorn barnacle semibalanus balanoides: correlative imaging, biological form and function, and bioinspiration," *Journal of the Royal Society Interface*, vol. 16, no. 157, p. 20190218, 2019.

[472] Z. Gholamvand, D. McAteer, A. Harvey, C. Backes, and J. N. Coleman, "Electrochemical applications of two-dimensional nanosheets: the effect of nanosheet length and thickness," *Chemistry of Materials*, vol. 28, no. 8, pp. 2641–2651, 2016.

[473] L. Lavery, W. Harris, J. Gelb, and A. Merkle, "Recent advancements in 3d x-ray microscopes for additive manufacturing," *Microscopy and Microanalysis*, vol. 21, no. S3, pp. 131–132, 2015.

[474] I. Arganda-Carreras, V. Kaynig, C. Rueden, K. W. Eliceiri, J. Schindelin, A. Cardona, and H. Sebastian Seung, "Trainable weka segmentation: a machine learning tool for microscopy pixel classification," *Bioinformatics*, vol. 33, no. 15, pp. 2424–2426, 2017.

[475] X. Ronot and Y. Usson, *Imaging of nucleic acids and quantitation in photonic microscopy*. CRC Press, 2001.

[476] I. Sobel, "Camera models and machine perception," tech. rep., Computer Science Department, Technion, 1972.

[477] F. Supek, N. Škunca, J. Repar, K. Vlahoviček, and T. Šmuc, "Translational selection is ubiquitous in prokaryotes," *PLoS Genet*, vol. 6, no. 6, p. e1001004, 2010.

[478] L. Breiman, "Random forests," *Machine learning*, vol. 45, no. 1, pp. 5–32, 2001.

[479] H. Giesche, "Mercury porosimetry: a general (practical) overview," *Particle & particle systems characterization*, vol. 23, no. 1, pp. 9–19, 2006.

[480] S. Bolte and F. P. Cordelières, "A guided tour into subcellular colocalization analysis in light microscopy," *Journal of microscopy*, vol. 224, no. 3, pp. 213–232, 2006.

[481] S. P. Koenig, N. G. Boddeti, M. L. Dunn, and J. S. Bunch, "Ultrastrong adhesion of graphene membranes," *Nature nanotechnology*, vol. 6, no. 9, p. 543, 2011.

[482] A. C. De Moraes, W. J. Hyun, N. S. Luu, J.-M. Lim, K.-Y. Park, and M. C. Hersam, "Phase-inversion polymer composite separators based on hexagonal boron nitride nanosheets for high-temperature lithium-ion batteries," *ACS Applied Materials & Interfaces*, vol. 12, no. 7, pp. 8107–8114, 2020.

[483] A. R. Ubbelohde and F. A. Lewis, *Graphite and its crystal compounds*. Clarendon Press, 1960.

[484] F. Guo, M. Creighton, Y. Chen, R. Hurt, and I. Külaots, "Porous structures in stacked, crumpled and pillared graphene-based 3d materials," *Carbon*, vol. 66, pp. 476–484, 2014.

[485] C. J. Zhang, S.-H. Park, S. E. O'Brien, A. Seral-Ascaso, M. Liang, D. Hanlon, D. Krishnan, A. Crossley, N. McEvoy, J. N. Coleman, *et al.*, "Liquid exfoliation of interlayer spacing-tunable 2d vanadium oxide nanosheets: High capacity and rate handling li-ion battery cathodes," *Nano Energy*, vol. 39, pp. 151–161, 2017.

[486] C. Zheng, X. Zhou, H. Cao, G. Wang, and Z. Liu, "Synthesis of porous graphene/activated carbon composite with high packing density and large specific surface area for supercapacitor electrode material," *Journal of power sources*, vol. 258, pp. 290–296, 2014.

[487] J. Li, H. Fan, and X. Jia, "Multilayered zno nanosheets with 3d porous architectures: synthesis and gas sensing application," *The Journal of Physical Chemistry C*, vol. 114, no. 35, pp. 14684–14691, 2010.

[488] Z. Ju, Y. Zhu, X. Zhang, D. M. Lutz, Z. Fang, K. J. Takeuchi, E. S. Takeuchi, A. C. Marschilok, and G. Yu, "Understanding thickness-dependent transport kinetics in nanosheet-based battery electrodes," *Chemistry of Materials*, vol. 32, no. 4, pp. 1684–1692, 2020.

[489] A. G. Kelly, D. Finn, A. Harvey, T. Hallam, and J. N. Coleman, "All-printed capacitors from graphene-bn-graphene nanosheet heterostructures," *Applied Physics Letters*, vol. 109, no. 2, p. 023107, 2016.

[490] R. Jan, P. May, A. P. Bell, A. Habib, U. Khan, and J. N. Coleman, "Enhancing the mechanical properties of bn nanosheet–polymer composites by uniaxial drawing," *Nanoscale*, vol. 6, no. 9, pp. 4889–4895, 2014.

[491] G. Wang, J. Zhang, S. Yang, F. Wang, X. Zhuang, K. Müllen, and X. Feng, "Vertically aligned mos2 nanosheets patterned on electrochemically exfoliated graphene for high-performance lithium and sodium storage," *Advanced Energy Materials*, vol. 8, no. 8, p. 1702254, 2018.

[492] C. Zhao, P. Zhang, J. Zhou, S. Qi, Y. Yamauchi, R. Shi, R. Fang, Y. Ishida, S. Wang, A. P. Tomsia, *et al.*, "Layered nanocomposites by shear-flow-induced alignment of nanosheets," *Nature*, vol. 580, no. 7802, pp. 210–215, 2020.

[493] C. E. Ayres, B. S. Jha, H. Meredith, J. R. Bowman, G. L. Bowlin, S. C. Henderson, and D. G. Simpson, "Measuring fiber alignment in electrospun scaffolds: a user's guide to the 2d fast fourier transform approach," *Journal of Biomaterials Science, Polymer Edition*, vol. 19, no. 5, pp. 603–621, 2008.

[494] S. W. Smith *et al.*, *The scientist and engineer's guide to digital signal processing*. California Technical Pub. San Diego, 1997.

[495] Z.-Q. Liu, "Scale space approach to directional analysis of images," *Applied optics*, vol. 30, no. 11, pp. 1369–1373, 1991.

[496] S. H. Aboutalebi, M. M. Gudarzi, Q. B. Zheng, and J.-K. Kim, "Spontaneous formation of liquid crystals in ultralarge graphene oxide dispersions," *Advanced Functional Materials*, vol. 21, no. 15, pp. 2978–2988, 2011.

[497] T. Yanase, F. Uehara, I. Naito, T. Nagahama, and T. Shimada, "Healing sulfur vacancies in monolayer mos2 by high-pressure sulfur and selenium annealing: Implication for high-performance transistors," *ACS Applied Nano Materials*, 2020.

[498] C. Fager, M. Röding, A. Olsson, N. Lorén, C. von Corswant, A. Särkkä, and E. Olsson, "Optimization of fib–sem tomography and reconstruction for soft, porous, and poorly conducting materials," *Microscopy and Microanalysis*, pp. 1–9, 2020.

[499] C. Steger, "An unbiased detector of curvilinear structures," *IEEE Transactions on pattern analysis and machine intelligence*, vol. 20, no. 2, pp. 113–125, 1998.

[500] V. I. Räisänen, M. J. Alava, K. J. Niskanen, and R. M. Nieminen, "Does the shear-lag model apply to random fiber networks?," *Journal of materials research*, vol. 12, no. 10, pp. 2725–2732, 1997.

[501] J. Åström, S. Saarinen, K. Niskanen, and J. Kurkijärvi, "Microscopic mechanics of fiber networks," *Journal of applied physics*, vol. 75, no. 5, pp. 2383–2392, 1994.